PLASTIC ANISOTROPY OF HEXAGONAL CLOSED PACKED METALS

By

BRIAN W. PLUNKETT

A DISSERTATION PRESENTED TO THE GRADUATE SCHOOL
OF THE UNIVERSITY OF FLORIDA IN PARTIAL FULFILLMENT
OF THE REQUIREMENTS FOR THE DEGREE OF
DOCTOR OF PHILOSOPHY

UNIVERSITY OF FLORIDA

2005

ACKNOWLEDGMENTS

The author thanks each member of his supervisory committee for their suggestions and support. Special appreciation is extended to Dr. Oana Cazacu for her enthusiasm and support throughout the course of this study. The author also wishes to thank Dr. Jeong-Whan Yoon, Alcoa Technical Center, for advice on the implementation of material models into finite element code. The author sincerely appreciates the US Air Force Air Armament Center, Engineering Directorate (AAC/EN) for their financial support and for providing the opportunity to pursue this study, and to the Air Force Research Lab, Munitions Directorate, Computational Mechanics Branch (AFRL/MNAC) for employment and future research opportunities.

Of course, this degree would not have been possible without the moral support of fellow graduate students Mike Nixon and Stefan Soare. Saving the most important for last, the author also wishes to thank his wife Tiffany Plunkett for her love and support during the duration of this degree program, and God for all things.

TABLE OF CONTENTS

LIST OF TABLES

LIST OF FIGURES

Abstract of Dissertation Presented to the Graduate School
of the University of Florida in Partial Fulfillment of the
Requirements for the Degree of Doctor of Philosophy

PLASTIC ANISOTROPY OF HEXAGONAL CLOSED PACKED METALS

By

Brian W. Plunkett

December 2005

Chair: Oana Cazacu
Major Department: Mechanical and Aerospace Engineering

Due to the effects of twinning and texture evolution, the yield surface for hexagonal closed packed (hcp) metals displays an asymmetry between the yield in tension and compression, and significantly changes its shape with accumulated plastic deformation. Traditional initial yield criteria or hardening assumptions such as isotropic or kinematic hardening cannot accurately model these phenomena. In this dissertation, a macroscopic anisotropic model that can describe both the initial yielding and influence of evolving texture on the plastic response of hexagonal metals is proposed. Initial yielding is described by a newly developed macroscopic yield criterion that accounts for both anisotropy and asymmetry between yielding in tension and compression. The coefficients involved in this proposed yield criterion as well as the size of the elastic domain are then considered to be functions of the accumulated plastic strain. Viscoplastic self-consistent polycrystal simulations and a newly developed interpolation technique are then used to determine the evolution laws. The proposed model was

implemented into the implicit finite element code ABAQUS and used to simulate the three-dimensional deformation of a pure zirconium beam subjected to four-point bend tests along different directions with respect to the texture orientation. Comparison between predicted and measured macroscopic strain fields and beam sections shows that the proposed model describes very well the contribution of twinning to deformation.

The proposed model is then extended to include the effects of strain rate and the temperate increase within the material due to mechanical work. The proposed rate and temperature dependent model was implemented into ABAQUS/EXPLICIT and used to simulate the three-dimensional Taylor impact experiment for specimens made from pure zirconium and from a tantalum alloy. The post experiment data and simulation results are shown to be in very good agreement.

CHAPTER 1
INTRODUCTION

Weight reduction while maintaining functional requirements is one of the major goals of engineering design and manufacturing so that materials, energy, and costs are saved and environmental damage reduced. Because of their low density, thermal properties, damping capacity, fatigue properties, dimensional stability, and machinability, hexagonal closed packed (hcp) metals such as magnesium and titanium alloys offer great potential to reduce weight and thus replace the most commonly used materials, i.e., steel and polymers, plastics. Currently, the use of hcp metal sheets is restricted because of a lack of fundamental understanding of their three-dimensional flow behavior.

Plastic deformation of polycrystalline metals occurs by either slip or twinning (see Figure 1.1). Whether slip or twinning is the dominant deformation mechanism depends on which mechanism requires the least stress to initiate and sustain plastic deformation. Metals with cubic crystal symmetry have many slip systems, so twinning is usually not a significant deformation mechanism at ambient temperatures, but may become important as the temperature decreases or the strain rate increases (Blewitt et al., 1957, Huang et al., 1996). In low symmetry materials such as hcp metals, which have too few slip systems to accommodate any shape change, twinning may become a dominant mechanism. Twinning, unlike slip, is sensitive to the sign of the applied stress; i.e., if a particular twin can be formed under a shear stress, it will not be formed by a shear stress of opposite sense. Because of the polar nature of twinning, hcp materials display a strong asymmetry between the yield in tension and compression.

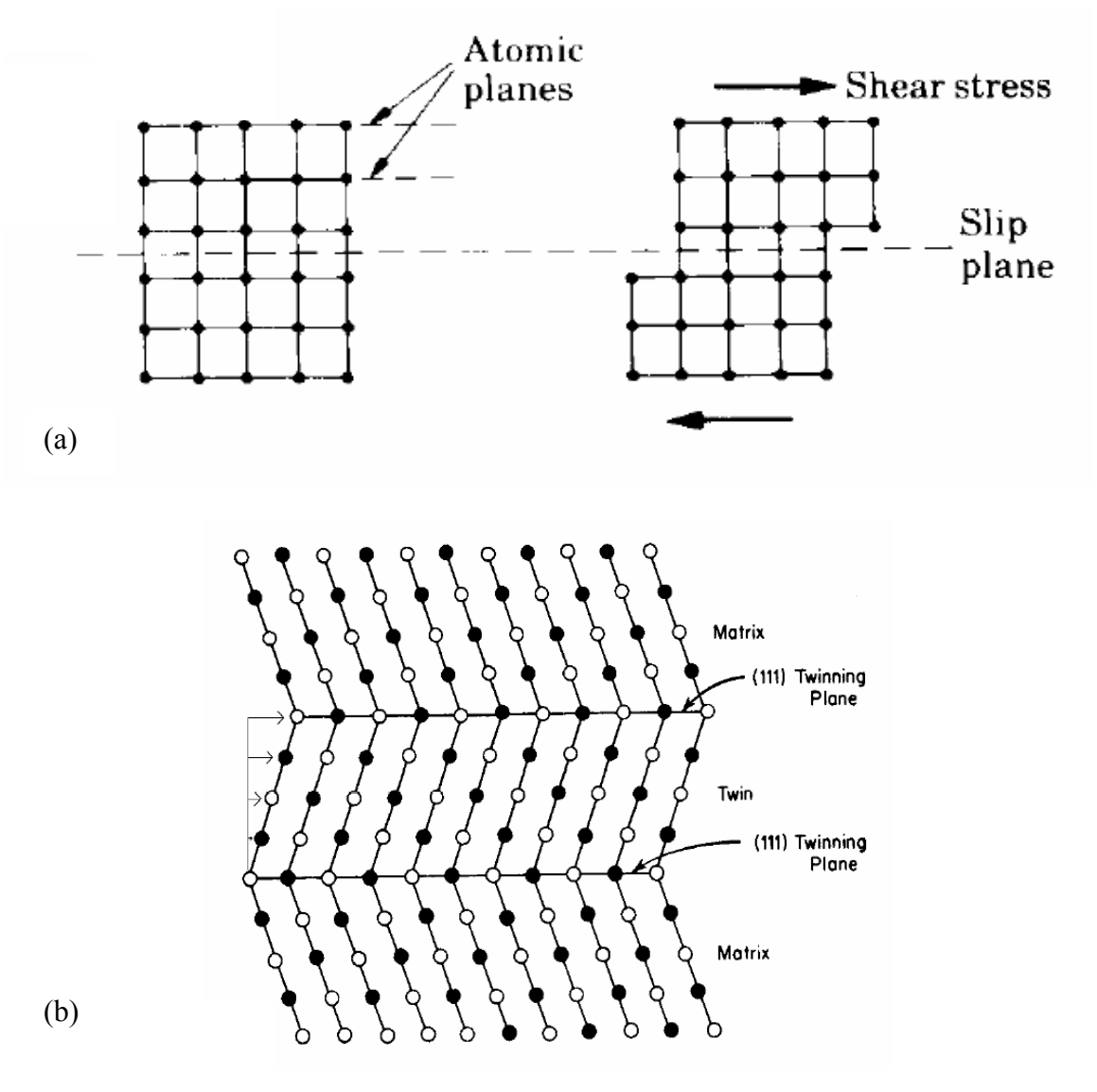

Figure 1.1 Schematic of (a) slip and (b) deformation twinning

Due to the strong crystallographic texture induced by the rolling process, the yield loci for cold rolled sheets of hcp metal may also exhibit a pronounced anisotropy (Hosford, 1993). Texture refers to the non-uniform distribution of crystallographic orientations in a polycrystalline aggregate. Most cold-rolled hcp alloy sheets have basal or nearly basal textures, i.e., the basal planes of the grains are aligned with the sheet, with a degree of spread from this ideal texture by up to $\pm 20^{o}$ about the transverse direction for

magnesium while for alpha titanium and zirconium alloys the spread is up to 40º (see Hosford, 1966). The easiest slip directions are the closed-packed $\langle 11\bar{2}0 \rangle$ directions which are normal to the c-axis, but slip on these systems does not produce any elongation or shortening parallel to the c-axis (see Figure 1.2). Thus, only twinning or pyramidal slip can allow inelastic shape changes in the ***c*** direction. For most hcp metals, the most easily activated twinning mode is the tensile twin $\{1012\} < 10\bar{1}1 >$, which is activated by compression in the plane of the sheet or tension in the normal direction of the sheet, i.e., through-thickness tension. Since the pyramidal slip and compression twinning are much harder than the primary deformation modes of basal slip and tension twinning, most hcp sheets display a resistance to thinning, and a very pronounced difference between the stress-strain behavior in tension and compression is observed (see for example, Tomé et al., 2001).

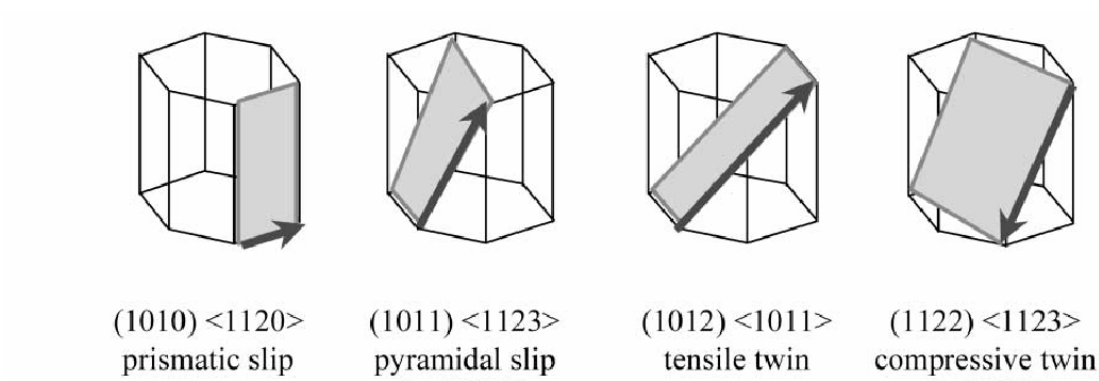

Figure 1.2 Typical deformation systems for hexagonal closed packed metals.

The correct modeling of this strong asymmetry between tension and compression due to deformation twinning remains a challenge. As discussed by Van Houtte (1978) and Tome et al. (1991), a major obstacle in extending the crystal plasticity framework to include deformation twinning is the difficulty in handling the large number of orientations created by twinned regions. Twinning activity plays an important role in the

evolution of hardening by creating barriers to the propagation of dislocations or other twin systems. In addition, twinning influences anisotropy evolution by reorienting the grains (Kaschner et al., 2001). Although progress has been made and models that track the evolution of the twinned regions in the grain and account for predominant twin reorientation (e.g. Tome and Lebensohn, 2004b) or intergranular mechanisms (e.g., Staroselsky and Anand, 2003) have been proposed, the use of such models for forming analyses is still limited because of rather large computation time.

Unlike the recent progress in the formulation, numerical implementation, and validation of macroscopic plasticity models for cubic materials, macroscopic modeling of hcp materials is less developed. Due to the lack of adequate macroscopic criteria for hcp materials, hcp sheet forming finite element simulations are still performed using classic anisotropic formulations for cubic metals such as Hill (1948) (see for example, Takuda et al., 1999; Kuwabara et al., 2001).

General presentation of the dissertation. This dissertation is a contribution to modeling and simulation of plastic anisotropy and strength differential effects in hcp metals. Chapter 2 consists of a survey of major contributions to the description of plastic behavior of metals at different length scales. Macroscopic plasticity models will be discussed including isotropic and orthotropic yield criteria that describe the onset of plastic behavior, and hardening laws which model subsequent plastic deformation. Then, two of the most widely used mesoscopic plasticity models, the Taylor-Bishop-Hill model and the viscoplastic self-consistent (vpsc) model, will be described.

Chapter 3 is devoted to the development of a new yield criterion for hcp metals. This yield function is capable of describing both the tension/compression asymmetry and

the anisotropic behavior of hcp metals and alloys. The approach used in constructing this criterion was first to develop an isotropic yield criterion that can capture the asymmetry between tension and compression, and then extend this criterion to include orthotropy. The expression of the isotropic criterion was based on numerical tests using the vpsc model. Specifically, since there are no isotropic pressure insensitive materials that exhibit tension/compression asymmetry, the vpsc model was used to obtain information concerning the shape of yield loci for randomly oriented polycrystals (isotropic) deforming by twinning (directional shear mechanism). The proposed isotropic criterion involves only two parameters k and a, where a represents the degree of homogeneity of the yield function. For a fixed, the parameter k is expressible solely in terms of the ratio between the yield stress in tension and the yield stress in compression. Comparisons with the results of polycrystalline simulations show that the proposed macroscopic criterion describes very well the strength differential effect due to twinning in body centered cubic (bcc), face centered cubic (fcc), and hcp polycrystals. An orthotropic extension of the isotropic yield criterion is developed. Orthotropy is introduced through a linear transformation applied to the deviator of the Cauchy stress tensor. Then, the yield loci obtained using the proposed orthotropic criterion are compared with experimental yield loci for sheets of textured polycrystalline binary Mg-Th, Mg-Li alloys, pure Mg (data after Kelley and Hosford, 1968), and α Titanium (data after Lee and Backofen, 1966). Very good agreement between theoretical and experimental yield loci is obtained. In addition, we compare the yield loci predicted by the proposed orthotropic criterion with the calculated yield loci obtained using the vpsc model for AZ31B magnesium and pure zirconium.

Next, in chapter 4 a new and rigorous method for describing anisotropic hardening due to evolving texture during plastic deformation is proposed. The anisotropy coefficients as well as the size of the elastic domain are considered to be functions of the accumulated plastic strain. An interpolation technique is introduced to determine the evolution laws based on the results from mechanical tests and/or numerical tests performed with polycrystal models in the absence of experimental data for the corresponding strain paths. The proposed model was implemented into the implicit finite element code ABAQUS and used to simulate the three-dimensional deformation of pure zirconium and magnesium alloys subjected to different loading conditions. Validation of the model for strain paths that have not been used for parameter identification is given for zirconium (data after Kaschner et al., 2001). Comparison between predicted and measured macroscopic strain fields and beam sections for zirconium beams subjected to 4-point bending experiments shows that the proposed model describes very well the contribution of twinning to deformation. The difference in response between the tensile and compressive fibers and the shift of the neutral axis is particularly well captured.

In chapter 5, an extension of the proposed elasto-plastic anisotropic model that includes the effect of strain-rate and temperature is presented. To introduce rate effects in the inviscid (elasto-plastic) model, two different modeling approaches are considered: the Perzyna overstress method (Perzyna, 1966) and the consistency method (Wang et al., 1997). Both approaches will be used to simulate the high strain-rate Taylor impact test. The simulated results will be compared to experimental Taylor impact tests for pure zirconium (data after Kaschner et al., 1999). For comparison purposes, we also simulated the high strain rate behavior of a metal with bcc structure (tantalum) by setting the

strength differential parameter k to zero and using isotropic hardening. The influence of the crystallographic structure on the high strain rate response was clearly demonstrated for both zirconium and tantalum. In the case of zirconium, the model reproduces correctly the very high hardening rate which is due to twinning; thus the profile of the zirconium post-test specimen displays a much less pronounced mushrooming effect. For tantalum which deforms only by slip, mushrooming is significant.

Chapter 6 is devoted to the description of plastic anisotropy in metals having cubic crystal structure. Focus is on modeling of the behavior of an aluminum alloy that exhibits strength differential effects as well as orthotropy. The proposed model is an extension to orthotropy of the isotropic yield criterion presented in Chapter 3. Two linear transformations were introduced to capture both the anisotropy in the yield stresses for tensile and compressive loadings and the Lankford coefficients (r-values). Thus, the number of independent coefficients involved in the formulation was doubled. The proposed modified criterion was then applied to the prediction of the earing profile of a circular cup drawn from 2090-T3 aluminium.

Conclusions and future research directions opened by this research are presented in Chapter 7. It is also worth mentioning that this dissertation has thus far resulted in three journal articles that have been submitted or accepted for publication in *International Journal of Plasticity* and *Acta Materialia*.

CHAPTER 2
STATE OF THE ART IN MODELING PLASTICITY OF METALS

2.1 Description of Initial Yielding

2.1.1 Isotropic Yield Criteria

For sufficiently small values of stress and strain, a metal will reassume its original shape upon unloading. When loaded beyond this reversible (elastic) range, the specimen will not reassume its original shape upon unloading, but will exhibit a permanent (plastic) deformation. In the plastic range, it is typical for metals to work harden; i.e., the flow stress monotonically increases with accumulated plastic strain. After a specimen has been subjected to a stress exceeding the yield limit which separates the elastic and plastic ranges, the current stress becomes the new yield limit if the material is unloaded. For a multi-axial state of stress, a material's yield limit is mathematically described by a yield criterion.

The oldest yield criterion was proposed by Tresca in 1864. According to Tresca's criterion, the material transitions to a plastic state when the maximum shear stress reaches a critical value. The Tresca criterion is given by

$$\max\left\{|\sigma_1 - \sigma_2|, |\sigma_2 - \sigma_3|, |\sigma_3 - \sigma_1|\right\} = Y \tag{2.1}$$

where σ_1, σ_2, and σ_3 are the principal stresses, and Y is the yield stress in uniaxial tension. The projection of Tresca's yield surface on the π-plane (the plane which passes through the origin and is perpendicular to the hydrostatic axis) is a hexagon centered on the origin whose size depends on the magnitude of Y.

Possibly the most widely used isotropic yield criterion is the one proposed independently by Huber in 1904, von Mises in 1913, and Hencky in 1924. This criterion is usually referred to as the von Mises criterion. The von Mises criterion is based on the observation that a hydrostatic pressure cannot cause yielding of the material. The plastic state corresponds to a critical value of the elastic energy of distortion, i.e.

$$J_2 = k^2 \tag{2.2}$$

where k is a constant and J_2 is the second invariant of the Cauchy stress deviator given by

$$J_2 = \frac{1}{6}\left[(\sigma_1 - \sigma_2)^2 + (\sigma_2 - \sigma_3)^2 + (\sigma_3 - \sigma_1)^2\right] \tag{2.3}$$

or alternatively,

$$J_2 = \frac{1}{2}(S_1^2 + S_2^2 + S_3^2) \tag{2.4}$$

where S_1, S_2, and S_3 are the principal values of the Cauchy stress deviator, defined as

$$S_{ij} = \sigma_{ij} - \frac{1}{3}\sigma_{kk}\delta_{ij} \qquad (i,j,k = 1,2,3) \tag{2.5}$$

The projection of the von Mises yield locus on the π-plane is a circle that circumscribes the Tresca hexagon.

Experimental evidence has shown that the yield loci for most isotropic metals with cubic crystal structure lie between the yield loci predicted by the Tresca and the von Mises criteria (see Taylor and Quinney, 1931). In order to represent the behavior of certain metals (e.g., aluminum alloys) for which the yield loci are located between the Tresca and von Mises yield loci, Drucker (1949) proposed the following criterion:

$$J_2^3 - cJ_3^2 = F \tag{2.6}$$

where J_3 is the third invariant of the Cauchy stress deviator, and c and F are material constants. In order to ensure that the yield surface is convex, c is limited to a given numerical range, $c \in [-27/8,\ 2.25]$.

Unlike the isotropic yield criteria mentioned so far, which were postulated on the basis of macroscopic experiments, Hershey in 1954 and then Hosford in 1972 used Taylor-Bishop-Hill polycrystalline simulations (for an explanation see section 2.3.2) to arrive at the following macroscopic yield criterion.

$$(\sigma_1 - \sigma_2)^m + (\sigma_2 - \sigma_3)^m + (\sigma_3 - \sigma_1)^m = 2Y^m \tag{2.7}$$

In (2.7), Y is the uniaxial yield stress and m is the degree of homogeneity which can vary between 1 and ∞. Equation 1.7 reduces to the Tresca criterion for $m = 1$ or $m = \infty$, and to the von Mises criterion for $m = 2$ or $m = 4$. It has been shown that the yield loci of fcc and bcc metals are best represented with $m = 8$ and $m = 6$ respectively (Logan and Hosford, 1980, Hosford, 1993, Hosford, 1996).

2.1.2 Orthotropic Yield Criteria

Due to thermo-mechanical processing, metal sheets exhibit orthotropic symmetry with the axes of orthotropy being aligned with the rolling direction, the transverse direction, and the normal direction to the plane of the sheet (x, y, and z, respectively). In 1948, Hill proposed a generalization of the von Mises isotropic yield criterion to orthotropy. Thus, this yield criterion is expressed by a quadratic function of the form:

$$F(\sigma_y - \sigma_z)^2 + G(\sigma_z - \sigma_x)^2 + H(\sigma_x - \sigma_y)^2 + 2L\tau_{yz}^2 + 2M\tau_{zx}^2 + 2N\tau_{xy}^2 = 1 \tag{2.8}$$

where F, G, H, L, M, and N are anisotropy constants, and x, y, and z are the orthotropy axes (axes perpendicular to the 3 mutually orthogonal planes of symmetry of the

material). When $F = G = H = 1/6k^2$ and $L = M = N = 1/2k^2$, equation (2.8) reduces to the von Mises criterion (2.2).

The coefficients involved in the expression of Hill's yield criterion can be determined from simple mechanical tests. Denoting the tensile yield stresses for the *x*, *y*, and *z* directions as *X*, *Y*, and *Z*, respectively, it can be shown that according to Hill's theory

$$X = \sqrt{\frac{1}{G+H}},\ Y = \sqrt{\frac{1}{H+F}},\ Z = \sqrt{\frac{1}{F+G}},$$

thus,

$$2F = \frac{1}{Y^2} + \frac{1}{Z^2} - \frac{1}{X^2};\ 2G = \frac{1}{Z^2} + \frac{1}{X^2} - \frac{1}{Y^2};\ 2H = \frac{1}{X^2} + \frac{1}{Y^2} - \frac{1}{Z^2} \tag{2.9}$$

Denoting the shear yield stresses as *R*, *S*, and *T* corresponding to the *yz*, *zx*, and *xy* directions respectively, then:

$$2L = \frac{1}{R^2};\ 2M = \frac{1}{S^2};\ 2N = \frac{1}{T^2} \tag{2.10}$$

The thinning resistance of metal sheets is generally characterized by the Lankford coefficients, commonly referred to as *r*-values. The Lankford coefficients are defined as the width-to-thickness strain ratio during a uniaxial test. In classic plasticity theory, the plastic strain increments are derived from a plastic potential, which for metals is generally supposed to coincide with the yield function (associated flow rule) such that

$$d\boldsymbol{\varepsilon}^p = d\lambda \frac{\partial f}{\partial \boldsymbol{\sigma}} \tag{2.11}$$

where $d\boldsymbol{\varepsilon}^p$ is the plastic strain increment, λ is a scalar variable, and *f* is the yield function. Therefore, the strain increment vector is orthogonal to the yield surface. Assuming

plastic incompressibility, the Lankford coefficient for a uniaxial tensile loading in the *x*-direction can be written as

$$r_{xx} = \frac{d\varepsilon_{yy}}{d\varepsilon_{zz}} = -\frac{d\varepsilon_{yy}}{d\varepsilon_{xx} + d\varepsilon_{yy}} = -\frac{\dfrac{\partial f}{\partial \sigma_{yy}}}{\dfrac{\partial f}{\partial \sigma_{xx}} + \dfrac{\partial f}{\partial \sigma_{yy}}} \tag{2.12}$$

Likewise, r_α, the strain ratio corresponding to a uniaxial tensile loading at an arbitrary angle, α, to the x-direction (see Figure 2.1) is given by

$$r_\alpha = -\frac{\sin^2\alpha \dfrac{\partial f}{\partial \sigma_{xx}} - \sin 2\alpha \dfrac{\partial f}{\partial \sigma_{xy}} + \cos^2\alpha \dfrac{\partial f}{\partial \sigma_{yy}}}{\dfrac{\partial f}{\partial \sigma_{xx}} + \dfrac{\partial f}{\partial \sigma_{yy}}} \tag{2.13}$$

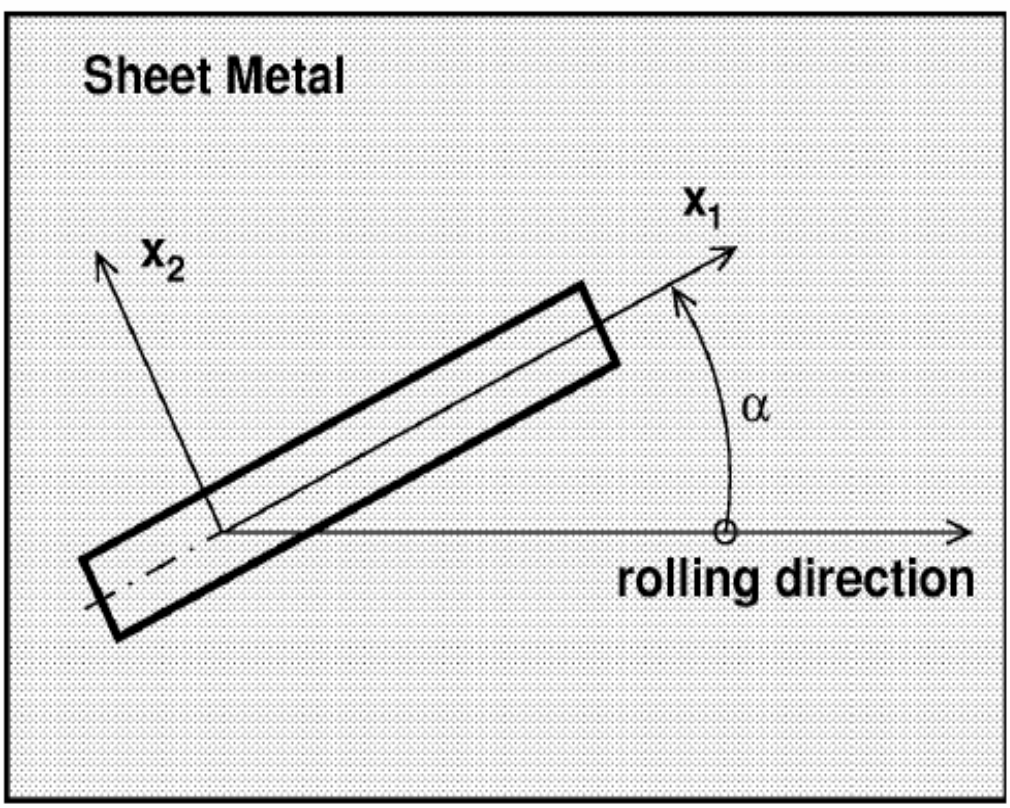

Figure 2.1 Orientation of test specimen with the rolling direction of the sheet

According to Hill's criterion, the Lankford coefficients can be expressed in terms of the anisotropy coefficients as

$$r_0 = \frac{H}{G}, \quad r_{90} = \frac{H}{F}; \quad r_{45} = \frac{N}{F+G} - \frac{1}{2} \tag{2.14}$$

Thus, the anisotropy coefficients can be expressed in terms of yield stresses in the rolling, at 45 degrees to the rolling, and in the transverse directions, or as functions of the *r*-values. In general, the yield loci obtained based on *r*-values differ from those obtained based on the yield stresses (Barlat et al., 2005).

Hill's yield criterion (2.8) is the most widely used criterion for describing yielding of textured metals. However, (2.8) can not adequately represent the behavior of certain aluminum alloys which have an average value of the Lankford coefficients less than 1 and the yield stress in biaxial tension is greater than the yield stress in uniaxial tension (Banabic et al., 2000). Therefore, in order to better represent yielding of aluminum alloys, Hill developed another yield criterion in 1979 of the form:

$$\begin{aligned} &F\left|\sigma_2 - \sigma_3\right|^m + G\left|\sigma_3 - \sigma_1\right|^m + H\left|\sigma_1 - \sigma_2\right|^m + L\left|2\sigma_1 - \sigma_2 - \sigma_3\right|^m \\ &+ M\left|2\sigma_2 - \sigma_3 - \sigma_1\right|^m + N\left|2\sigma_3 - \sigma_1 - \sigma_2\right|^m = Y^m \end{aligned} \tag{2.15}$$

This yield criterion has a major limitation since it is written in terms of the principal Cauchy stresses. In order for this criterion to be valid, the principal stress axes and anisotropy axes must be superimposed thus any state involving shear stresses cannot be accounted for.

Barlat et al. (1991) proposed a six-component yield criterion denoted Yld91, that extends the isotropic Hershey and Hosford criterion (see eq 2.7) to orthotropy. The extension to orthotropy is accomplished by replacing the principal values of the Cauchy stress tensor in the expression of the isotropic criterion by those of a transformed stress

tensor. The transformed stress tensor is obtained from the Cauchy stress tensor modified with weighting coefficients. This procedure is equivalent with the application of a fourth order linear transformation operator on the Cauchy stress tensor. The orthotropic criterion is written as

$$\left(\Sigma_1-\Sigma_2\right)^m+\left(\Sigma_2-\Sigma_3\right)^m+\left(\Sigma_3-\Sigma_1\right)^m=2Y^m \tag{2.16}$$

where

$$\boldsymbol{\Sigma}=\boldsymbol{L}\boldsymbol{\sigma}\,, \tag{2.17}$$

Σ_1, Σ_2, and Σ_3 are the principal values of the tensor $\boldsymbol{\Sigma}$, $\boldsymbol{\sigma}$ is the Cauchy stress tensor, and $\boldsymbol{L}$ is a fourth order tensor of orthotropic symmetry. Thus, with respect to (*x,y,z*) the symmetry axes,

$$\boldsymbol{L}=\frac{1}{3}\begin{bmatrix} c_2+c_3 & -c_3 & -c_2 & & & \\ -c_3 & c_3+c_1 & -c_1 & & & \\ -c_2 & -c_1 & c_1+c_2 & & & \\ & & & 3c_4 & & \\ & & & & 3c_5 & \\ & & & & & 3c_6 \end{bmatrix} \tag{2.18}$$

where c_1, c_2, c_3,…, and c_6 are constants. Note that plastic anisotropy is represented by the same number of coefficients as Hill's criterion (2.8).

In order to improve the accuracy of Yld91, Barlat et al. (1997) proposed a new orthotropic criterion (denoted Yld96) of the form:

$$\alpha_3\left(\Sigma_1-\Sigma_2\right)^m+\alpha_1\left(\Sigma_2-\Sigma_3\right)^m+\alpha_2\left(\Sigma_3-\Sigma_1\right)^m=2Y^m \tag{2.19}$$

where α_1, α_2, α_3 are functions of the principal directions of $\sum$, and are defined as

$$\alpha_k=\alpha_x p_{1k}^2+\alpha_y p_{2k}^2+\alpha_z p_{3k}^2 \tag{2.20}$$

where p_{ij} are the ith component of the kth principal direction of the tensor $\boldsymbol{\Sigma}$ with respect to the anisotropy axes of the material. Additionally, α_x, α_y, and α_z are three functions given by

$$\alpha_x = \alpha_{x0}\cos^2 2\theta_1 + \alpha_{x1}\sin^2 2\theta_1$$

$$\alpha_y = \alpha_{y0}\cos^2 2\theta_2 + \alpha_{y1}\sin^2 2\theta_2 \tag{2.21}$$

$$\alpha_z = \alpha_{z0}\cos^2 2\theta_3 + \alpha_{z1}\sin^2 2\theta_3$$

where θ_1, θ_2, and θ_3 represent the angle between the major principal directions of $\boldsymbol{\Sigma}$ and the axes of anisotropy, and the quantities α_{x0}, α_{x1}, α_{y0}, α_{y1}, α_{z0}, α_{z1} are anisotropy coefficients. The yield funtion (2.19) reduces to the yield function (2.16) if each value of α is set to unity, and further reduces to the Hershey and Hosford criterion (2.7) when $\boldsymbol{L}$ is the identity tensor.

Barlat et al. (2005) showed that any pressure independent isotropic yield function written in terms of the principal values of the Cauchy stress deviator can be generalized to anisotropy through a linear transformation acting on the Cauchy stress tensor. The principal values of the transformed tensor (2.22) will then replace the principal values of the Cauchy stress deviator from the isotropic yield criterion.

$$\boldsymbol{\Sigma} = \boldsymbol{Cs} = \boldsymbol{CT\sigma} = \boldsymbol{L\sigma} \tag{2.22}$$

Here, $\boldsymbol{\Sigma}$ is the transformed tensor, $\boldsymbol{C}$ is an anisotropic linear tensor, and $\boldsymbol{T}$ transforms the Cauchy stress tensor $\boldsymbol{\sigma}$ into its deviator $\boldsymbol{s}$. Barlat et al. (2005) also recently proposed an orthotropic yield criterion (denoted Yld2004-18p) (2.23) which involves 18 anisotropy coefficients. This orthotropic yield criterion is a generalization of the Hershey and Hosford criterion in which anisotropy is introduced through two linear transformations each containing 9 independent coefficients. The expression of this yield criterion is

$$\begin{aligned}&\left|\Sigma_1^{'}-\Sigma_1^{''}\right|^a+\left|\Sigma_1^{'}-\Sigma_2^{''}\right|^a+\left|\Sigma_1^{'}-\Sigma_3^{''}\right|^a+\\&\left|\Sigma_2^{'}-\Sigma_1^{''}\right|^a+\left|\Sigma_2^{'}-\Sigma_2^{''}\right|^a+\left|\Sigma_2^{'}-\Sigma_3^{''}\right|^a+\\&\left|\Sigma_3^{'}-\Sigma_1^{''}\right|^a+\left|\Sigma_3^{'}-\Sigma_2^{''}\right|^a+\left|\Sigma_3^{'}-\Sigma_3^{''}\right|^a=4Y^a\end{aligned} \tag{2.23}$$

where

$$\boldsymbol{\Sigma}^{'}=\boldsymbol{C}^{'}\boldsymbol{s}=\boldsymbol{C}^{'}\boldsymbol{T}\boldsymbol{\sigma}=\boldsymbol{L}^{'}\boldsymbol{\sigma} \tag{2.24}$$

and

$$\boldsymbol{\Sigma}^{''}=\boldsymbol{C}^{''}\boldsymbol{s}=\boldsymbol{C}^{''}\boldsymbol{T}\boldsymbol{\sigma}=\boldsymbol{L}^{''}\boldsymbol{\sigma} \tag{2.25}$$

When $\boldsymbol{C}^{'}=\boldsymbol{C}^{''}$ (or $\boldsymbol{L}^{'}=\boldsymbol{L}^{''}$), and the number of independent coefficients is imposed to be 6, Yld2004-18p (2.23) reduces to Yld91 (2.16). This criterion represents yield loci of aluminum alloys with increased accuracy.

Another approach to extend any isotropic criterion to anisotropy is through generalized invariants (Cazacu and Barlat, 2001 and 2003) using the theory of representation of tensor functions (e.g. Boehler, 1978 and Liu, 1982). Using the generalized invariants approach, Cazacu and Barlat (2001) extended Drucker's isotropic yield criterion to orthotropy as follows:

$$\left(J_2^0\right)^3-c\left(J_3^0\right)^2=F \tag{2.26}$$

where

$$J_2^0=\frac{a_1}{6}\left(\sigma_x-\sigma_y\right)^2+\frac{a_2}{6}\left(\sigma_y-\sigma_z\right)^2+\frac{a_3}{6}\left(\sigma_x-\sigma_z\right)^2+a_4\tau_{xy}^2+a_5\tau_{xz}^2+a_6\tau_{yz}^2 \tag{2.27}$$

and

$$
\begin{aligned}
J_3^0 = {} & \frac{1}{27}(b_1+b_2)\sigma_x^3 + \frac{1}{27}(b_3+b_4)\sigma_y^3 + 2b_{11}\sigma_{xy}\sigma_{xz}\sigma_{yz} + \frac{1}{27}(2(b_1+b_4)-b_2-b_3)\sigma_z^3 \\
& + \frac{2}{9}(b_1+b_4)\sigma_x\sigma_y\sigma_z - \frac{1}{9}(b_1\sigma_y + b_2\sigma_z)\sigma_x^2 - \frac{1}{9}(b_3\sigma_z + b_4\sigma_x)\sigma_y^2 \\
& - \frac{1}{9}\left[(b_1-b_2+b_4)\sigma_x + (b_1-b_3+b_4)\sigma_y\right]\sigma_z^2 - \frac{\sigma_{xz}^2}{3}\left[2b_9\sigma_y - b_8\sigma_z - (2b_9-b_8)\sigma_x\right] \\
& - \frac{\sigma_{xy}^2}{3}\left[2b_{10}\sigma_z - b_5\sigma_y - (2b_{10}-b_5)\sigma_x\right] - \frac{\sigma_{yz}^2}{3}\left[(b_6-b_7)\sigma_x - b_6\sigma_y - b_7\sigma_z\right]
\end{aligned}
\tag{2.28}
$$

All of the yield criteria discussed, both isotropic and anisotropic, make the assumption that yield in tension and compression coincide. This basic assumption makes these yield criteria inadequate for modeling hcp metals.

2.1.3 Modeling Asymmetry Between Tensile and Compressive Yield

To describe the asymmetry in yielding due to twinning, Cazacu and Barlat (2004) proposed an isotropic yield criterion of the form:

$$
f \equiv (J_2)^{\frac{3}{2}} - cJ_3 = F \tag{2.29}
$$

where

$$
c = \frac{3\sqrt{3}\left(\sigma_T^3 - \sigma_C^3\right)}{2\left(\sigma_T^3 + \sigma_C^3\right)}, \tag{2.30}
$$

σ_T and σ_C being the uniaxial yield stresses in tension and compression, respectively. Note that for equal yield stresses in tension and compression: $c = 0$ hence the proposed criterion reduces to the von Mises yield criterion. For the isotropic yield function (2.29) to be convex, the constant c is limited to a given numerical range: $c \in [-3\sqrt{3}/2,\ 3\sqrt{3}/4]$. For any $c \neq 0$, the yield function is homogeneous of degree 3 in stresses and equation (2.29) represents a "triangle" with rounded corners. This isotropic yield criterion was extended to include orthotropy using the generalized invariants approach and applied to the description of magnesium and its alloys. Having a fixed degree of homogeneity (of

order 3), this criterion is not flexible enough to represent yielding of certain hcp alloys which have nearly elliptical yield loci. A yield criterion capable of capturing both anisotropy and yield asymmetry between tension and compression of such materials is needed.

2.2 Hardening Laws

The plastic behavior of metal for a multi-axial state of stress is described by a yield criterion, a flow rule, and a hardening law. The two most common hardening laws are isotropic hardening and kinematic hardening (see Figure 2.2).

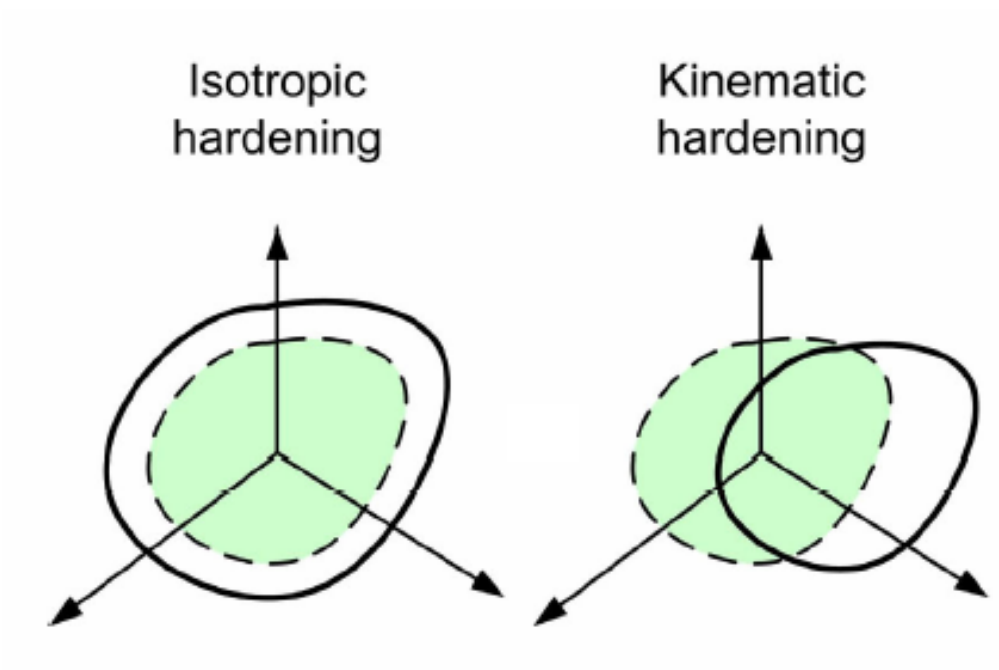

Figure 2.2 Pictorial description of various hardening rules

Isotropic hardening assumes that the yield surface maintains its shape, but it expands with accumulated plastic deformation. Generally, the size of the yield locus is given in terms of a scalar hardening variable such as the effective plastic strain in equation (2.31)

$$f(\boldsymbol{\sigma}) - Y(\bar{\varepsilon}_p) = 0 \tag{2.31}$$

where $f(\boldsymbol{\sigma})$ is the yield function that depends on the Cauchy stress, and $Y(\bar{\varepsilon}_p)$ is the hardening function that depends on the effective plastic strain, $\bar{\varepsilon}_p$. The effective plastic strain is an invariant of the plastic strain tensor, i.e., $\bar{\varepsilon}_p = \alpha\sqrt{tr\left(\varepsilon_p^2\right)}$, where α is a constant that is determined such that $\bar{\varepsilon}_p$ reduces to the strain in the loading direction for a uniaxial test. Due to its simplicity, isotropic hardening is the most common method used in sheet metal forming simulations (Yoon et al., 1999, 2000, and 2004). Since the yield loci expand without changing shape or the location of their center, isotropic hardening is a good approximation for monotonic loading along a certain strain path for materials deforming by slip. This model can not represent phenomena such as the Bauschinger effect or different strain paths hardening at different rates due to deformation twinning. The Baushcinger effect is a common phenomena in metals, and occurs when a material is deformed up to a given plastic strain, then unloaded and loaded in the reverse direction. The yield strength after the strain reversal is lower than it would have been before the first deformation step.

Introduced by Prager in 1955, kinematic hardening allows for a translation of the yield surface without changing its size or shape. Thus, if the initial yield surface $f(\boldsymbol{\sigma}) = 0$, then for a given plastic state, the yield condition is given by

$$f(\boldsymbol{\sigma} - \boldsymbol{\alpha}) = 0 \tag{2.32}$$

where $\boldsymbol{\alpha}$ (a second order tensor called the backstress tensor) defines the updated center of the yield surface. This model can be used to represent phenomena like the Bauschinger effect due to load reversals. Kinematic hardening can be used in combination with isotropic hardening to describe both expansion and translation of the yield surface during

plastic deformation. Models such as those proposed by Teodosiu et al. (1995) and Li et al. (2003) take into account other microstructural phenomena associated with changes in strain path, such as the evolution of dislocation structure in cubic metals, through the addition of other tensorial hardening variables to the kinematic hardening model.

As previously mentioned, twinning produces a major reorientation of the grains. The blockage of further slip or twinning due to grain reorientation results in higher work hardening rates for strain paths where twinning is the dominant mechanism as compared to strain paths that would involve only slip. Therefore, due to the fact that the hardening rate and the evolution of the texture depend on the strain path, the evolution of the yield surface for an hcp metal is highly anisotropic. In order to correctly model hcp metals, a hardening rule would need to allow for the distortion of the yield surface due to the evolving texture with accumulated plastic deformation.

2.3 Survey of Mesoscale Plasticity Modeling (Polycrystalline Models)

Crystalline structure is a key factor in the mechanical response of a metal since the individual crystals are anisotropic in both their elastic and plastic behaviors. Plastic deformation mechanisms within a single crystal, such as slip and twinning, are linked to crystallographic planes and directions, making the crystal strength inherently anisotropic. If a polycrytalline material contains a large number of grains whose lattice orientations are randomly distributed, the strength of the polycrystal would exhibit little if any anisotropy. However, as a result of thermomechanical processes such as cold-rolling, most metals display crystallographic texture, i.e. a patterned or a non-random lattice orientation. Therefore, the anisotropy of the polycrystal is directly related to the anisotropy of the single crystal and the distribution of the crystal lattice orientation.

Polycrystalline models that derive the polycrystal behavior from that of its constituents using homogenization techniques have been proposed. The first step in constructing such models is defining a representative volume element (rve). This volume element must be small enough to be regarded as having uniform properties (including orientation) such that stress and strain distribution within this volume be treated as homogeneous. For metallic materials, a single crystal is considered as an rve. The next step is to give a description of the behavior at the rve level and the interaction laws between each grain and its surroundings. Polycrystal models typically neglect elastic strains. The constitutive law of the single crystal consists of a kinematical relationship and an energetic assumption. The kinematical relationship, further described in the next section, relates the velocity gradient with the deformation rates of all active slip or twin systems within the crystal. There are several versions of the energetic assumption, including those of the Taylor model and the vpsc model which will be discussed in sections 2.3.2 and 2.3.3, respectively.

Assuming that the rate of deformation and stress distribution is known for each single crystal, the rate of deformation and the stress for the macroscopically homogeneous polycrystal is given by a volume average over each crystal.

$$\boldsymbol{D} = \left\langle \boldsymbol{D}^c \right\rangle \text{ and } \boldsymbol{\sigma} = \left\langle \boldsymbol{\sigma}^c \right\rangle \tag{2.33}$$

While equation (2.33) is a straightforward problem to solve, its inverse of partitioning a given macroscopic component into the grain-level components, depends on the assumptions made about the interaction of the grain with its surroundings. The most common assumption is that of Taylor (1938) for which each grain in the polycrystal is subject to the same strain rate as that applied to the overall polycrystal, which enforces

compatibility but results in an upper bound approximation of the stress. In Self-consistent models such as the vpsc model the interaction of each grain with its surroundings is based on the geometry of each grain and the average properties of the polycrystal. The self-consistent models do not require that the strain distribution is constant within the polycrystal which is a much more accurate assumption than the Taylor assumption. Furthermore, the Taylor model assumes that a fixed number of slip systems are active for a given plastic deformation, while rate-dependent models like the vpsc model do not. Therefore, the vpsc model can better represent materials that possess a limited number of available deformation systems such as hcp metals.

Since polycrystal models can track the lattice rotation of each individual grain, the material anisotropy is naturally evolutional, which makes this approach very attractive. These models can also be very useful for providing information about yield behavior for stress paths for which no experimental data is available. For example, if the single crystal properties and initial texture of a given material are known, the effect of texture evolution caused by plastic deformations on yielding can be studied. Furthermore, the effects that certain mechanisms such as twinning have on the yield behavior of materials can be explored. In the following, we present the Taylor model followed by the vpsc model that will be further used to obtain information about the evolution of yield loci.

2.3.1 Kinematics of a Polycrystal

Within a single crystal, slip (see Figure 1.1) along a given plane with a unit normal vector $\boldsymbol{n}$ causes a displacement of the upper half of the crystal with respect to the lower half in a certain direction of a unit vector $\boldsymbol{b}$ (commonly referred to as the burgers vector) (see Figure 2.3). Deformation twinning is similar in its kinematic aspects (Figure 2.3) in that it acts on a given plane in a particular direction. The processes of both slip and

twining are considered to be 'simple shears' not 'pure shears' since they correspond to a displacement in the direction of ***b*** on one side of a plane perpendicular to ***n***, but do not result in an equal displacement in the direction of ***n*** on the plane perpendicular to ***b***. Simple shears involve rotations, which cause the evolution of the texture during the plastic deformation of a polycrystal.

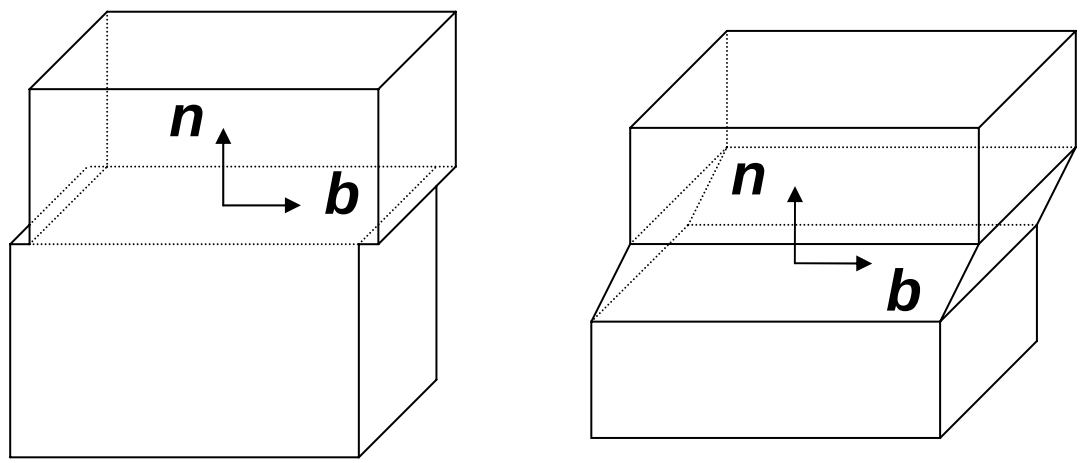

(a) (b)

Figure 2.3 Notations for (a) slip and (b) deformation twinning in a single crystal.

The velocity gradient for a crystal is given by the sum of the shear rates from each slip or twin system. In the crystal coordinate system which is parallel with a set of orthogonal crystal axes, the velocity gradient is given by

$$L_{ij}^{c} = \sum_{s} \dot{\gamma}^{s} b_i^s n_j^s \tag{2.34}$$

In (2.34) $\dot{\gamma}^{s}$ is the shear rate for a given slip or twin system (s). Thus, the rate of deformation tensor, $\boldsymbol{D}^c$, which is the symmetric part of $\boldsymbol{L}^c$, and the spin tensor, $\boldsymbol{W}^c$, which is the antisymmetric part of $\boldsymbol{L}^c$ are given by

$$D_{ij}^{c} = \sum_{s} \dot{\gamma}^{s} m_{ij}^{s} \tag{2.35}$$

$$W_{ij}^{c} = \sum_{s} \dot{\gamma}^{s} q_{ij}^{s} \tag{2.36}$$

where ***m*** (commonly referred to as the Schmid tensor) and ***q*** are defined as

$$m_{ij}^{s} = \frac{1}{2}\left(b_i n_j + b_j n_i\right) \tag{2.37}$$

$$q_{ij}^{s} = \frac{1}{2}\left(b_i n_j - b_j n_i\right) \tag{2.38}$$

When solving a problem incrementally, the incremental strain and incremental rotation for a single crystal become:

$$d\varepsilon_{ij}^{c} = \sum_{s} d\gamma^{s} m_{ij}^{s} \tag{2.39}$$

$$dw_{ij}^{c} = \sum_{s} d\gamma^{s} q_{ij}^{s} \tag{2.40}$$

After each deformation step, the texture of the material is updated by equations (2.39) and (2.40), thus the model is capable of capturing the effects of evolving texure.

2.3.2 Taylor Model

Assuming that plastic deformation only occurs by slip, the resolved shear stress acting on a slip system (*s*) due to a general state of stress acting on a single crystal (*c*), is given by

$$\tau^{s} = \sigma_{ij}^{c} m_{ij}^{s} \tag{2.41}$$

where m^{s} is defined in equation (2.37). In particular, for a single crystal subjected to uniaxial tension, the tensile stress is $\sigma = F/A$. The force acting along the direction of slip is $F\cos\beta$ and the area of the slip plane is $A/\cos\alpha$ (see Figure 2.4). Therefore, the resolved shear stress on a single slip plane is

$$\tau^{s} = \sigma^{c} \cos\alpha \cos\beta \tag{2.42}$$

The activation criterion for a given slip system is given by Schmid's law which states that slip will occur when the resolved shear stress on the slip system reaches a critical value

$$\tau^s \geq \tau^s_{cr} \tag{2.43}$$

where τ^s_{cr} is the critical resolved shear stress for the slip system.

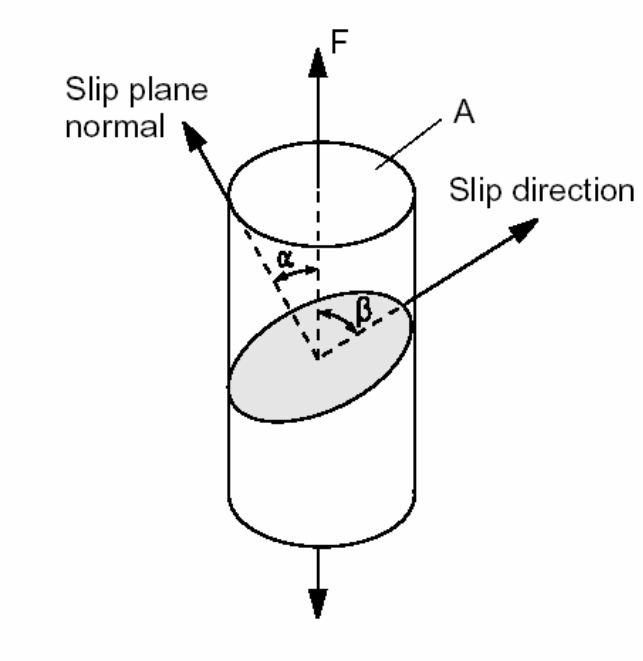

Figure 2.4 Geometry of a slip system within a single crystal

When a polycrystal deforms, the shape change in each crystal must be compatible with that in the neighboring crystals. In order to satisfy this requirement, Taylor (1938) assumed that all grains undergo the same shape change as the entire polycrystal. It has been shown that to accommodate the five independent strain components necessary for plastic deformation in a pressure independent material, five independent slip systems are generally required (von Mises, 1928). Taylor then hypothesized that among all possible combinations of five slip systems capable of accommodating the imposed strains, the active combination is the one that would require the minimum amount of plastic work.

The plastic work per volume (neglecting elastic strains), dW, that is expended by the active slip systems within a single crystal is:

$$dW = \sigma_{ij}^{c} d\varepsilon_{ij}^{c} = \sigma_{ij}^{c} \sum_{s} d\gamma^{s} m_{ij}^{s} = \tau_{cr} \sum_{s} d\gamma^{s} \tag{2.44}$$

Implicit in (2.44) is the assumption that the critical stress required for slip is the same for all slip systems. Thus, the five active slip systems within the single crystal are the five that give the minimum value of $\sum_{s} d\gamma^{s}$ corresponding to the strain increment applied to the crystal (Hosford, 1993).

Once the active slip systems in each crystal have been identified, it is possible to determine the strains, stresses, and lattice rotations by equations (2.39), (2.42), and (2.41), respectively, and thus update the texture. The assumption of uniform strain in all grains irregardless of orientation leads to stress discontinuities at the grain boundaries. However, this model has been used with success at predicting textures for large deformations. Bishop and Hill (1951) later proposed a similar, mathematically equivalent approach. Thus the polycrystalline model given by equations (2.41) - (2.44) is often referred to as the Taylor-Bishop-Hill model. The original formulation did not include twinning, however, Chin et al. (1969) and Hosford (1973) incorporated twinning in the Taylor-Bishop-Hill model. These authors assumed that twinning is analogous to slip with the exception that twinning is directional, i.e. twinning only occurs if a positive shear acting on a given twin system reaches a critical value.

2.3.3 Visco-Plastic Self-Consistent (vpsc) Model

In the vpsc polycrystal formulation, originally proposed by Molinari et al. (1987), the polycrystal is represented as an aggregate of orientations with weights that represent volume fractions chosen to reproduce the initial texture. Each grain is treated as an

anisotropic, visco-plastic, ellipsoidal inclusion embedded in an anisotropic, visco-plastic, homogeneous effective medium (HEM) with the stress applied at the boundary of the medium. The method is called self-consistent because the overall properties for the HEM are determined from the known properties of the grains. The following description of the vpsc model is based on the following references: Kocks et al. (2000), Molinari (1997), Tome et al. (2001), Tome and Lebensohn (2004a and 2004b), and Asaro (1983).

The plastic flow on a slip system (s) within a particular grain is governed by the rate sensitive law

$$\dot{\gamma}^s = \dot{\gamma}_0 \left(\frac{\boldsymbol{m}^s : \boldsymbol{S}^c}{\tau_c^s} \right)^n \tag{2.45}$$

where $\dot{\gamma}^s$ is the rate of shearing on the slip system, $\dot{\gamma}_0$ is a material parameter, $\boldsymbol{S}^c$ is the deviatoric stress, $\boldsymbol{m}^s$ is the Schmid tensors for the grain, and n is the strain rate sensitivity. τ_c^s is the critical resolved shear stress for the slip system and may be represented by a Voce-type hardening law such as

$$\tau_c^s = \tau_0^s + \left(\tau_1^s + \theta_1^s \Gamma\right)\left\{1 - \exp\left(-\frac{\theta_0^s \Gamma}{\tau_1^s}\right)\right\} \tag{2.46}$$

where τ_0^s, τ_1^s, θ_0^s, and θ_1^s are material parameters, and Γ is the accumulated plastic strain for the deformation system. In rate-dependent formulations such as the vpsc model, all available deformation systems are considered active. However, in practice, for large values of n ($n >> 1$), yielding would appear to occur abruptly as $\tau^s \geq \tau_c^s$ in equation (2.45). For $\tau^s < \tau_c^s$ the corresponding $\dot{\gamma}^s$ is very small when $n >> 1$.

The plastic strain rate for the grain is given by the sum of the shears contributed by all systems (assuming that elastic deformations are negligible)

$$D_{ij}^{c} = \sum_{s} \dot{\gamma}^{s} m_{ij}^{s} \tag{2.47}$$

which can be combined with (2.45) to give

$$D_{ij}^{c} = \dot{\gamma}_0 \sum_{s} m_{ij}^{s} \left(\frac{\boldsymbol{m}^{s} : \boldsymbol{S}^{c}}{\tau_c^{s}} \right)^{n} = \left\{ \dot{\gamma}_0 \sum_{s} \frac{m_{ij}^{s} m_{kl}^{s}}{\tau_c^{s}} \left(\frac{\boldsymbol{m}^{s} : \boldsymbol{S}^{c}}{\tau_c^{s}} \right)^{n-1} \right\} S_{kl}^{c} = P_{ijkl}^{c(\sec)} S_{kl}^{c} \tag{2.48}$$

where

$$P_{ijkl}^{c(\sec)} = \dot{\gamma}_0 \sum_{s} \frac{m_{ij}^{s} m_{kl}^{s}}{\tau_c^{s}} \left(\frac{\boldsymbol{m}^{s} : \boldsymbol{S}^{c}}{\tau_c^{s}} \right)^{n-1} \tag{2.49}$$

here $\boldsymbol{D}^c$ and $\boldsymbol{P}^{c(sec)}$ are the strain rate and the visco-plastic secant compliance for the grain, respectively. $\boldsymbol{P}^{c(sec)}$ is not a material property of the crystal since it depends on the stress state, except for when n = 1. When the stress is uniform within the grain, (2.48) is exact, however, a linear relation valid in the vicinity of a point $\boldsymbol{S}^0$ can be obtained through a first order Taylor series expansion of (2.48) about the point $\boldsymbol{S}^0$

$$D_{ij}^{c}(\boldsymbol{S}^{c}) = D_{ij}^{c}(\boldsymbol{S}^{c0}) + \frac{\partial D_{ij}^{c}}{S_{ij}^{c}} \Big|_{\boldsymbol{S}^{c0}} (\boldsymbol{S}^{c} - \boldsymbol{S}^{c0}) \tag{2.50}$$

which can be rewritten as

$$D_{ij}^{c}(\boldsymbol{S}^{c}) = P_{ijkl}^{c(\tan)} S_{kl}^{c} + D_{ij}^{c0} \tag{2.51}$$

where the tangent modulus is defined as

$$\boldsymbol{P}^{c(\tan)} = \frac{\partial D_{ij}^{c}}{S_{ij}^{c}} \Big|_{\boldsymbol{S}^{c0}} = n\boldsymbol{P}^{c(\sec)} \tag{2.52}$$

and the back extrapolated term

$$\boldsymbol{D}^{c0} = (\boldsymbol{P}^{c(\sec)} - \boldsymbol{P}^{c(\tan)})\boldsymbol{S}^{c0} = (1-n)\boldsymbol{D}^{c} \tag{2.53}$$

The secant approximation (2.48) has been proven to be too stiff, giving results close to the upper bound results. The tangent approximation (2.51) gives a much more compliant

response. Similarly, at the polycrystal level, the overall strain rate and stress are related through either a secant or a tangent relationship.

$$\bar{\boldsymbol{D}} = \bar{\boldsymbol{P}}^{\text{sec}} : \bar{\boldsymbol{S}} \tag{2.54a}$$

or,

$$\bar{\boldsymbol{D}} = \bar{\boldsymbol{P}}^{\tan} : \bar{\boldsymbol{S}} + \bar{\boldsymbol{D}}^{0} = n\bar{\boldsymbol{P}}^{\text{sec}} : \bar{\boldsymbol{S}} + \bar{\boldsymbol{D}}^{0} \tag{2.54b}$$

and the macro-scale polycrystal compliance is a function of the overall stress. Within the HEM, the local response of the medium is also governed by the macro-scale polycrystal compliance such that

$$\boldsymbol{D}(\boldsymbol{x}) = \bar{\boldsymbol{P}}^{\text{sec}} : \boldsymbol{S}(\boldsymbol{x}) \tag{2.55a}$$

or

$$\boldsymbol{D}(\boldsymbol{x}) = n\bar{\boldsymbol{P}}^{\text{sec}} : \boldsymbol{S}(\boldsymbol{x}) + \bar{\boldsymbol{D}}^{0} \tag{2.55b}$$

such that $\boldsymbol{x}$ represents the physical coordinate system of the polycrystal. Self-consistent models impose equilibrium on the grain-to-HEM interaction, but not on grain-to-grain interaction. Therefore, solving for equilibrium for a grain whose constitutive response is given by (2.48), embedded in an effective medium (response given by 2.55) leads to the interaction equation

$$(\boldsymbol{D}^{c} - \bar{\boldsymbol{D}}) = \tilde{\boldsymbol{M}}^{c} : (\boldsymbol{S}^{c} - \bar{\boldsymbol{S}}) \tag{2.56}$$

where

$$\tilde{\boldsymbol{M}}^{c} = n^{eff}(\boldsymbol{I} - \boldsymbol{E})^{-1} : \boldsymbol{E} : \bar{\boldsymbol{P}}^{\text{sec}} \tag{2.57}$$

Here, $\tilde{\boldsymbol{M}}^{c}$ is the accommodation tensor and $\boldsymbol{E}$ is the Eshelby tensor which is a function of the overall compliance of the polycrystal and of the geometry of the ellipsoid that

represents the grain. The parameter n^{eff} depends on the interaction between the grains and the HEM, in particular n^{eff} is related to the interactions indicated in (2.58).

$$n^{eff} = \begin{cases} 0 & \rightarrow \text{ Taylor} \\ 1 & \rightarrow \text{ Secant} \\ n & \rightarrow \text{ Tangent} \\ 1 < n^{eff} < n & \rightarrow \text{ Effective Interaction} \end{cases} \tag{2.58}$$

When $n^{eff} = 0$, the strain rate in the grain equals the strain rate in the polycrystal, therefore the Taylor interaction is recovered. The fourth case allows for an effective interaction between the secant and the tangent interactions. In particular, for the simulations used in this dissertation research, n = 20 while $n^{eff} = 10$.

Combining equations (2.48), (2.54a), and (2.56), the stresses in a grain and the stresses for polycrystal are related by

$$\boldsymbol{S}^c = \boldsymbol{B}^c : \bar{\boldsymbol{S}} \tag{2.59}$$

where

$$\boldsymbol{B}^c = (\boldsymbol{P}^{c(\sec)} + n^{eff}(\boldsymbol{I} - \boldsymbol{E})^{-1} : \boldsymbol{E} : \bar{\boldsymbol{P}}^{\sec})^{-1} : (\bar{\boldsymbol{P}}^{\sec} + n^{eff}(\boldsymbol{I} - \boldsymbol{E})^{-1} : \boldsymbol{E} : \bar{\boldsymbol{P}}^{\sec}) \tag{2.60}$$

Now, the condition that the weighted average of stress and strain rate over the grains must equal the corresponding macroscopic magnitudes provides an expression from which the macro-scale polycrystal secant compliance and macro-scale back extrapolated term can be calculated.

$$\bar{\boldsymbol{P}}^{\sec} = \left\langle \boldsymbol{P}^{c(\sec)} : \boldsymbol{B}^c \right\rangle \tag{2.61}$$

$$\bar{\boldsymbol{D}}^0 = \left\langle \boldsymbol{P}^{c(\sec)} : \boldsymbol{\Phi} + \boldsymbol{D}^{c0} \right\rangle \tag{2.62}$$

where

$$\boldsymbol{\Phi} = (\boldsymbol{P}^{c(\sec)} + n^{eff}(\boldsymbol{I} - \boldsymbol{E})^{-1} : \boldsymbol{E} : \bar{\boldsymbol{P}}^{\sec})^{-1} : (\bar{\boldsymbol{D}}^0 - \boldsymbol{D}^{c0}) \tag{2.63}$$

and $\langle\ \rangle$ refers to the weighted average. Equations (2.60) and (2.61) are valid when n^{eff} is constant for each grain within the polycrystal, and each grain has the same shape. Equation (2.61) indicates that the polycrystal compliance is given by a weighted average of the single crystal compliances and the localization tensor, $\boldsymbol{B}^c$. However, $\boldsymbol{B}^c$ is a function of $\bar{\boldsymbol{P}}^{\sec}$ (see equation 2.60), therefore, equation (2.60) represents an implicit equation from which $\bar{\boldsymbol{P}}^{\sec}$ must be obtained iteratively.

Twinning is incorporated into the vpsc model by assuming that it is analogous to slip, in that a twin system has a critical resolved shear stress that will activate deformation. However, twinning differs from slip in its directionality, since twinning will only be activated by a "positive" shear. The fact that twinned regions contribute to the texture of the aggregate, and more importantly, act as effective barriers for further slip and twinning is also taken into account by the vpsc model through latent hardening coefficients coupled with the Voce hardening law for each deformation system. The critical resolved stress for each system is updated by (2.64) using the latent hardening coefficients ($h^{ss'}$) which account for the effect of dislocations caused by other slip or twin systems (*s*') on the current system (*s*).

$$\Delta\tau_c^s = \frac{\partial\tau_c^s}{\partial\Gamma}\sum_{s'} h^{ss'}\Delta\gamma^{s'} \tag{2.64}$$

A predominant twin reorientation scheme proposed by Tome et al. (1991) is also incorporated into the model that selectively reorients certain grains affected by twinning. Under this scheme, the shear strain contributed by each twin system within each grain is tracked, and the sum of all twin systems over all grains associated with a given twin

mode are calculated. Some grains are fully reoriented during an incremental step once a threshold value is accumulated for a given twin system.

Since the overall properties of the polycrystal are not known a priori, the vpsc model must be solved iteratively as follows:

- Given: $\bar{\boldsymbol{D}}$ and a time step Δt

Outer loop:

- Estimate an initial stress in each grain by enforcing a Taylor interaction
- Calculate $\boldsymbol{P}^{c(\sec)}$ (2.49) and $\boldsymbol{D}^{c0}$ (2.53) for each grain
- Estimate the $\bar{\boldsymbol{P}}^{\sec}$ and $\bar{\boldsymbol{D}}^{0}$ as the averages of the corresponding grain values

Inner loop:

- Calculate the Eshelby tensor based on the estimated $\bar{\boldsymbol{P}}^{\sec}$ and the current shape of the ellipsoidal grain.
- Calculate $\tilde{\boldsymbol{M}}^{c}$ (2.57), $\boldsymbol{B}^{c}$ (2.60), and $\boldsymbol{\Phi}$ (2.63)
- Calculate $\bar{\boldsymbol{P}}^{\sec}$ (2.61) and $\bar{\boldsymbol{D}}^{0}$ (2.62) and compare to the estimation from the outer loop. If they are within a tolerance, exit this loop. If not, use this updated $\bar{\boldsymbol{P}}^{\sec}$ and $\bar{\boldsymbol{D}}^{0}$ to restart the loop and iterate until the tolerance has been met.

End of inner loop

- Use $\bar{\boldsymbol{P}}^{\sec}$ and $\bar{\boldsymbol{D}}^{0}$ from the inner loop to calculate $\bar{\boldsymbol{S}}$ (2.54)
- Calculate $\tilde{\boldsymbol{M}}^{c}$ (2.57)
- Using (2.59) and (2.48) calculate $\boldsymbol{D}^{c}$ (2.51)
- Calculate the weighted average stress and strain rate from each grain
- Calculate the overall stress (2.55)
- Compare the average stress and strain rate with the overall stress and imposed strain rate.
- Compare the previous stress in each grain to the recalculated stress in the grain.

- If all three are within a tolerance then exit the outer loop, if not use the new value of the stress in each grain and return to the beginning of the outer loop

End of Outer Loop.

Once convergence has been obtained for the stress and strain rate in each grain, the hardening for each deformation system is updated using the Voce hardening law (2.40), and the grain orientation and grain shape are updated as well. The process is then repeated for the next strain increment.

The vpsc model can better model low-symmetry materials such as hcp metals that are characterized by a variety of active deformation modes present in each grain, non-negligible twinning activity, and significantly anisotropic single crystals (Kocks et al., 2000). Therefore, this model was used in this dissertation to determine the yield properties for both isotropic and anisotropic materials.

CHAPTER 3
PROPOSED YIELD CRITERION

3.1 Proposed Isotropic Yield Criterion

Twinning and martensitic shear are directional deformation mechanisms, and if they occur, yielding will depend on the sign of the stress (Hosford, 1993). Early polycrystal simulation results by Chin *et al.* (1969), who analyzed deformation by mixed slip and twining in fcc crystals, predicted a yield stress in uniaxial tension 25% lower than that in uniaxial compression. Hosford and Allen (1973) extended the calculations to other types of loading. Based on the simulation results they concluded that yield loci with a strong asymmetry between tension and compression should be expected in any isotropic pressure insensitive material that deforms by twinning or directional slip.

An isotropic yield criterion capable of describing strength differentials between tension and compressive yield is proposed of the form

$$\left(\left|S_1\right| - kS_1\right)^a + \left(\left|S_2\right| - kS_2\right)^a + \left(\left|S_3\right| - kS_3\right)^a = F \tag{3.1}$$

where S_i, i = 1…3 are the principal values of the Cauchy stress deviator. At difference with the yield criterion (2.29), the proposed yield function (3.1) is a homogeneous function in stresses of degree a, which could range from 1 to ∞. Also, in (3.1) k is a material constant, while F gives the size of the yield locus and depends on the chosen hardening rule. The physical significance of the material parameter k may be revealed from uniaxial tests. Indeed, according to the proposed criterion (3.1), the ratio of tensile to compressive uniaxial yield stress is given by

$$\frac{\sigma_T}{\sigma_C}=\left\{\frac{\left(\frac{2}{3}(1+k)\right)^a+2\left(\frac{1}{3}(1-k)\right)^a}{\left(\frac{2}{3}(1-k)\right)^a+2\left(\frac{1}{3}(1+k)\right)^a}\right\}^{\frac{1}{a}} \tag{3.2a}$$

or

$$k=\frac{1-\left\{\frac{2^a-2(\sigma_T/\sigma_C)^a}{(2\sigma_T/\sigma_C)^a-2}\right\}^{\frac{1}{a}}}{1+\left\{\frac{2^a-2(\sigma_T/\sigma_C)^a}{(2\sigma_T/\sigma_C)^a-2}\right\}^{\frac{1}{a}}} \tag{3.2b}$$

Hence, for a fixed, the parameter k is expressible solely in terms of the ratio σ_T/σ_C (see 3.2b). Note that for any value of the exponent a, if $k = 0$, there is no difference between tension and compression. In particular, for $k = 0$ and $a = 2$, the proposed criterion reduces to von Mises yield criterion. From (3.2b) follows that for a given exponent "a", for the parameter k to be real, σ_T/σ_C should belong to

$$2^{\frac{1-a}{a}} \le \sigma_T/\sigma_C \le 2^{\frac{a-1}{a}} \tag{3.3}$$

Specifically,

- For $2^{\frac{1-a}{a}} \le \sigma_T/\sigma_C \le 1 \quad \Rightarrow \quad -1 \le k \le 0$,
- For $1 \le \sigma_T/\sigma_C \le 2^{\frac{a-1}{a}} \quad \Rightarrow \quad 0 \le k \le 1$

As an example, in Figure 3.1 are shown the representation in the plane stress yield loci (3.1) corresponding to a =2 (fixed) and $\sigma_T/\sigma_C = \sqrt{2}$, 1.26, 1.13, and 1 (von Mises), respectively (i.e., corresponding to k =1; 0.4; 0.2; 0, respectively). Note that the highest the ratio between the yield stress in tension and compression, the greater is the departure

from the von Mises ellipse; for the highest admissible value for k, the yield function (3.1) represents a triangle with rounded corners.

Furthermore, $k\left(\sigma_T/\sigma_C\right) = -k\left(\sigma_C/\sigma_T\right)$ (see equation 3.2b). To illustrate this property of the proposed yield function, in Figure 3.2 are represented the plane stress yield loci (3.1) corresponding to σ_T/σ_C = 1.13 (k = 0.2) and σ_T/σ_C = 1/1.13 (k = -0.2). It is clearly seen that a change in the sign of k results in a mirror image of the yield surface.

The variation of σ_T/σ_C with k is illustrated in Figure 3.3 for different values of the exponent a. If k =1 then $\sigma_T/\sigma_C = 2^{(a-1)/a}$, so for a = 1, $\sigma_T = \sigma_C$, while for $a \to \infty$, $\sigma_T/\sigma_C \to 2$. If k = -1 then $\sigma_T/\sigma_C = 2^{(1-a)/a}$, so for a = 1 there is no difference between tension and compression, while if $a \to \infty$, then $\sigma_T/\sigma_C \to 1/2$. For any value of the exponent a and for $-1 \le k \le 1$, the yield function (3.1) is convex (for the proof, see section 3.1.2).

Figure 3.4 shows the representations in the deviatoric π-plane of the proposed yield loci (3.1) for various values of the coefficient k between 0 and 1 and a = 2 (fixed) , along with the von Mises and Tresca yield loci for comparison. As k increases, the ratio σ_T/σ_C is increasing and the yield loci depart drastically from the circular von Mises locus.

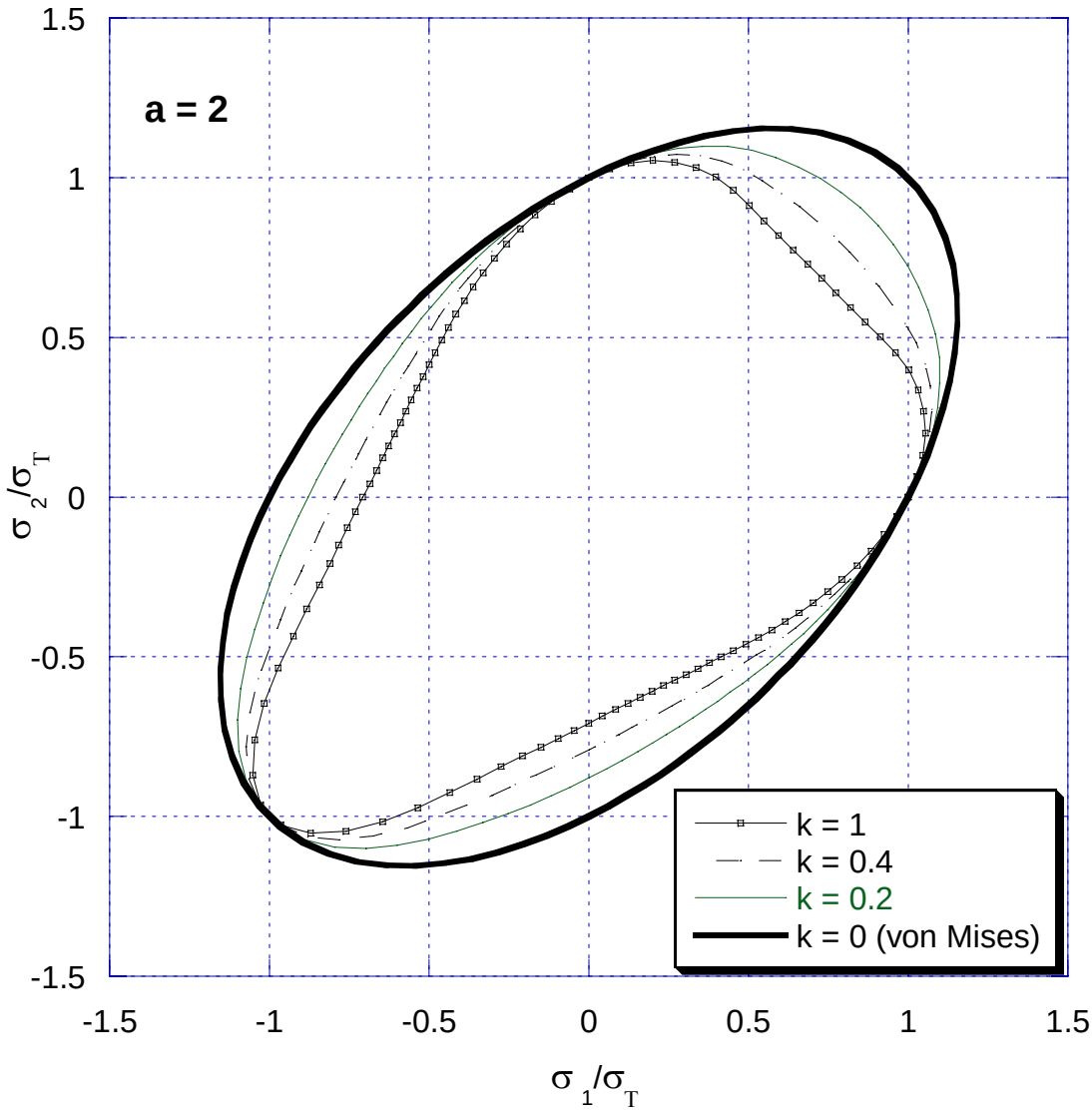

Figure 3.1 Plane stress yield loci for different values of the ratio σ_T/σ_C between the yield stress in tension and compression, in comparison with the von Mises locus (σ_1. and σ_2 are the principal values of the Cauchy stress).

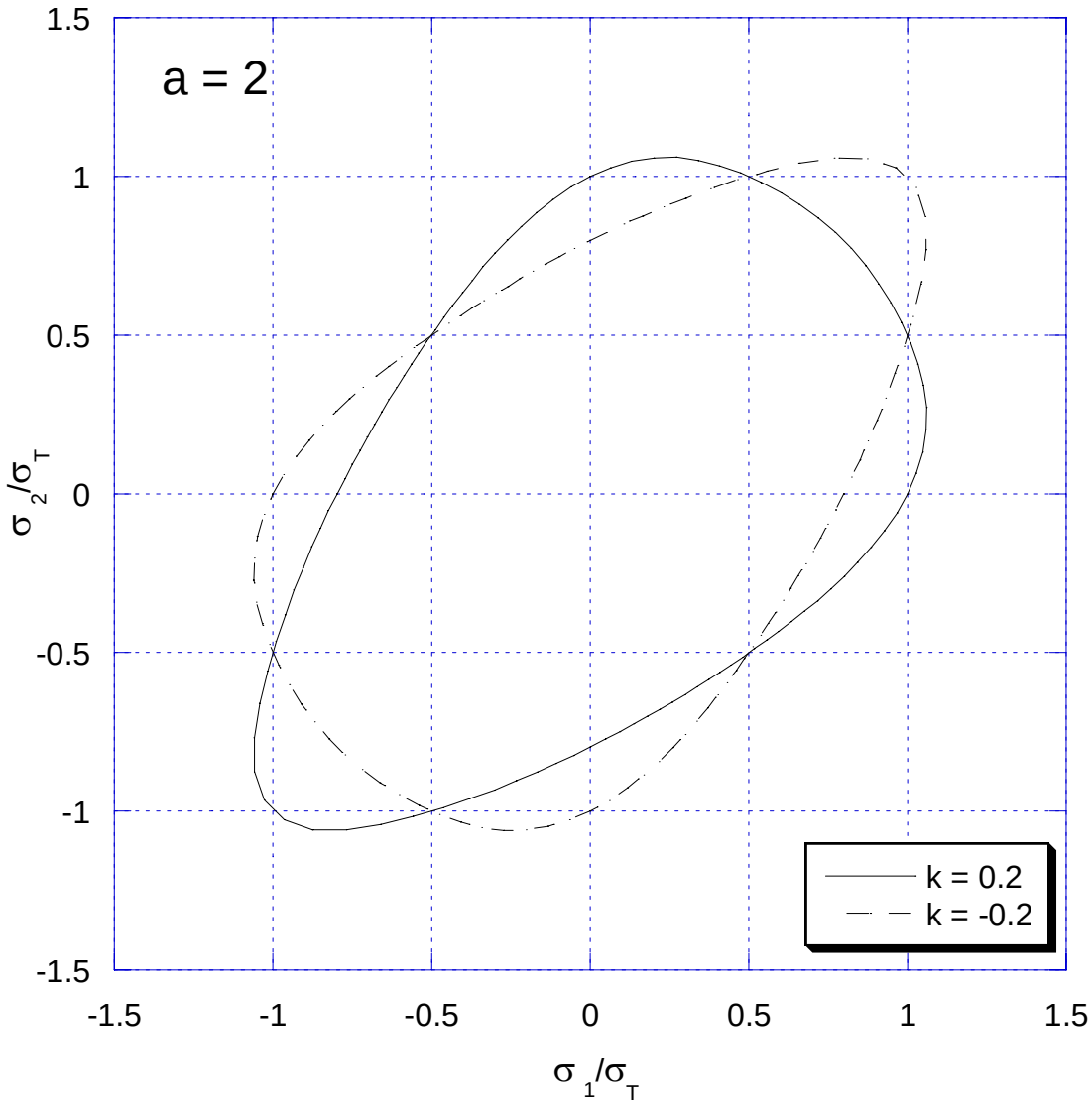

Figure 3.2 Plane stress yield loci corresponding to σ_T / σ_C = 1.13 (k = 0.2) and σ_T / σ_C = 1/1.13 (k = -0.2).

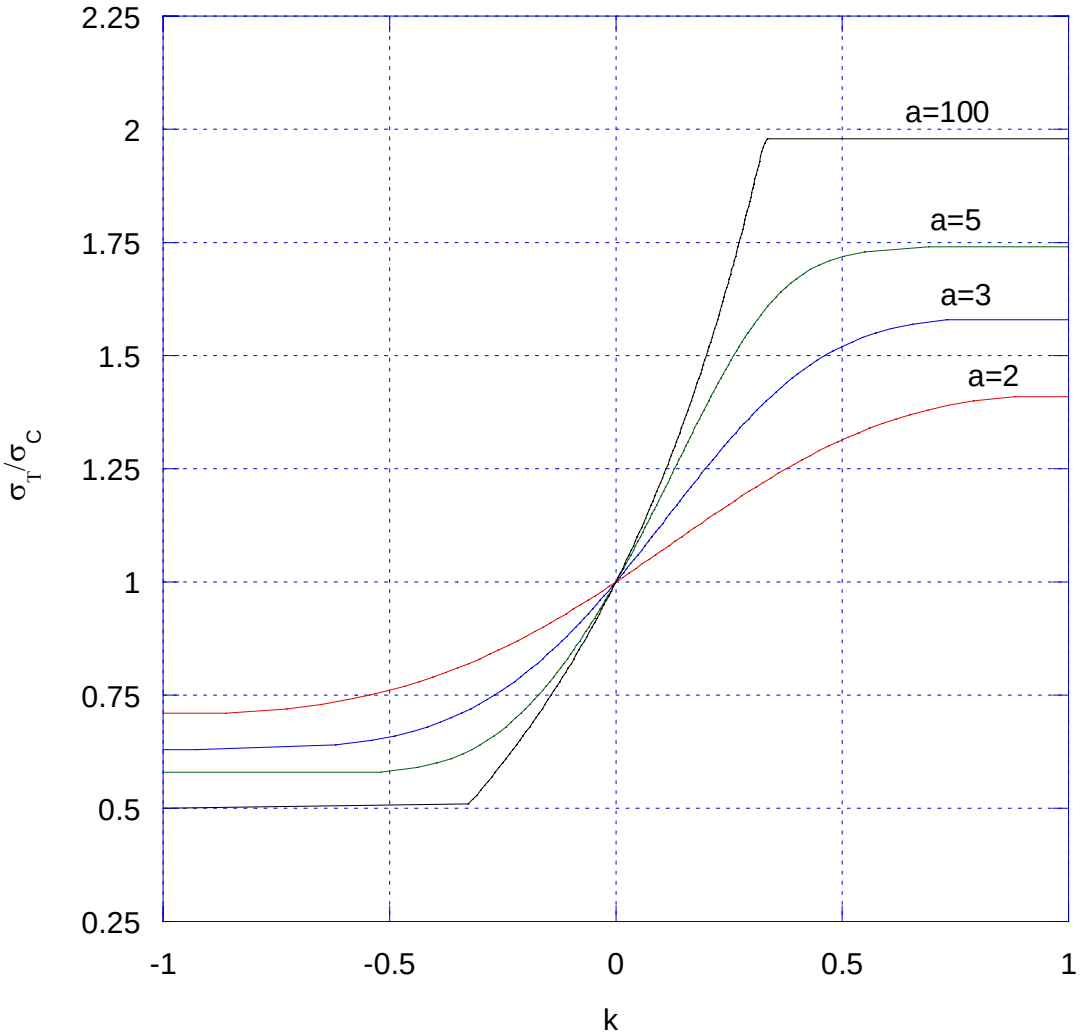

Figure 3.3 The influence of the value of the parameter k on the ratio σ_T / σ_C of the uniaxial yield stress in tension and compression, for various values of the exponent a.

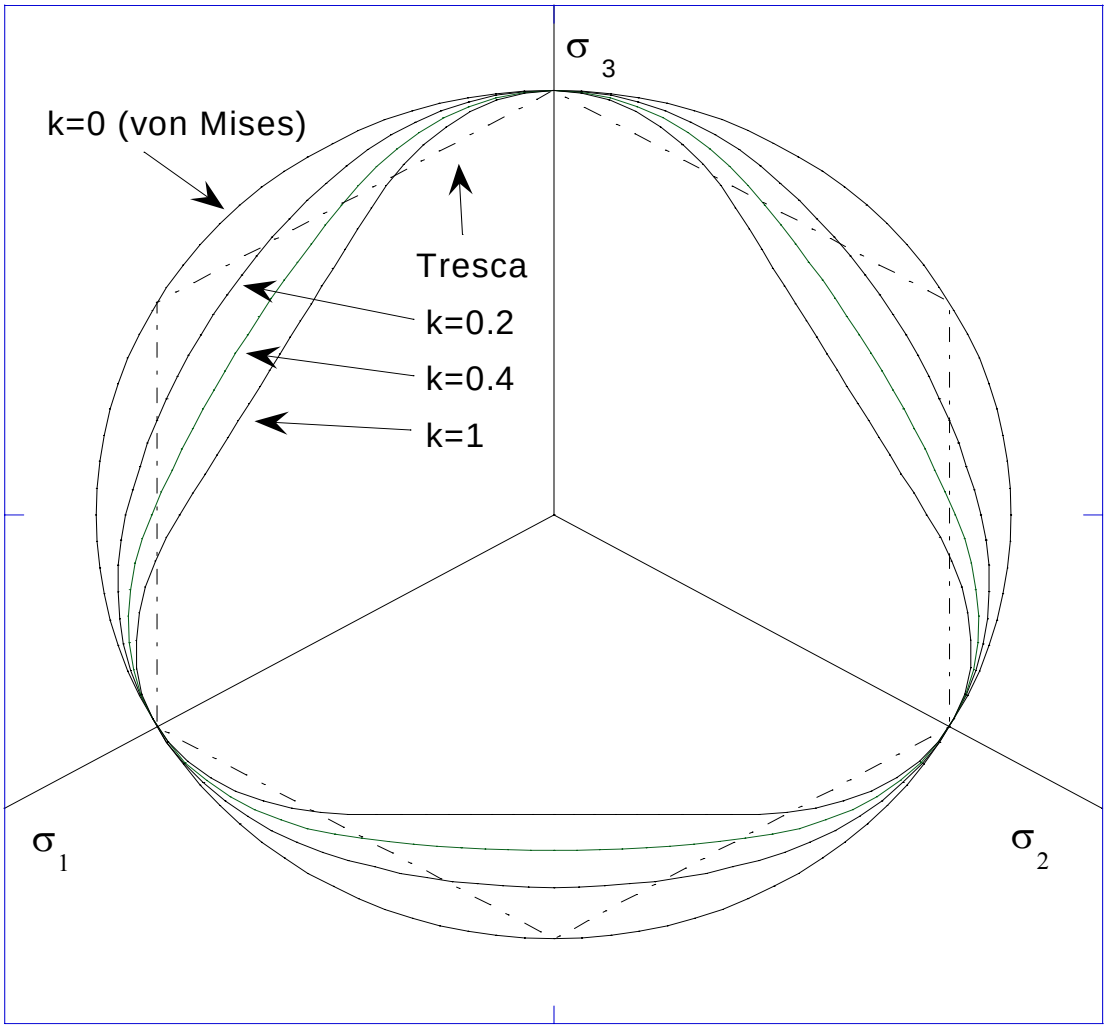

Figure 3.4 Projection in the deviatoric π plane of the yield loci (3.1) for $a = 2$ and various values of k in comparison to von Mises and Tresca loci.

For combined tension and torsion conditions where the uniaxial tensile stress is set equal to σ, the shear stress is set equal to τ, and all other stress components are zero, the proposed yield criterion becomes

$$\left(\frac{\sigma}{6}+\sqrt{\frac{\sigma^2}{4}+\tau^2}\right)^a(1-k)^a+\left(\frac{\sigma}{6}-\sqrt{\frac{\sigma^2}{4}+\tau^2}\right)^a(1+k)^a+\left(\frac{\sigma}{3}\right)^a(1+k)^a=F \tag{3.4}$$

Figure 3.5 shows the representation in the tension-torsion plane $(\sigma/\sigma_T,\tau/\sigma_T)$ of the proposed yield loci corresponding to a fixed value of a (a = 2) and several different values of k. Note the clear deviation from both Tresca and Mises criteria for k different from zero.

It is also worth noting that the proposed yield criterion (3.1) is capable of predicting ratcheting due to shear loading reversal. Indeed, inspection of Figure 3.5 indicates that a loading in pure shear could produce plastic strains along the axial direction. In order to predict such a phenomena $\frac{\partial f}{\partial \sigma_x}\neq 0$, where f is defined by equation (3.1), when all stresses equal zero except the shear stress τ. The principal values of the deviator of the Cauchy stress tensor are defined as

$$\begin{aligned}
S_1 &= 2\cos(\alpha_1)\sqrt{\frac{J_2}{3}}\\
S_2 &= 2\cos\left(\alpha_1-\frac{2\pi}{3}\right)\sqrt{\frac{J_2}{3}}\\
S_3 &= 2\cos\left(\alpha_1+\frac{2\pi}{3}\right)\sqrt{\frac{J_2}{3}}
\end{aligned} \tag{3.5}$$

where α_1 is the angle satisfying $0\le 3\alpha_1\le\pi$ and whose cosine is given by

$$\cos(3\alpha_1) = \frac{J_3}{2}\left(\frac{3}{J_2}\right)^{\frac{3}{2}} \tag{3.6}$$

where J_2 and J_3 are the second and third invariants of the stress deviator (see Malvern, 1969).

Therefore,

$$\frac{\partial f}{\partial \sigma_x} = \frac{\partial f}{\partial S_i}\left\{\frac{\partial S_i}{\partial \alpha}\left[\frac{\partial \alpha}{\partial J_2}\frac{\partial J_2}{\partial \sigma_x} + \frac{\partial \alpha}{\partial J_3}\frac{\partial J_3}{\partial \sigma_x}\right] + \frac{\partial S_i}{\partial J_2}\frac{\partial J_2}{\partial \sigma_x}\right\} \tag{3.7}$$

but for the case when only one shear stress component is non-zero, $\frac{\partial J_2}{\partial \sigma_x} = 0$, so equation (3.7) reduces to the following form

$$\frac{\partial f}{\partial \sigma_x} = \frac{\partial f}{\partial S_i}\frac{\partial S_i}{\partial \alpha}\frac{\partial \alpha}{\partial J_3}\frac{\partial J_3}{\partial \sigma_x} \tag{3.8}$$

After substitution of (3.1), (3.5), and (3.6), equation (3.8) reduces to the form given by equation (3.9) when all stresses equal zero except for one shear stress component, τ .

$$\frac{\partial f}{\partial \sigma_x} = \frac{a(1-k)(|\tau| - k\tau)}{6} + \frac{a(-1-k)(|\tau| + k\tau)}{6} \tag{3.9}$$

Figure 3.6 shows the plot of the variation of $\partial f / \partial \sigma_x$ with k given by equation (3.9). Note that according to the proposed criterion, pure shear will result in axial plastic strains for any case other than $k = 0$. The direction of the axial strains is independent of the sign of the applied shear stress, thus the proposed criterion (3.1) can predict a “ratcheting” effect due to shear loading reversals in the presence of a strength differential between tension and compression.

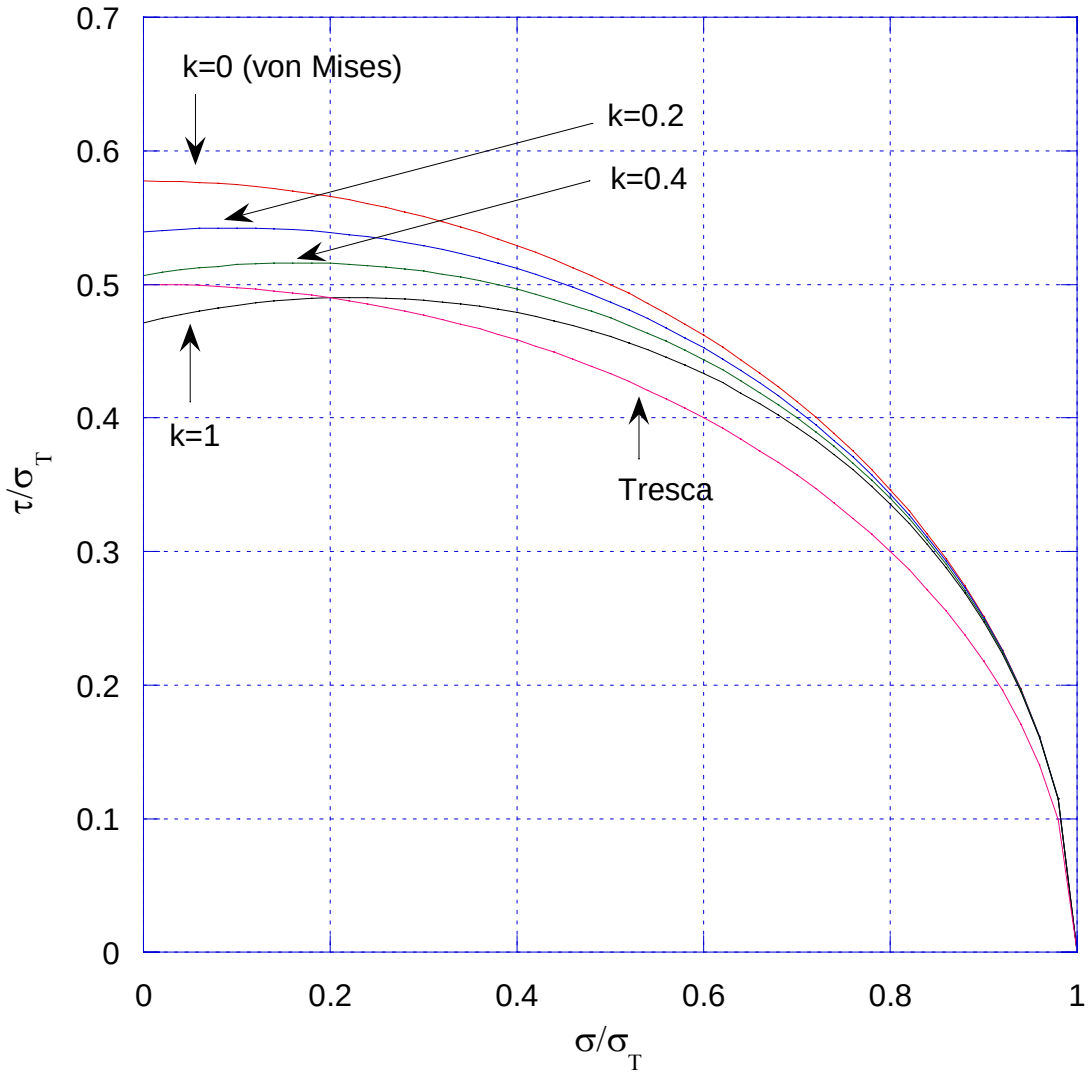

Figure 3.5 Projections in the tension-torsion plane of the proposed yield loci (3.1) for various k -values and $a = 2$ (fixed), in comparison with Tresca and von Mises (k=0, a=2) loci.

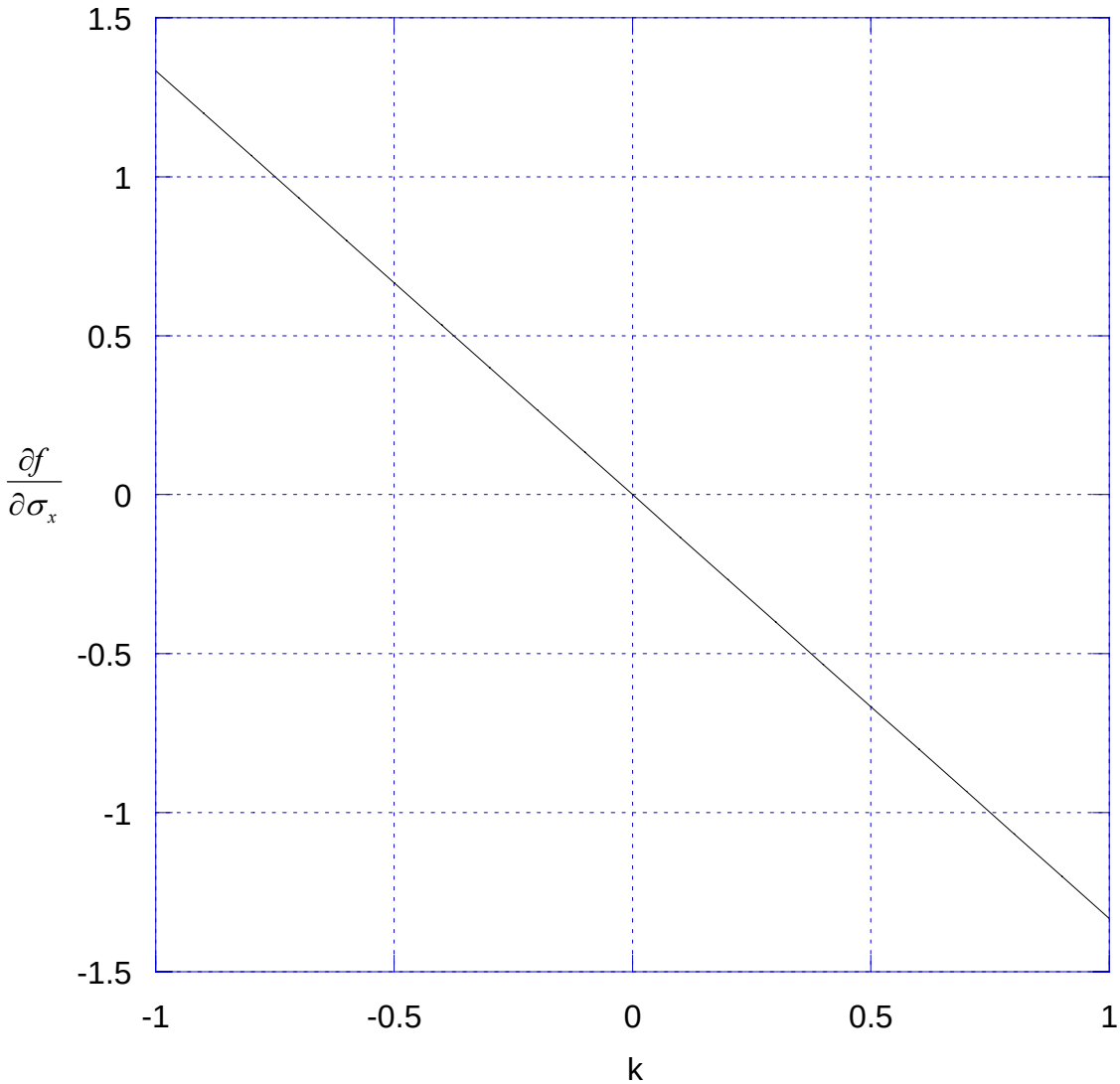

Figure 3.6 $\frac{\partial f}{\partial \sigma_x}$ vs. k for the case of pure shear ($a = 2$).

3.1.1 Comparison to Polycrystal Simulation

Since no data is available on the yield behavior for an isotropic pressure-insensitive material, the vpsc model was used to calculate the initial yield loci for randomly oriented fcc polycrystals deforming solely by $\{111\}\langle 11\bar{2}\rangle$ twinning, bcc polycrystals deforming solely by $\{112\}\langle \bar{1}\,\bar{1}\,1\rangle$ twinning, and hcp polycrystals deforming solely by tensile twinning $\{10\bar{1}2\}\langle 10\bar{1}1\rangle$ and compressive twinning $\{11\bar{2}2\}\langle 11\bar{2}\bar{3}\rangle$. Due to the polarity of twinning, this type of simulation will produce an isotropic yield locus that has different yield strengths in tension and compression. The orientation distribution function describing a random orientation of the crystallographic texture was constructed by varying the Euler angles which describe the orientation of each crystal by $\Delta\varphi_1, \Delta\cos\phi, \Delta\varphi_2$, using the notation of Bunge (see Kocks et al., 2000).

To demonstrate the predictive capabilities of the proposed isotropic criterion, we compare the yield loci obtained using the proposed criterion (3.1) with the isotropic yield loci calculated using the vpsc polycrystal model described in the section 2.3.3. The proposed yield condition (3.1) involves 2 parameters: the exponent *a* and the parameter *k*, which for *a* fixed is expressible solely in terms of the σ_T / σ_C ratio (see equation 3.2). The vpsc model predicted a ratio of 0.83 between the yield stress in tension and compression for the randomly oriented fcc polycrystal deforming only by twinning. Assuming $a = 2$, we obtain $k = -0.3098$ for the proposed criterion. Figures 3.7 (a) and (b) show the yield stresses (open circles) obtained using the vpsc model and the projection of the yield locus predicted by the proposed criterion (3.1) for $a = 2$, $k = -0.3098$ (solid line) for plane stress ($\sigma_{xy} = 0$) and on the π-plane, respectively. It is clearly seen that the

proposed isotropic criterion describes very well the asymmetry in yielding due to activation of twinning. On the same figures are shown the comparison between the yield loci obtained with the VPSC model for randomly oriented bcc polycrystals deforming solely by twinning (solid circles) and the yield loci according to the proposed criterion (3.1) with a = 2 and for k = 0.3098 (which correspond to a ratio between the yield stress in tension and compression of 1.20, which is the reciprocal of the value corresponding to fcc polycrystals). Figures 3.8 (a) and (b) show a comparison between the yield loci obtained using the proposed criterion (for a = 3 and k = -0.0645) with the yield loci for randomly oriented hcp zirconium polycrystals deforming solely by tensile and compressive twinning calculated using the VPSC model. Again, the strength differential effect is very well captured.

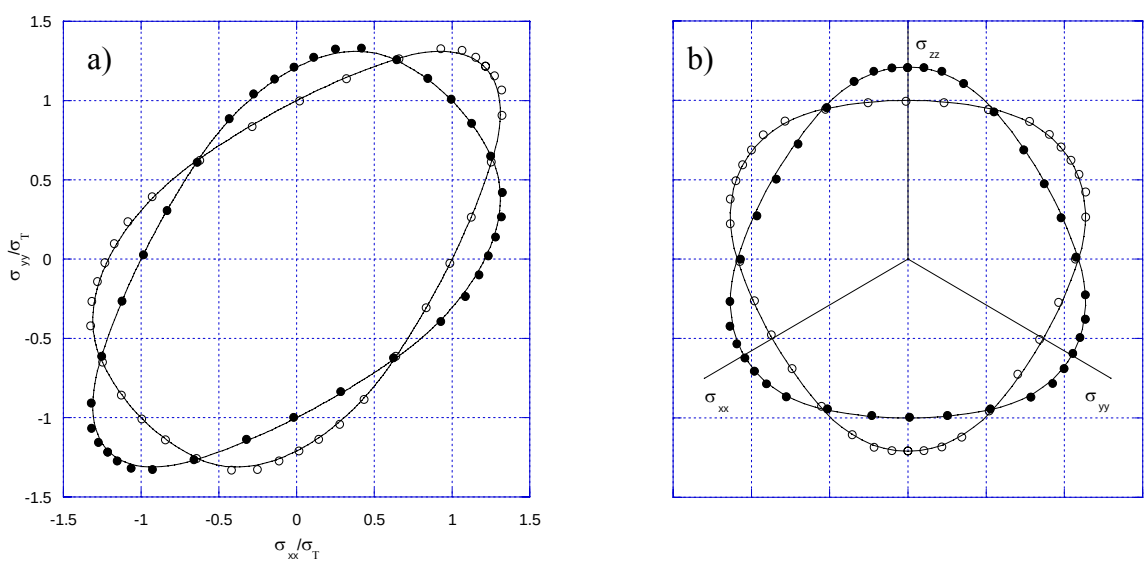

Figure 3.7 Comparison between the vpsc yield locus for randomly oriented fcc (open circles) and bcc (closed circles) polycrystals deforming solely by twinning and the predictions of the proposed criterion: (a) for plane stress (σ_{xy} = 0) (b) on the π-plane.

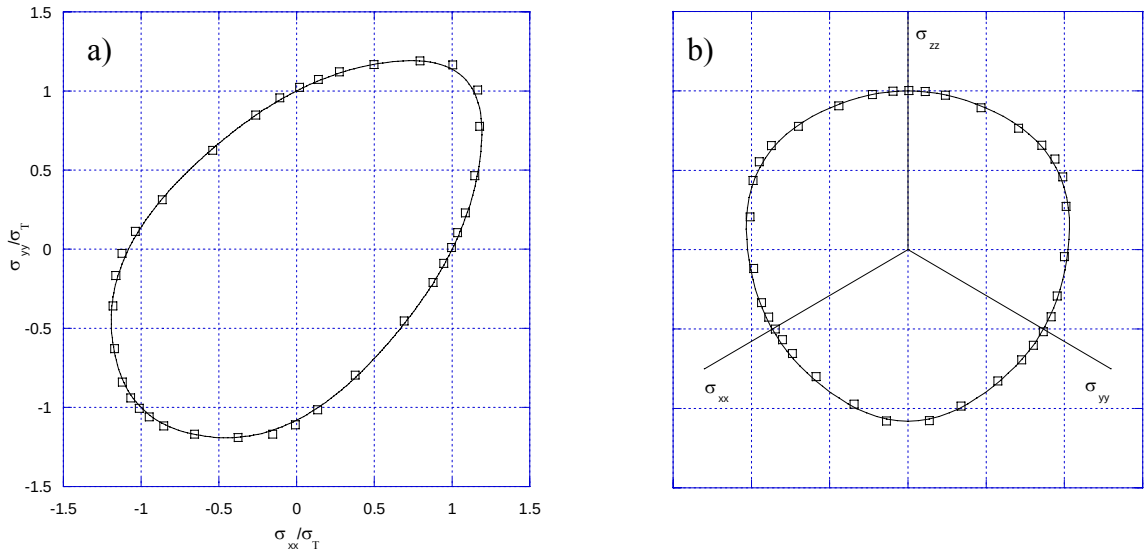

Figure 3.8 Comparison between the VPSC yield locus for randomly oriented hcp zirconium polycrystals deforming solely by twinning (open rectangles) and the predictions of the proposed criterion (3.1): (a) plane stress ($\sigma_{xy} = 0$) (b) on the π-plane.

3.1.2 Yield Surface Derivatives and Convexity

The associated flow rule used to obtain the plastic strain increments is given by equation (2.11), but restated here as

$$d\boldsymbol{\varepsilon}^p = d\lambda \frac{\partial f}{\partial \boldsymbol{\sigma}}$$

Therefore, it is necessary to determine the first derivatives of the yield criterion. The proposed isotropic yield criterion (3.1) is of the form

$$\left(|S_1| - kS_1\right)^a + \left(|S_2| - kS_2\right)^a + \left(|S_3| - kS_3\right)^a = F$$

where for the general 3-dimensional case, the principal values of the deviator of the Cauchy stress tensor can be defined as

$$S_1 = 2\cos(\alpha_1)\sqrt{\frac{J_2}{3}}$$

$$S_2 = 2\cos\left(\alpha_1 - \frac{2\pi}{3}\right)\sqrt{\frac{J_2}{3}}$$

$$S_3 = 2\cos\left(\alpha_1 + \frac{2\pi}{3}\right)\sqrt{\frac{J_2}{3}}$$

where $S_1 \geq S_2 \geq S_3$ and α_1 is the angle satisfying $0 \leq 3\alpha_1 \leq \pi$ and whose cosine is given by

$$\cos(3\alpha_1) = \frac{J_3}{2}\left(\frac{3}{J_2}\right)^{\frac{3}{2}}$$

where J_2 and J_3 are the second and third invariants of the stress deviator. Note that for $\alpha = 0,\ \pi/6,$ and $\pi/3$ the state of stress corresponds to uniaxial tension, pure shear, and uniaxial compression, respectively. Similar to equation (3.7), the general form of the first derivative of the proposed isotropic yield criterion is

$$\frac{\partial F}{\partial \sigma_{ij}} = \frac{\partial F}{\partial S_k}\left\{\frac{\partial S_k}{\partial \alpha}\left[\frac{\partial \alpha}{\partial J_2}\frac{\partial J_2}{\partial \sigma_{ij}} + \frac{\partial \alpha}{\partial J_3}\frac{\partial J_3}{\partial \sigma_{ij}}\right] + \frac{\partial S_k}{\partial J_2}\frac{\partial J_2}{\partial \sigma_{ij}}\right\} \tag{3.10}$$

where,

$$\frac{\partial F}{\partial S_k} = a\left(|S_k| - kS_k\right)^{a-1}\left(\frac{|S_k|}{S_k} - k\right),$$

$$\frac{\partial S_1}{\partial \alpha} = -2\sin\alpha\sqrt{\frac{J_2}{3}},\ \frac{\partial S_2}{\partial \alpha} = -2\sin\left(\alpha - \frac{2\pi}{3}\right)\sqrt{\frac{J_2}{3}},\ \frac{\partial S_3}{\partial \alpha} = -2\sin\left(\alpha + \frac{2\pi}{3}\right)\sqrt{\frac{J_2}{3}},$$

$$\frac{\partial S_1}{\partial J_2} = \frac{1}{3}\cos\alpha\left(\frac{J_2}{3}\right)^{-\frac{1}{2}},\ \frac{\partial S_2}{\partial J_2} = \frac{1}{3}\cos\left(\alpha - \frac{2\pi}{3}\right)\left(\frac{J_2}{3}\right)^{-\frac{1}{2}},\ \frac{\partial S_3}{\partial J_2} = \frac{1}{3}\cos\left(\alpha + \frac{2\pi}{3}\right)\left(\frac{J_2}{3}\right)^{-\frac{1}{2}},$$

$$\frac{\partial \alpha}{\partial J_2} = \frac{\sqrt{3}}{2}\frac{J_3}{(J_2)^{\frac{5}{2}}}\frac{1}{\sin 3\alpha},\ \frac{\partial \alpha}{\partial J_3} = -\frac{1}{6\sin 3\alpha}\left(\frac{3}{J_2}\right)^{\frac{3}{2}},$$

$$\frac{\partial J_2}{\partial \sigma_{ij}} = S_{ij}, \text{ where } S_{ij} = \sigma_{ij} - \frac{\sigma_{kk}}{3}\delta_{ij},$$

$$\frac{\partial J_3}{\partial \sigma_{ij}} = S_{ik} S_{kj} - \frac{2}{3} J_2 \delta_{ij}$$

Clearly, singularities exist when $\alpha = 0$ and $\alpha = \pi/3$ in the terms $\partial\alpha/\partial J_2$ and $\partial\alpha/\partial J_3$.

When using shell elements in finite element models or for calculating the r-value expressions (2.13), plane stress conditions ($\sigma_{33} = \sigma_{13} = \sigma_{23} = 0$) can be assumed. For plane stress, the computation of the first derivatives is simplified. Now, instead of using relations (3.12) and (3.13), the following relations may be used to determine the principal values of the deviator of the Cauchy stress tensor

$$S_1 = \frac{2}{3}\sigma_1 - \frac{1}{3}\sigma_2, \quad S_2 = \frac{2}{3}\sigma_2 - \frac{1}{3}\sigma_1, \quad S_3 = -\frac{1}{3}\sigma_1 - \frac{1}{3}\sigma_2$$

where,

$$\sigma_1 = \frac{\sigma_{11} + \sigma_{22}}{2} + \sqrt{\frac{1}{4}\left(\sigma_{11} + \sigma_{22}\right)^2 + \left(\sigma_{12}\right)^2}$$

$$\sigma_2 = \frac{\sigma_{11} + \sigma_{22}}{2} - \sqrt{\frac{1}{4}\left(\sigma_{11} + \sigma_{22}\right)^2 + \left(\sigma_{12}\right)^2}$$

The general form of the first derivative of the proposed isotropic criterion for plane stress conditions becomes

$$\frac{\partial F}{\partial \sigma_{ij}} = \frac{\partial F}{\partial S_k} \frac{\partial S_k}{\partial \sigma_l} \frac{\partial \sigma_l}{\partial \sigma_{ij}} \tag{3.11}$$

for which no singularities exist.

In order for a material to be a stable plastic material, a yield surface must be convex. The convexity of a yield surface also guarantees a unique relationship between the stresses and plastic strain increments assuming an associated flow rule (Malvern,

1969). For the yield function to be convex, its Hessian matrix must be positive semi-definite. Let H be the Hessian matrix, i.e.,

$$H_{ij} = \frac{\partial^2 f}{\partial \sigma_i \partial \sigma_j}, \tag{3.12}$$

where $i, j = 1 \ldots 3$ and σ_i are the principal stresses. We shall prove that for $k \in [-1,1]$ and any integer $a \geq 1$, the proposed yield function (3.1) is convex. Isotropy dictates three fold symmetry of the yield surface, thus it is sufficient to prove its convexity for stress states in terms of the principal stresses corresponding to $\sigma_1 \geq \sigma_2 \geq \sigma_3$.

For $0 \leq \alpha_1 < \pi/6$, the principal values of the deviator of the Cauchy stress tensor are $S_1 > 0,\ S_2 < 0,\ S_3 < 0$, and

$$H_{11} = \frac{a(a-1)}{9}\left\{4(1-k)^a S_1^{a-2} + (1+k)^a (-1)^a (S_2^{a-2} + S_3^{a-2})\right\}$$

$$H_{22} = \frac{a(a-1)}{9}\left\{(1-k)^a S_1^{a-2} + (1+k)^a (-1)^a (4S_2^{a-2} + S_3^{a-2})\right\}$$

$$H_{33} = \frac{a(a-1)}{9}\left\{(1-k)^a S_1^{a-2} + (1+k)^a (-1)^a (S_2^{a-2} + 4S_3^{a-2})\right\}$$

$$H_{12} = \frac{a(a-1)}{9}\left\{-2(1-k)^a S_1^{a-2} - (1+k)^a (-1)^a (2S_2^{a-2} - S_3^{a-2})\right\}$$

$$H_{13} = \frac{a(a-1)}{9}\left\{-2(1-k)^a S_1^{a-2} - (1+k)^a (-1)^a (-S_2^{a-2} + 2S_3^{a-2})\right\}$$

$$H_{23} = \frac{a(a-1)}{9}\left\{(1-k)^a S_1^{a-2} + (1+k)^a (-1)^a (-2S_2^{a-2} - 2S_3^{a-2})\right\} \tag{3.13}$$

Note that $\sum_{j=1}^{3} H_{ij} = 0$, for any $i = 1$, 2, or 3. Thus, the determinant of H is zero and its principal values are λ_1, λ_2, and $\lambda_3 = 0$. Furthermore,

$$tr(\boldsymbol{H}) = \lambda_1 + \lambda_2 = \frac{6a(a-1)}{9}\left\{(1-k)^a S_1^{a-2} + (1+k)^a (-1)^a (S_2^{a-2} + S_3^{a-2})\right\}$$

$$tr_2(\boldsymbol{H}) = \lambda_1\lambda_2 = \frac{a^2(a-1)^2}{9}\left[\begin{array}{l}(1-k)^{2a}\left(S_1^2\right)^{a-2} + (1+k)^{2a}\left(S_2^2\right)^{a-2} + \left(1-k^2\right)^a (S_1)^{a-2}(-S_2)^{a-2} + \\ 3\left(1-k^2\right)^a (S_1)^{a-2}(-S_3)^{a-2} + 3(1+k)^{2a}(-S_2)^{a-2}(-S_3)^{a-2}\end{array}\right]$$

Since $S_1 > 0,\ S_2 < 0,\ S_3 < 0$, it follows that for $k \in (-1,1)$ and any integer $a \geq 1$:

tr($\boldsymbol{H}$) = $\lambda_1 + \lambda_2 \geq 0$ and $tr_2(\boldsymbol{H}) = \lambda_1\lambda_2 \geq 0$, i.e., the Hessian is always positive semi-definite.

For the case $\pi/6 < \alpha_1 \leq \pi/3$

$$H_{11} = \frac{a(a-1)}{9}\left\{(1-k)^a(4S_1^{a-2} + S_2^{a-2}) + (1+k)^a(-1)^a S_3^{a-2}\right\}$$

$$H_{22} = \frac{a(a-1)}{9}\left\{(1-k)^a(S_1^{a-2} + 4S_2^{a-2}) + (1+k)^a(-1)^a S_3^{a-2}\right\}$$

$$H_{33} = \frac{a(a-1)}{9}\left\{(1-k)^a(S_1^{a-2} + S_2^{a-2}) + 4(1+k)^a(-1)^a S_3^{a-2}\right\}$$

$$H_{12} = \frac{a(a-1)}{9}\left\{-2(1-k)^a(S_1^{a-2} + S_2^{a-2}) + (1+k)^a(-1)^a S_3^{a-2}\right\}$$

$$H_{13} = \frac{a(a-1)}{9}\left\{(1-k)^a(-2S_1^{a-2} + S_2^{a-2}) - 2(1+k)^a(-1)^a S_3^{a-2}\right\} \tag{3.14}$$

$$H_{23} = \frac{a(a-1)}{9}\left\{(1-k)^a(S_1^{a-2} - 2S_2^{a-2}) - 2(1+k)^a(-1)^a S_3^{a-2}\right\}$$

It follows that $\sum_{j=1}^{3} H_{ij} = 0$, for any i =1…3. Thus, the determinant of H is zero and

$$tr(\boldsymbol{H}) = \frac{6a(a-1)}{9}\left\{(1-k)^a(S_1^{a-2} + S_2^{a-2}) + (1+k)^a(-1)^a S_3^{a-2}\right\}$$

$$tr_2\left(\boldsymbol{H}\right)=\lambda_1\lambda_2=\frac{a^2\left(a-1\right)^2}{9}\left[\begin{array}{l}\left(1-k^2\right)^a\left(S_2^2\right)^{a-2}+\left(1-k\right)^{2a}\left(S_2^2\right)^{a-2}+\left(1-k\right)^{2a}\left(S_1\right)^{a-2}\left(S_2\right)^{a-2}+\\3\left(1+k\right)^{2a}\left(S_2\right)^{a-2}\left(-S_3\right)^{a-2}+3\left(1+k\right)^{2a}\left(S_1\right)^{a-2}\left(-S_3\right)^{a-2}\end{array}\right]$$

Since $S_1>0,\ S_2>0,\ S_3<0$, it follows that for $k\in\left(-1,1\right)$ and any integer $a\geq 1$:

tr($\boldsymbol{H}$) $\geq$ 0 and $tr_2\left(\boldsymbol{H}\right)\geq 0$. Thus, for $k\in\left[-1,1\right]$ and any integer $a\geq 1$ the yield function is convex.

3.2 Extension of the Proposed Isotropic Yield Criterion to Include Orthotropy

To describe both the asymmetry between yield in tension and compression and the anisotropy observed in hcp metal sheets, we extend the proposed isotropic criterion (3.1) to orthotropy. For the description of incompressible plastic anisotropy, Cazacu and Barlat (2001, 2003) introduced a general and rigorous method which is based on the theory of representation of tensor functions (see equation 2.26). It consists in substituting in the expression of any given isotropic criterion, the 2nd and 3rd invariants of the stress deviator with generalizations of these invariants compatible with the symmetry group of the material considered. However, with this approach, convexity is reinforced only numerically. For this reason, a particular case of this general theory, which is based on applying a fourth-order linear transformation operator on the Cauchy stress tensor or its deviator, has received more attention (Sobodka, 1969; Barlat et al., 1991; Karafillis and Boyce, 1993; etc.). It is worth noting that by using the linear transformation approach, the convexity of the resulting anisotropic extension is automatically satisfied (Rockafellar, 1974).

Following Barlat et al. (2005), orthotropy is introduced by means of a linear transformation on the deviator of the Cauchy stress tensor, i.e., in the expression of the

isotropic criterion (3.1), the principal values of the Cauchy stress deviator are substituted by the principal values of the transformed tensor **Σ** defined as

$$\Sigma_{ij} = L_{ijkl} S_{kl} \tag{3.15}$$

where ***L*** is a 4th order tensor whose coefficients assign a weight to different stress components. Thus, the proposed orthotropic criterion is of the form

$$\left(\left|\Sigma_1\right| - k\Sigma_1\right)^a + \left(\left|\Sigma_2\right| - k\Sigma_2\right)^a + \left(\left|\Sigma_3\right| - k\Sigma_3\right)^a = F \tag{3.16}$$

where $\Sigma_1, \Sigma_2, \Sigma_3$ are the principal values of **Σ**. In the absence of any shear stresses, the values of Σ_{xx}, Σ_{yy}, and Σ_{zz} are the principal values of **Σ**. However, if the shear stresses are present and $\sigma_3 \neq 0$, the principal values of **Σ** are the roots of the 3rd order algebraic equation

$$X^3 - H_1 X^2 + H_2 X - H_3 = 0 \tag{3.17}$$

where,

$H_1 = \Sigma_{xx} + \Sigma_{yy} + \Sigma_{zz}$,

$H_2 = \Sigma_{yy}\Sigma_{zz} + \Sigma_{zz}\Sigma_{xx} + \Sigma_{xx}\Sigma_{yy} - (\Sigma_{yz}^2 + \Sigma_{zx}^2 + \Sigma_{xy}^2)$, and

$H_3 = 2\Sigma_{yz}\Sigma_{zx}\Sigma_{xy} + \Sigma_{xx}\Sigma_{yy}\Sigma_{zz} - \Sigma_{xx}\Sigma_{yz}^2 - \Sigma_{yy}\Sigma_{zx}^2 - \Sigma_{zz}\Sigma_{xy}^2$.

The tensor ***L*** satisfies the major and minor symmetry and the requirement of invariance with respect to the orthotropy group. Thus, for 3-D stress conditions the orthotropic criterion involves 9 independent anisotropy coefficients, and reduces to the isotropic criterion (3.1) for ***L*** equal to the identity tensor.

Let (*x*,*y*,*z*) be the reference frame associated with orthotropy. In the case of a sheet, *x*, y, and z represent the rolling direction, the long transverse direction, and the short

transverse direction or the through thickness direction, respectively. Relative to the orthotropy axes (x,y,z), the tensor $\mathbf{\Sigma}$ (in vector form) is represented by

$$\begin{vmatrix} \Sigma_{xx} \\ \Sigma_{yy} \\ \Sigma_{zz} \\ \Sigma_{yz} \\ \Sigma_{zx} \\ \Sigma_{xy} \end{vmatrix} = \begin{bmatrix} L_{11} & L_{12} & L_{13} & & & \\ L_{12} & L_{22} & L_{23} & & & \\ L_{13} & L_{23} & L_{33} & & & \\ & & & L_{44} & & \\ & & & & L_{55} & \\ & & & & & L_{66} \end{bmatrix} \begin{vmatrix} S_{xx} \\ S_{yy} \\ S_{zz} \\ S_{yz} \\ S_{zx} \\ S_{xy} \end{vmatrix}$$

or in terms of the Cauchy stresses

$$\begin{vmatrix} \Sigma_{xx} \\ \Sigma_{yy} \\ \Sigma_{zz} \\ \Sigma_{yz} \\ \Sigma_{zx} \\ \Sigma_{xy} \end{vmatrix} = \begin{bmatrix} L_{11} & L_{12} & L_{13} & & & \\ L_{12} & L_{22} & L_{23} & & & \\ L_{13} & L_{23} & L_{33} & & & \\ & & & L_{44} & & \\ & & & & L_{55} & \\ & & & & & L_{66} \end{bmatrix} \begin{bmatrix} \frac{2}{3} & -\frac{1}{3} & -\frac{1}{3} & & & \\ -\frac{1}{3} & \frac{2}{3} & -\frac{1}{3} & & & \\ -\frac{1}{3} & -\frac{1}{3} & \frac{2}{3} & & & \\ & & & 1 & & \\ & & & & 1 & \\ & & & & & 1 \end{bmatrix} \begin{vmatrix} \sigma_{xx} \\ \sigma_{yy} \\ \sigma_{zz} \\ \sigma_{yz} \\ \sigma_{zx} \\ \sigma_{xy} \end{vmatrix}$$

Taking into account that S is traceless, (3.15) can also be written as

$$\begin{vmatrix} \Sigma_{xx} \\ \Sigma_{yy} \\ \Sigma_{zz} \\ \Sigma_{yz} \\ \Sigma_{zx} \\ \Sigma_{xy} \end{vmatrix} = \begin{bmatrix} 0 & L_{12}-L_{11} & L_{13}-L_{11} & & & \\ L_{12}-L_{22} & 0 & L_{23}-L_{22} & & & \\ L_{13}-L_{33} & L_{23}-L_{33} & 0 & & & \\ & & & L_{44} & & \\ & & & & L_{55} & \\ & & & & & L_{66} \end{bmatrix} \begin{vmatrix} S_{xx} \\ S_{yy} \\ S_{zz} \\ S_{yz} \\ S_{zx} \\ S_{xy} \end{vmatrix}$$

In the case of a thin sheet, plane stress conditions can be assumed. Using these assumptions, the only non-zero stress components are the in-plane stresses $\left(\sigma_{xx}, \sigma_{yy}, \sigma_{xy}\right)$, and the principal values of $\mathbf{\Sigma}$ are

$$\Sigma_1 = \frac{1}{2}\left(\Sigma_{xx} + \Sigma_{yy} + \sqrt{\left(\Sigma_{xx} - \Sigma_{yy}\right)^2 + 4\Sigma_{xy}^2}\right) \tag{3.18}$$

$$\Sigma_2 = \frac{1}{2}\left(\Sigma_{xx} + \Sigma_{yy} - \sqrt{\left(\Sigma_{xx} - \Sigma_{yy}\right)^2 + 4\Sigma_{xy}^2}\right)$$

$$\Sigma_3 = \Sigma_{zz}$$

where

$$\Sigma_{xx} = \left(\frac{2}{3}L_{11} - \frac{1}{3}L_{12} - \frac{1}{3}L_{13}\right)\sigma_{xx} + \left(-\frac{1}{3}L_{11} + \frac{2}{3}L_{12} - \frac{1}{3}L_{13}\right)\sigma_{yy} \tag{3.19}$$

$$\Sigma_{yy} = \left(\frac{2}{3}L_{12} - \frac{1}{3}L_{22} - \frac{1}{3}L_{23}\right)\sigma_{xx} + \left(-\frac{1}{3}L_{12} + \frac{2}{3}L_{22} - \frac{1}{3}L_{23}\right)\sigma_{yy}$$

$$\Sigma_{zz} = \left(\frac{2}{3}L_{13} - \frac{1}{3}L_{23} - \frac{1}{3}L_{33}\right)\sigma_{xx} + \left(-\frac{1}{3}L_{13} + \frac{2}{3}L_{23} - \frac{1}{3}L_{33}\right)\sigma_{yy}$$

$$\Sigma_{xy} = L_{66}\sigma_{xy}$$

If σ_0^T and σ_0^C define the yield stress in tension and compression along the rolling direction x, according to the proposed orthotropic criterion (3.16) it follows that

$$\sigma_0^T = \left\{\frac{F}{\left[\left|\Phi_1\right| - k\Phi_1\right]^a + \left[\left|\Phi_2\right| - k\Phi_2\right]^a + \left[\left|\Phi_3\right| - k\Phi_3\right]^a}\right\}^{\frac{1}{a}} \tag{3.20}$$

$$\sigma_0^C = \left\{\frac{F}{\left[\left|\Phi_1\right| + k\Phi_1\right]^a + \left[\left|\Phi_2\right| + k\Phi_2\right]^a + \left[\left|\Phi_3\right| + k\Phi_3\right]^a}\right\}^{\frac{1}{a}}$$

where

$$\Phi_1 = \left(\frac{2}{3} L_{11} - \frac{1}{3} L_{12} - \frac{1}{3} L_{13} \right) \tag{3.21}$$

$$\Phi_2 = \left(\frac{2}{3} L_{12} - \frac{1}{3} L_{22} - \frac{1}{3} L_{23} \right)$$

$$\Phi_3 = \left(\frac{2}{3} L_{13} - \frac{1}{3} L_{23} - \frac{1}{3} L_{33} \right)$$

Similarly, if σ_{90T} and σ_{90C} are tensile and compressive yield stresses in the transverse direction, *y*, then

$$\sigma_{90}^{T} = \left\{ \frac{F}{\left[|\Psi_1| - k\Psi_1 \right]^a + \left[|\Psi_2| - k\Psi_2 \right]^a + \left[|\Psi_3| - k\Psi_3 \right]^a} \right\}^{\frac{1}{a}} \tag{3.22}$$

$$\sigma_{90}^{C} = \left\{ \frac{F}{\left[|\Psi_1| + k\Psi_1 \right]^a + \left[|\Psi_2| + k\Psi_2 \right]^a + \left[|\Psi_3| + k\Psi_3 \right]^a} \right\}^{\frac{1}{a}}$$

where

$$\Psi_1 = \left(-\frac{1}{3} L_{11} + \frac{2}{3} L_{12} - \frac{1}{3} L_{13} \right) \tag{3.23}$$

$$\Psi_2 = \left(-\frac{1}{3} L_{12} + \frac{2}{3} L_{22} - \frac{1}{3} L_{23} \right)$$

$$\Psi_3 = \left(-\frac{1}{3} L_{13} + \frac{2}{3} L_{23} - \frac{1}{3} L_{33} \right)$$

Yielding under pure shear parallel to the orthotropy axes occurs when σ_{xy} is equal to

$$\tau^0 = \left\{ \frac{F}{\left[\left|L_{66}\right| + kL_{66}\right]^a + \left[\left|C_{66}\right| - kL_{66}\right]^a} \right\}^{\frac{1}{a}} \tag{3.24}$$

Yielding under equibiaxial tension occurs when σ_{xx} and σ_{yy} are both equal to

$$\sigma_b^T = \left\{ \frac{F}{\left[\left|\Omega_1\right| - k\Omega_1\right]^a + \left[\left|\Omega_2\right| - k\Omega_2\right]^a + \left[\left|\Omega_3\right| - k\Omega_3\right]^a} \right\} \tag{3.25}$$

while yielding under equibiaxial compression occurs when $\sigma_{xx} = \sigma_{yy} = \sigma_b^C$,

$$\sigma_b^C = \left\{ \frac{F}{\left[\left|\Omega_1\right| + k\Omega_1\right]^a + \left[\left|\Omega_2\right| + k\Omega_2\right]^a + \left[\left|\Omega_3\right| + k\Omega_3\right]^a} \right\} \tag{3.26}$$

where,

$$\Omega_1 = \left(\frac{1}{3} L_{11} + \frac{1}{3} L_{12} - \frac{2}{3} L_{13} \right) \tag{3.27}$$

$$\Omega_2 = \left(\frac{1}{3} L_{12} + \frac{1}{3} L_{22} - \frac{2}{3} L_{23} \right)$$

$$\Omega_3 = \left(\frac{1}{3} L_{13} + \frac{1}{3} L_{23} - \frac{2}{3} L_{33} \right)$$

Furthermore, we assume that the plastic potential coincides with the yield function. According to the proposed orthotropic criterion, the Lankford coefficients which are defined as the width to thickness strain ratios in a uniaxial loading (see equation 2.13), become

$$r_0^T = -\frac{(1-k)^a \Phi_1^{a-1} \Psi_1 + (-1-k)^a (\Phi_2^{a-1} \Psi_2 + \Phi_3^{a-1} \Psi_3)}{(1-k)^a \Phi_1^{a-1} (\Psi_1 + \Phi_1) + (-1-k)^a (\Phi_2^{a-1} \Psi_2 + \Phi_3^{a-1} \Psi_3 + \Phi_2^a + \Phi_3^a)} \tag{3.28}$$

$$r_{90}^T = -\frac{(1-k)^a \Psi_2^{a-1} \Phi_2 + (-1-k)^a (\Psi_1^{a-1} \Phi_1 + \Psi_3^{a-1} \Phi_3)}{(1-k)^a \Psi_2^{a-1} (\Phi_2 + \Psi_2) + (-1-k)^a (\Psi_1^{a-1} \Phi_1 + \Psi_3^{a-1} \Phi_3 + \Psi_1^a + \Psi_3^a)}$$

$$r_0^C = -\frac{(-1-k)^a \Phi_1^{a-1}\Psi_1 + (1-k)^a(\Phi_2^{a-1}\Psi_2 + \Phi_3^{a-1}\Psi_3)}{(-1-k)^a \Phi_1^{a-1}(\Psi_1 + \Phi_1) + (1-k)^a(\Phi_2^{a-1}\Psi_2 + \Phi_3^{a-1}\Psi_3 + \Phi_2^a + \Phi_3^a)}$$

$$r_{90}^C = -\frac{(-1-k)^a \Psi_2^{a-1}\Phi_2 + (1-k)^a(\Psi_1^{a-1}\Phi_1 + \Psi_3^{a-1}\Phi_3)}{(-1-k)^a \Psi_2^{a-1}(\Phi_2 + \Psi_2) + (1-k)^a(\Psi_1^{a-1}\Phi_1 + \Psi_3^{a-1}\Phi_3 + \Psi_1^a + \Psi_3^a)}$$

with Φ_1 to Φ_3 given by (3.7), Ψ_1 to Ψ_3 given by (3.9), and the superscripts T and C designating tensile and compressive states, respectively.

Using equations (3.20) – (3.28), the coefficients for the yield criterion (3.16) can be determined by minimizing an error function of the form

$$Error = \sum_n weight\left(1 - \frac{\sigma_{predicted}^n}{\sigma_{data}^n}\right)^2 + \sum_m weight\left(1 - \frac{r_{predicted}^m}{r_{data}^m}\right)^2 \tag{3.29}$$

where the index n represents the number of experimental yield stresses available, and m represents the number of experimental r-values. Each term has an assigned weight which can be used to distinguish yield stresses from r-values. A better accuracy for the yield stresses is usually required because a difference of a few percent in the flow stress is much more significant than in the r-values (Barlat et al., 2005).

Although the transformed tensor $\mathbf{\Sigma}$ is not deviatoric, the proposed orthotropic criterion is nevertheless independent of hydrostatic pressure. In order to prove this concept, we shall show that the derivative of the proposed orthotropic yield function, F, with respect to the hydrostatic pressure, p, is zero. The proposed orthotropic yield condition is

$$f(\Sigma_1, \Sigma_2, \Sigma_3) = \left(|\Sigma_1| - k\Sigma_1\right)^a + \left(|\Sigma_2| - k\Sigma_2\right)^a + \left(|\Sigma_3| - k\Sigma_3\right)^a,$$

whose derivative with respect to hydrostatic pressure is

$$\frac{\partial f}{\partial p} = \frac{\partial f}{\partial \Sigma_m}\frac{\partial \Sigma_m}{\partial \Sigma_{ij}}\frac{\partial \Sigma_{ij}}{\partial p}, \tag{3.30}$$

where Σ_i are the principal values of the transformed stress tensor $\mathbf{\Sigma}$. We shall prove that $\frac{\partial \Sigma_{ij}}{\partial p}$=0, hence $\frac{\partial f}{\partial p}$ = 0, i.e., the condition of plastic incompressibility is satisfied. Indeed, the transformed stress tensor $\mathbf{\Sigma}$ can be expressed as

$$\mathbf{\Sigma} = \boldsymbol{L}\boldsymbol{S} = \boldsymbol{L}\boldsymbol{T}\boldsymbol{\sigma}, \tag{3.31}$$

where $\boldsymbol{T}$ denotes the 4th order deviatoric projection that transforms a 2nd order tensor in its deviator. Thus,

$$\frac{\partial \Sigma_{ij}}{\partial p} = -B_{ijkl}\delta_{kl} = -B_{ijkk} \qquad i,j,\ k = 1\ldots 3, \tag{3.32}$$

where $\boldsymbol{B} = \boldsymbol{L}\ \boldsymbol{T}$ is the 4th order orthotropic tensor that relates the transformed tensor $\mathbf{\Sigma}$ to the Cauchy stress $\boldsymbol{\sigma}$. Relative to ($\boldsymbol{x},\boldsymbol{y},\boldsymbol{z}$), the tensor $\boldsymbol{L}$ is represented by

$$\boldsymbol{L} = \begin{bmatrix} L_{11} & L_{12} & L_{13} & & & \\ L_{12} & L_{22} & L_{23} & & & \\ L_{13} & L_{23} & L_{33} & & & \\ & & & L_{44} & & \\ & & & & L_{55} & \\ & & & & & L_{66} \end{bmatrix} \tag{3.33}$$

while $\boldsymbol{T}$ is given by

$$\boldsymbol{T} = \frac{1}{3}\begin{bmatrix} 2 & -1 & -1 & & & \\ -1 & 2 & -1 & & & \\ -1 & -1 & 2 & & & \\ & & & 3 & & \\ & & & & 3 & \\ & & & & & 3 \end{bmatrix}$$

In (3.33) we used the simplified contracted indices convention of Voigt was adopted ($L_{11} \overset{def}{=} L_{1111}$; $L_{12} \overset{def}{=} L_{1122}$; $L_{13} \overset{def}{=} L_{1133}$, etc.). It follows that the non-zero components of the 4th order tensor $\boldsymbol{B}$ are

$$B_{11} = \left(2L_{11} - L_{12} - L_{13}\right)/3$$

$$B_{12} = \left(-L_{11} + 2L_{12} - L_{13}\right)/3$$

$$B_{13} = \left(-L_{11} - L_{12} + 2L_{13}\right)/3$$

$$B_{21} = \left(2L_{12} - L_{22} - L_{23}\right)/3$$

$$B_{22} = \left(-L_{12} + 2L_{22} - L_{23}\right)/3$$

$$B_{31} = \left(-L_{32} + 2L_{31} - L_{33}\right)/3$$

$$B_{32} = \left(-L_{31} + 2L_{32} - L_{33}\right)/3$$

$$B_{33} = \left(-L_{31} + 2L_{33} - L_{32}\right)/3$$

Hence, we obtain

$$\begin{cases} B_{11} + B_{12} + B_{13} = 0 \\ B_{21} + B_{22} + B_{23} = 0 \\ B_{31} + B_{32} + B_{33} = 0 \end{cases}. \tag{3.34}$$

Thus, $\frac{\partial \Sigma_{ij}}{\partial p}$=0 and $\frac{\partial f}{\partial p}$ = 0 satisfying the condition of plastic incompressibility.

3.2.1 Application of the Proposed Criterion to the Description of Yielding of Hcp Metals

3.2.1.1 Magnesium Alloys

Kelley and Hosford (1968) reported the results of an experimental investigation into the anisotropy and asymmetry in yielding of textured polycrystalline pure Mg and

binary Mg-Th (0.5 % Th) and Mg-Li (4% Li) alloys. The data consists of the results of uniaxial compression tests in the rolling, transverse, and normal directions, respectively, uniaxial tensile tests in the rolling and transverse directions, as well as plane-strain compression tests. Based on these data, the experimental yield loci corresponding to several constant levels (1, 5, and 10%) of the effective plastic strain were reported (see Figures 3.9, 3.10, and 3.11 where experimental data are represented by symbols).

Due to the mechanical processing of a cold rolled sheet, magnesium alloy sheets have a strong basal pole alignment in the thickness direction. Therefore, the easily deformed $\{10\bar{1}2\}\langle 10\bar{1}1\rangle$ tensile twin system about magnesium's c-axis is activated by compression in the plane of the sheet. However, this twin system is not active due to tension within the plane of the sheet. The effect of $\{10\bar{1}2\}\langle 10\bar{1}1\rangle$ twinning is clearly evident by the initially low compressive strengths with respect to tensile strengths at 1% effective plastic strain. By 10% strain, the third quadrant strengths are comparable to those in the first quadrant owing to the extra barriers to further deformation processes due to the reoriented twins created by loadings in the third quadrant.

Figure 3.8 shows the section of the theoretical plane stress yield loci (equation 3.16) with $\sigma_{xy} = 0$ for Mg-Th together with the experimental data reported in Hosford and Kelley (1968). The constant a was set to 2 while the anisotropy coefficients involved in the expression of the theoretical yield loci for biaxial stress states as well as the constant k were determined using equations (3.20) to (3.29) and the data corresponding to the given strain level. The obtained values of these parameters corresponding to the 1%, 5%, and 10% effective plastic strain surfaces are given in Table 3.1. Note that the proposed theory reproduces very well the observed asymmetry in yielding.

The experimental yield loci for the Mg-Li alloy sheets are similar in shape to those for the Mg-Th alloy, but with much reduced yield stresses due to the occurrence of prism slip and to the weaker crystallographic texture. The effect of $\{10\bar{1}2\}\langle 10\bar{1}1\rangle$ twinning is evident in the low compressive strengths at 1% and 5% strains. Figure 3.10 shows the theoretical yield loci for Mg-Li along with the data reported by Kelley and Hosford. The constant *a* was chosen to be 2 for this material. The coefficients involved in the expressions of the biaxial yield loci are given in Table 3.2.

The yield locus for the textured pure magnesium has a highly asymmetrical shape for the 1% and 5% yield locus due to twinning. Note the much greater strength in tension than in compression and the higher tensile strength in the transverse direction than in the rolling direction. The yield locus at 5% strain shows asymmetry similar to that of the locus at 1% strain. At 10% strain, the third quadrant strengths are comparable to the first quadrant strengths due to the hardening effects of $\{10\bar{1}2\}\langle 10\bar{1}1\rangle$ twinning. Figure 3.11 shows the yield loci of the present theory with the 5 data points for each level of strain given by Kelley and Hosford. The constant *a* was chosen to be 3 for the 1% and 5% locus due to the asymmetry. This constant was chosen to be 2 for the 10% locus since the yield locus becomes more elliptical. The yield locus generated by the present theory is in good agreement with the published data. The coefficients involved in the expressions of the biaxial yield loci are given in Table 3.3.

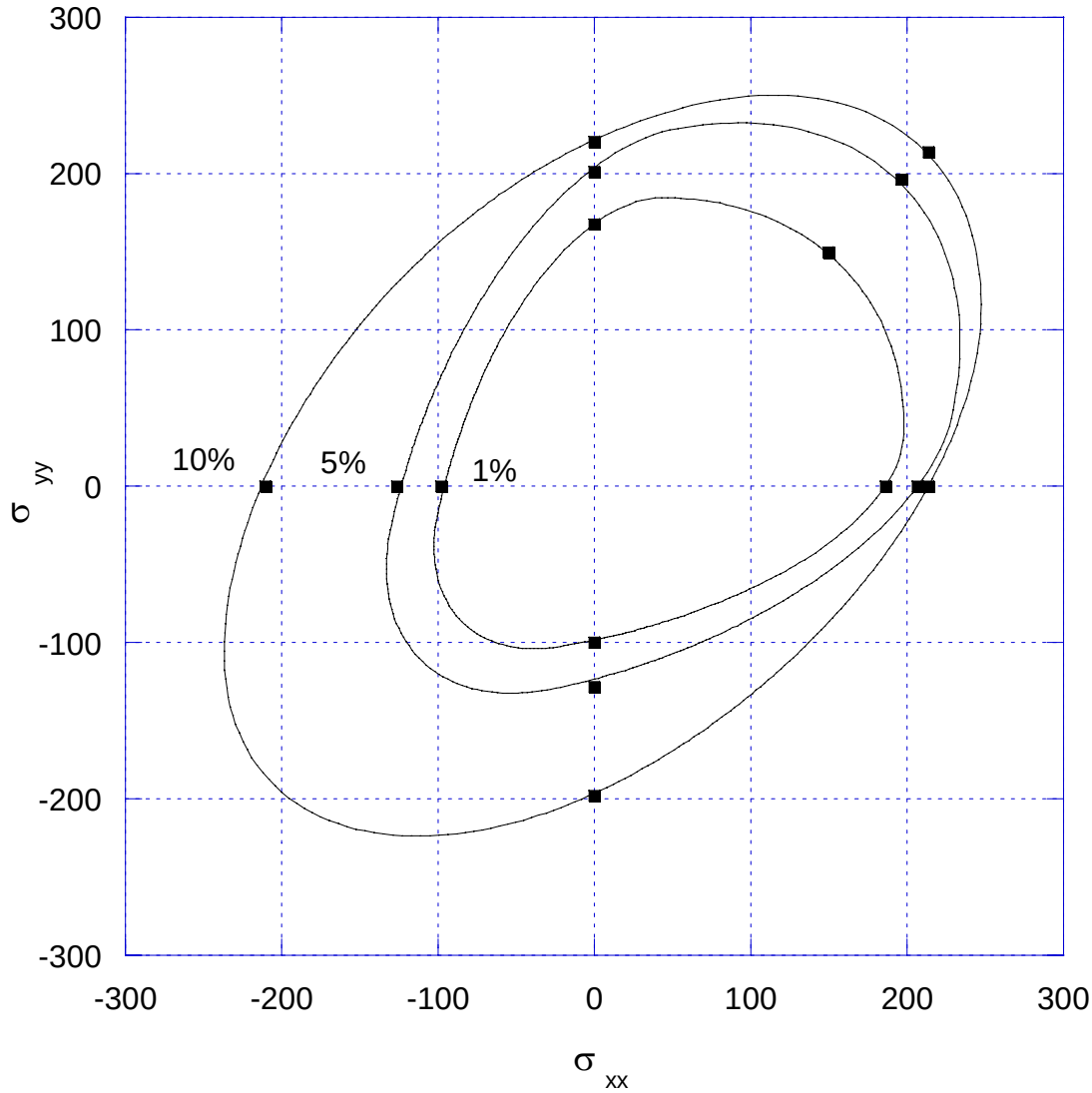

Figure 3.9 Comparison between the plane stress yield loci ($\sigma_{xy} = 0$) for a Mg-0.5% Th sheet predicted by the proposed theory (solid lines) and experiments (symbols). Data after Kelly and Hosford (1968). Stresses in Mpa

Table 3.1 MG-TH yield surface coefficients

	a	k	L_{11}	L_{12}	L_{13}	L_{22}	L_{23}	L_{33}
1%	2	0.3539	1.0	0.4802	0.2592	0.9517	0.2071	0.4654
5%	2	0.2763	1.0	0.3750	0.0858	0.9894	0.0659	0.1238
10%	2	0.0598	1.0	0.6336	0.2332	1.4018	0.5614	0.7484

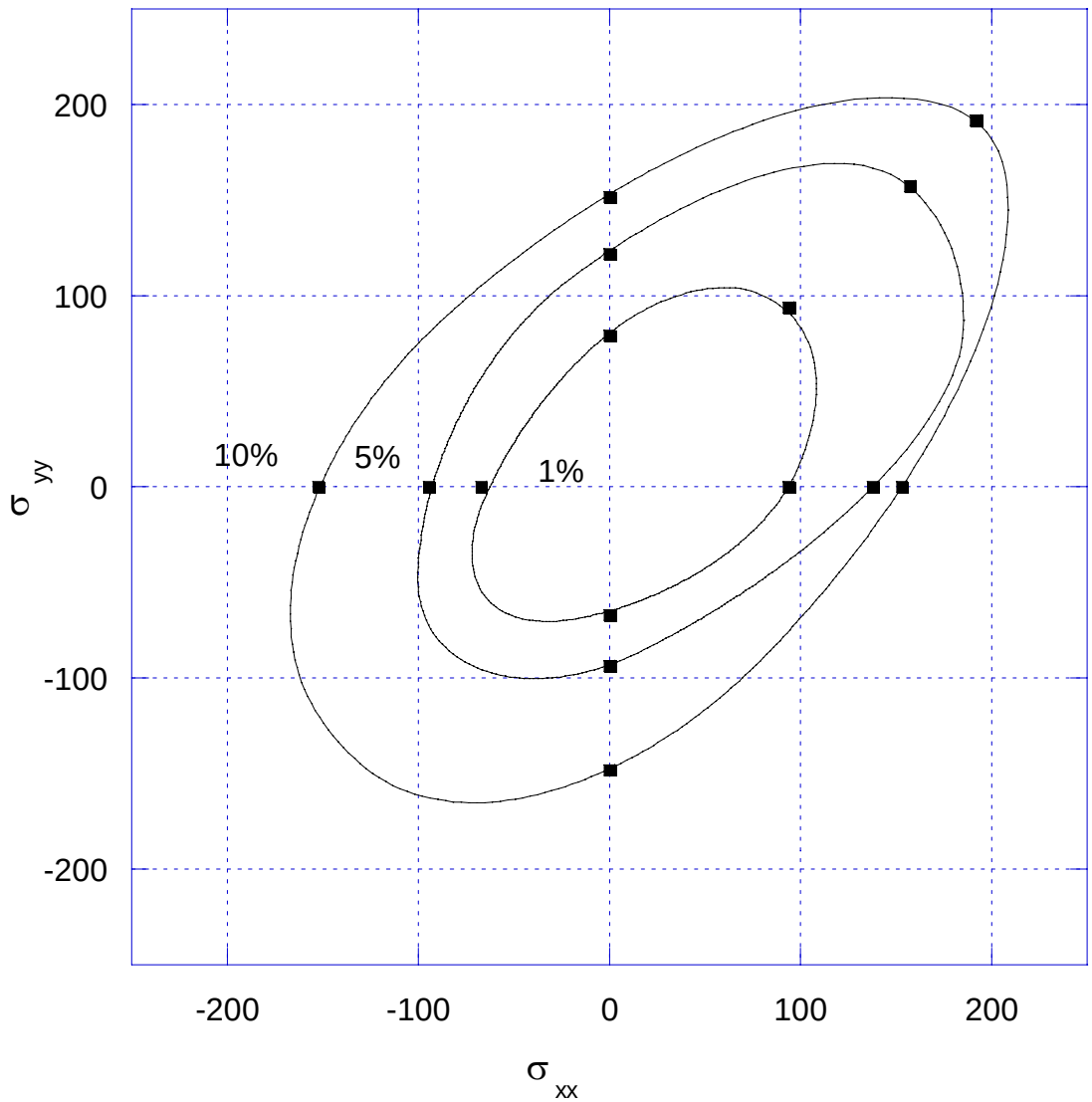

Figure 3.10 Comparison between the plane stress yield loci ($\sigma_{xy} = 0$) for a Mg-4% Li sheet predicted by the proposed theory (solid lines) and experiments (symbols). Data after Kelly and Hosford (1968). Stresses in MPa

Table 3.2 MG-LI yield surface coefficients

	a	k	L_{11}	L_{12}	L_{13}	L_{22}	L_{23}	L_{33}
1%	2	0.2026	1.0	0.5871	0.6975	0.9783	0.2840	0.1497
5%	2	0.2982	1.0	0.6103	0.8056	1.0940	0.5745	0.1764
10%	2	0.1763	1.0	0.5324	0.8602	1.0437	0.8404	0.2946

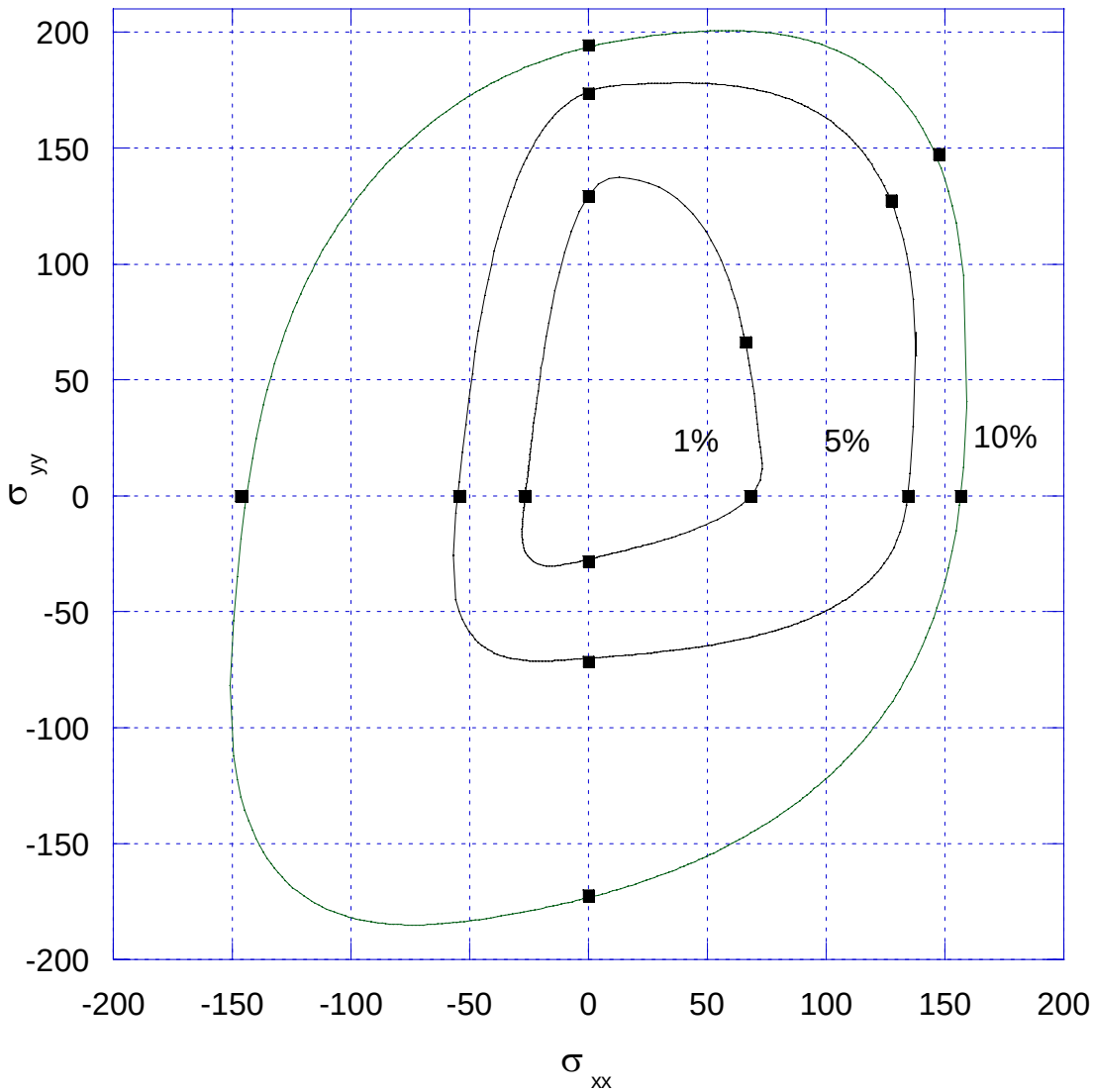

Figure 3.11 Comparison between the plane stress yield loci ($\sigma_{xy} = 0$) for a pure Mg sheet predicted by the proposed theory (solid lines) and experiments (symbols). Data after Kelly and Hosford (1968). Stresses in MPa

Table 3.3 MG yield surface coefficients

	a	k	L_{11}	L_{12}	L_{13}	L_{22}	L_{23}	L_{33}
1%	3	0.6293	1.0	0.4349	-0.0513	1.0178	0.1294	0.3417
5%	3	0.4320	1.0	0.4123	-0.0119	0.8617	0.0570	0.2024
10%	2	0.0776	1.0	0.2807	-0.0338	0.9916	0.1219	0.6874

3.2.1.2 Titanium Alloys

In the following, we apply the proposed orthotropic criterion (3.16) to the description of the anisotropy and tension-compression asymmetry of 4Al-1/4 O_2 textured α (hcp) titanium alloy (data after Lee and Backofen, 1966). True stress-strain curves were reported for different loading paths: uniaxial tension in the x direction (rolling direction), uniaxial compression in the z-direction (through-thickness compression), and plane strain compression in the z and y (transverse) directions. The material had nearly ideal basal texture with a deviation of about 25 degrees from the sheet normal toward the transverse direction. Based on these data, the experimental yield loci corresponding to several constant levels of the largest principal strain were reported (see Figure 3.12, experimental data are represented by symbols). Due to the strong basal pole alignment in the direction of the normal to the sheet, $\{10\bar{1}2\}$ twinning was activated by compression perpendicular to this direction, but is no twinning was revealed in tension testing within the plane (see Lee and Backofen, 1966). The effect of $\{10\bar{1}2\}$ twinning is clearly evident in the low compressive strengths in the rolling and transverse directions.

Figure 3.4 also shows the theoretical yield loci along with the experimental data. The coefficients involved in the expressions of the theoretical yield loci are given in Table 3.4. Note the ability of the proposed criterion to correctly describe the asymmetry in yielding of 4Al-1/4 O_2.

In order to account for the eccentricity of the yield surfaces of titanium and its alloys, Hosford (1966) proposed a modification of the Hill criterion to include terms linear in stress

$$A\sigma_x + B\sigma_y + (-B - A)\sigma_z + F(\sigma_y - \sigma_z)^2 + G(\sigma_z - \sigma_x)^2 + H(\sigma_x - \sigma_y)^2 = 1 \qquad (3.35)$$

The linear terms in equation (3.35) allow for the center of the yield surface to shift, thus allowing for different yield strengths in tension and compression. However, by adding these terms, the criterion is no longer pressure-independent, nor is it as accurate as using the proposed yield criterion. Hosford's (1966) yield function given by Eq. (3.35) was applied to the same 4Al-1/4 O_2 textured α titanium alloy (see Figure 3.13). Comparison between theoretical and experimental yield loci show that the proposed criterion (3.16) describes with greater accuracy the yield behavior of the titanium alloy.

3.2.2 Derivatives of the Orthotropic Yield Function

The proposed orthotropic yield criterion (3.16) is of the form

$$\left(\left|\Sigma_1\right| - k\Sigma_1\right)^a + \left(\left|\Sigma_2\right| - k\Sigma_2\right)^a + \left(\left|\Sigma_3\right| - k\Sigma_3\right)^a = F$$

where $\Sigma_1, \Sigma_2, \Sigma_3$ are the principal values of the transformed tensor $\Sigma_{ij} = L_{ijkl} S_{kl}$. For a general 3-dimensional problem, it is necessary to develop an expression between the principal values of $\mathbf{\Sigma}$ and its components in order to determine the derivatives of the yield function. This expression can be developed through the use of the deviator of $\mathbf{\Sigma}$, denoted by $\bar{\mathbf{\Sigma}}$, since the cubic equation (3.17) would then lack the quadratic term upon substitution of $\bar{\mathbf{\Sigma}}$ for $\mathbf{\Sigma}$. Once an expression is obtained between the principal values of $\bar{\mathbf{\Sigma}}$ and its components, the spherical component of $\mathbf{\Sigma}$ can be added to obtain a relationship between the principal values of $\mathbf{\Sigma}$ and its components.

Substituting $\bar{\mathbf{\Sigma}}$ ($\bar{\mathbf{\Sigma}}_{ij} = \mathbf{\Sigma}_{ij} - \delta_{ij} I_\Sigma / 3$, where I_Σ is the first invariant of $\mathbf{\Sigma}$) into equation (3.17) yields a relationship whose roots are the principal values of $\bar{\mathbf{\Sigma}}$

$$X^3 - J_{2\bar{\mathbf{\Sigma}}} X - J_{3\bar{\mathbf{\Sigma}}} = 0 \tag{3.36}$$

where $J_{2\bar{\mathbf{\Sigma}}}$ and $J_{3\bar{\mathbf{\Sigma}}}$ are the second and third scalar invariants of $\bar{\mathbf{\Sigma}}$. Solving for the roots

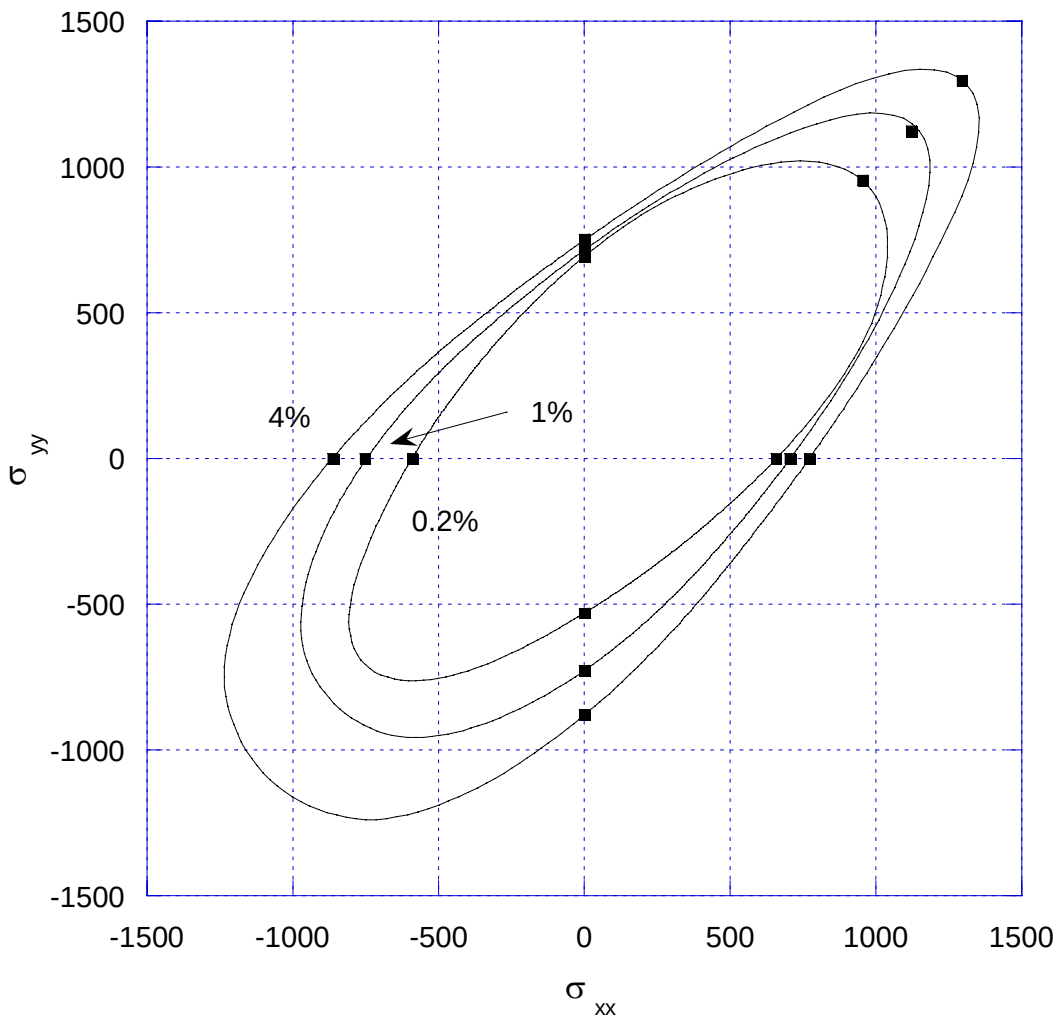

Figure 3.12 Comparison between the plane stress yield loci ($\sigma_{xy} = 0$) for a 4Al-1/4O_2 sheet predicted by the proposed theory (solid lines) and experiments (symbols). Data after Lee and Backofen (1966). (Stresses in MPa)

Table 3.4 4Al-1/4O_2 coefficients

	a	k	L_{11}	L_{12}	L_{13}	L_{22}	L_{23}	L_{33}
0.2%	2	0.1556	1.0	0.2285	0.0374	1.2967	0.2439	0.3244
1%	2	-0.1868	1.0	0.0431	0.3369	0.9562	0.3139	1.0861
4%	2	-0.2577	1.0	0.2178	0.3635	1.0422	0.3754	0.8825

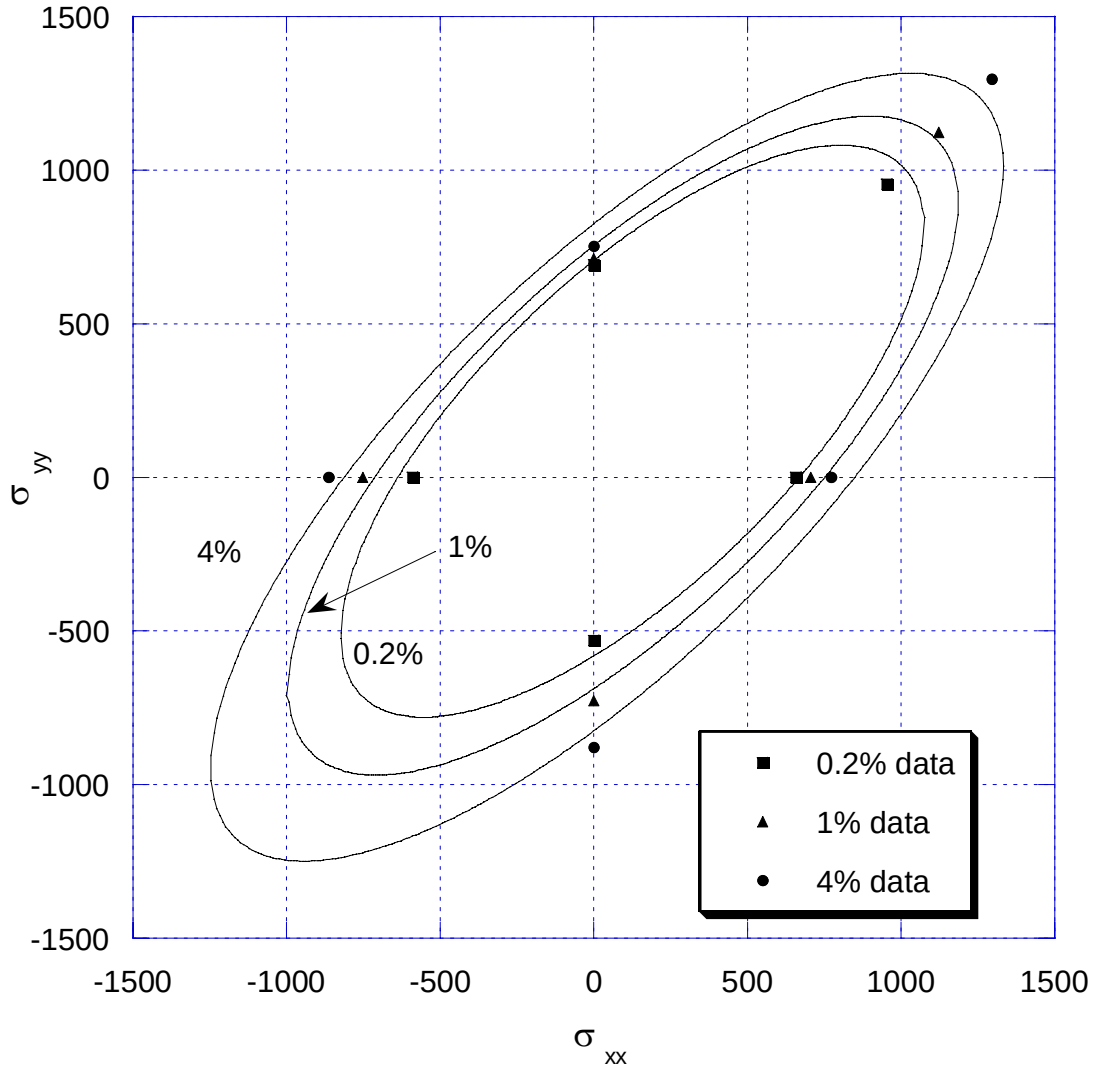

Figure 3.13 Comparison between the plane stress yield loci ($\sigma_{xy} = 0$) for a 4Al-1/4 O_2 sheet predicted by Hosford's 1966 modified Hill criterion (solid lines) and experiments (symbols). Data after Lee and Backofen (1966). (Stresses in Mpa)

of equation (3.36) and adding the spherical portion of $\boldsymbol{\Sigma}$ yields an expression for the principal values of $\boldsymbol{\Sigma}$

$$\Sigma_1 = 2\cos(\alpha_1)\sqrt{\frac{J_{2\bar{\boldsymbol{\Sigma}}}}{3}} + \frac{I_{\boldsymbol{\Sigma}}}{3}$$

$$\Sigma_2 = 2\cos\left(\alpha_1 - \frac{2\pi}{3}\right)\sqrt{\frac{J_{2\bar{\boldsymbol{\Sigma}}}}{3}} + \frac{I_{\boldsymbol{\Sigma}}}{3} \tag{3.37}$$

$$\Sigma_3 = 2\cos\left(\alpha_1 + \frac{2\pi}{3}\right)\sqrt{\frac{J_{2\bar{\boldsymbol{\Sigma}}}}{3}} + \frac{I_{\boldsymbol{\Sigma}}}{3}$$

where $\Sigma_1 \geq \Sigma_2 \geq \Sigma_3$ and α_1 is the angle satisfying $0 \leq 3\alpha_1 \leq \pi$ and whose cosine is given by

$$\cos\left(3\alpha_1\right) = \frac{J_{3\bar{\boldsymbol{\Sigma}}}}{2}\left(\frac{3}{J_{2\bar{\boldsymbol{\Sigma}}}}\right)^{\frac{3}{2}} \tag{3.38}$$

Now, the first derivatives of the proposed orthotropic yield criterion (3.16) can be written as

$$\frac{\partial F}{\partial \sigma_{ij}} = \frac{\partial F}{\partial \Sigma_q}\left\{\left[\frac{\partial \Sigma_q}{\partial \alpha}\left(\frac{\partial \alpha}{\partial J_{2\bar{\boldsymbol{\Sigma}}}}\frac{\partial J_{2\bar{\boldsymbol{\Sigma}}}}{\partial \Sigma_{kl}} + \frac{\partial \alpha}{\partial J_{3\bar{\boldsymbol{\Sigma}}}}\frac{\partial J_{3\bar{\boldsymbol{\Sigma}}}}{\partial \Sigma_{kl}}\right) + \frac{\partial \Sigma_q}{\partial J_{2\bar{\boldsymbol{\Sigma}}}}\frac{\partial J_{2\bar{\boldsymbol{\Sigma}}}}{\partial \Sigma_{kl}} + \frac{\partial \Sigma_q}{\partial I_{\boldsymbol{\Sigma}}}\frac{\partial I_{\boldsymbol{\Sigma}}}{\partial \Sigma_{kl}}\right]\frac{\partial \Sigma_{kl}}{\partial S_{mn}}\frac{\partial S_{mn}}{\partial \sigma_{ij}}\right\} \tag{3.39}$$

where,

$$\frac{\partial F}{\partial \Sigma_q} = a\left(\left|\Sigma_q\right| - k\Sigma_q\right)^{a-1}\left(\frac{\left|\Sigma_q\right|}{\Sigma_q} - k\right),$$

$$\frac{\partial \Sigma_1}{\partial \alpha} = -2\sin\alpha\sqrt{\frac{J_{2\bar{\boldsymbol{\Sigma}}}}{3}},\ \frac{\partial \Sigma_2}{\partial \alpha} = -2\sin\left(\alpha - \frac{2\pi}{3}\right)\sqrt{\frac{J_{2\bar{\boldsymbol{\Sigma}}}}{3}},\ \frac{\partial \Sigma_3}{\partial \alpha} = -2\sin\left(\alpha + \frac{2\pi}{3}\right)\sqrt{\frac{J_{2\bar{\boldsymbol{\Sigma}}}}{3}},$$

$$\frac{\partial \Sigma_1}{\partial J_{2\bar{\Sigma}}} = \frac{1}{3}\cos\alpha\left(\frac{J_{2\bar{\Sigma}}}{3}\right)^{-\frac{1}{2}},\ \frac{\partial \Sigma_2}{\partial J_{2\bar{\Sigma}}} = \frac{1}{3}\cos\left(\alpha - \frac{2\pi}{3}\right)\left(\frac{J_{2\bar{\Sigma}}}{3}\right)^{-\frac{1}{2}},$$

$$\frac{\partial \Sigma_3}{\partial J_{2\bar{\Sigma}}} = \frac{1}{3}\cos\left(\alpha + \frac{2\pi}{3}\right)\left(\frac{J_{2\bar{\Sigma}}}{3}\right)^{-\frac{1}{2}},$$

$$\frac{\partial \Sigma_q}{\partial I_{\Sigma}} = \frac{1}{3},$$

$$\frac{\partial \alpha}{\partial J_{2\bar{\Sigma}}} = \frac{3\sqrt{3}}{4}\frac{J_{3\bar{\Sigma}}}{\left(J_{2\bar{\Sigma}}\right)^{\frac{5}{2}}}\frac{1}{\sin 3\alpha},\ \frac{\partial \alpha}{\partial J_{3\bar{\Sigma}}} = -\frac{1}{6\sin 3\alpha}\left(\frac{3}{J_{2\bar{\Sigma}}}\right)^{\frac{3}{2}},$$

$$\frac{\partial J_{2\bar{\Sigma}}}{\partial \Sigma_{ij}} = \bar{\Sigma}_{ij}, \text{ where } \bar{\Sigma}_{ij} = \Sigma_{ij} - \frac{I_{\Sigma}}{3}\delta_{ij},$$

$$\frac{\partial J_{3\bar{\Sigma}}}{\partial \Sigma_{ij}} = \bar{\Sigma}_{ik}\bar{\Sigma}_{kj} - \frac{2}{3}J_{2\bar{\Sigma}}\delta_{ij},\ \frac{\partial I_{\Sigma}}{\partial \Sigma_{ij}} = \delta_{ij},$$

$$\frac{\partial \Sigma_{kk}}{\partial S_{nn}} = L_{kn},\ \frac{\partial \Sigma_{23}}{\partial S_{23}} = L_{44},\ \frac{\partial \Sigma_{31}}{\partial S_{31}} = L_{55},\ \frac{\partial \Sigma_{12}}{\partial S_{12}} = L_{66}, \text{ all other } \frac{\partial \Sigma_{kl}}{\partial S_{mn}} = 0,$$

$$\frac{\partial S_{ii}}{\partial \sigma_{ii}} = \frac{2}{3},\ \frac{\partial S_{ii}}{\partial \sigma_{jj}} = -\frac{1}{3} \text{ for } i \neq j,\ \frac{\partial S_{ij}}{\partial \sigma_{ij}} = 1 \text{ for } i \neq j, \text{ all other } \frac{\partial S_{mn}}{\partial \sigma_{ij}} = 0.$$

As was the case for the isotropic criterion (3.1), singularities exist for the orthotropic criterion when $\alpha = 0$ and $\alpha = \pi/3$ in the terms $\partial\alpha/\partial J_{2\bar{\Sigma}}$ and $\partial\alpha/\partial J_{3\bar{\Sigma}}$.

CHAPTER 4
PROPOSED HARDENING LAW

4.1 Introduction

Characterization of a metal's plastic response requires the specification of a yield function and a flow rule by which subsequent inelastic deformation can be calculated for specified loadings and displacements. Traditionally, the evolution of the yield surface is described by a combination of isotropic and kinematic hardening laws. Isotropic hardening implies a proportional expansion of the surface, without any changes in shape or position. An isotropic hardening model is only truly valid for monotonic loading along a given strain path assuming that every strain path hardens at the same rate. In the case of simulation of sheet forming operations of cubic metals (both fcc and bcc), the assumption of isotropic hardening is reasonably adequate (Yoon et al., 2004).

Pure translation of the initial yield surface could be described by the classic linear kinematic hardening laws. To better model the smooth elastic-plastic transition upon reverse loading, multi-surface models as well as non-linear kinematic hardening models have been proposed. Recently, physically-based models of the evolution of the anisotropic work-hardening of bcc materials (mild steel) under arbitrary strain path changes that involve several tensorial hardening variables have been proposed (e.g. Teodosiu et al., 1995 and Li et al., 2003). It is to be noted that none of these models account for the evolution of texture during work-hardening. Due to non-negligible twinning activity accompanied by grain reorientation and highly directional grain interactions, the influence of the texture evolution on work-hardening of hcp materials

cannot be neglected even for the simplest monotonic loading paths. Existing macro-scale phenomenological plasticity models cannot describe the experimentally observed change in shape of the yield loci with accumulated plastic deformation.

A general framework for the description of yielding anisotropy and its evolution with accumulated deformation for both quasi-static and dynamic loading conditions is offered by polycrystal plasticity. Recently, many efforts have been undertaken to incorporate anisotropy due to crystallographic texture into finite element simulations (e.g. Tome et al., 2001). Direct implementation of polycrystal viscoplasticity models into FE codes, where a polycrystalline aggregate is associated with each finite element integration point, has the advantage that it follows the evolution of anisotropy due to texture development. However such finite element calculations are computationally very intensive, thus limiting the applicability of this approach to problems that do not require a fine spatial resolution.

The objective of the present chapter is to propose a macroscopic anisotropic model that can describe the influence of evolving texture on the plastic response of hexagonal metals. Initial yielding is described by the proposed orthotropic yield criterion (3.16) that accounts for both anisotropy and asymmetry in yielding between tension and compression. Experimental measurements of the crystallographic texture for a given material are used to calculate the flow stress in a finite number of loading directions using the vpsc model. Then an interpolation technique is used to construct the evolution of the yield surface. The anisotropy coefficients as well as the size of the elastic domain are considered to be functions of the accumulated plastic strain. The proposed model was implemented into the implicit FE code ABAQUS (2003) and used to simulate the three-

dimensional deformation of pure zirconium and AZ31B magnesium specimens subjected to various loading conditions. Comparison between predicted and experimentally measured macroscopic strain fields for pure zirconium shows that the proposed model describes very well the contribution of twinning to deformation.

4.2 Elasto-Plastic Problem

Some assumptions of rate-independent plasticity theory include a yield function or stress potential, Q, which separates elastic and plastic states,

$$Q = \tilde{\sigma} - Y \tag{4.1}$$

the additive decomposition of the total strain increment into an elastic and plastic part,

$$d\boldsymbol{\varepsilon} = d\boldsymbol{\varepsilon}_e + d\boldsymbol{\varepsilon}_p \tag{4.2}$$

an associated flow rule relating the plastic strain-rate to the stress potential,

$$\dot{\boldsymbol{\varepsilon}}_p = \dot{\lambda}\frac{\partial Q}{\partial \boldsymbol{\sigma}} \tag{4.3}$$

and Hooke's law in incremental form

$$d\boldsymbol{\sigma} = \boldsymbol{C} d\boldsymbol{\varepsilon}_e \tag{4.4}$$

where $\tilde{\sigma}$ is the scalar effective stress, Y represents the material's hardening, λ is the scalar plastic multiplier and is equivalent to the effective plastic strain, an overhead dot represents the time derivative, and $\boldsymbol{C}$ is the elastic stiffness tensor. An effective stress must be a homogeneous function of degree 1, and be able to reduce to the hardening relationship (i.e., uniaxial tension for a given direction) under that state of stress. For example, the effective stress based upon the proposed isotropic criterion (3.1) assuming that the hardening relationship, Y, is based upon uniaxial tension about the x-direction is given by

$$\tilde{\sigma}(\boldsymbol{\sigma},\bar{\varepsilon}_p) = A\left[\left(|S_1| - kS_1\right)^a + \left(|S_2| - kS_2\right)^a + \left(|S_3| - kS_3\right)^a\right]^{\frac{1}{a}} \tag{4.5}$$

where,

$$A = \left[\frac{1}{\left(\frac{2}{3} - \frac{2}{3}k\right)^a + 2\left(\frac{1}{3} + \frac{1}{3}k\right)^a}\right]^{\frac{1}{a}} \tag{4.6}$$

and for the proposed orthotropic criterion (3.16)

$$\tilde{\sigma}(\boldsymbol{\sigma},\bar{\varepsilon}_p) = B\left[\left(|\Sigma_1| - k\Sigma_1\right)^a + \left(|\Sigma_2| - k\Sigma_2\right)^a + \left(|\Sigma_3| - k\Sigma_3\right)^a\right]^{\frac{1}{a}} \tag{4.7}$$

where,

$$B = \left[\frac{1}{\left(|\Phi_1| - k\Phi_1\right)^a + \left(|\Phi_2| - k\Phi_2\right)^a + \left(|\Phi_3| - k\Phi_3\right)^a}\right]^{\frac{1}{a}} \tag{4.8}$$

and,

$$\Phi_1 = \left(\frac{2}{3}L_{11} - \frac{1}{3}L_{12} - \frac{1}{3}L_{13}\right) \tag{4.9}$$

$$\Phi_2 = \left(\frac{2}{3}L_{12} - \frac{1}{3}L_{22} - \frac{1}{3}L_{23}\right)$$

$$\Phi_3 = \left(\frac{2}{3}L_{13} - \frac{1}{3}L_{23} - \frac{1}{3}L_{33}\right).$$

Note that for the case of $a = 2$, $k = 0$, A reduces to $\sqrt{3/2}$ which is the constant associated with the von Mises effective stress.

The basic problem in elasto-plasticity is to obtain stresses that fulfill both the Kuhn-Tucker conditions and the consistency condition. The Kuhn-Tucker conditions

require that $\dot{\lambda} \geq 0$, $Q \leq 0$, and $\dot{\lambda} Q = 0$, while the consistency condition requires that the stress state remain on the yield surface during plastic loadings.

The usual starting point for the elasto-plasticity problem is the non-linear differential equation

$$d\boldsymbol{\sigma} = \boldsymbol{C}^{ep} d\boldsymbol{\varepsilon} \tag{4.10}$$

whose solution is given by

$$\boldsymbol{\sigma}_{n+1} = \boldsymbol{\sigma}_n + \int_{\varepsilon_n}^{\varepsilon_{n+1}} \boldsymbol{C}^{ep} d\boldsymbol{\varepsilon} = \boldsymbol{\sigma}_n + \Delta\boldsymbol{\sigma}_{n+1} \tag{4.11}$$

where n is a counter and stands for a certain time step of the deformation process. $\boldsymbol{C}^{ep}$ is the elasto-plastic tangent modulus, and depends on the updated state of the problem. Since $\boldsymbol{C}^{ep}$ is unknown for the updated state, an iterative scheme must be applied.

The first step in an iterative scheme is to choose a starting point, and in elasto-plasticity the usual starting point is to assume the stress state is purely elastic, i.e.,

$$\boldsymbol{\sigma}_{n+1}^{trial} = \boldsymbol{\sigma}_n + \boldsymbol{C}\Delta\boldsymbol{\varepsilon} \tag{4.12}$$

If this starting stress, commonly referred to as the trial elastic stress, satisfies $Q \leq 0$ then the trial stress is accepted as the current stress state. If $Q > 0$ then the stress state must be returned to the yield surface. The stress state is returned to the yield surface through a plastic corrector step in which the yield surface also expands due to hardening. This method is an implicit and direct method since the resulting equations become implicit in the unknown variables, and the consistency condition is directly used to determine the increment of effective plastic strain. This approach is also referred to as a return-mapping method since the increment of the effective plastic strain is adjusted such that the stress is returned to the yield surface.

4.3 Proposed Anisotropic Hardening Law

The proposed hardening law allows for the change in shape of the yield loci during the deformation process by letting the yield criterion coefficients be functions of the hardening parameter. Thus, the yield function would take the form

$$Q(\boldsymbol{\sigma}, \bar{\varepsilon}_p) = \tilde{\sigma}(\boldsymbol{\sigma}, \bar{\varepsilon}_p) - Y(\bar{\varepsilon}_p) \leq 0 \tag{4.13}$$

where $\tilde{\sigma}$ is the effective stress based on the stress potential, $\boldsymbol{\sigma}$ is the Cauchy stress tensor, Y is the effective stress-effective plastic strain relationship in a given direction (e.g. the tensile rolling direction), and $\bar{\varepsilon}_p$ is the effective plastic strain which will be used as the hardening parameter.

If $Q(\boldsymbol{\sigma}_{n+1}^{trial}, \bar{\varepsilon}_{p\,n+1}^{trial}) > 0$, the effective plastic strain increment $\Delta\lambda$ for global step n+1 must be determined to bring the stress state back to the yield surface through a local iterative process (see Simo and Hughes, 1998). Denoting the elastic trial state according to equation (4.12) as iteration $i = 0$ (i being the local iteration counter), the stress increment update for iterations $i > 0$ take the effects of the plastic strains into account according to (4.14) using the flow rule (4.3).

$$\Delta\boldsymbol{\sigma}_{n+1}^{i+1} = \Delta\boldsymbol{\sigma}_{n+1}^{i} + \delta\sigma_{n+1}^{i+1} = \Delta\boldsymbol{\sigma}_{n+1}^{i} - \delta\lambda_{n+1}^{i+1}\boldsymbol{C}\left[\frac{\partial\tilde{\sigma}}{\partial\boldsymbol{\sigma}}\right]_{n+1}^{i+1} \tag{4.14}$$

In equation (4.14) $-\delta\lambda\boldsymbol{C}\dfrac{\partial\tilde{\sigma}}{\partial\boldsymbol{\sigma}}$ is the stress correction due to the plastic strains, and δ denotes the variation of the variable between local iterations i+1 and i, i.e., $\Delta\lambda_{n+1}^{i+1} = \Delta\lambda_{n+1}^{i} + \delta\lambda_{n+1}^{i+1}$. The gradient of the stress potential based upon the unknown updated state (iteration i+1) may be approximated using a Taylor series expansion about the previous state and the variation of $\Delta\lambda$ during the previous iteration (iteration i) by

$$\left[\frac{\partial\tilde{\sigma}}{\partial\boldsymbol{\sigma}}\right]_{n+1}^{i+1} \approx \left[\frac{\partial\tilde{\sigma}}{\partial\boldsymbol{\sigma}}\right]_{n+1}^{i} + \Theta\left\{\left[\frac{\partial^2\tilde{\sigma}}{\partial\boldsymbol{\sigma}^2}\right]_{n+1}^{i}\delta\sigma + \left[\frac{\partial^2\tilde{\sigma}^n}{\partial\bar{\varepsilon}_p\partial\boldsymbol{\sigma}}\right]_{n+1}^{i}\delta\lambda\right\} \tag{4.15}$$

When Θ=0, the stress state is returned to the yield surface along a vector normal to the current state, and when Θ=1 the stress state is returned normal to the updated state. The method is fully implicit when Θ=1. After combining equations (4.14) and (4.15), the stress correction can be approximated as

$$\delta\boldsymbol{\sigma}_{n+1}^{i+1} \approx -\left[\boldsymbol{C}^{-1} + \Theta\delta\lambda_{n+1}^{i}\frac{\partial^2\tilde{\sigma}}{\partial\boldsymbol{\sigma}^2}\right]^{-1}\left[\delta\lambda_{n+1}^{i+1}\frac{\partial\tilde{\sigma}}{\partial\boldsymbol{\sigma}} + \Theta\delta\lambda_{n+1}^{i+1}\delta\lambda_{n+1}^{i}\frac{\partial^2\tilde{\sigma}}{\partial\bar{\varepsilon}_p\partial\boldsymbol{\sigma}}\right] \tag{4.16}$$

where all derivatives are evaluated at the current state. The incremental variation of the consistency parameter, or effective plastic strain, $\delta\lambda_{n+1}^{i+1}$ may be obtained through a Taylor expansion of the yield criterion about the current state

$$Q(\boldsymbol{\sigma}_{n+1}^{i+1}, \bar{\varepsilon}_{p\,n+1}^{i+1}) \approx Q(\boldsymbol{\sigma}_{n+1}^{i}, \bar{\varepsilon}_{p\,n+1}^{i}) + \left[\frac{\partial Q}{\partial\boldsymbol{\sigma}}\right]_{n+1}^{i}\delta\boldsymbol{\sigma}_{n+1}^{i+1} + \left[\frac{\partial Q}{\partial\bar{\varepsilon}_p}\right]_{n+1}^{i}\delta\lambda_{n+1}^{i+1} = 0 \tag{4.17}$$

Substituting equation (4.16) into (4.17) and realizing that all derivatives are evaluated for the previous step (step *j*) yields

$$Q(\boldsymbol{\sigma}_{n+1}^{i}, \bar{\varepsilon}_{p\,n+1}^{i}) - \delta\lambda_{n+1}^{i+1}\frac{\partial\tilde{\sigma}}{\partial\boldsymbol{\sigma}}\boldsymbol{H}\left[\frac{\partial\tilde{\sigma}}{\partial\boldsymbol{\sigma}} + \Theta\delta\lambda_{n+1}^{i}\frac{\partial^2\tilde{\sigma}}{\partial\lambda\partial\boldsymbol{\sigma}}\right] - \delta\lambda_{n+1}^{i+1}\frac{\partial Y}{\partial\bar{\varepsilon}_p} + \delta\lambda_{n+1}^{i+1}\frac{\partial\tilde{\sigma}}{\partial\bar{\varepsilon}_p} = 0 \tag{4.18}$$

thus

$$\delta\lambda_{n+1}^{i+1} = \frac{Q(\boldsymbol{\sigma}_{n+1}^{i}, \bar{\varepsilon}_{p\,n+1}^{i})}{\frac{\partial\tilde{\sigma}}{\partial\boldsymbol{\sigma}}\boldsymbol{H}\left[\frac{\partial\tilde{\sigma}}{\partial\boldsymbol{\sigma}} + \Theta\delta\lambda_{n+1}^{i}\frac{\partial^2\tilde{\sigma}}{\partial\bar{\varepsilon}_p\partial\boldsymbol{\sigma}}\right] + \frac{\partial Y}{\partial\bar{\varepsilon}_p} - \frac{\partial\tilde{\sigma}}{\partial\bar{\varepsilon}_p}} \tag{4.19}$$

where,

$$\boldsymbol{H} = \left[\boldsymbol{C}^{-1} + \Theta \delta \lambda_{n+1}^{i} \frac{\partial^2 \tilde{\sigma}}{\partial \boldsymbol{\sigma}^2} \right]^{-1} \tag{4.20}$$

The stresses and plastic strains are then updated through $\delta\lambda$, and the yield criterion $Q(\boldsymbol{\sigma}_{n+1}^{i+1}, \bar{\varepsilon}_{p\,n+1}^{i+1})$ is checked to within a specified tolerance. If the tolerance has not been met, the plastic corrector step will be repeated until convergence has been obtained. Once convergence is obtained, the updated stresses and strains are accepted as the current state. Note that if $\partial\tilde{\sigma}/\partial\lambda$ equals zero, then this model reduces to that of isotropic hardening.

The consistent tangent modulus relates the current stress increment to the current total strain increment, and is used to predict the total strain increment for the next iteration. Taking the derivative of (4.13) yields

$$dQ = \frac{\partial Q}{\partial \boldsymbol{\sigma}} d\boldsymbol{\sigma} + \frac{\partial Q}{\partial \lambda} d\lambda = 0 \tag{4.21}$$

which leads to the following relationship in incremental form after the substitution of equation (4.16) with $\Theta = 0$ since we are using the current step.

$$\frac{\partial \tilde{\sigma}}{\partial \boldsymbol{\sigma}} \boldsymbol{C} \Delta \boldsymbol{\varepsilon} - \Delta\lambda \frac{\partial \tilde{\sigma}}{\partial \boldsymbol{\sigma}} \boldsymbol{C} \frac{\partial \tilde{\sigma}}{\partial \boldsymbol{\sigma}} - \Delta\lambda \frac{\partial Y}{\partial \lambda} + \Delta\lambda \frac{\partial \tilde{\sigma}}{\partial \lambda} = 0 \tag{4.22}$$

Using (4.22) to solve for the effective plastic strain increment based on the current state gives

$$\Delta\lambda_{current} = \frac{\dfrac{\partial \tilde{\sigma}}{\partial \boldsymbol{\sigma}} \boldsymbol{C} \Delta \boldsymbol{\varepsilon}}{\dfrac{\partial \tilde{\sigma}}{\partial \boldsymbol{\sigma}} \boldsymbol{C} \dfrac{\partial \tilde{\sigma}}{\partial \boldsymbol{\sigma}} + \dfrac{\partial Y}{\partial \lambda} - \dfrac{\partial \tilde{\sigma}}{\partial \lambda}} \tag{4.23}$$

The combination of (4.23), (4.2) – (4.4), and (4.10) yields a relationship between the stress increment and total strain increment from which the consistent tangent modulus can be found.

$$\Delta\boldsymbol{\sigma} = \left[\boldsymbol{C} - \frac{\frac{\partial\tilde{\sigma}}{\partial\boldsymbol{\sigma}}\boldsymbol{C}\otimes\boldsymbol{C}\frac{\partial\tilde{\sigma}}{\partial\boldsymbol{\sigma}}}{\frac{\partial\tilde{\sigma}}{\partial\boldsymbol{\sigma}}\boldsymbol{C}\frac{\partial\tilde{\sigma}}{\partial\boldsymbol{\sigma}} + \frac{\partial Y}{\partial\lambda} - \frac{\partial\tilde{\sigma}}{\partial\lambda}} \right]\Delta\boldsymbol{\varepsilon} \tag{4.24}$$

Here the term in brackets is the consistent tangent modulus and $\otimes$ represents the tensor product.

The procedures for implementing the proposed hardening model using $\Theta = 0$ are summarized:

1. Given: $\tilde{\sigma}_n, \bar{\varepsilon}_{p\,n}, \Delta\boldsymbol{\varepsilon}$ where n represents the previous time step and $\Delta\boldsymbol{\varepsilon}$ is the total strain increment for the current time step.

2. Calculate the trial state (i = 0): $\boldsymbol{\sigma}_{n+1}^{trial} = \boldsymbol{\sigma}_n + \boldsymbol{C}\Delta\boldsymbol{\varepsilon}$ and $\bar{\varepsilon}_{p\,n+1}^{0} = \bar{\varepsilon}_{p\,n}$

3. Check for consistency: If $Q(\boldsymbol{\sigma}_{n+1}^{trial}, \bar{\varepsilon}_{p\,n+1}^{0}) \le tolerance \Rightarrow$ elastic stress state. Accept the trial stress state as the current state and the total strain increment as an elastic strain increment and exit. Else $\Rightarrow$ continue

4. Determine the starting values for the iteration (i = 0)

   a) $Y_{n+1}^{0} = Y\left(\bar{\varepsilon}_{p\,n+1}^{0}\right)$

   b) $k_{n+1}^{0} = k\left(\bar{\varepsilon}_{p\,n+1}^{0}\right)$, here k represents all yield criterion coefficients

   c) $h_{n+1}^{0} = \frac{\partial Y}{\partial\bar{\varepsilon}_p}\Big|_{\bar{\varepsilon}_{p\,n+1}^{0}}$

   d) $r_{n+1}^{0} = \frac{\partial k}{\partial\bar{\varepsilon}_p}\Big|_{\bar{\varepsilon}_{p\,n+1}^{0}}$

   e) $\tilde{\sigma}_{n+1}^{0} = \tilde{\sigma}(\boldsymbol{\sigma}_{n+1}^{trial}, \bar{\varepsilon}_{p\,n+1}^{0})$

f) $\boldsymbol{q}_{n+1}^{0} = \dfrac{\partial \tilde{\sigma}}{\partial \boldsymbol{\sigma}} \Big|_{\boldsymbol{\sigma}_{n+1}^{trial}, k_{n+1}^{0}}$

g) $p_{n+1}^{0} = \dfrac{\partial \tilde{\sigma}}{\partial k} \Big|_{\sigma_{n+1}^{trial}, k_{n+1}^{0}}$

5. Begin Iteration loop (i = 0…N)

a) $\delta\lambda_{n+1}^{i+1} = \dfrac{\tilde{\sigma}_{n+1}^{i} - Y_{n+1}^{i}}{\boldsymbol{q}_{n+1}^{i}\boldsymbol{C}\boldsymbol{q}_{n+1}^{i} + h_{n+1}^{i} - p_{n+1}^{i} r_{n+1}^{i}}$

b) $\boldsymbol{\sigma}_{n+1}^{i+1} = \boldsymbol{\sigma}_{n+1}^{i} - \delta\lambda_{n+1}^{i+1}\boldsymbol{C}\boldsymbol{q}_{n+1}^{i}$

c) $\bar{\varepsilon}_{p\,n+1}^{i+1} = \bar{\varepsilon}_{p\,n+1}^{i} + \delta\lambda_{n+1}^{i+1}$

6. Check for consistency: If $Q(\boldsymbol{\sigma}_{n+1}^{i+1}, \bar{\varepsilon}_{p\,n+1}^{i+1}) \le tolerance \Rightarrow$ Accept the current state of stress and strain (i = i+1) and go to step 9 then exit. Else $\Rightarrow$ continue.

7. Continue with Iteration loop

a) $Y_{n+1}^{i+1} = Y\left(\bar{\varepsilon}_{p\,n+1}^{i+1}\right)$

b) $k_{n+1}^{i+1} = k\left(\bar{\varepsilon}_{p\,n+1}^{i+1}\right)$

c) $h_{n+1}^{i+1} = \dfrac{\partial Y}{\partial \bar{\varepsilon}_{p}} \Big|_{\bar{\varepsilon}_{p\,n+1}^{i+1}}$

d) $r_{n+1}^{i+1} = \dfrac{\partial k}{\partial \bar{\varepsilon}_{p}} \Big|_{\bar{\varepsilon}_{p\,n+1}^{i+1}}$

e) $\tilde{\sigma}_{n+1}^{i+1} = \tilde{\sigma}(\boldsymbol{\sigma}_{n+1}^{i+1}, \bar{\varepsilon}_{p\,n+1}^{i+1})$

f) $\boldsymbol{q}_{n+1}^{i+1} = \dfrac{\partial \tilde{\sigma}}{\partial \boldsymbol{\sigma}} \Big|_{\boldsymbol{\sigma}_{n+1}^{i+1}, k_{n+1}^{i+1}}$

g) $p_{n+1}^{i+1} = \dfrac{\partial \tilde{\sigma}}{\partial k} \Big|_{\boldsymbol{\sigma}_{n+1}^{i+1}, k_{n+1}^{i+1}}$

8. Go to step 5

9. Calculate the elasto-plastic tangent modulus

a) $\boldsymbol{C}_{n+1}^{ep} = \boldsymbol{C} - \dfrac{\left(\boldsymbol{C}\boldsymbol{q}_{n+1}^{i}\right) \otimes \left(\boldsymbol{C}\boldsymbol{q}_{n+1}^{i}\right)^{T}}{\boldsymbol{q}_{n+1}^{i}\boldsymbol{C}\boldsymbol{q}_{n+1}^{i} + h_{n+1}^{i} - p_{n+1}^{i} \cdot r_{n+1}^{i}}$

In order to improve the stability of the return-mapping algorithm such as the one just described, Yoon et al. (2004) proposed a multi-step procedure to be used if the strain increment is very large. This procedure requires that the consistency condition be solved in several steps when the initial consistency check yields a value large compared to the initial yield stress. During the first step, the convergence tolerance would be on the order of the magnitude of the initial consistency check minus the yield stress. Subsequent steps would converge towards progressively smaller magnitudes until the convergence tolerance equals the original tolerance value near zero. Then the state of stress and strain would be accepted as the current state, and the iteration loop exited.

4.4 Application for an Isotropic Material

Let us use the numerical procedure described in the previous section to model the response of an isotropic material obeying an isotropic yield criterion of the form $\tilde{\sigma}\left(\boldsymbol{\sigma},\bar{\varepsilon}_p\right)=Y\left(\bar{\varepsilon}_p\right)$ where $\tilde{\sigma}\left(\boldsymbol{\sigma},\bar{\varepsilon}_p\right)$ is the effective stress associated with the proposed isotropic criterion (3.1). The evolution of the yield surface is dictated by $k=k(\bar{\varepsilon}_p)$, thus the effective stress is dependant upon the effective plastic strain. Allowing a variation of the coefficient k with $\bar{\varepsilon}_p$ captures the change in the ratio between the yield in tension and compression with accumulated plastic deformation. We assume a law of variation of k of the form

$$k = A - B\bar{\varepsilon}_p \text{ for } 0.0 \le \bar{\varepsilon}_p \le \bar{\varepsilon}_p^{\,critical} \tag{4.25}$$

$$k = 0 \text{ for } \bar{\varepsilon}_p > \bar{\varepsilon}_p^{\,critical}$$

where A and B are material constants. It means that above a critical level of $\bar{\varepsilon}_p$, the yield in tension is equal to the yield in compression, i.e., no strength differential effects exist

above a critical level of $\bar{\varepsilon}_p$. For illustration purposes, let us assume that $A = 0.4$, $B = \frac{0.4}{0.05}$, and $\bar{\varepsilon}_p^{\,critical} = 0.05$ with a constant degree of homogeneity of $a = 2$. For $k \in [0, 0.4]$) a nearly linear relationship exists between k and σ_T / σ_C when $a = 2$ (see Figure 3.3). Thus, equation (4.25) with the assumed constant values will give a nearly linear response between k and σ_T / σ_C. Figure 4.1 shows the evolution of the shape of the yield surface for k varying according to (4.25) with the assumed constant values. A power hardening law will also be used

$$Y(\bar{\varepsilon}_p) = E(D + \bar{\varepsilon}_p)^m \tag{4.26}$$

with assumed values for illustration purposes of $E = 650$, $D = 0.0463$, and $m = 0.227$.

Uniaxial compression tests were carried out for k varying according to (4.25), as well as for k held constant at $k = 0$, $k = 0.4$ for comparison. Note that the cases for which k is held constant, the proposed hardening law reduces to isotropic hardening. The response for uniaxial compression for $k = 0$ is identical to that of tensile yield, since for $a = 2$, $k = 0$, the yield criterion (3.1) reduces to von Mises. For the case of k held constant at 0.4, the material has an initial compressive yield stress lower than the tensile yield stress, with the hardening rate being the same for both loading paths. In the case when k varies according to (4.25), the material initially yields at the same level of compressive stress as in the case when k is fixed at 0.4, but then hardens at a much higher rate than uniaxial tension until $\bar{\varepsilon}_p = 0.05$ when k becomes 0, and the yield stress in tension and compression become equal. These results are shown in Figure 4.2.

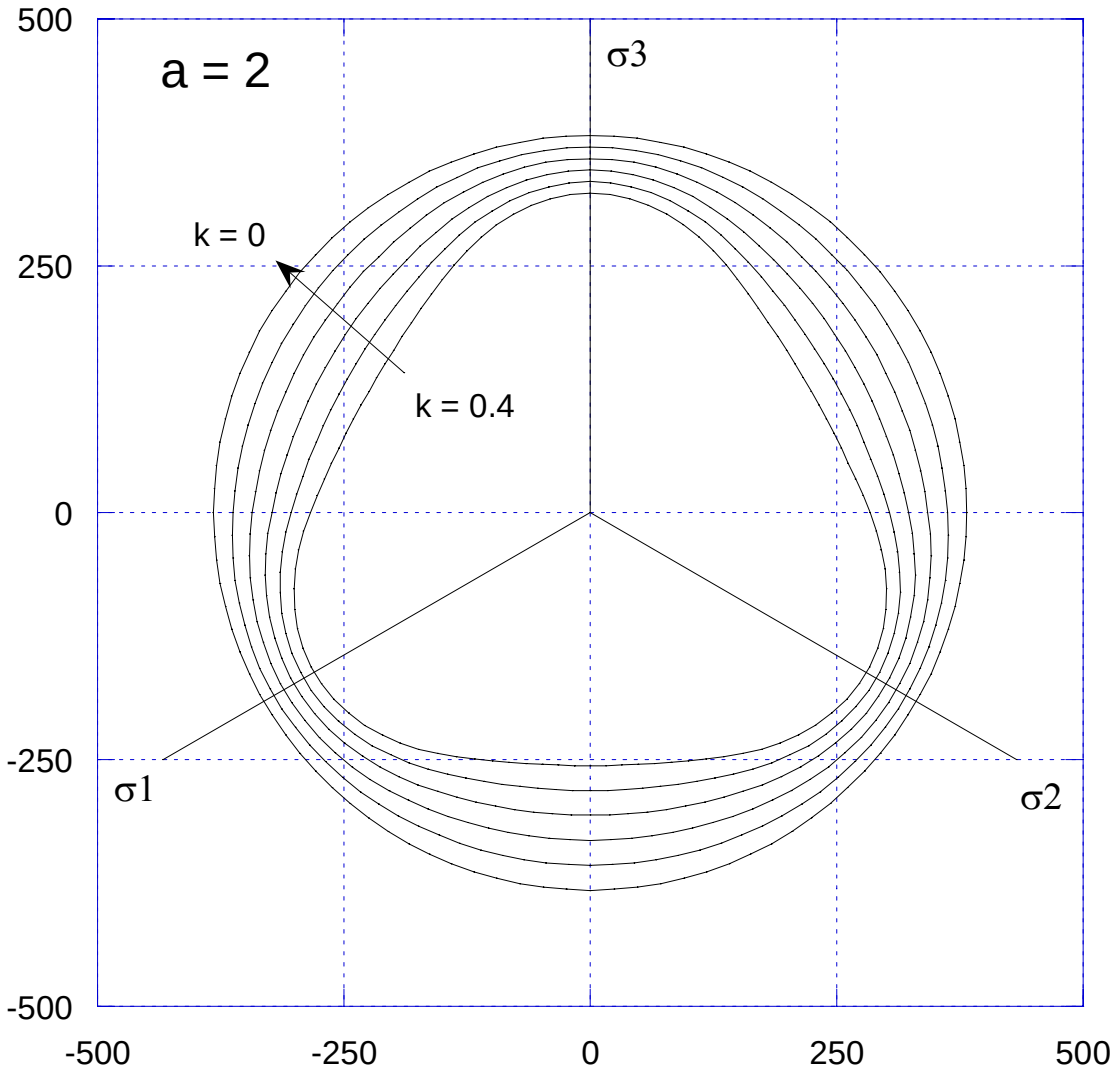

Figure 4.1 Evolution of the yield surface for varying *k*.

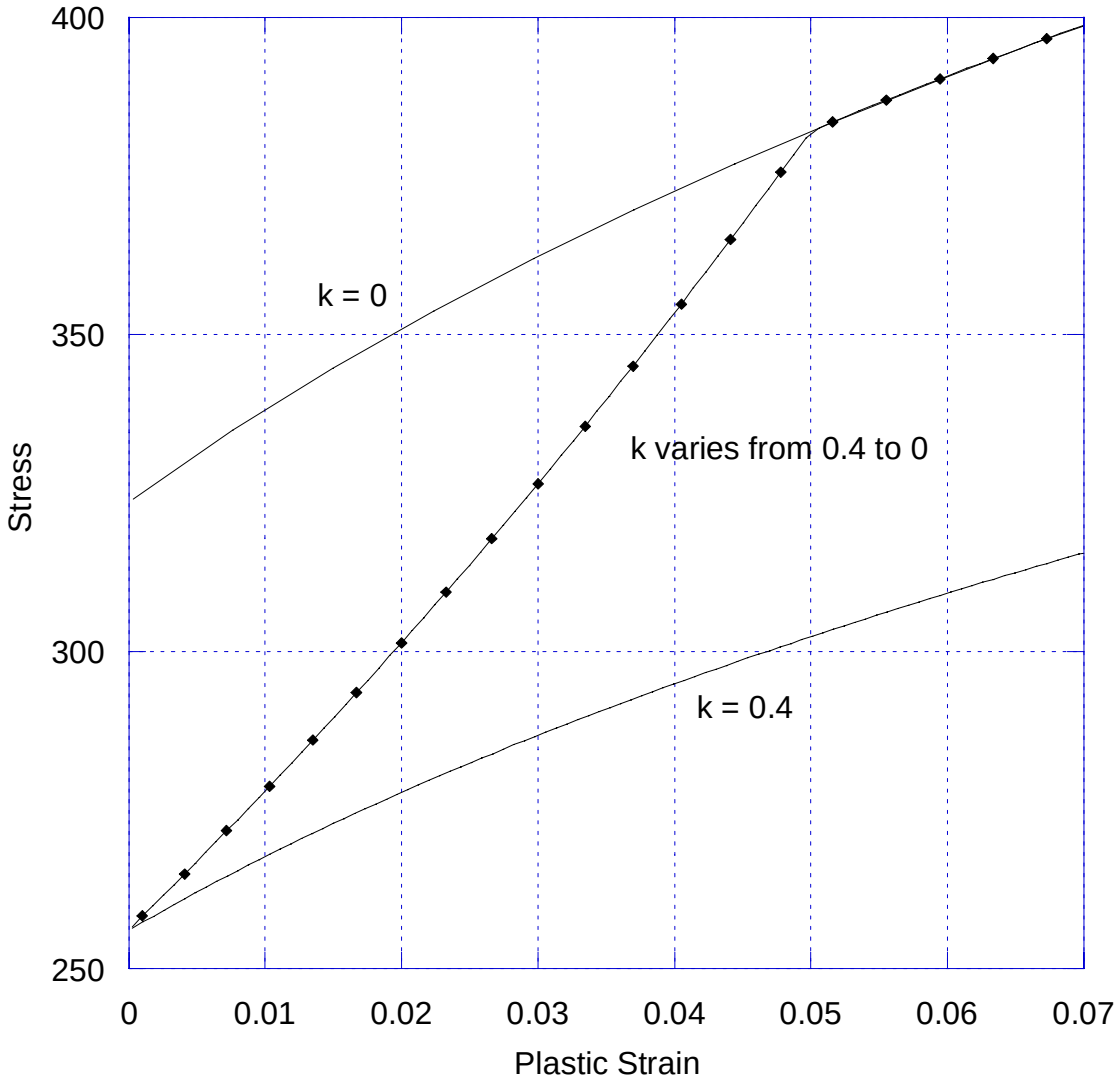

Figure 4.2 Results of single element compression tests for $a = 2$.

4.5 Alternate Method for Anisotropic Hardening Implementation – Interpolation

By applying a linear transformation to extend the isotropic yield criterion (3.1) to orthotropy, 9 additional coefficients are added. It is not trivial to determine analytical expressions for all of the coefficients in terms of the hardening variable. The available experimental data provides information about the shape of the yield surfaces corresponding to different given levels of effective plastic strain based on results of monotonic loading tests (see Kelley and Hosford, 1968 and Lee and Backofen, 1966). However, even if the expressions of L_{ij}, k, and a for a given level of strain can be determined based on the data, establishing $L_{ij}(\bar{\varepsilon}_p)$ requires a large amount of data. Therefore, an alternative approach to the hardening law is proposed.

From experimental and/or numerical results from polycrystal calculations, we can identify the coefficients involved in the proposed orthotropic yield criterion (3.16) for a set of values of equivalent plastic strain, say $\bar{\varepsilon}_p^1 < \bar{\varepsilon}_p^2 < \ldots < \bar{\varepsilon}_p^m$, and calculate the effective stress $\tilde{\sigma}^j = \tilde{\sigma}\{\boldsymbol{\sigma}, \boldsymbol{L}(\bar{\varepsilon}_p^j), \mathrm{k}(\bar{\varepsilon}_p^j), a(\bar{\varepsilon}_p^j)\}$, as well as $\mathrm{Y}^j = \mathrm{Y}(\bar{\varepsilon}_p^j)$, corresponding to each of the individual levels of effective plastic strain $\bar{\varepsilon}_p^j$, j = 1…m. Then, an interpolation procedure can be used to obtain the yield surfaces corresponding to any given level of accumulated strain. Thus, for a given arbitrary $\bar{\varepsilon}_p$, the anisotropic yield function is of the form

$$\mathrm{Q}(\boldsymbol{\sigma}, \bar{\varepsilon}_p) = \Gamma(\boldsymbol{\sigma}, \bar{\varepsilon}_p) - \Pi(\bar{\varepsilon}_p), \tag{4.27}$$

with

$$\Gamma = \xi(\bar{\varepsilon}_p)\tilde{\sigma}^j + (1 - \xi(\bar{\varepsilon}_p))\tilde{\sigma}^{j+1} \tag{4.28}$$

and

$$\Pi = \xi(\overline{\varepsilon}_p)Y^j + (1-\xi(\overline{\varepsilon}_p))Y^{j+1} \tag{4.29}$$

for any $\overline{\varepsilon}_p^j \le \overline{\varepsilon}_p \le \overline{\varepsilon}_p^{j+1}$, j = 1…m-1. For linear interpolation, the weighting parameter $\xi(\overline{\varepsilon}_p)$ appearing in equations (4.27) and (4.28) is defined as

$$\xi(\overline{\varepsilon}_p) = \frac{\overline{\varepsilon}_p^{j+1} - \overline{\varepsilon}_p}{\overline{\varepsilon}_p^{j+1} - \overline{\varepsilon}_p^{j}} \tag{4.30}$$

such that $\xi(\overline{\varepsilon}_p^j) = 1$ and $\xi(\overline{\varepsilon}_p^{j+1}) = 0$. By considering that the anisotropy coefficients L_{ij}, the strength differential parameter *k*, and the homogeneity parameter *a* evolve with the plastic deformation, the observed distortion and change in shape of the yield loci of hcp materials could be captured. Obviously, if these coefficients are taken constant, the proposed hardening law reduces to the classic isotropic hardening law.

The derivatives for Γ and Π needed for stress integration become,

$$\frac{\partial\Gamma}{\partial\boldsymbol{\sigma}} = \xi(\overline{\varepsilon}_p)\frac{\partial\tilde{\sigma}^j}{\partial\boldsymbol{\sigma}} + (1-\xi(\overline{\varepsilon}_p))\frac{\partial\tilde{\sigma}^{j+1}}{\partial\boldsymbol{\sigma}} \tag{4.31}$$

$$\frac{\partial\Gamma}{\partial\overline{\varepsilon}_p} = \frac{\tilde{\sigma}^{j+1} - \tilde{\sigma}^j}{\overline{\varepsilon}_p^{j+1} - \overline{\varepsilon}_p^j} \tag{4.32}$$

$$\frac{\partial\Pi}{\partial\overline{\varepsilon}_p} = \frac{Y^{j+1} - Y^j}{\overline{\varepsilon}_p^{j+1} - \overline{\varepsilon}_p^j} \tag{4.33}$$

$$\frac{\partial^2\Gamma}{\partial\boldsymbol{\sigma}^2} = \xi(\overline{\varepsilon}_p)\frac{\partial^2\tilde{\sigma}^j}{\partial\boldsymbol{\sigma}^2} + (1-\xi(\overline{\varepsilon}_p))\frac{\partial^2\tilde{\sigma}^{j+1}}{\partial\boldsymbol{\sigma}^2} \tag{4.34}$$

and,

$$\frac{\partial^2\Gamma}{\partial\overline{\varepsilon}_p\partial\boldsymbol{\sigma}} = \frac{\frac{\partial\Gamma}{\partial\boldsymbol{\sigma}}^{j+1} - \frac{\partial\Gamma}{\partial\boldsymbol{\sigma}}^{j}}{\overline{\varepsilon}_p^{j+1} - \overline{\varepsilon}_p^j} \tag{4.35}$$

The values of Γ, Π, $\partial\Gamma/\partial\boldsymbol{\sigma}$, $\partial\Gamma/\partial\bar{\varepsilon}_p$, $\partial\Pi/\partial\bar{\varepsilon}_p$, $\partial^2\Gamma/\partial\boldsymbol{\sigma}^2$, and $\partial^2\Gamma/\partial\bar{\varepsilon}_p\partial\boldsymbol{\sigma}$ will replace the values of $\tilde{\sigma}$, Y, $\partial\tilde{\sigma}/\partial\boldsymbol{\sigma}$, $\partial\tilde{\sigma}/\partial\bar{\varepsilon}_p$, and $\partial Y/\partial\bar{\varepsilon}_p$, $\partial^2\tilde{\sigma}/\partial\boldsymbol{\sigma}^2$, and $\partial^2\tilde{\sigma}/\partial\bar{\varepsilon}_p\partial\boldsymbol{\sigma}$ respectively, in the stress integration algorithm.

To illustrate how the yield surface will evolve using the interpolation method, this method will be applied to the yield surfaces for the cold rolled plate of the magnesium alloy mg-th displayed in Figure 3.1. Using the three discrete yield loci corresponding to 1%, 5%, and 10% levels of effective plastic strain (represented by solid lines) as $\bar{\varepsilon}_p^1$, $\bar{\varepsilon}_p^2$, and $\bar{\varepsilon}_p^3$, respectively, intermediate yield surfaces (represented by dashed lines) for $\bar{\varepsilon}_p^1 < \bar{\varepsilon}_p < \bar{\varepsilon}_p^2$ and $\bar{\varepsilon}_p^2 < \bar{\varepsilon}_p < \bar{\varepsilon}_p^3$ can be calculated according to equation (4.27) by varying the interpolation parameter $\xi(\bar{\varepsilon}_p)$ (see equation 4.30). The results are plotted in Figure 4.3.

The procedures to implement the alternate interpolation method of the proposed hardening model assuming $\Theta = 0$ are as follows:

1. Given: $\tilde{\sigma}_n, \bar{\varepsilon}_{p\,n}, \Delta\boldsymbol{\varepsilon}$ where n represents the previous time step and $\Delta\boldsymbol{\varepsilon}$ is the total strain increment for the current time step.
2. Calculate the trial state (i = 0): $\boldsymbol{\sigma}_{n+1}^{trial} = \boldsymbol{\sigma}_n + \boldsymbol{C}\Delta\boldsymbol{\varepsilon}$ and $\bar{\varepsilon}_{p\,n+1}^0 = \bar{\varepsilon}_{p\,n}$
3. Check for consistency
   a) Determine which levels of effective plastic strain the current state lies within $\bar{\varepsilon}_p^j \le \bar{\varepsilon}_{p\,n+1}^0 \le \bar{\varepsilon}_p^{j+1}$, i.e., determine the appropriate *j* and *j+1*. (Caution, *j* and *j+1* represent discrete levels of the yield criterion, not to be confused with *i* and *i+1* which represent time steps)
   b) $\xi_{n+1}^0 = \dfrac{\bar{\varepsilon}_p^{j+1} - \bar{\varepsilon}_{p\,n+1}^0}{\bar{\varepsilon}_p^{j+1} - \bar{\varepsilon}_p^j}$
   c) If $Q(\boldsymbol{\sigma}_{n+1}^{trial}, \bar{\varepsilon}_{p\,n+1}^0) \le tolerance \Rightarrow$ elastic stress state. Accept the trial stress state as the current state and the total strain increment as an elastic strain increment and exit. Else $\Rightarrow$ continue

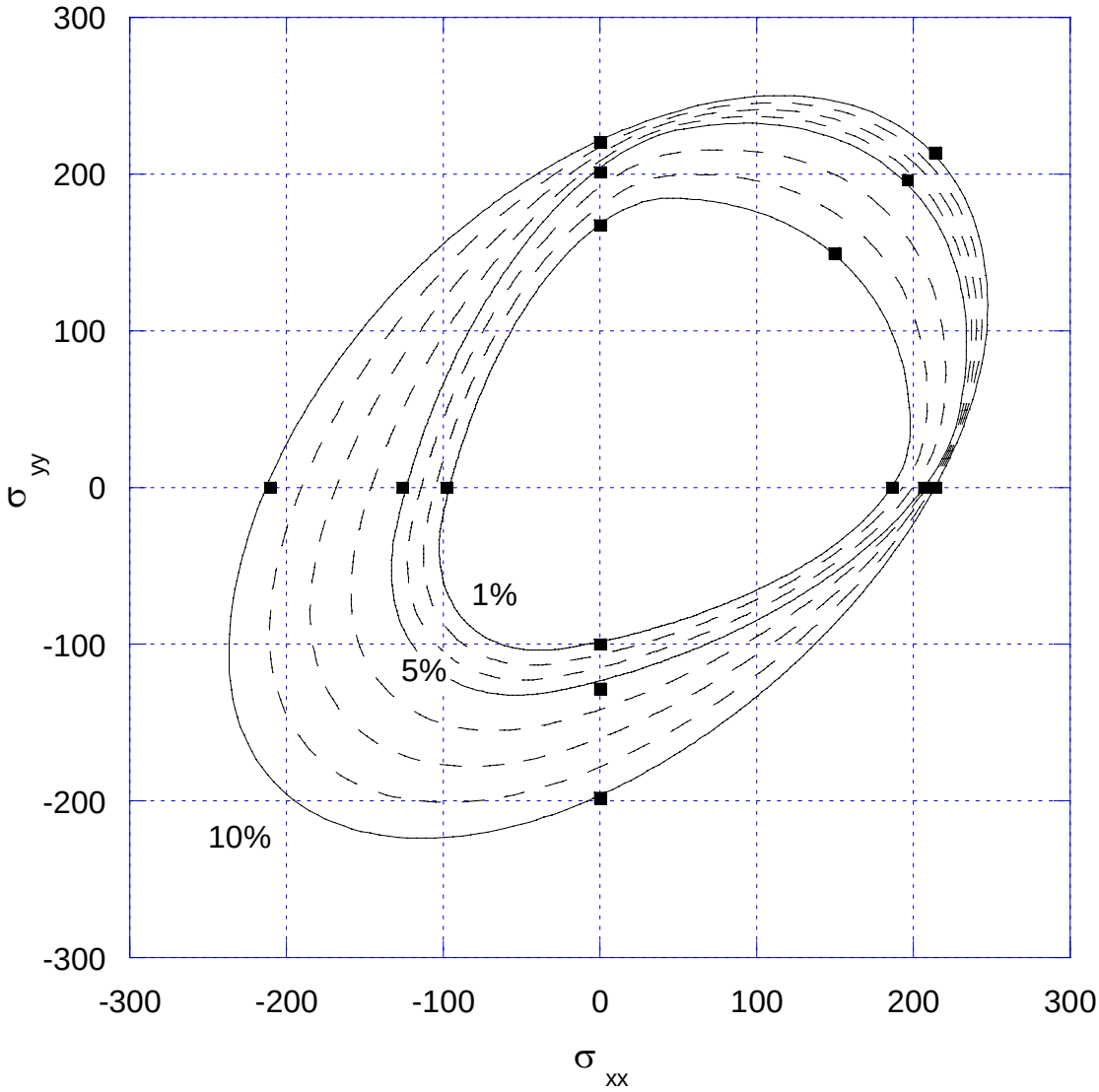

Figure 4.3 Yield surface evolution for a cold rolled sheet of mg-th using the interpolation method. Solid lines represent calculated yield loci from experimental data. Dashed lines represent yield loci determined by interpolation.

4. Determine the starting values for the iteration (i = 0)

   a) $\Pi^0_{n+1} = \xi^0_{n+1} Y(\bar{\varepsilon}^j_p) + (1-\xi^0_{n+1}) Y(\bar{\varepsilon}^{j+1}_p)$

   b) $h^0_{n+1} = \dfrac{\partial \Pi}{\partial \bar{\varepsilon}_p} = \dfrac{Y(\bar{\varepsilon}^{j+1}_p) - Y(\bar{\varepsilon}^j_p)}{\bar{\varepsilon}^{j+1}_p - \bar{\varepsilon}^j_p}$

   c) Determine the appropriate $\boldsymbol{L}(\bar{\varepsilon}^j_p)$, $k(\bar{\varepsilon}^j_p)$, and $a(\bar{\varepsilon}^j_p)$ for j and $j+1$

   d) $\tilde{\sigma}^{0,j}_{n+1} = \tilde{\sigma}\{\boldsymbol{\sigma}^{trial}_{n+1}, \boldsymbol{L}(\bar{\varepsilon}^j_p), k(\bar{\varepsilon}^j_p), a(\bar{\varepsilon}^j_p)\}$

   e) $\tilde{\sigma}^{0,j+1}_{n+1} = \tilde{\sigma}\{\boldsymbol{\sigma}^{trial}_{n+1}, \boldsymbol{L}(\bar{\varepsilon}^{j+1}_p), k(\bar{\varepsilon}^{j+1}_p), a(\bar{\varepsilon}^{j+1}_p)\}$

   f) $\Gamma^0_{n+1} = \xi^0_{n+1} \tilde{\sigma}^{0,j}_{n+1} + (1-\xi^0_{n+1}) \tilde{\sigma}^{0,j+1}_{n+1}$

   g) $\boldsymbol{t}^{0,j}_{n+1} = \dfrac{\partial \tilde{\sigma}\{\boldsymbol{\sigma}, \boldsymbol{L}(\bar{\varepsilon}^j_p), k(\bar{\varepsilon}^j_p), a(\bar{\varepsilon}^j_p)\}}{\partial \boldsymbol{\sigma}} \Big|_{\boldsymbol{\sigma}^{trial}_{n+1}}$

   h) $\boldsymbol{t}^{0,j+1}_{n+1} = \dfrac{\partial \tilde{\sigma}\{\boldsymbol{\sigma}, \boldsymbol{L}(\bar{\varepsilon}^{j+1}_p), k(\bar{\varepsilon}^{j+1}_p), a(\bar{\varepsilon}^{j+1}_p)\}}{\partial \boldsymbol{\sigma}} \Big|_{\boldsymbol{\sigma}^{trial}_{n+1}}$

   i) $\boldsymbol{q}^0_{n+1} = \dfrac{\partial \Gamma}{\partial \boldsymbol{\sigma}} = \xi^0_{n+1} \boldsymbol{t}^{0,j}_{n+1} + (1-\xi^0_{n+1}) \boldsymbol{t}^{0,j+1}_{n+1}$

   j) $v^0_{n+1} = \dfrac{\partial \Gamma}{\partial \bar{\varepsilon}_p} = \dfrac{\tilde{\sigma}^{0,j+1}_{n+1} - \tilde{\sigma}^{0,j}_{n+1}}{\bar{\varepsilon}^{j+1}_p - \bar{\varepsilon}^j_p}$

5. Begin Iteration loop (i = 0…N)

   a) $\delta\lambda^{i+1}_{n+1} = \dfrac{\Gamma^i_{n+1} - \Pi^i_{n+1}}{\boldsymbol{q}^i_{n+1} \boldsymbol{C} \boldsymbol{q}^i_{n+1} + h^i_{n+1} - v^i_{n+1}}$

   b) $\boldsymbol{\sigma}^{i+1}_{n+1} = \boldsymbol{\sigma}^i_{n+1} - \delta\lambda^{i+1}_{n+1} \boldsymbol{C} \boldsymbol{q}^i_{n+1}$

   c) $\bar{\varepsilon}^{i+1}_{p\,n+1} = \bar{\varepsilon}^i_{p\,n+1} + \delta\lambda^{i+1}_{n+1}$

6. Check for consistency: If $Q(\boldsymbol{\sigma}^{i+1}_{n+1}, \bar{\varepsilon}^{i+1}_{p\,n+1}) \le tolerance \Rightarrow$ Accept the current state of stress and strain (i = i+1) and go to step 9 then exit. Else $\Rightarrow$ continue.

7. Continue with Iteration loop

   a) Determine which levels of effective plastic strain the current state lies within $\bar{\varepsilon}^j_p \le \bar{\varepsilon}^{i+1}_{p\,n+1} \le \bar{\varepsilon}^{j+1}_p$, i.e., determine the appropriate j and $j+1$. (Caution, j and $j+1$ represent discrete levels of the yield criterion, not to be confused with i and $i+1$ which represent time steps)

b) $\xi_{n+1}^{i+1} = \dfrac{\bar{\varepsilon}_p^{j+1} - \bar{\varepsilon}_{p\,n+1}^{i+1}}{\bar{\varepsilon}_p^{j+1} - \bar{\varepsilon}_p^{j}}$

c) $\Pi_{n+1}^{i+1} = \xi_{n+1}^{i+1} Y(\bar{\varepsilon}_p^{j}) + (1 - \xi_{n+1}^{i+1}) Y(\bar{\varepsilon}_p^{j+1})$

d) $h_{n+1}^{i+1} = \dfrac{\partial \Pi}{\partial \bar{\varepsilon}_p} = \dfrac{Y(\bar{\varepsilon}_p^{j+1}) - Y(\bar{\varepsilon}_p^{j})}{\bar{\varepsilon}_p^{j+1} - \bar{\varepsilon}_p^{j}}$

e) Determine the appropriate $\boldsymbol{L}(\bar{\varepsilon}_p^{j})$, $k(\bar{\varepsilon}_p^{j})$, and $a(\bar{\varepsilon}_p^{j})$ for j and $j+1$

f) $\tilde{\sigma}_{n+1}^{i+1,j} = \tilde{\sigma}\{\boldsymbol{\sigma}_{n+1}^{i+1}, \boldsymbol{L}(\bar{\varepsilon}_p^{j}), k(\bar{\varepsilon}_p^{j}), a(\bar{\varepsilon}_p^{j})\}$

g) $\tilde{\sigma}_{n+1}^{i+1,j+1} = \tilde{\sigma}\{\boldsymbol{\sigma}_{n+1}^{i+1}, \boldsymbol{L}(\bar{\varepsilon}_p^{j+1}), k(\bar{\varepsilon}_p^{j+1}), a(\bar{\varepsilon}_p^{j+1})\}$

h) $\Gamma_{n+1}^{i+1} = \xi_{n+1}^{0} \cdot \tilde{\sigma}_{n+1}^{i+1,j} + (1 - \xi_{n+1}^{0}) \cdot \tilde{\sigma}_{n+1}^{i+1,j+1}$

i) $\boldsymbol{t}_{n+1}^{i+1,j} = \dfrac{\partial \tilde{\sigma}\{\boldsymbol{\sigma}, \boldsymbol{L}(\bar{\varepsilon}_p^{j}), k(\bar{\varepsilon}_p^{j}), a(\bar{\varepsilon}_p^{j})\}}{\partial \boldsymbol{\sigma}} \Big|_{\boldsymbol{\sigma}_{n+1}^{i+1}}$

j) $\boldsymbol{t}_{n+1}^{i+1,j+1} = \dfrac{\partial \tilde{\sigma}\{\boldsymbol{\sigma}, \boldsymbol{L}(\bar{\varepsilon}_p^{j+1}), k(\bar{\varepsilon}_p^{j+1}), a(\bar{\varepsilon}_p^{j+1})\}}{\partial \boldsymbol{\sigma}} \Big|_{\boldsymbol{\sigma}_{n+1}^{i+1}}$

k) $\boldsymbol{q}_{n+1}^{i+1} = \dfrac{\partial \Gamma}{\partial \boldsymbol{\sigma}} = \xi_{n+1}^{i+1} \boldsymbol{t}_{n+1}^{i+1,j} + (1 - \xi_{n+1}^{i+1}) \boldsymbol{t}_{n+1}^{i+1,j+1}$

l) $v_{n+1}^{i+1} = \dfrac{\partial \Gamma}{\partial \bar{\varepsilon}_p} = \dfrac{\tilde{\sigma}_{n+1}^{i+1,j+1} - \tilde{\sigma}_{n+1}^{i+1,j}}{\bar{\varepsilon}_p^{j+1} - \bar{\varepsilon}_p^{j}}$

8. Go to step 5

9. Calculate the elasto-plastic tangent modulus

a) $\boldsymbol{C}_{n+1}^{ep} = \boldsymbol{C} - \dfrac{\left(\boldsymbol{C} q_{n+1}^{i}\right) \otimes \left(\boldsymbol{C} q_{n+1}^{i}\right)^{T}}{\boldsymbol{q}_{n+1}^{i} \boldsymbol{C} \boldsymbol{q}_{n+1}^{i} + h_{n+1}^{i} - p_{n+1}^{i} \cdot r_{n+1}^{i}}$

The interpolation approach was also implemented for the isotropic yield criterion (3.1) in order to compare the results directly with the continuous approach described in the previous section. Three discrete surfaces were used to represent the evolution of the yield surface from $0 \le \bar{\varepsilon}_p \le 0.05$, in particular $\bar{\varepsilon}_p^{1} = 0$, k = 0.4; $\bar{\varepsilon}_p^{2} = 0.025$, k = 0.2; and $\bar{\varepsilon}_p^{3} = 0.05$, k = 0 while the homogeneity coefficient was set equal to 2. For $\bar{\varepsilon}_p > 0.05$ the surface was allowed to harden isotropically with k = 0, a = 2. These yield loci, along

with the interpolation of the yield stresses corresponding to the three levels of effective plastic strain from (4.26) are shown in Figure 4.4. The results of a single element compression simulation using the interpolation method are compared with the results from the continuous method in Figure 4.5. The results are very close since the linear interpolation scheme is compared to a linear law of variation for yield surface coefficient *k* with a nearly linear hardening law. Clearly, if the law of variation for *k* was not linear, the accuracy of a linear interpolation scheme would increase as more interpolation points are used.

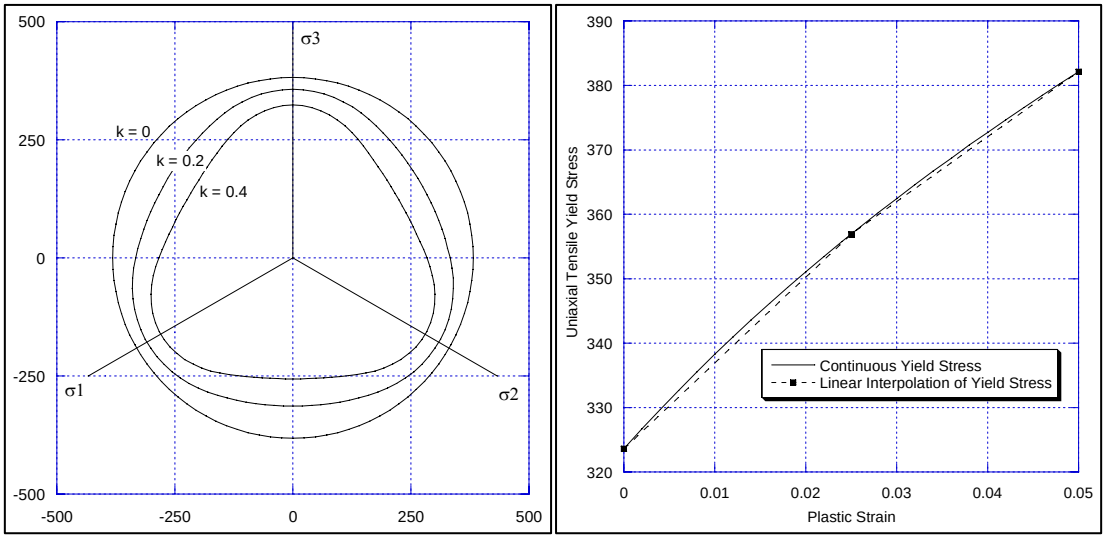

Figure 4.4 Discrete yield loci and yield stresses used for the interpolation method.

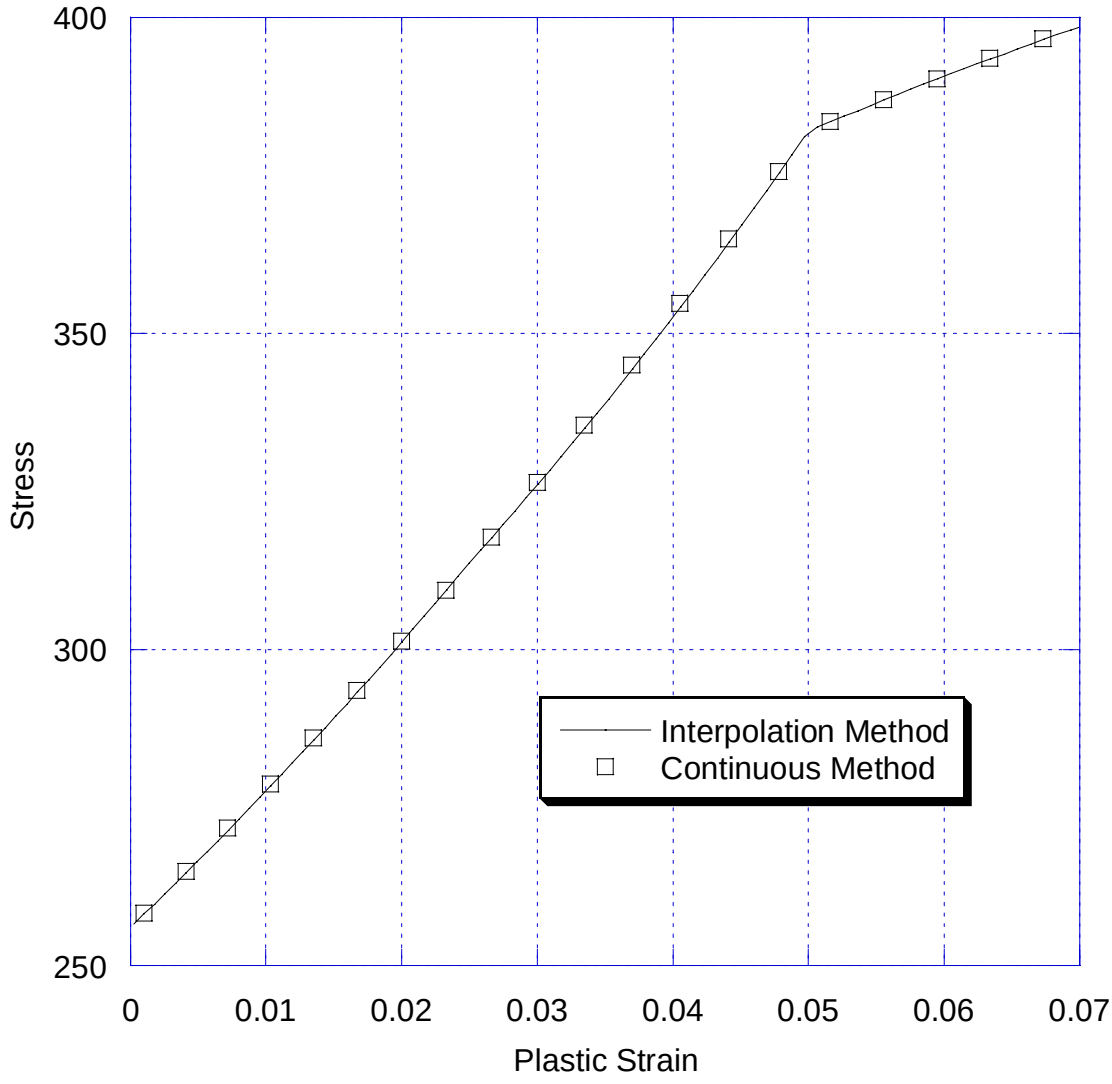

Figure 4.5 Results of the interpolation method compared to the continuous method from a single element compression test

4.6 Application to Zirconium

Kaschner et al. (2000), Kaschner et al. (2001), and Tomé et al. (2001) have conducted experimental studies on the anisotropy of the deformation of textured polycrystalline pure zirconium. This material is highly anisotropic both at the single crystal and polycrystal level. It was processed through a series of clock-rolling and annealing cycles to produce a plate with strong basal texture (<c>-axes of the crystals predominantly oriented along the plate normal direction). The process of multiple rolling passes while rotating the plate between passes was used in order to obtain a nearly isotropic in plane texture. Right-circular cylindrical test specimens were sectioned from both the through-thickness and in-plane plate directions. Quasi-static ($10^{-3}s^{-1}$) compression tests were conducted on these samples, while quasi-static tension tests were conducted only in the in-plane direction. While the experiments reported in Kaschner et al. (2001) and Tomé et al. (2001) correspond to two different temperatures (room and liquid nitrogen), in what follows we will use only the room temperature results to validate our approach. The tests have shown that the mechanical response is strongly dependent on the predominant orientation of the <c>-axes with respect to the loading direction.

To obtain the yield stresses for through-thickness tension and pure shear load paths for the identification of the anisotropy coefficients involved in the proposed orthotropic yield criterion, numerical tests with the vpsc polycrystal model were performed using the reported initial texture, deformation systems operational at room temperature (i.e., prismatic <*a*>-slip, pyramidal <*c*+*a*>-slip, and tensile twinning), and the values for the crystallographic coefficients for the single crystal, see Tomé et al. (2001). Voce hardening parameters (see equation 2.46) were adjusted for each active deformation

system for a strain rate of $10^{-3}s^{-1}$ until the predicted loading from the vpsc model reproduced the experimental response of the clock-rolled plate of zirconium from Tome et al. (2001). The set of parameters that gave the best fit to the data are given in Table 4.1. A comparison between the calculated response using the vpsc model and the experimental data for uniaxial tension and compression in the plane of the sheet and for through-thickness compression is presented in Figure 4.6.

Table 4.1 Voce hardening parameters for zirconium for a strain rate of $10^{-2}s^{-1}$

	τ_0	τ_1	θ_0	θ_1
prismatic slip	5	30	1500	50
pyramidal slip	60	280	3500	45
tensile twin	50	0	100	100

Using the yield stress data from mechanical tests and the results of the numerical tests, the yield surfaces for five different levels of accumulated plastic strain: $\tilde{\varepsilon}_p^1$=0.002, $\tilde{\varepsilon}_p^2$=0.01, $\tilde{\varepsilon}_p^3$=0.05, $\tilde{\varepsilon}_p^4$= 0.1 and $\tilde{\varepsilon}_p^5$= 0.15 were identified. The numerical values for the coefficients for each level of accumulated plastic strain are given in the Table 4.2. For each level of plastic strain the coefficient L_{11} was equal to 1.0, therefore, L_{11} was not listed in Table 4.2. Next, for each individual strain level $\tilde{\varepsilon}_p^j$, j =1…5, $Y^j = Y(\tilde{\varepsilon}_p^j)$ was calculated using the experimental in-plane tension loading curve, and $\tilde{\sigma}^j = \tilde{\sigma}\{\boldsymbol{\sigma}, \boldsymbol{L}(\tilde{\varepsilon}_p^j), k(\tilde{\varepsilon}_p^j), a(\tilde{\varepsilon}_p^j)\}$. Finally, the yield surface corresponding to any given level of accumulated plastic deformation (between 0 and 0.15) can be obtained using the interpolation technique described in section 4.5. Figure 4.7 shows the biaxial plane $(\sigma_{xx}, \sigma_{yy})$ projections of the five individual yield surfaces (solid lines) using equation

(3.16), and of several yield loci (dashed lines) obtained using the proposed interpolation technique (see equations (4.27)- (4.30)).

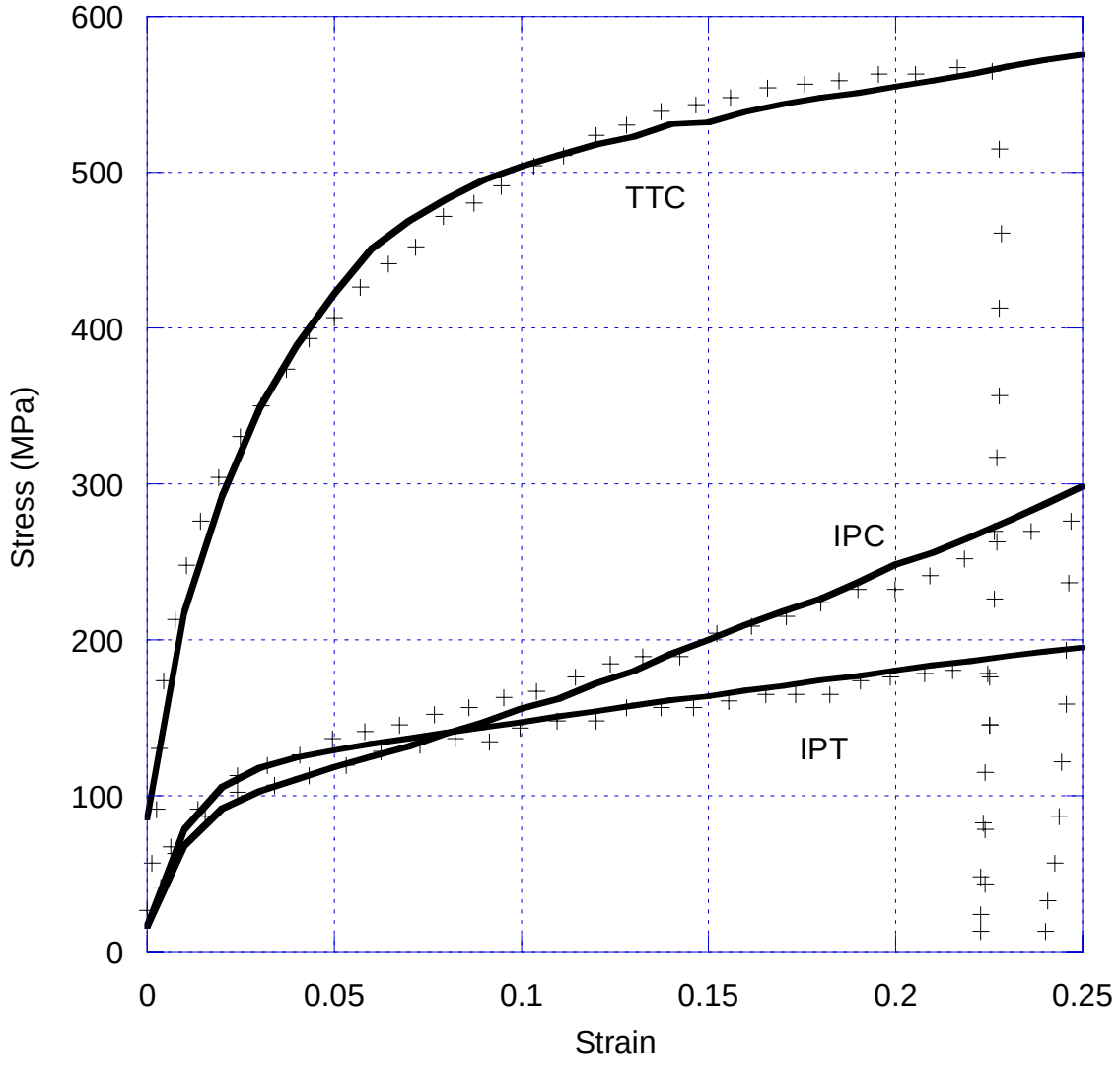

Figure 4.6 Stress-strain response for a clock-rolled plate of zirconium for in-plane compression (IPC), in-plane tension (IPT), and through-thickness compression (TTC). Solid lines represent vpsc calculations. Symbols represent experimental data (after Tome et al. 2001)

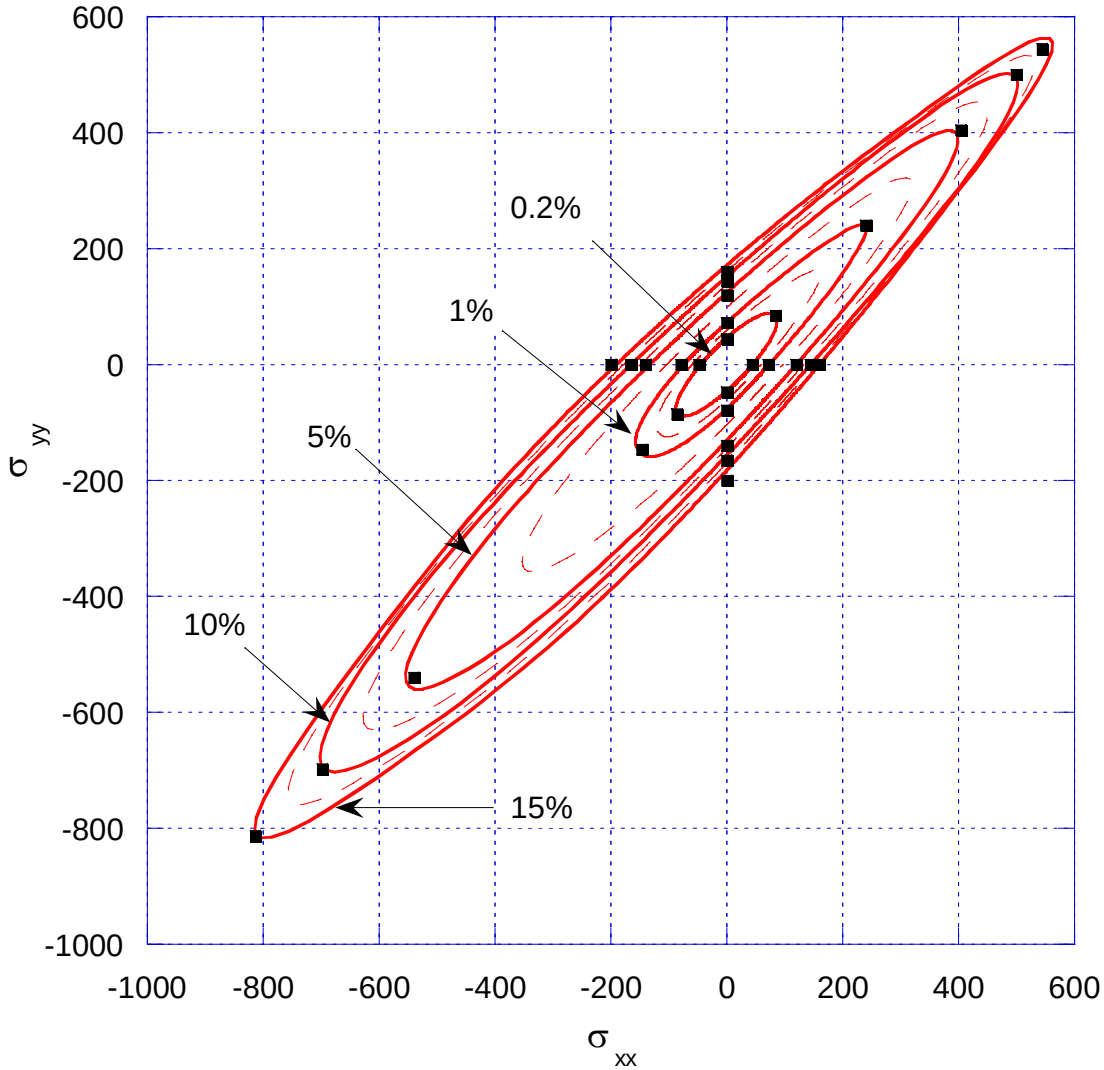

Figure 4.7 Yield surface evolution for a clock-rolled plate of zirconium. Predicted yield surfaces using the proposed criterion are represented by solid lines. Interpolated intermediate yield surfaces are represented by dashed lines. Vpsc calculations represented by symbols.

Table 4.2 Zirconium coefficients corresponding to the yield surface evolution depicted in Figure 4.7 (L_{11} = 1.0 for each case)

	a	k	L_{12}	L_{13}	L_{22}	L_{23}	L_{33}	L_{44}	L_{55}	L_{66}
0.2%	2	-0.0017	3.7403	2.1468	0.9926	2.0845	0.5393	1.2958	1.4085	5.1832
1%	2	0.2756	2.7390	2.0252	0.9413	1.9900	1.2506	0.4906	0.5560	1.9010
5%	2	-0.1621	3.2358	1.6811	0.8142	1.5974	1.3113	0.6567	0.6290	2.7404
10%	2	-0.1659	3.2749	1.6275	0.6188	1.5191	1.3190	0.7695	0.7021	3.0585
15%	2	-0.1828	3.1351	1.6353	0.7201	1.5212	1.1806	0.7549	0.6858	2.9195

Calculations were carried out using the above interpolation model to simulate the response of zirconium at room temperature, for the cases of in-plane tension, in-plane compression, and through-thickness compression. For comparison purposes, we have also performed simulations for the same material assuming fixed values of the anisotropy coefficients (these values correspond to yield stress data at 0.002 equivalent plastic strain) which is equivalent to isotropic hardening. Figure 4.8 shows the stress-strain curves obtained using the proposed model according to the yield surface evolution depicted by Figure 4.7 (solid lines), together with those obtained by means of the proposed orthotropic yield criterion but assuming isotropic hardening (dashed lines), and the data from mechanical tests (symbols). Note that the proposed model captures well the experimental trends. Obviously, since isotropic hardening implies that the material hardens at the same rate in every testing direction, it cannot adequately describe deformation that involves the activation of deformation mechanisms different from the ones operational during in-plane tension (i.e., the test used to adjust the values of $Y^j = Y(\bar{\varepsilon}_p^j)$).

The proposed model will be used to simulate a series of four-point bending tests at room temperature reported in Kaschner et al. (2001). The experiments were carried out on rectangular bars of square section cut from the same clock-rolled zirconium. Before loading, the beams were aligned in one of the two possible orientations with respect to the main texture component: with the main texture component contained in the bending plane, i.e., <c>-axes mostly aligned with the z-axis of the beam (case C0), and perpendicular to it, i.e., <c>-axes mostly aligned with the x-axis of the beam (case C90) (see also Figure 4.9 for a schematic of the test). The initial dimensions of the beams were

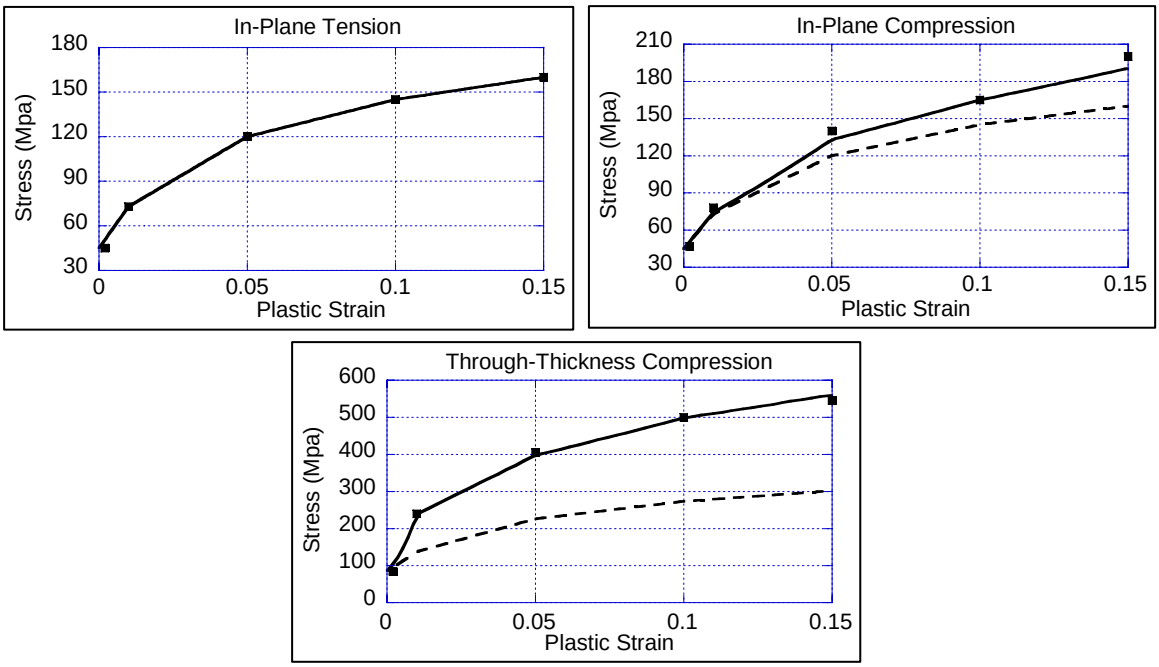

Figure 4.8 Comparison between experimental data (solid rectangles) and simulation results using the proposed model coupled with VPSC (solid lines) and using an isotropic hardening law (dashed lines) for a clock-rolled zirconium plate. Data after Tome et al. (2001).

6.35 x 6.35 x 50.8 mm. The beams were bent as the upper dowel pins were displaced downwards by 6mm and the lower pins were held rigid. Special experimental techniques were developed to map and measure the local strain field. Detailed information concerning the variation of each strain component as a function of the location along the width of the specimen were reported. Also, a detailed finite element analysis of the bending tests using the explicit finite element code EPIC coupled with the vpsc model was performed in Kaschner et al. (2001) assuming the presence of a polycrystal at each integration point. For a detailed description of the linkage between the finite element code and the polycrystal model, see Tome et al. (2001).

ABAQUS finite element simulations of the zirconium bent beam tests using the proposed model were performed. Due to the symmetry of the problem, only half of the beam was analyzed using 2916 three-dimensional linear brick elements. Free-surface boundary

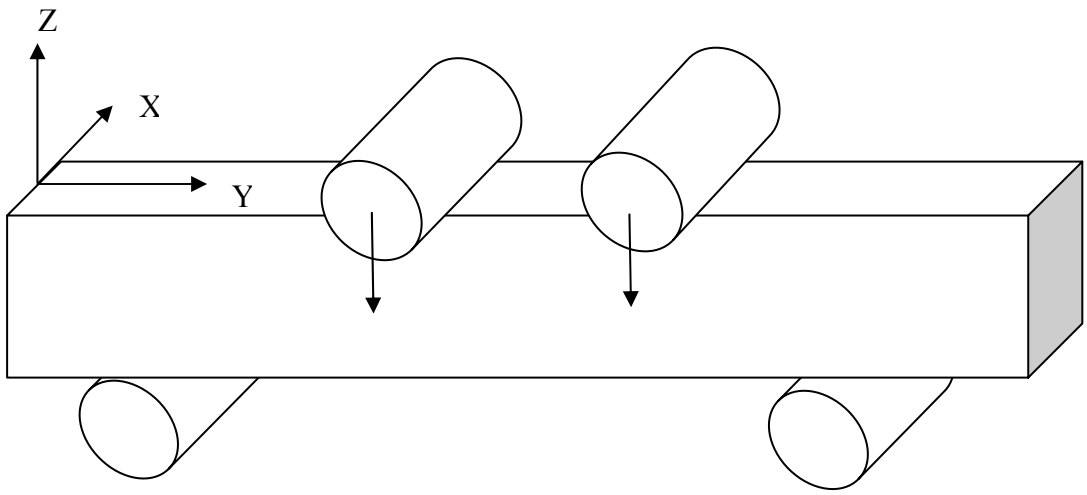

Figure 4.9 Schematic of the four-point bend test.

conditions were imposed on the beam except at the nodes that coincide with the contact points of the dowel pins. The results from these simulations, along with the experimental data, and the VPSC/EPIC predictions reported in Kaschner et al. (2001) are shown in Figures 4.10 (case C0) and 4.11 (case C90).

Inspection of Figure 4.10 (case C90) reveals that the simulation results using either VPSC/EPIC or the proposed model are reasonably close to the experimental data. Both models capture very well the rigidity of the beam response along the hard-to-deform <c>-axes preferential orientation, which in this case is parallel to the z-axis. Also, both models capture the asymmetry between tension and compression (i.e., the differences in yield values and hardening rates) and thus correctly predict an upward shift of the neutral plane. The deformation along the beam axis is better predicted by the proposed model, since the VPSC/EPIC model under predicts the deformation in the lower half of the beam. Also, the proposed model gives a more accurate prediction for the final location of the neutral plane. For the case when the major texture component is aligned with the x-axis of the beam (C90, Figure 4.11), the VPSC/EPIC overpredicts the strains for the

upper half of the beam. Also, the predicted VPSC/EPIC neutral plane remains at the center of the beam. The proposed model, on the other hand, predicts more accurate results for this case, including the experimentally observed upward shift of the neutral plane.

Figures 4.12 and 4.13 present the calculated strain distributions using the yield surface evolving according to isotropic hardening adjusted to the in-plane tensile loading response of the original zirconium plate for the cases C0 and C90, respectively. Since an isotropic hardening law cannot capture the difference in hardening rates between tension and compression, the simulations are less accurate than those obtained when the yield surface evolves according to the proposed anisotropic hardening model.

Figure 4.14 shows the final configurations for the photographed experimental x-z cross-section of the bent beams superimposed to the predictions obtained with VPSC/EPIC (white dots), as reported in Kaschner et al. (2001). The figure also shows the calculated x-z cross-sections of the bent beams obtained using the proposed model (Figures 4.14a and 4.14b). Note that both models predict wedged cross-sections only for the case C0 (Figs. 4.14a and 4.14c) when the hard-to-deform <c>-axes are predominantly parallel to the z-axis. For the case C90 (Figures 4.14b and 4.14d) when <c>-axes is aligned with the x-axis, both models describe correctly the rigidity in the hard direction, and the final cross-section remains rectangular.

In Figure 4.7, the yield surface for the zirconium plate associated with a given level of plastic deformation is represented by yield stresses corresponding to uniaxial tests conducted for different loading directions. This yield surface representation is capable of accurately predicting whether or not a given state of stress will produce plastic

deformation, however, it does not guarantee that the r-values corresponding to that given state of stress will be correctly predicted. Initially, the r-values for the zirconium plate due to in-plane loadings are very high (>>1) indicated by the steep slope of the yield surface. Due to the initial hardness of the through thickness direction as compared to the in plane directions, and to the high hardening rate observed in the through thickness direction, the very high predicted r-values remain for all in-plane loading directions at each level of plastic strain according to Figure 4.7. However, twinning acts to randomize the material's texture. This effect becomes significant for in plane compression at higher levels of accumulated plastic strain (greater than 15%), and consequently the r-values begin to decrease with accumulated deformation. Therefore, while the yield surface evolution according to the method shown in Figure 4.7 is a good approximation for low to moderated levels of plastic strain for any given loading direction, the 'true' yield surface corresponding to the updated texture of the material needs to be used to accurately simulate deformations involving twinning at higher levels of deformation for the zirconium plate.

For example, in order to determine the 'true' yield surface for an evolved texture due to plastic deformation along a given strain path, the material must first be pre-strained along that strain path. Then, specimens cut from the pre-strained material should be tested to determine the yield strength under different loading conditions to construct the updated yield surface. After repeating this procedure for different levels of pre-strain, the evolution of the yield surface is determined for the given strain path. This type of experimental characterization would take numerous experiments, which may not even be possible in compression for high levels of pre-strain due to buckling.

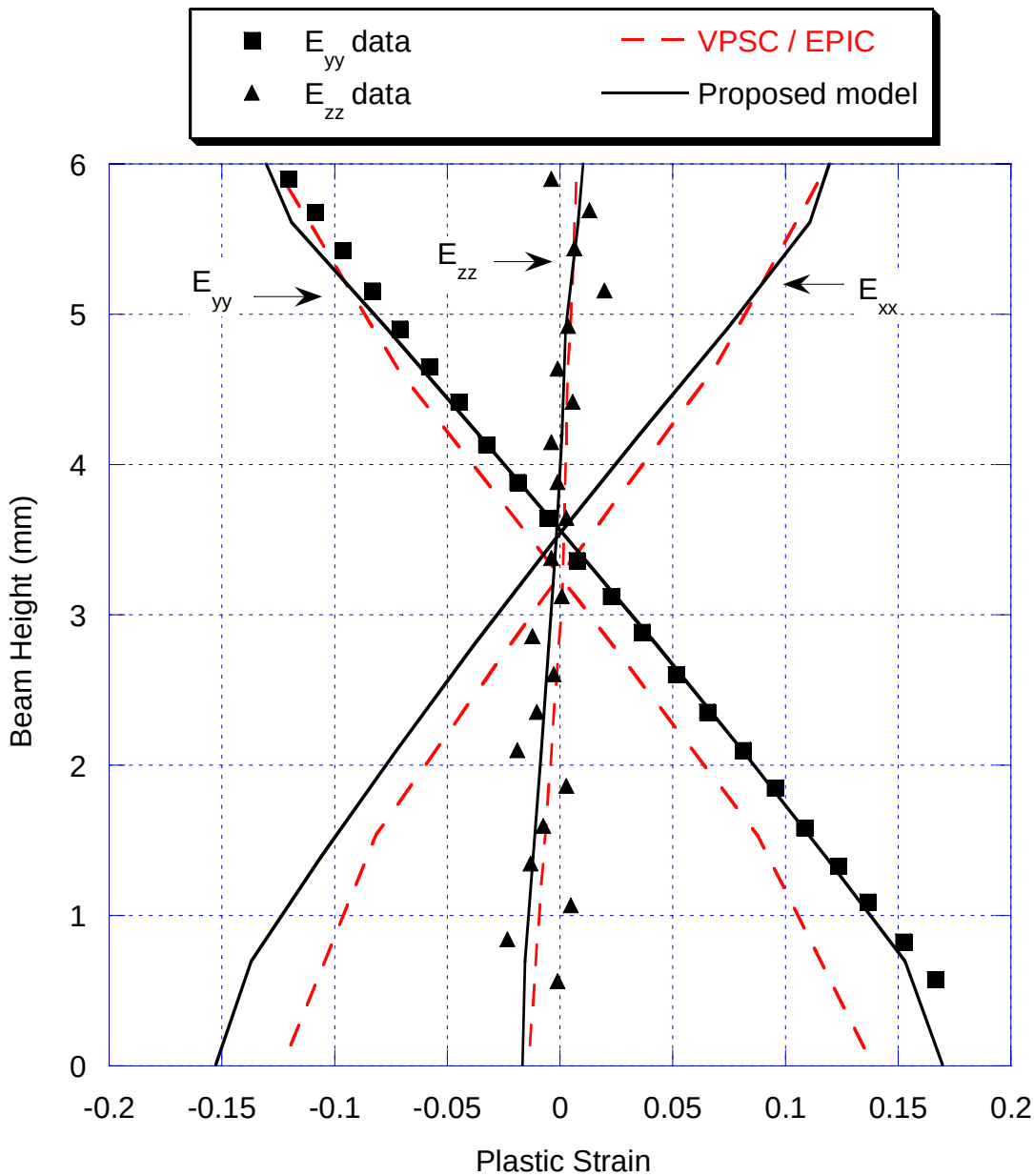

Figure 4.10 Comparison of the experimentally measured strain distributions (symbols) with the results of finite element simulations using the proposed model (solid lines) and VPSC linked directly to EPIC (dashed lines) for the case C0 (i.e., when the <c>-axes are predominantly contained in the bending plane). Data and VPSC/EPIC simulations results reported in Kaschner et al. (2001).

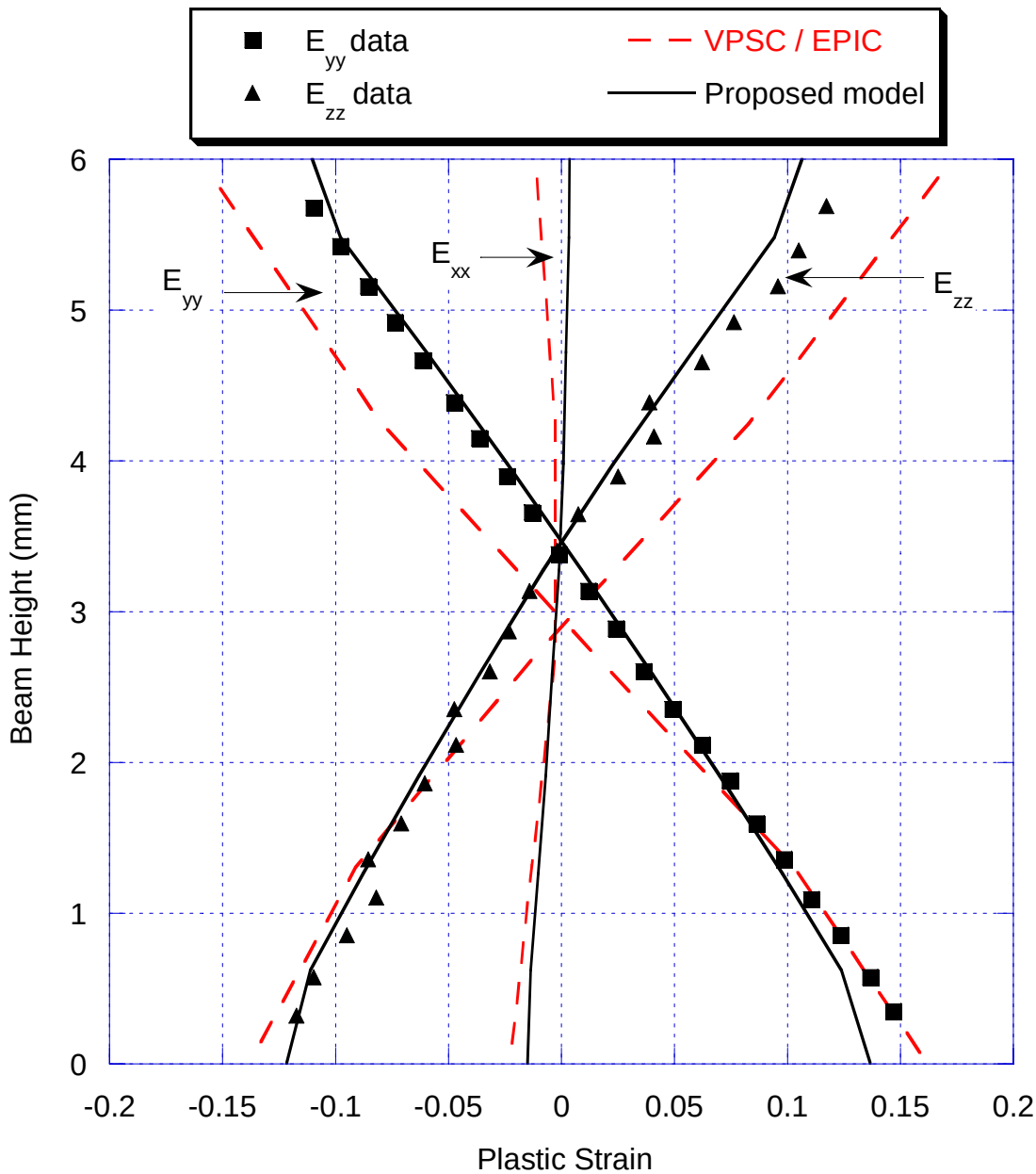

Figure 4.11 Comparison of the experimentally measured strain distributions (symbols) with the results of finite element simulations using the proposed model (solid lines) and VPSC linked directly to EPIC (dashed lines) for the case C90 (i.e., when the <c>-axes are predominantly perpendicular to the bending plane). Data and VPSC/EPIC simulations results reported in Kaschner et al. (2001).

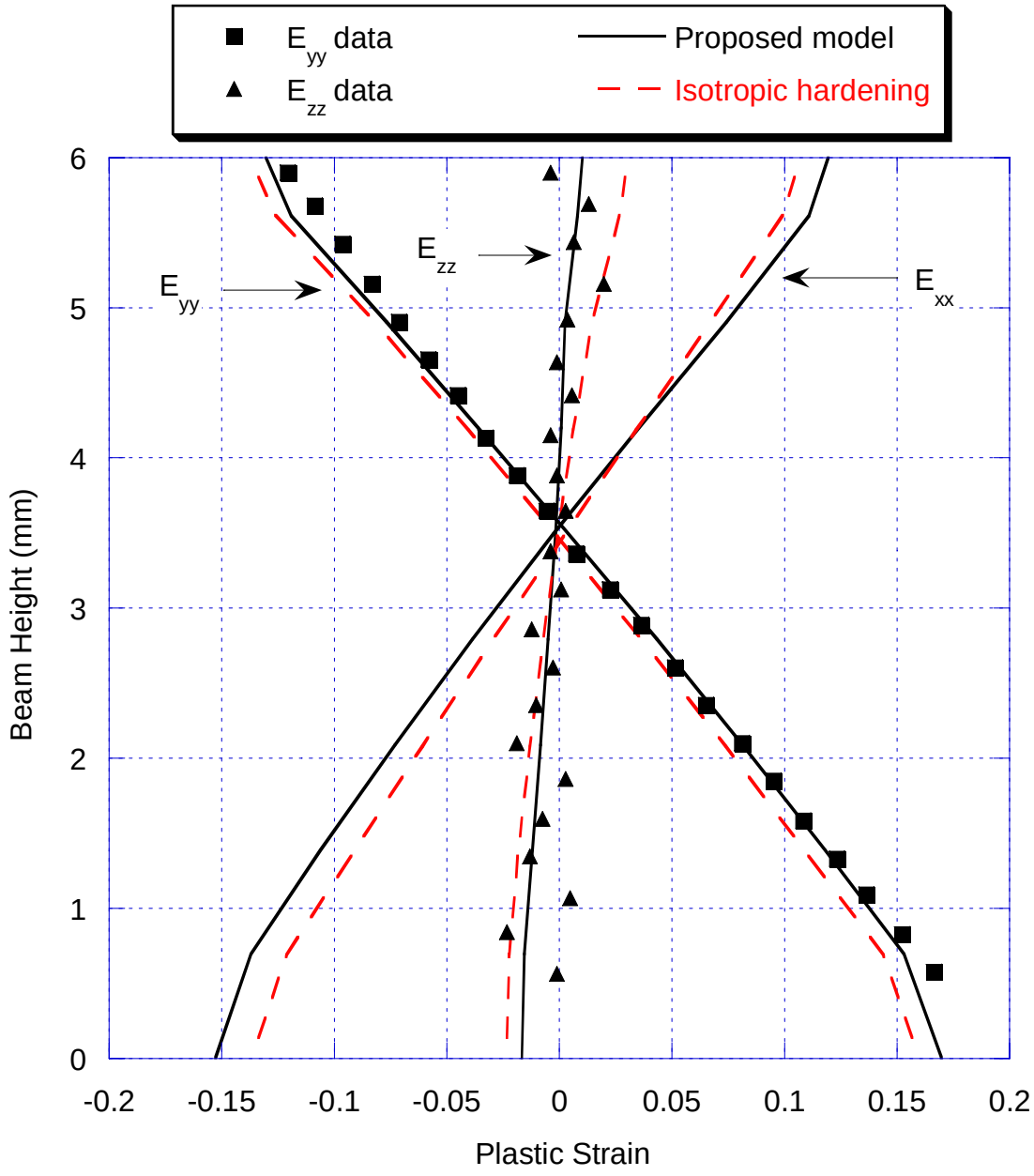

Figure 4.12 Comparison of the experimentally measured plastic strains distributions (symbols) and the ABAQUS finite element predictions using the proposed model (solid lines) and the proposed yield criterion with isotropic hardening (dashed lines) for the C0 case. Data after Kaschner et al. (2001).

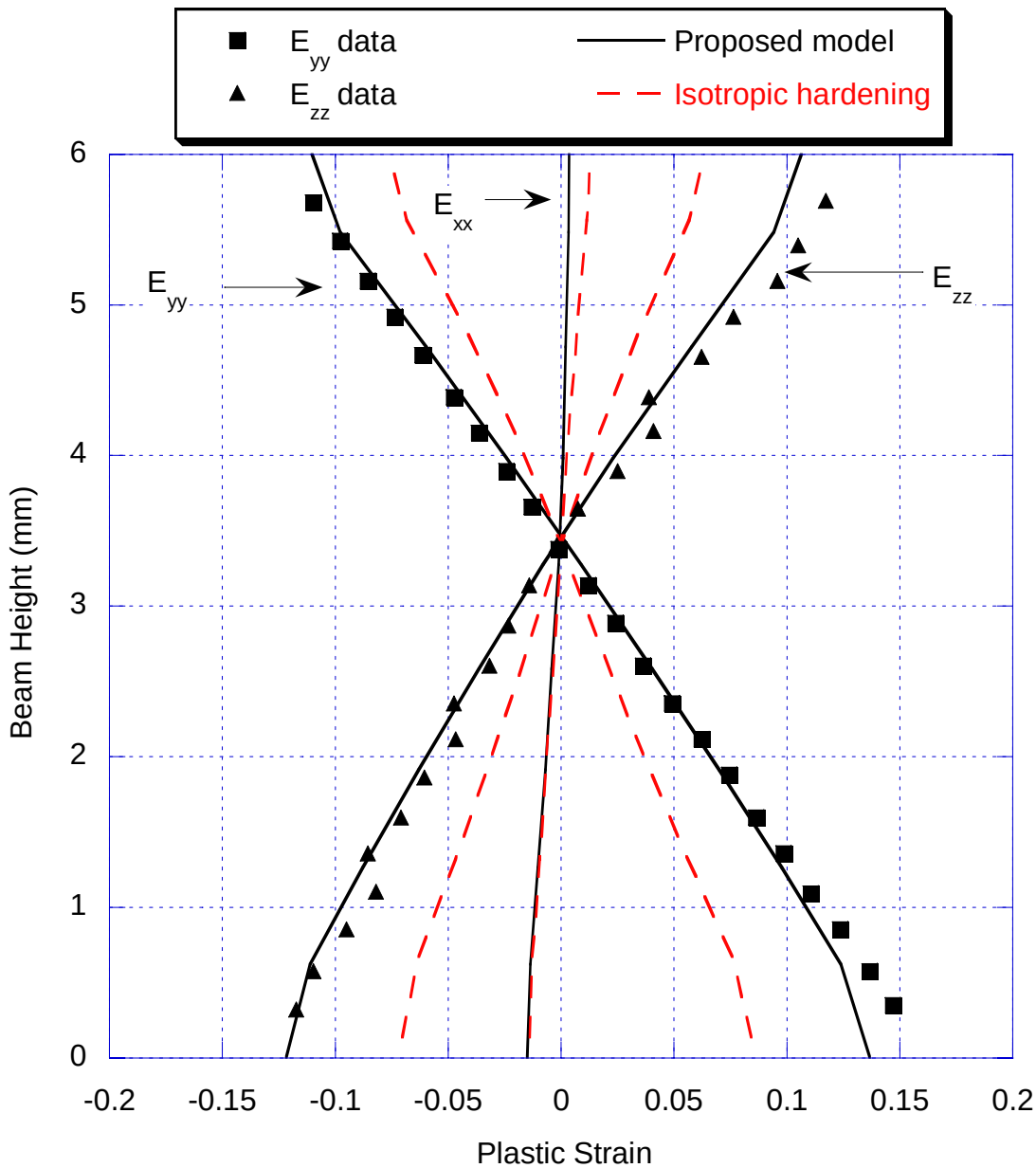

Figure 4.13 Comparison of the experimental plastic strains distributions (symbols) and the ABAQUS finite element predictions using the proposed model (solid lines) and the proposed yield criterion with isotropic hardening (dashed lines) for the C90 case. Data after Kaschner et al. (2001).

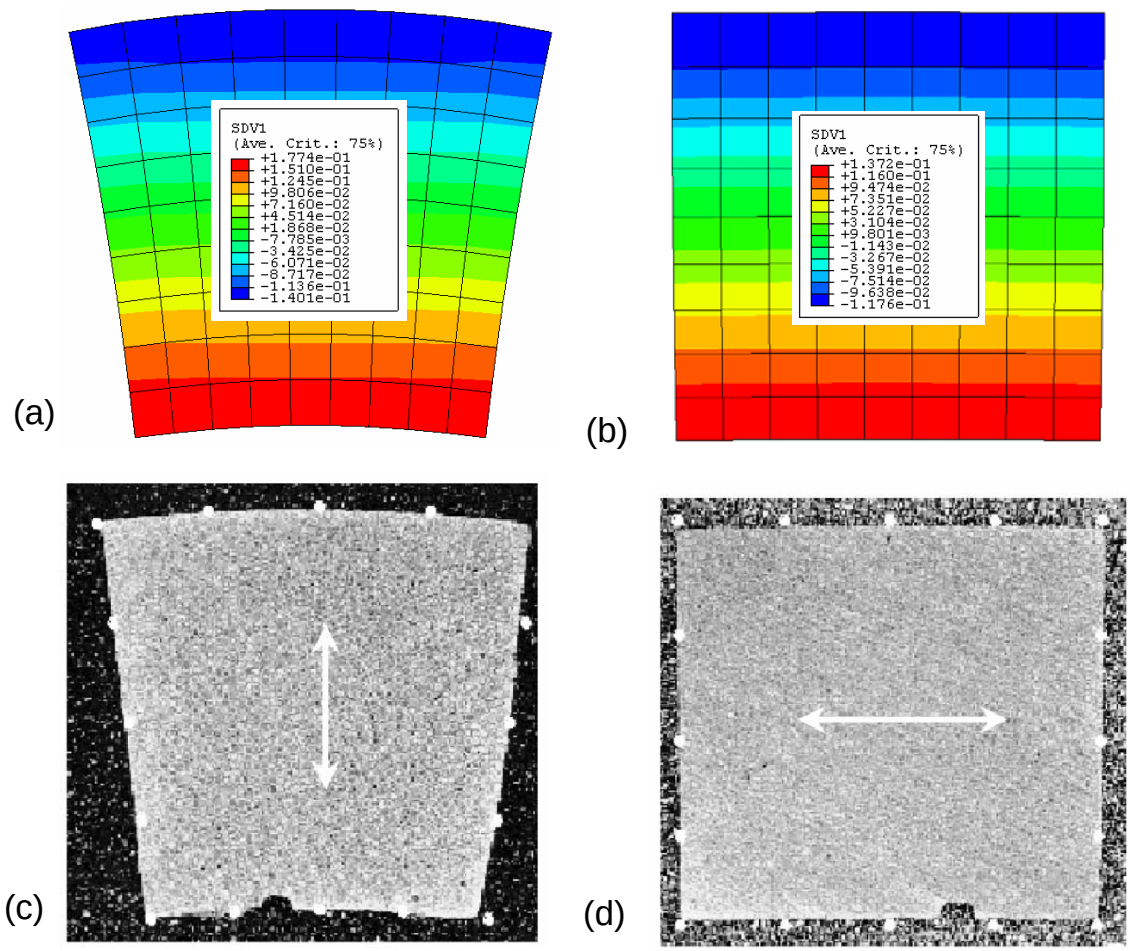

Figure 4.14 Comparison of experimentally photographed x-z cross-section of the bent bars versus the predictions of VPSC/EPIC (white dots) and the proposed model (Exx contours); (a) and (c) correspond to the case C0 (<c>-axes mostly parallel to the z-axis) while (b) and (d) correspond to the case C90 (<c>-axes mostly aligned with the x-axis of the beam, respectively). The orientation of the basal poles is indicated by the arrows (data and VPSC/EPIC simulations after Kaschner et al., 2001).

Alternatively, the vpsc model can be used to determine such a yield surface evolution. Specifically, using the vpsc model, the evolving yield function for in plane compression was determined by pre-straining the polycrystal to a given level of deformation for in plane compression then numerically probing the polycrystal along different loading directions. In Figure 4.15, the yield points obtained with the VPSC model are represented by symbols. For each prestraining level, these data points are further used to determine the coefficients involved in the proposed orthotropic yield criterion. The values of the coefficients for each surface are listed in Table 4.3. Then, using the interpolation procedure described in Section 4.5, the anisotropic yield function (4.27) associated with the evolution of texture during in plane compression is determined. This procedure was repeated for through thickness compression as illustrated in Figure 4.16 and Table 4.4.

This yield function is in turn used in ABAQUS simulations of the in-plane compression of right cylinders of circular cross section to 28% strain, and compared with the experimental results reported in Tome et al. (2001) (see Figure 4.17). The cylinders were initially 17.7 mm long and 2.25 mm in diameter. One was machined with its axis parallel to the plane of the plate, and the other with its axis parallel to the through thickness direction of the sheet. For the in-plane compression cylinder, the measured post-test in-plane expansion was of 22% while the out-of-plane expansion was of 6% and the model prediction using the yield surface evolution according to Figure 4.15 agrees exactly with the experimental results. Figure 4.17a shows the final FE mesh. For comparison, the photograph of the IP compression sample cross-section, along with the VPSC/EPIC simulation results (dashed line) are shown in Figure 4.17b (after Tome et al.,

2001). The comparison demonstrates that a very good agreement with the experiments is obtained when using an appropriate yield surface representation and anisotropic evolution laws that take into account geometrical and mechanical hardening. On the other hand, if the proposed orthotropic yield surface is used, but its evolution is adjusted using an isotropic hardening model, the predicted expansions were 27% and 1% for the in-plane and out-of-plane directions, respectively, i.e., the ovalization is clearly over predicted using isotropic hardening. Since the ovalization of the cylinder due to a compressive loading is determined by the r-values, the ovalization is similarly over predicted using the method to determine the yield surface evolution according to Figure 4.7 due to the very high r-values.

In through-thickness compression, compression takes place along the axis of symmetry of the sample, which remains cylindrical in section. Since twinning due to compression along the <c>-axis was not reported as a significant mode of deformation at room temperature (Tome et al., 2001), the material's texture does not significantly change due to compression along the thickness direction of the plate. Thus, there is not a considerable change in the r-values due to deformation for this loading direction. Therefore, using the yield surface evolution according to Figure 4.16 or Figure 4.7 will correctly predict the final circular cross section experimentally observed (see Figures 4.17c-4.17d).

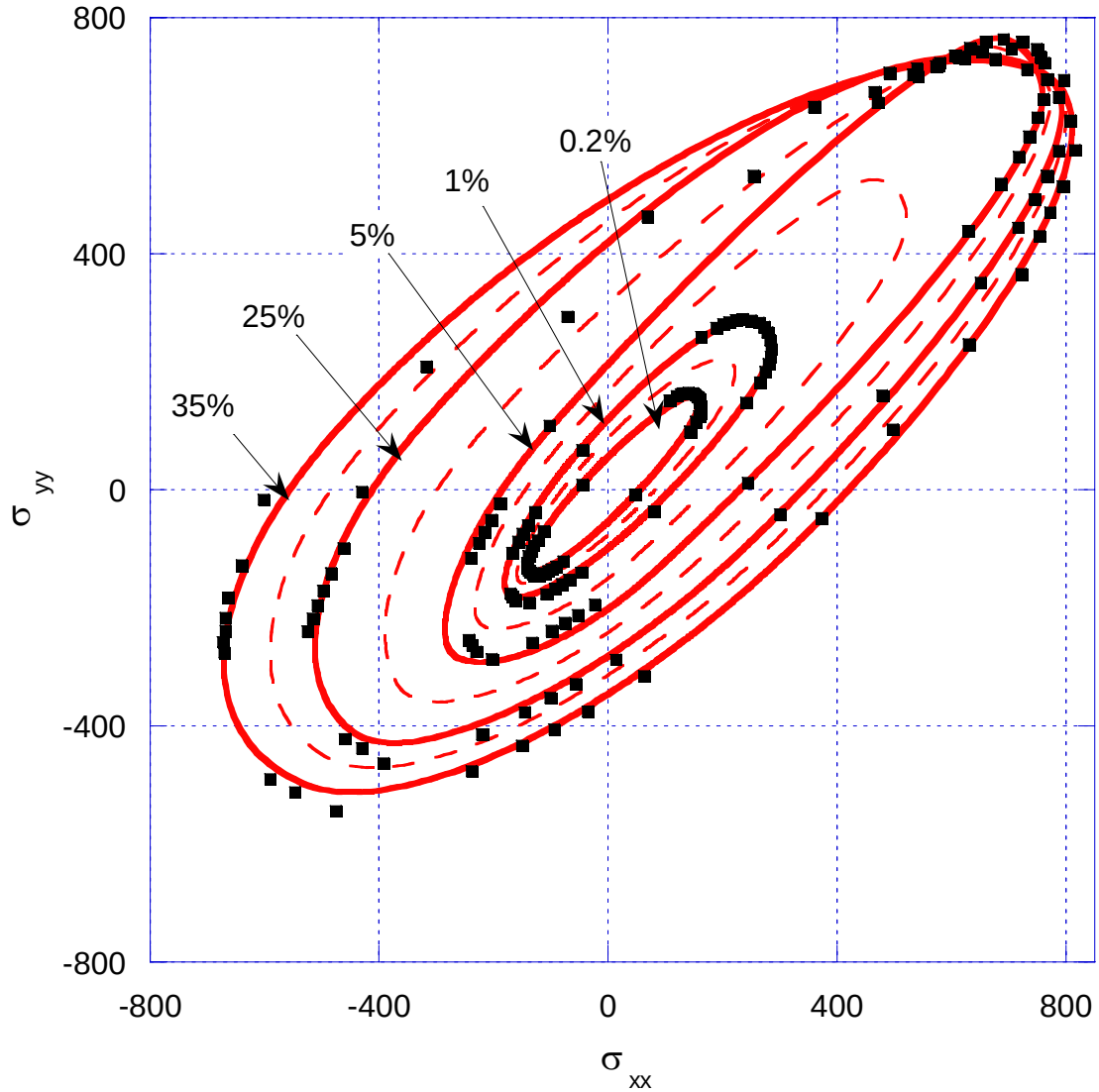

Figure 4.15 Yield surface evolution for a zirconium clock-rolled plate during in-plane compression. Symbols represent yield points calculated using the vpsc code; solid lines represent yield surfaces using the proposed yield criterion; dashed lines represent the yield surface evolution using the interpolation method.

Table 4.3 Zirconium coefficients corresponding to the yield surface for in-plane compression

	a	k	L_{12}	L_{13}	L_{22}	L_{23}	L_{33}	L_{44}	L_{55}	L_{66}
0.2%	2	0.0706	2.8831	1.8747	1.2517	1.9649	1.2040	0.9890	1.0750	3.9560
1%	2	0.2242	2.1498	1.4068	1.1789	1.4383	0.8922	0.6041	0.6167	1.6914
5%	2	0.5001	2.9227	1.8231	0.8649	1.7452	0.4181	0.9844	1.1450	2.9802
25%	2	0.2632	2.7041	1.7271	1.8211	2.0558	0.8686	0.9493	0.7906	1.4031
35%	2	0.1738	2.5052	1.6829	2.3196	2.0535	1.0118	0.8888	0.6942	1.0977

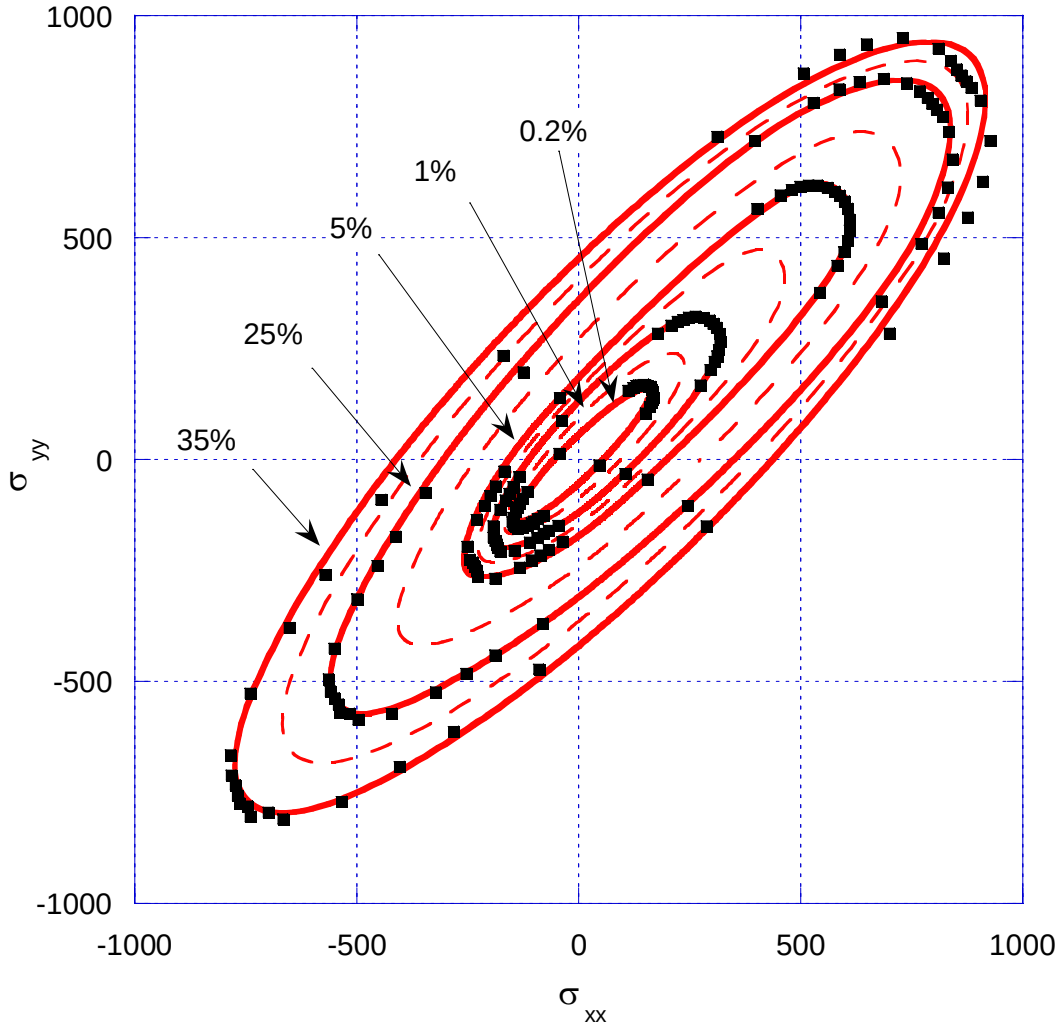

Figure 4.16 Yield surface evolution for a zirconium clock-rolled plate during through thickness compression. Symbols represent yield points calculated using the vpsc code; solid lines represent yield surfaces using the proposed yield criterion; dashed lines represent the yield surface evolution using the interpolation method.

Table 4.4 Zirconium coefficients corresponding to the yield surface for in-plane compression

	a	k	L_{12}	L_{13}	L_{22}	L_{23}	L_{33}	L_{44}	L_{55}	L_{66}
0.2%	2	0.0706	2.8831	1.8747	1.2517	1.9649	1.2040	0.9890	1.0750	3.9560
1%	2	0.2370	2.9643	1.5555	0.8027	1.4756	0.4332	1.1522	1.1726	3.3126
5%	2	0.4062	2.6516	1.6192	0.8131	1.5413	0.5825	0.9879	1.1270	2.8578
25%	2	0.1983	3.3478	1.5745	1.0389	1.5247	0.6025	1.8829	2.0812	3.3910
35%	2	0.0839	3.2715	1.5235	1.1200	1.4708	0.6405	2.1223	2.3116	3.8467

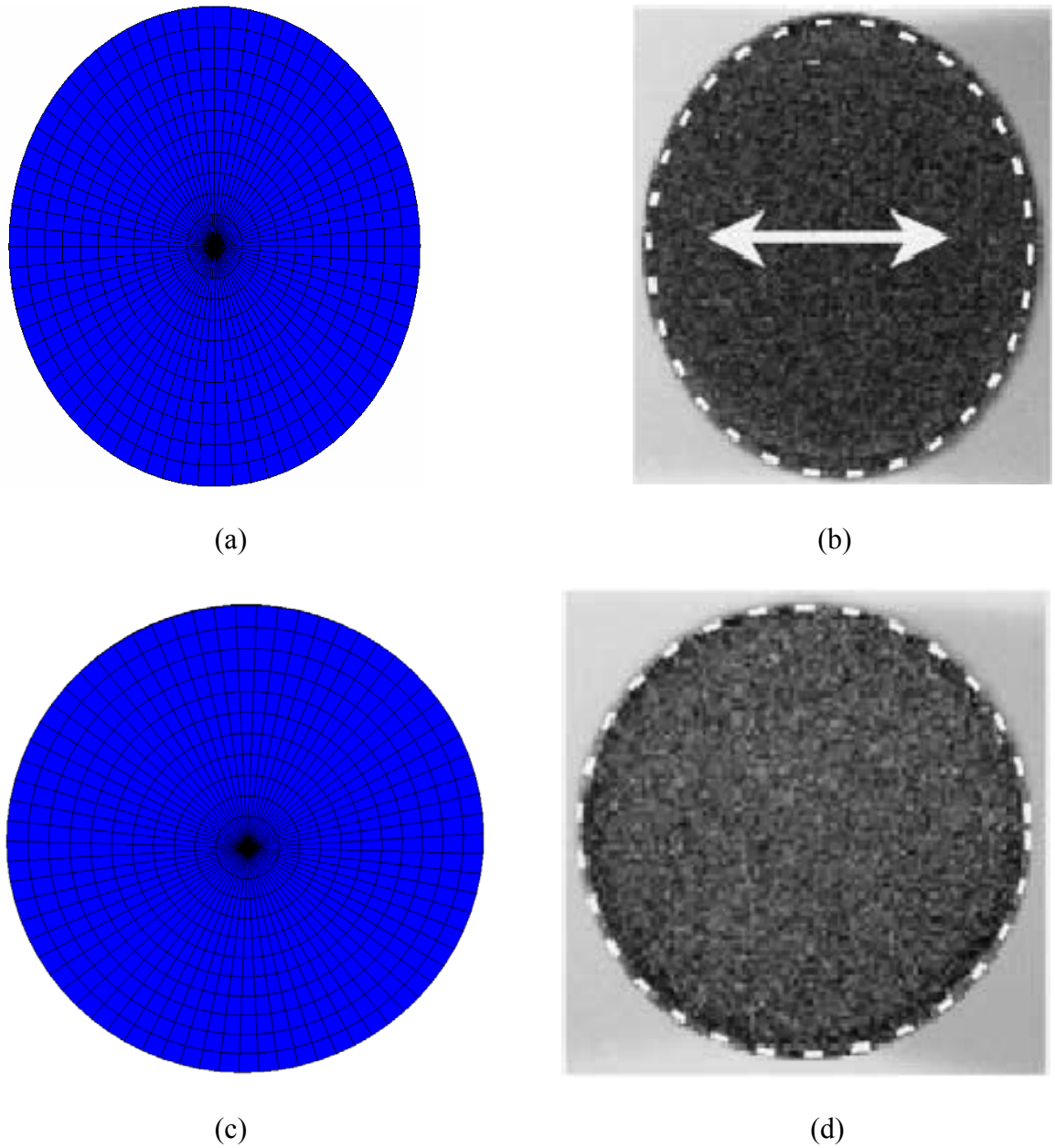

Figure 4.17 Comparison of the final sections of the zirconium cylinders after: a,b) in-plane compression, c,d) through-thickness compression. The photographs of the experimental shapes and simulated final shapes using VPSC/EPIC (dotted lines superimposed on the photographs) are taken from Tome et al. (2001).

4.7 Application to Magnesium Alloys

4.7.1 Application To Mg-Th

The proposed hardening law and the proposed orthotropic yield criterion (3.16) were used to model the response of a cold-rolled sheet of magnesium alloyed with thorium (see Figure 4.3). Uniaxial tension, uniaxial compression, and balanced biaxial tension simulations were carried out using the proposed method for the cold rolled sheet of Mg-Th. The same simulations were run using an isotropic hardening rule based on the coefficients determined for the 1% effective plastic strain yield surface. For modeling purposes, the yield surface corresponding to 1% effective plastic strain was assumed to be the initial yield surface. The results using the proposed hardening law (solid lines) are plotted along with the results using the isotropic hardening law (dashed lines), and the experimental data (symbols) in Figure 4.18. The proposed method captures the data for each loading direction very well. Since isotropic hardening assumes that the yield surface expands without any change to its shape, the material hardens at the same rate for each strain path. Therefore, isotropic hardening is not able to represent the behavior for loading directions other than that on which the hardening law was based, i.e., tension in the rolling direction of the sheet.

4.7.2 Application to AZ31B

Agnew et al. (2001) reports that the major deformation systems active at room temperature for AZ31B magnesium are basal slip, pyramidal slip, and tensile twinning (see Figure 1.2). The reported Voce hardening parameters for each system are given in Table 4.5.

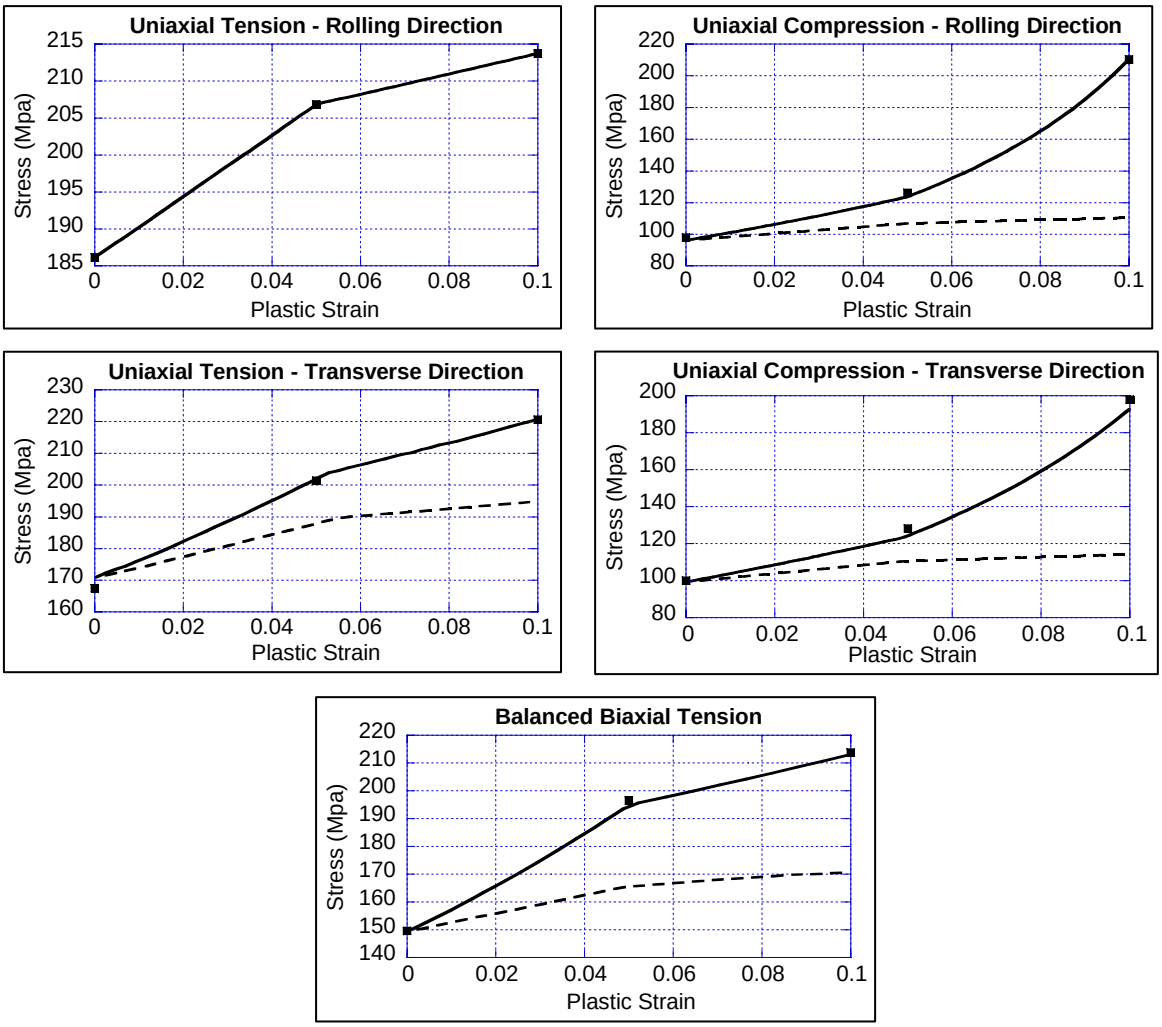

Figure 4.18 Comparison between experimental data (symbols) and simulation results using the proposed hardening law (solid lines) and using isotropic hardening (dashed lines) for a cold rolled sheet of MG-TH alloy. Data after Kelley and Hosford (1968).

Table 4.5 Voce hardening parameters for AZ31B magnesium

	τ_0	τ_1	θ_0	θ_1
basal slip	30	30	300	0
pyramidal slip	90	80	800	0
tensile twin	15	0	30	30

Styczynski et al. (2004) presents a metallurgical evaluation of cold rolled sheets of AZ31 magnesium. From the results of metallurgical studies, the authors suggest that the texture of the sheet can be described by varying equally weighted Euler angles using two components such that $\varphi_1, \Phi, \varphi_2 = +90^0, 15^0, \varphi_2$ and $\varphi_1, \Phi, \varphi_2 = -90^0, 15^0, \varphi_2$.

Using a vpsc model along with the single crystal properties for AZ31B magnesium and the orientation distribution function describing the initial texture for a cold-rolled sheet of AZ31B yield strengths were calculated for different levels of effective plastic strain corresponding to uniaxial tension and uniaxial compression in the rolling, transverse, and through-thickness directions of the sheet, as well as in pure shear for a strain rate of $10^{-3} s^{-1}$. Just like for zirconium, anisotropy coefficients for the proposed yield criterion (3.16) were calculated for the different levels of effective plastic strain (listed in Table 4.6) using these calculated data points. The resulting yield loci shown in Figure 4.19 represent yielding for monotonic loading along a given path. Intermediate yield surfaces can be calculated using the interpolation method (4.27).

Although AZ31B magnesium has been reported to fail due to in-plane compression at room temperatures at approximately $\bar{\varepsilon}_p \approx 14\%$ (Agnew et al., 2005), in-plane tensile loadings at room temperature do not fail until well after $\bar{\varepsilon}_p = 50\%$ (Agnew et al., 2001). Therefore, the evolution of the yield surface was determined using vpsc calculations for

strain levels of up to $\bar{\varepsilon}_p = 50\%$. In order to predict failure in this material, a proper failure criterion must be established since different load paths cause the material to fail at different levels of stress and strain.

Furthermore, since the sheet of AZ31B magnesium does not exhibit an extremely hard through thickness direction like the plate of zirconium, the predicted r-values for AZ31B are not so high when using monotonic loading yield stresses to approximate the yield surface. Therefore, using this approach may not be as inaccurate for simulating deformations at higher levels of strain for AZ31B as it was for zirconium.

Uniaxial tension and compression simulations were carried out in ABAQUS using the interpolation method (4.27) for cold rolled sheets of AZ31B magnesium. The same simulations were run using an isotropic hardening rule based on the coefficients determined for the 0.2% effective plastic strain yield surface. The results from the interpolation method of the proposed model (solid lines) are plotted along with the results from the isotropic hardening model (dashed lines), and the calculated data points from the vpsc model (symbols) in Figure 4.20. The proposed method captures the data for each loading direction very well. Similar to the previous section, isotropic hardening is not able to give an adequate fit to the yield stresses in any direction except for the direction that the hardening was based upon, i.e., tension in the rolling direction of the sheet.

Strain paths in AZ31B magnesium which deform by significant amounts of $\{10\bar{1}2\}$ $<10\bar{1}1>$ tensile twinning, i.e., in plane compression and thru-thickness tension, initially yield at lower stresses than strain paths that do not involve tensile twinning. However, the material hardens at a much faster rate for these strain paths than for strain

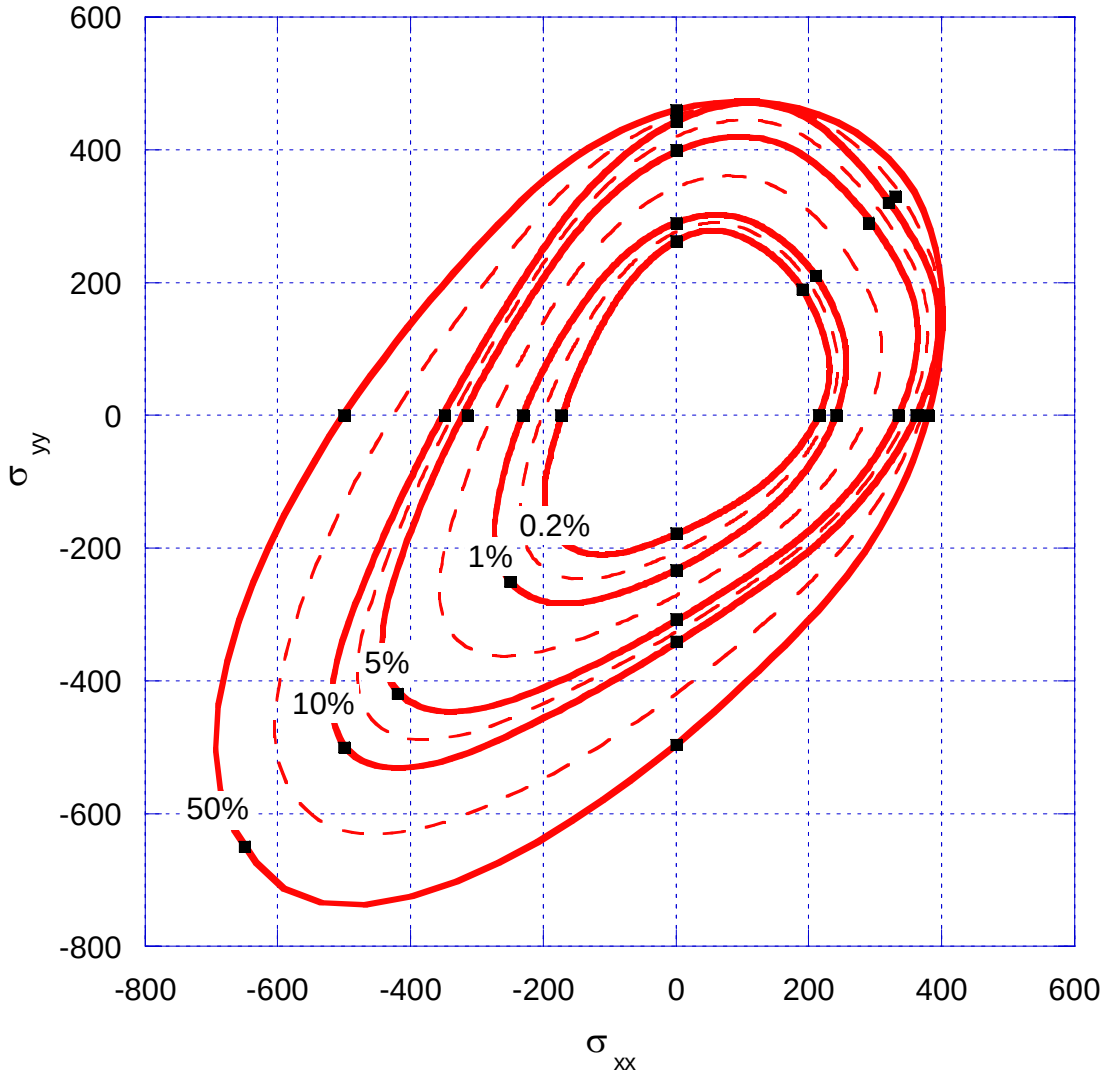

Figure 4.19 Comparison between the plane stress yield loci ($\sigma_{xy} = 0$) for a AZ31B magnesium cold rolled sheet predicted by the proposed theory (solid lines) and yield strengths calculated using the vpsc polycrystal model (symbols). (Stresses in Mpa)

Table 4.6 AZ31B coefficients corresponding to the yield surface evolution depicted in Figure 4.19

	a	k	L_{12}	L_{13}	L_{22}	L_{23}	L_{33}	L_{44}	L_{55}	L_{66}
0.2%	2	0.2941	0.1724	-0.0701	1.0503	0.0552	0.7723	0.7547	1.2899	1.0641
1%	2	0.2290	0.0091	-0.1160	1.1598	0.0585	1.2048	1.6770	2.1879	1.2230
5%	2	0.3575	-0.0014	0.0342	1.1384	0.1493	1.2361	1.9628	2.2370	1.5302
10%	2	0.4097	-0.0551	0.0177	1.1270	0.1506	1.2578	1.9373	2.0409	1.5667
50%	2	0.2995	-0.2387	0.4351	1.2409	0.6143	2.2740	2.2647	2.6521	1.6595

paths that primarily involve slip such as in plane tension. Therefore, if an isotropic hardening model utilizing the initial yield loci for AZ31B magnesium were used to simulate the deformation of a bending beam, one would expect to see an increased amount of compressive deformation along the axis of the beam compared to the proposed model which can account for the increased hardening rates.

Finite element simulations were performed in ABAQUS for a three-dimensional beam made from a cold rolled sheet of AZ31B magnesium subjected to a four-point bending test. This beam was initially 100mm long with a square cross-section of 3mm, however only half of the beam's length was modeled due to symmetry, and 1872 linear brick elements were used to simulate the beam. The beam's axis was assumed to be aligned with the sheet's x-axis (rolling direction). Free-surface boundary conditions were imposed for the beam except at the points of the pins. The upper pins were located at ±6mm and the lower pins were located at ±12mm from the center of the beam. The beam bends as the upper pins were displaced down by a magnitude of 8mm.

As expected, the proposed model predicted much higher compressive axial stresses and lower compressive axial strains than the isotropic hardening model. The proposed model also predicts a further shift in the neutral axis of the beam in order to balance the tensile and compressive stresses. In Figure 4.21 the axial stresses are plotted as a function of beam height for a path along the center of the beam's center cross-section. Although no experimental data exists for specimens made from AZ31B to validate the proposed model for AZ31B, the uniaxial and beam bending simulations clearly demonstrate the ability of the proposed model to capture the anisotropic hardening behavior of such a material, while an isotropic hardening assumption could not.

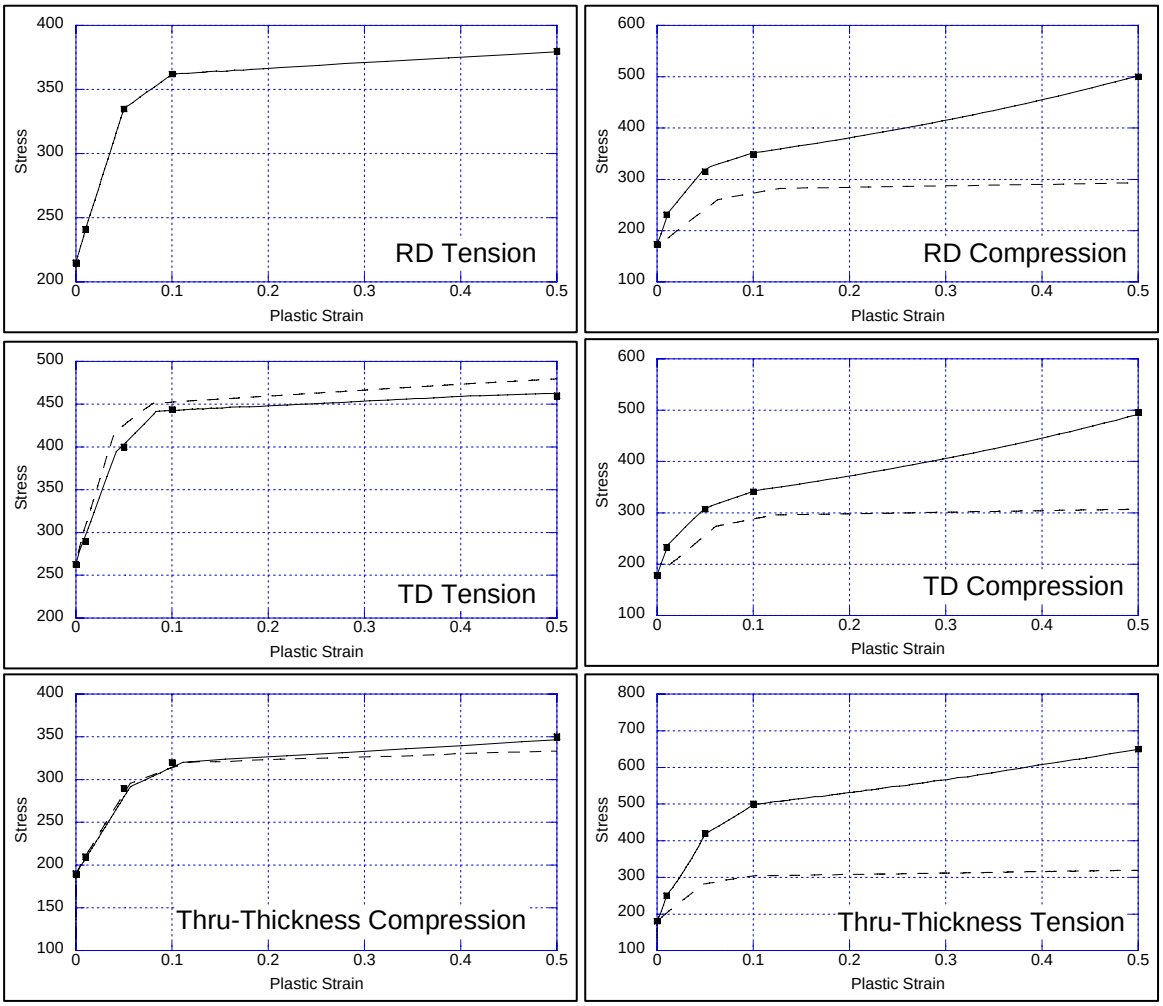

Figure 4.20 Comparison between calculated data using a VPSC model (symbols) and simulation results using the proposed hardening law (solid lines) and using isotropic hardening (dashed lines) for a cold rolled sheet of AZ31B magnesium.

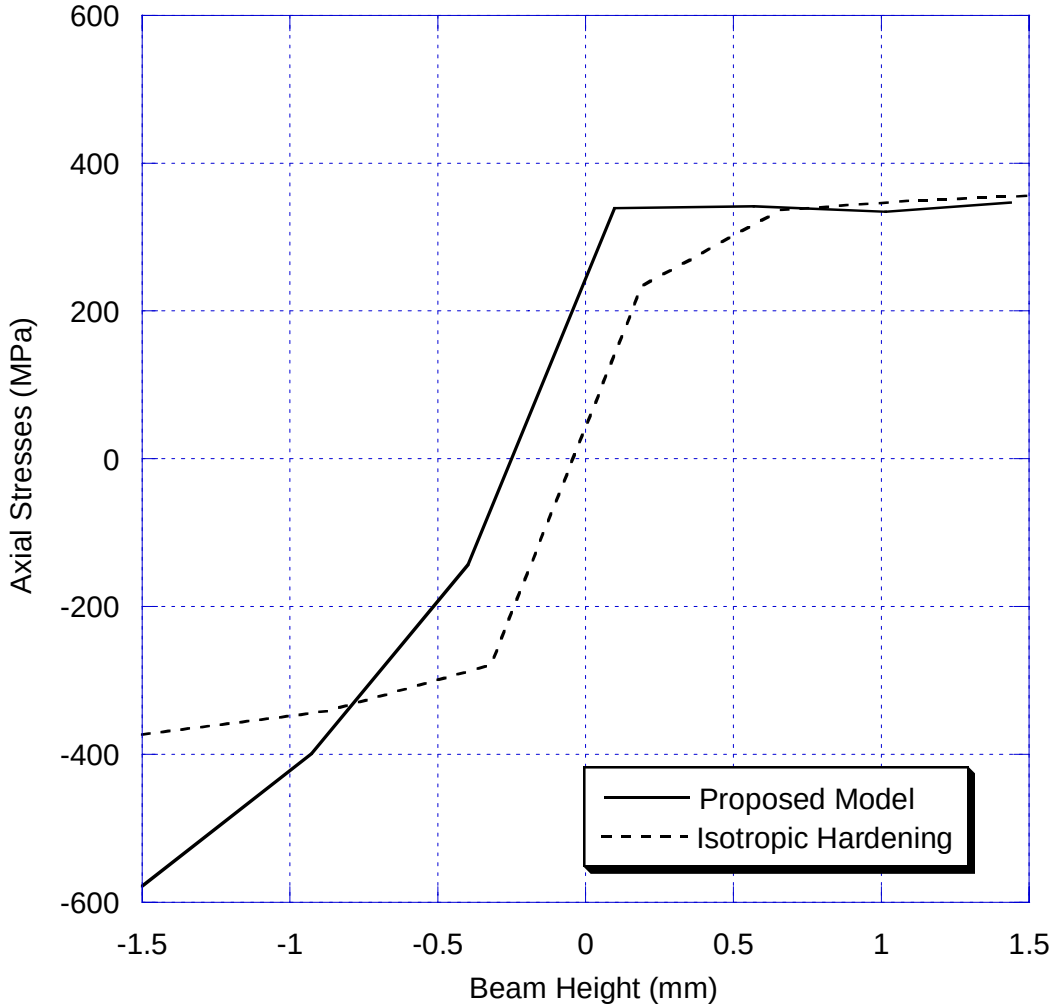

Figure 4.21 Axial stress distribution along the beam's center cross-sections.

CHAPTER 5
INCORPORATING THE EFFECTS OF STRAIN-RATE AND TEMPERATURE

5.1 Introduction

Thus far, we have considered only the quasi-static deformation of metals for which an appropriate modeling framework is that of the plasticity theory. Experimental evidence suggests that the plastic deformation of metals depends on the applied strain rate and is also sensitive to temperature (Kaschner et al., 2000, Maudlin et al., 1999a and 1999b, Perzyna, 1966).

The main goal of this chapter is to develop a model capable of describing the dynamic and temperature dependent anisotropic plastic response of hcp textured metals. We begin with a presentation of Perzyna's approach (Perzyna, 1966) and the consistency approach (Wang et al., 1997) which are the two most widely used methods for extending rate-independent elasto-plastic models such as to include the effect of strain rate. Both approaches are used in the current work to incorporate strain rate effects in the anisotropic elasto-plastic models developed for hcp metals (see Chapter 4). Next, the algorithmic aspects related to the finite element implementation of the rate dependent anisotropic formulations developed will be presented along with the stress-strain response for various loading paths and strain rate conditions. Validation of the proposed anisotropic rate dependent formulations is provided by comparing simulation results to Taylor impact data on pure zirconium (data after Maudlin et al., 1999b) and on a tantalum alloy (data after Maudlin et al., 1999a). The very good agreement between the simulated and experimental post-test geometries in terms of major and minor side profiles

and impact-interface footprints shows the ability of the proposed model to describe the texture evolution due to deformation twinning.

5.2 Elasto-Viscoplastic Theory

5.2.1 Perzyna's Viscoplastic Approach

Perzyna's approach (Perzyna, 1966) is the most widely used method for introducing strain rate effects into elasto-plastic models. The basic assumption is that the viscous properties of materials become manifest only after the passage to the plastic state. Thus, the strain rate $\dot{\boldsymbol{\varepsilon}}$ can be decomposed additively into an elastic $\dot{\boldsymbol{\varepsilon}}_E$ and an inelastic $\dot{\boldsymbol{\varepsilon}}_{VP}$ part.

$$\dot{\boldsymbol{\varepsilon}} = \dot{\boldsymbol{\varepsilon}}_E + \dot{\boldsymbol{\varepsilon}}_{VP} \tag{5.1}$$

The inelastic portion of the strain rate represents combined viscous and plastic effects, therefore it is called viscoplastic.

The evolution of the viscoplastic strain rate is defined as (Perzyna, 1966)

$$\dot{\boldsymbol{\varepsilon}}_{VP} = \gamma \left\langle \phi(f) \right\rangle \frac{\partial g}{\partial \boldsymbol{\sigma}} \tag{5.2}$$

with γ a viscosity parameter, ϕ a function that depends on the rate-independent yield function $f(\boldsymbol{\sigma},\kappa)$, κ being the internal variable, while $g(\boldsymbol{\sigma},\kappa)$ is the rate-independent plastic potential. In equation (5.2), $\langle\ \rangle$ are the McCauley brackets such that

$$\left\langle \phi(f) \right\rangle = \begin{cases} 0 & \text{for } f \le 0, \\ \phi(f) & \text{for } f > 0. \end{cases} \tag{5.3}$$

The function ϕ must fulfill the following conditions: (1) to be continuous and convex in $[0,\infty)$ and (2) $\varphi(0) = 0$. The following expressions are generally used for the function $\phi(f)$ (see Perzyna, 1966)

$$\phi(f) = f^n,\ n \geq 1,\ \text{or}\ \phi(f) = \exp(f) - 1 \tag{5.4}$$

Note that equation (5.2) involves the assumption that there is flow (i.e., $\dot{\varepsilon}_{VP} > 0$) only if the current state of stress is outside the yield surface, the rate of increase of the viscoplastic strain being a function of the excess stresses above the yield criterion. Because of this feature, this viscoplastic theory is commonly called overstress law.

5.2.2 Consistency Approach

An alternative approach to model strain rate effects on the inelastic deformation which was proposed recently by De Borst and co-workers (see Wang et al., 1997; Heeres et al., 2002). These authors introduced a rate-dependent yield surface and imposed that during viscoplastic flow the stress state remain on the rate-dependent yield surface. The rate-dependent yield function f_{rd} is expressed as (see Wang et al., 1997)

$$f_{rd} = f_{rd}(\boldsymbol{\sigma}, \kappa, \dot{\kappa}) = 0 \tag{5.5}$$

where κ and $\dot{\kappa}$ incorporates rate effects. As in elasto-plasticity, the viscoplastic strain evolves according to the flow rule

$$\dot{\varepsilon}_{vp} = \dot{\lambda} \frac{\partial f_{rd}}{\partial \boldsymbol{\sigma}} \tag{5.6}$$

with λ a positive scalar called viscoplastic multiplier or consistency parameter which can be estimated from the Kuhn-Tuckner conditions (5.7).

$$f_{rd} \leq 0, \quad \lambda \geq 0, \quad \lambda f_{rd} = 0 \tag{5.7}$$

Since the consistency is reinforced through the Kuhn-Tuckner conditions, this model is called the consistency viscoplastic model.

5.3 Energy Balance

The energy equation is a consequence of the first law of thermodynamics, and involves an additional quantity, the internal energy of the material. This equation can be used to relate the temperature rise to the mechanical work applied to the material. Within a dynamic deformation event (<< 1 second) the effect of heat flux through the material becomes negligible. Furthermore, for a solid body subjected to a plastic deformation, the effects of an internal heat source may not be relevant. Therefore, the energy equation reduces to the following form (Malvern, 1969)

$$\rho \frac{\partial u}{\partial t} = \boldsymbol{\sigma} : \boldsymbol{D} \tag{5.8}$$

with ρ being the density of the material, u the internal energy, and $\boldsymbol{D}$ the rate of deformation tensor. From thermodynamics, the internal energy is given by

$$\Delta u = c_p \Delta T \tag{5.9}$$

where c_p is the specific heat of the material, and ΔT is the temperature change. Combining equations (5.8)-(5.9) and writing the equations in incremental form yields a relationship from which a rise in temperature is related to the current value of stress and the strain increment.

$$\Delta T = \frac{\boldsymbol{\sigma} : \Delta \boldsymbol{\varepsilon}}{\rho c_p} \tag{5.10}$$

5.4 Proposed Anisotropic Elastic/Viscoplastic Theory

5.4.1 Using the Perzyna Method

Our goal is to develop a macroscopic anisotropic elasto-viscoplastic model that can describe simultaneously the influence of strain rate and temperature along with the evolving texture on the inelastic response of hexagonal metals.

To this end, we use Perzyna's overstress approach to incorporate strain rate and temperature effects in the rate-independent elastic/plastic model developed for hcp materials (see Chapter 4). The yield function in this rate-independent formulation is given by

$$f(\boldsymbol{\sigma},\bar{\varepsilon}_{vp},T)=\frac{\tilde{\sigma}\left(\boldsymbol{\sigma},\bar{\varepsilon}_{vp}\right)}{Y\left(\bar{\varepsilon}_{vp},T\right)}-1 \tag{5.11}$$

where $\bar{\varepsilon}_{vp}$ is the effective viscoplastic strain which will be used as the hardening parameter. When using the interpolation method described in section 4.5,

$$\tilde{\sigma}(\boldsymbol{\sigma},\bar{\varepsilon}_{vp})=\xi(\bar{\varepsilon}_{vp})\tilde{\sigma}^{j}+(1-\xi(\bar{\varepsilon}_{vp}))\tilde{\sigma}^{j+1} \tag{5.12}$$

$$\xi\left(\bar{\varepsilon}_{vp}\right)=\frac{\bar{\varepsilon}_{vp}^{j+1}-\bar{\varepsilon}_{vp}}{\bar{\varepsilon}_{vp}^{j+1}-\bar{\varepsilon}_{vp}^{j}} \tag{5.13}$$

and,

$$\tilde{\sigma}^{j}\left(\boldsymbol{\sigma},\boldsymbol{L}(\bar{\varepsilon}_{vp}^{j}),k(\bar{\varepsilon}_{vp}^{j}),a(\bar{\varepsilon}_{vp}^{j})\right)=B\left[\left(\left|\Sigma_1\right|-k\Sigma_1\right)^{a}+\left(\left|\Sigma_2\right|-k\Sigma_2\right)^{a}+\left(\left|\Sigma_3\right|-k\Sigma_3\right)^{a}\right]^{\frac{1}{a}} \tag{5.14}$$

for $\bar{\varepsilon}_p^1<\bar{\varepsilon}_p^2<\ldots\bar{\varepsilon}_{vp}^{j}<\bar{\varepsilon}_{vp}^{j+1}\ldots<\bar{\varepsilon}_p^m$ with $\boldsymbol{\Sigma}=\mathbf{L}:\mathbf{S}$, $\mathbf{L}$ being a fourth-order orthotropic tensor which reflects the plastic anisotropy of the material, $\mathbf{S}$ the deviator of the Cauchy stress tensor, k is the strength differential parameter, B (see equation 4.8) is the constant which allows the yield criterion to reduce to the uniaxial loading direction hardening is based upon, and a is a homogeneity constant. $Y\left(\bar{\varepsilon}_{vp},T\right)$ is the rate independent hardening law that depends on the hardening variable, $\bar{\varepsilon}_{vp}$, and with the temperature, T. The rate independent plastic potential is assumed to coincide with the yield function, i.e.,

$g(\boldsymbol{\sigma},\kappa)=\tilde{\sigma}(\boldsymbol{\sigma},\kappa)$. We take $\phi(f)=f^m$, where m is a constant. Thus, the viscoplastic law (5.2) specifies to

$$\dot{\boldsymbol{\varepsilon}}_{vp}=\gamma\left\langle\left(\frac{\tilde{\sigma}\left(\boldsymbol{\sigma},\bar{\varepsilon}_{vp}\right)}{Y\left(\bar{\varepsilon}_{vp},T\right)}-1\right)^m\right\rangle\frac{\partial\tilde{\sigma}}{\partial\boldsymbol{\sigma}} \tag{5.15}$$

with γ a viscosity parameter and m a constant.

In displacement-based FE formulations, stress updates take place at the Gauss points for a prescribed nodal displacement. We start from time t, with the known converged state $\left[\boldsymbol{\varepsilon}^t,\boldsymbol{\varepsilon}_{vp}^t,\boldsymbol{\sigma}^t,\bar{\varepsilon}_{vp}^t,T^t\right]$ and calculate the corresponding values at time $t+\Delta t$: $\left[\boldsymbol{\varepsilon}^{t+\Delta t},\boldsymbol{\varepsilon}_{vp}^{t+\Delta t},\boldsymbol{\sigma}^{t+\Delta t},\bar{\varepsilon}_{vp}^{t+\Delta t},T^{t+\Delta t}\right]$. In this incremental process, the total strain increment $\Delta\boldsymbol{\varepsilon}$ is decomposed into an elastic $\Delta\boldsymbol{\varepsilon}_E$ part and a viscoplastic part $\Delta\boldsymbol{\varepsilon}_{vp}$ according to

$$\Delta\boldsymbol{\varepsilon}=\Delta\boldsymbol{\varepsilon}_E+\Delta\boldsymbol{\varepsilon}_{vp} \tag{5.16}$$

The stress increment is related to the elastic strain by Hooke's law

$$\Delta\boldsymbol{\sigma}=\boldsymbol{C}\Delta\boldsymbol{\varepsilon}_E=\boldsymbol{C}\left(\Delta\boldsymbol{\varepsilon}-\Delta\boldsymbol{\varepsilon}_{vp}\right) \tag{5.17}$$

where $\boldsymbol{C}$ is the fourth-order stiffness tensor. Next, a trial elastic stress: $\boldsymbol{\sigma}_{trial}^{t+\Delta t}=\boldsymbol{\sigma}^t+\boldsymbol{C}\Delta\boldsymbol{\varepsilon}$ is calculated. If $f(\boldsymbol{\sigma}_{trial}^{t+\Delta t},\bar{\varepsilon}_{vp})\le 0$ then $\boldsymbol{\sigma}^{t+\Delta t}=\boldsymbol{\sigma}_{trial}^{t+\Delta t}$, however, if $f(\boldsymbol{\sigma}_{trial}^{t+\Delta t},\bar{\varepsilon}_{vp})>0$ there is viscoplastic flow, and the viscoplastic strain increment $\Delta\boldsymbol{\varepsilon}_{vp}$ must be determined (see Simo and Hughes, 1998). The viscoplastic strain increment vector can be separated into a scalar $\Delta\chi$ (which is equal to an increment of effective viscoplastic strain), and direction given by the gradient of the plastic potential. Thus, we need to determine $\Delta\chi$ to update both the viscoplastic strain increment and the hardening parameter, $\bar{\varepsilon}_{vp}$.

$$\varepsilon_{vp}^{t+\Delta t} = \varepsilon_{vp}^{t} + \Delta\varepsilon_{vp} = \varepsilon_{vp}^{t} + \Delta\chi\left[\frac{\partial\tilde{\sigma}}{\partial\sigma}\right]^{t+\Delta t} \tag{5.18}$$

$$\bar{\varepsilon}_{vp}^{t+\Delta t} = \bar{\varepsilon}_{vp}^{t} + \Delta\chi \tag{5.19}$$

Therefore, combining equations (5.18) and (5.15) and assuming $\dot{\varepsilon} = \Delta\varepsilon/\Delta t$ yields

$$\Delta\varepsilon_{vp} = \gamma\left\langle\phi^{t+\Delta t}\right\rangle\Delta t\left[\frac{\partial f}{\partial\sigma}\right]^{t+\Delta t} = \Delta\chi\left[\frac{\partial f}{\partial\sigma}\right]^{t+\Delta t} \tag{5.20}$$

From (5.20), the viscoplastic multiplier $\Delta\chi$ may be determined by requiring the residual (see equation 5.21) to approach zero during a local iterative procedure.

$$r = \phi^{t+\Delta t} - \frac{\Delta\chi}{\gamma\Delta t} = 0 \tag{5.21}$$

Currently, the values of $\phi_{t+\Delta t}$ and $\Delta\chi$ are unknown, but may be determined through a limited Taylor series expansion of the residual about the previous step of the local iterative procedure (i.e., step *n*).

$$r_{n+1}^{t+\Delta t} \approx r_{n}^{t+\Delta t} + \left[\frac{\partial r}{\partial\Delta\chi}\right]_{n}^{t+\Delta t}\delta\chi_{n+1} + \left[\frac{\partial r}{\partial\boldsymbol{\sigma}}\right]_{n}^{t+\Delta t}\delta\boldsymbol{\sigma}_{n+1} + \left[\frac{\partial r}{\partial T}\right]_{n}^{t+\Delta t}\delta T_{n+1} \approx 0 \tag{5.22}$$

where *n* is a counter for the local iteration (*n*=0 denotes the trial elastic state), and all derivatives in equation (5.22) are evaluated at step *n*. In equation (5.22), δ denotes the variation of the variable between increments *n*+1 and *n*, i.e., $\Delta\chi_{n+1} = \Delta\chi_n + \delta\chi_{n+1}$, $\Delta\sigma_{n+1} = \Delta\sigma_n + \delta\sigma_{n+1}$, and $\Delta T_{n+1} = \Delta T_n + \delta T_{n+1}$.

The stress update for the trial state (*n*=0) is found by assuming that the total strain increment was elastic, however, the stress update for subsequent steps (*n*>0) are determined by considering the effect of the viscoplastic strain on the state of stress.

$$\Delta\sigma_{n+1} = \Delta\sigma_n + \delta\sigma_{n+1} = \Delta\sigma_n - C\delta\chi_{n+1}\left[\frac{\partial\tilde{\sigma}}{\partial\sigma}\right]_{n+1} \qquad \text{for } n>0 \tag{5.23}$$

The gradient of the stress potential based upon the unknown updated state (iteration n+1) may be approximated by a limited Taylor series expansion about the current state using the variation of $\Delta\chi$ during the iteration n (see equation 5.24).

$$\left[\frac{\partial\tilde{\sigma}}{\partial\sigma}\right]_{n+1} \approx \left[\frac{\partial\tilde{\sigma}}{\partial\sigma}\right]_n + \Theta\left\{\left[\frac{\partial^2\tilde{\sigma}}{\partial\sigma^2}\right]_n \delta\sigma + \left[\frac{\partial^2\tilde{\sigma}^n}{\partial\bar{\varepsilon}_{vp}\partial\sigma}\right]_n \delta\chi_n\right\} \tag{5.24}$$

In equation (5.24), Θ ($0 \le \Theta \le 1$) is an interpolation parameter. For $\Theta = 0$, the gradient is determined solely from the current state, thus approximating the direction of the updated viscoplastic strain increment from the current yield surface. Combining equations (5.23) and (5.24) yields

$$\delta\sigma_{n+1} \approx -\left[C^{-1} + \Theta\delta\chi_n \frac{\partial^2\tilde{\sigma}}{\partial\sigma^2}\right]^{-1}\left[\delta\chi_{n+1}\frac{\partial\tilde{\sigma}}{\partial\sigma} + \Theta\delta\chi_{n+1}\delta\chi_n \frac{\partial^2\tilde{\sigma}}{\partial\bar{\varepsilon}_{vp}\partial\sigma}\right] \tag{5.25}$$

Plugging (5.25) into (5.22) yields an expression from which the increment of effective viscoplastic strain may be found.

$$\delta\chi_{n+1} \approx \frac{r_n + \dfrac{\partial\phi}{\partial T}\Delta T}{\dfrac{\partial\phi}{\partial\sigma}H\left[\dfrac{\partial\tilde{\sigma}}{\partial\sigma} + \Theta\delta\chi_n \dfrac{\partial^2\tilde{\sigma}}{\partial\bar{\varepsilon}_{vp}\partial\sigma}\right] - \dfrac{\partial\phi}{\partial\bar{\varepsilon}_{vp}} + \dfrac{1}{\gamma\Delta t}} \tag{5.26}$$

where,

$$H = \left[C^{-1} + \Theta\delta\chi_n \frac{\partial^2\tilde{\sigma}}{\partial\sigma^2}\right]^{-1} \tag{5.27}$$

$$\frac{\partial\phi}{\partial\sigma} = m\left(\frac{\tilde{\sigma}}{Y} - 1\right)^{m-1}\frac{1}{Y}\frac{\partial\tilde{\sigma}}{\partial\sigma} \tag{5.28}$$

$$\frac{\partial \phi}{\partial \bar{\varepsilon}_{vp}} = m\left(\frac{\tilde{\sigma}}{Y} - 1\right)^{m-1}\left(\frac{1}{Y}\frac{\partial \tilde{\sigma}}{\partial \bar{\varepsilon}_{vp}} - \frac{\tilde{\sigma}}{Y^2}\frac{\partial Y}{\partial \bar{\varepsilon}_{vp}}\right) \tag{5.29}$$

$$\frac{\partial \phi}{\partial T} = -m\left(\frac{\tilde{\sigma}}{Y} - 1\right)^{m-1}\frac{\tilde{\sigma}}{Y^2}\frac{\partial Y}{\partial T} \tag{5.30}$$

and all derivatives are evaluated at the previous iteration (iteration *n*). The state of stress and strain are updated through equation (5.26) until the residual (5.21) meets a specified tolerance for convergence.

5.4.2 Using the Consistency Method

The consistency method (Wang et al., 1997) enforces the stress state for a viscoplastic loading to lie on the yield surface similar to rate-independent plasticity. Using the proposed anisotropic hardening law, the onset of viscoplastic behavior is governed by a scalar rate and temperature dependant yield condition of the form

$$f_{rd} \equiv \tilde{\sigma}(\boldsymbol{\sigma}, \bar{\varepsilon}_{vp}) - Y(\bar{\varepsilon}_{vp}, \dot{\bar{\varepsilon}}_{vp}, T) = 0 \tag{5.31}$$

where $\tilde{\sigma}$ is the effective stress which depends on the state of stress and the effective viscoplastic strain (see equations 5.12 – 5.14), Y is the hardening relationship based on a given loading direction such as uniaxial tension and is a function of the effective viscoplastic strain, viscoplastic strain rate, and temperature. Here the effective viscoplastic strain is equal to the viscoplastic multiplier or consistency parameter λ defined by the flow rule (5.6). For quasi-static conditions ($\dot{\varepsilon} << 1$), the proposed viscoplastic model (equation 5.31) reduces to the rate-independent model proposed in Chapter 4.

Like the Perzyna method, if the trial stress state ($\boldsymbol{\sigma}_{trial}^{t+\Delta t} = \boldsymbol{\sigma}^t + \boldsymbol{C}\Delta\boldsymbol{\varepsilon}$) lies outside of the yield surface viscoplastic flow occurs. At difference with the Perzyna method

consistency must be restored using the present method, thus the viscoplastic strain increment must be determined such that the state of stress is returned to the yield surface.

The effective viscoplastic strain increment (which is equal to the viscoplastic multiplier $\Delta\lambda$ from the flow rule (5.6)) needed to update the hardening, and from which the viscoplastic strain increment is determined, can be approximated through a limited Taylor series expansion of equation (5.31) about the current state (n=0 denotes the trial state)

$$\begin{aligned} & f_{rd}(\boldsymbol{\sigma}_{n+1}, \bar{\varepsilon}_{vp\,n+1}, \dot{\bar{\varepsilon}}_{vp\,n+1}, T) \approx \\ & f_{rd}(\boldsymbol{\sigma}_{n}, \bar{\varepsilon}_{vp\,n}, \dot{\bar{\varepsilon}}_{vp\,n}, T) + \frac{\partial f_{rd}}{\partial \boldsymbol{\sigma}} \delta\boldsymbol{\sigma}_{n+1} + \frac{\partial f_{rd}}{\partial \bar{\varepsilon}_{vp}} \delta\lambda_{n+1} + \frac{\partial f_{rd}}{\partial \dot{\bar{\varepsilon}}_{vp}} \delta\dot{\lambda}_{n+1} + \frac{\partial f_{rd}}{\partial T} \delta T_{n+1} \approx 0 \end{aligned} \tag{5.32}$$

where δ denotes the variation of the variable between increments n+1 and n (i.e., $\Delta\lambda_{n+1} = \Delta\lambda_n + \delta\lambda_{n+1}$) and all derivatives are evaluated at the current state. After introducing the stress variation (see equation 5.25) and replacing $\delta\dot{\lambda}$ with $\delta\lambda/\Delta t$ equation (5.32) can be rearranged to give an expression for $\delta\lambda_{n+1}$

$$\delta\lambda_{n+1} = \frac{f(\boldsymbol{\sigma_n}, \bar{\varepsilon}_{vp\,n}, \dot{\bar{\varepsilon}}_{vp\,n}) - \dfrac{\partial Y}{\partial T}\delta T}{\dfrac{\partial \tilde{\sigma}}{\partial \boldsymbol{\sigma}} \boldsymbol{H} \left[\dfrac{\partial \tilde{\sigma}}{\partial \boldsymbol{\sigma}} + \Theta \delta\lambda^n \dfrac{\partial^2 \tilde{\sigma}}{\partial \bar{\varepsilon}_{vp} \partial \boldsymbol{\sigma}} \right] + \dfrac{\partial Y}{\partial \bar{\varepsilon}_{vp}} - \dfrac{\partial \tilde{\sigma}}{\partial \bar{\varepsilon}_{vp}} + \dfrac{1}{\Delta t} \dfrac{\partial Y}{\partial \dot{\bar{\varepsilon}}_{vp}}} \tag{5.33}$$

where,

$$H = \left[C^{-1} + \Theta \delta\lambda_n \frac{\partial^2 \tilde{\sigma}}{\partial \sigma^2} \right]^{-1} \tag{5.34}$$

The stresses are then updated by equation (5.23) and the effective viscoplastic strain is updated by equation (5.19). Iterations will continue until the yield criterion (5.26) has been satisfied to within a given tolerance.

5.5 Numerical Examples

5.5.1 Using the Perzyna Method

In this section, we test the finite element implementation by simulating the response of a single integration point subject to uniaxial loading conditions at constant deformation rate. To simplify calculations, the effects of anisotropy on the plastic response were neglected (i.e., in equation (5.14) the tensor $\boldsymbol{L}$ was set equal to the fourth-order identity tensor). The specific form of the law of variation of the strength differential coefficient k was chosen such that initially the value of uniaxial compressive yield stress is less than the tensile uniaxial yield stress, but the yield in uniaxial tension and compression become equal at the critical level of effective viscoplastic strain, $\bar{\varepsilon}_{vp}^{critical}$, i.e.,

$$k\left(\bar{\varepsilon}_{vp}\right)=\begin{cases} A-B\bar{\varepsilon}_{vp}, & \text{for} \quad 0\le\bar{\varepsilon}_{vp}\le\bar{\varepsilon}_{vp}^{\,critical} \\ 0 & \text{for } \bar{\varepsilon}_{vp}>\bar{\varepsilon}_{vp}^{\,critical}. \end{cases} \tag{5.35}$$

with A, B being constants. The rate-independent constitutive hardening law was considered to be of the form

$$Y(\bar{\varepsilon}_{vp})=E(D+\bar{\varepsilon}_{vp})^{F} \tag{5.36}$$

with E, D, and F are constants. The numerical values for the parameters involved in the model are given in Table 5.1.

Table 5.1 Parameters used for numerical simulation

A	B	$\bar{\varepsilon}_{vp}^{critical}$	E (Mpa)	D	F	γ (s^{-1})	m	a	E (Young's Modulus) (Gpa)
0.4	8	0.05	650	0.0463	0.227	2000	2	2	100

Figure 5.1 depicts the simulated stress-viscoplastic strain response corresponding to uniaxial tension for both loading and unloading at the constant deformation rates $\dot{\varepsilon}_{11} = 0.001s^{-1}$, $10s^{-1}$, and $100s^{-1}$, respectively. The simulations were carried out for a total strain increment of $\Delta\varepsilon_{11} = 1x10^{-5}$ and a time step of $\Delta t = 1x10^{-2}s$, $\Delta t = 1x10^{-6}s$, and $\Delta t = 1x10^{-7}s$, respectively. The iterative procedure was considered to be converged if the square of the residual (5.21) becomes less or equal than 10^{-6}.

According to the Perzyna method, the viscoplastic strain rate is determined by the overstress, i.e., the stress state outside of the static yield surface. At the onset of viscoplastic flow, the state of stress lies on the static yield surface. For a viscoplastic deformation involving very high strain rates, the stress moves away from the static yield surface to account for the high rates of strain. As the stress moves away from the surface, the viscoplastic strain rate increases from zero to the final value depending on the constitute law. Consequently, during unloading, viscoplastic strains continue to accumulate until the state of stress decreases below the static yield surface when the viscoplastic strain rate finally decreases back to zero. During reloading at the same applied total strain rate, viscoplastic strains begin accumulating once the stress exceedes the static yield stress (see Figure 5.1).

Figure 5.2 shows the simulation results for uniaxial compression under constant axial deformation rate of $\dot{\varepsilon}_{11} = 0.001s^{-1}$, $10s^{-1}$, and $100s^{-1}$, respectively. Since the hardening relationship is based on the uniaxial stress-strain curve in tension and the material displays yielding asymmetry between tension and compression, the stress-strain response curves for uniaxial compression depend on the law of variation of *k*. Simulations were carried out using the law of variation for *k* given by equation (5.35) as

well as for k held constant at k = 0 (saturation value) and k = 0.4 (initial value), respectively. Note that k = constant corresponds to isotropic hardening. As expected, for the case when k varying according to (5.35) the material first yields at the same as the same stress level as in the case when k is held constant at 0.4, but then hardens at a much higher rate until $\bar{\varepsilon}_{vp} = \bar{\varepsilon}_{vp}^{critical}$ when k becomes 0, and the yield stress in tension and compression become equal.

Next, we have studied the effect of the strain rate and the size of the strain increment on the accuracy of the numerical results using the Perzyna method. For this purpose, simulations were conducted using various strain rates and strain increments for uniaxial tension to 5% viscoplastic strain. The results were compared to the one-dimensional (1-D) theoretical solution according to equation (5.15) by assuming uniaxial tension about the x-direction.

$$\sigma_x\left(\varepsilon_{vp\,x}, \dot{\varepsilon}_{vp\,x}\right) = \left[\left(\frac{\dot{\varepsilon}_{vp\,x}}{\gamma}\right)^{\frac{1}{m}} + 1\right] Y_0\left(\varepsilon_{vp\,x}\right) \tag{5.37}$$

For a very small strain rate (the ratio of the strain increment and the time increment) (i.e., 0.001s^{-1}) the terms used in the residual (5.15) become very small in magnitude, thus a given tolerance can be satisfied with a larger percent error than for larger strain rates which result in larger residual terms. Furthermore, a very small change in the viscoplastic strain can lead to large changes in the stress, thus the accuracy of the Perzyna method is sensitive to the strain rate as well as the size of the strain increment as indicated by Figure 5.3. In Figure 5.3, percent error refers to the comparison between the theoretical and numerical stress predictions after 5% accumulated viscoplastic strains, i.e., $\%error = \left(\sigma_{numerical} - \sigma_{theoretical}\right) / \sigma_{theoretical}$.

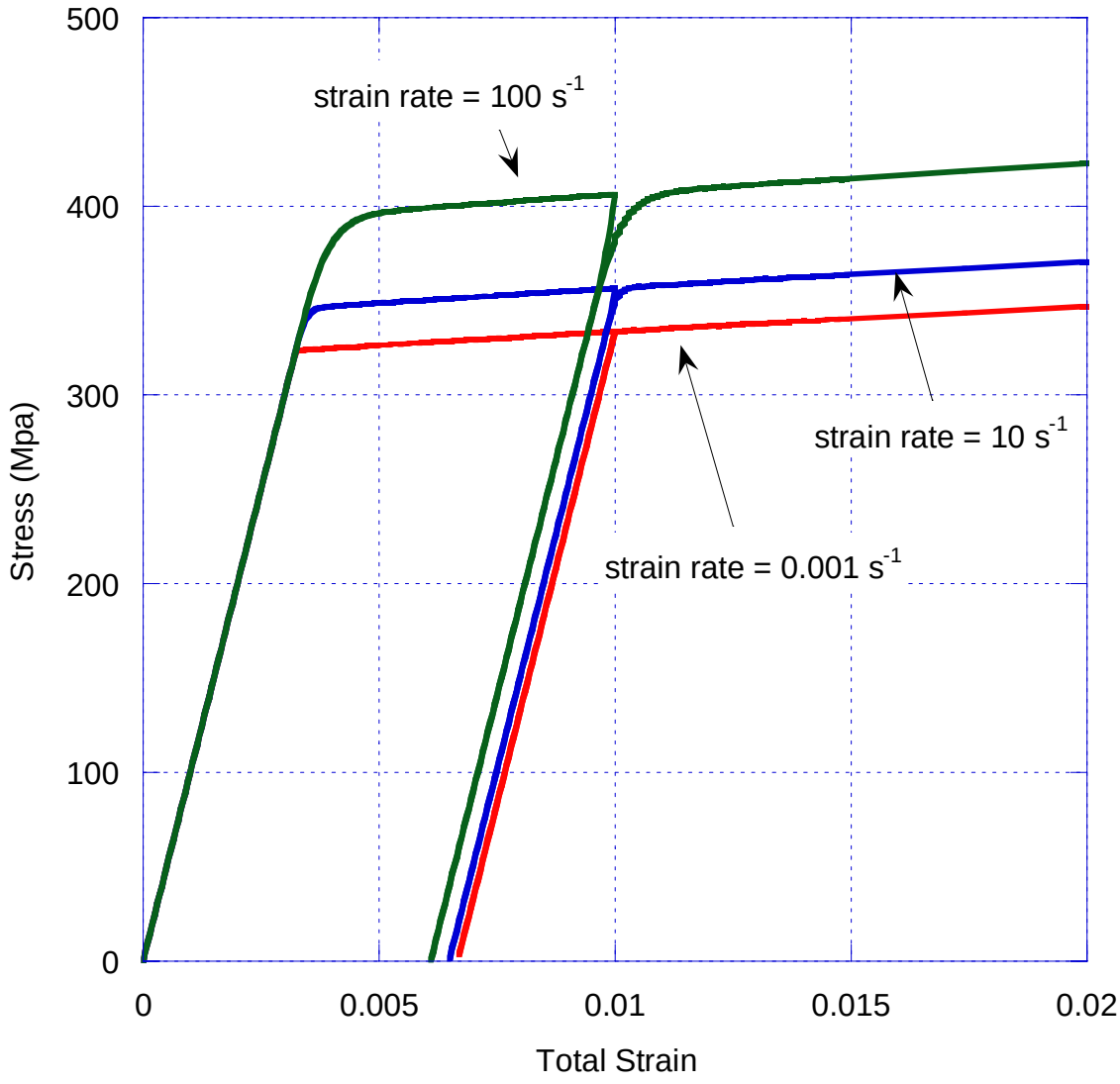

Figure 5.1 Simulation results using the Perzyna method for various strain rates corresponding to uniaxial tension for loading and unloading conditions.

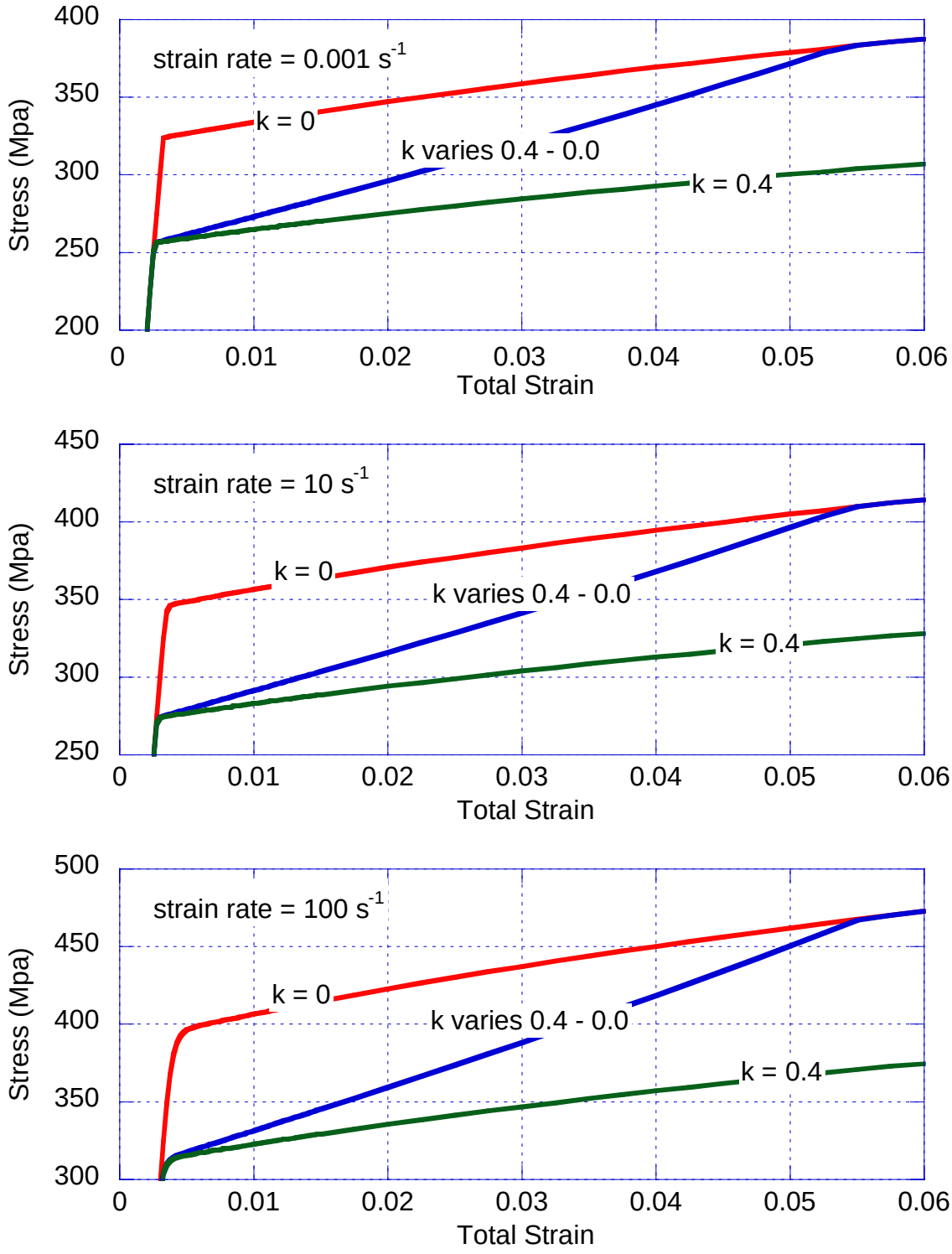

Figure 5.2 Simulation results using the Perzyna method for various strain rates corresponding to uniaxial compression for different variations of the strength differential coefficient k.

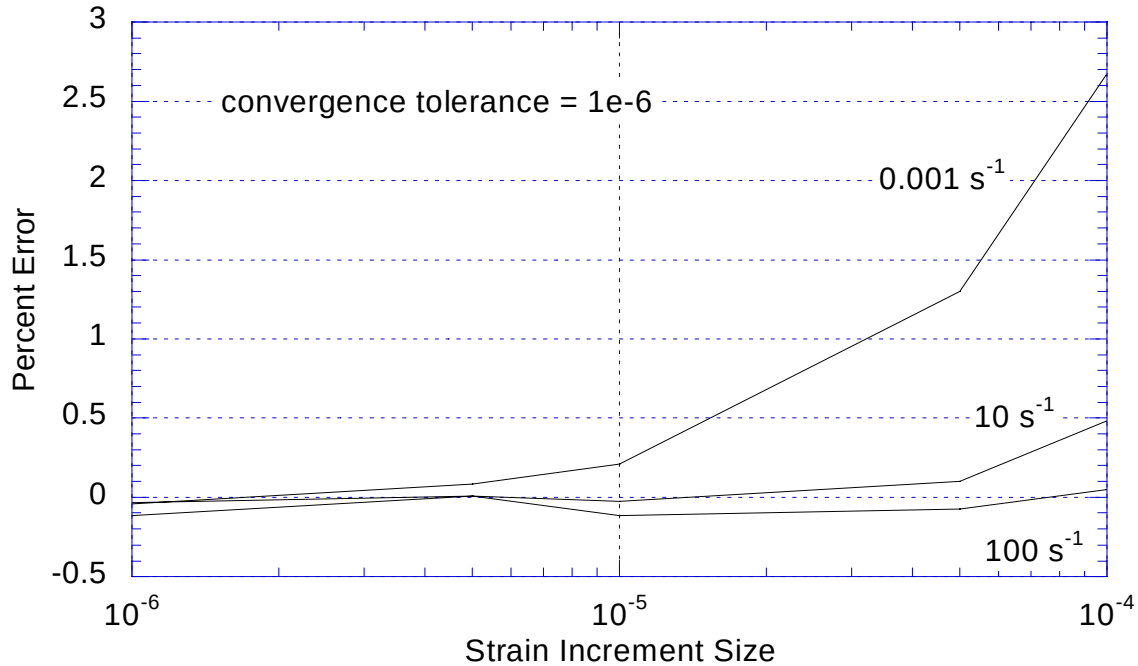

Figure 5.3 Effect of strain rate and the size of the strain increment on the accuracy of the Perzyna Method at 5% levels of viscoplastic strain.

The state of stress and strain within a given increment will be accepted as the current state once the square of the residual becomes less than a specified convergence tolerance. Therefore, the accuracy of the Perzyna method is also dependent on the tolerance for convergence since, as previously mentioned, a small change of the viscoplastic strain leads to a large change in stress. This is illustrated in Figure 5.4 for different strain increment sizes at a strain rate of $0.001s^{-1}$ for simulations conducted to 5% viscoplastic strain.

Choosing an appropriate strain increment size and convergence tolerance is a trade-off between accuracy and computational efficiency. A strain increment of $\Delta\varepsilon_{11} = 1x10^{-5}$ with a convergence tolerance of $1x10^{-6}$ was chosen for numerical simulation because this combination produced an acceptable level of accuracy for each level of strain rate while not being overly computationally expensive.

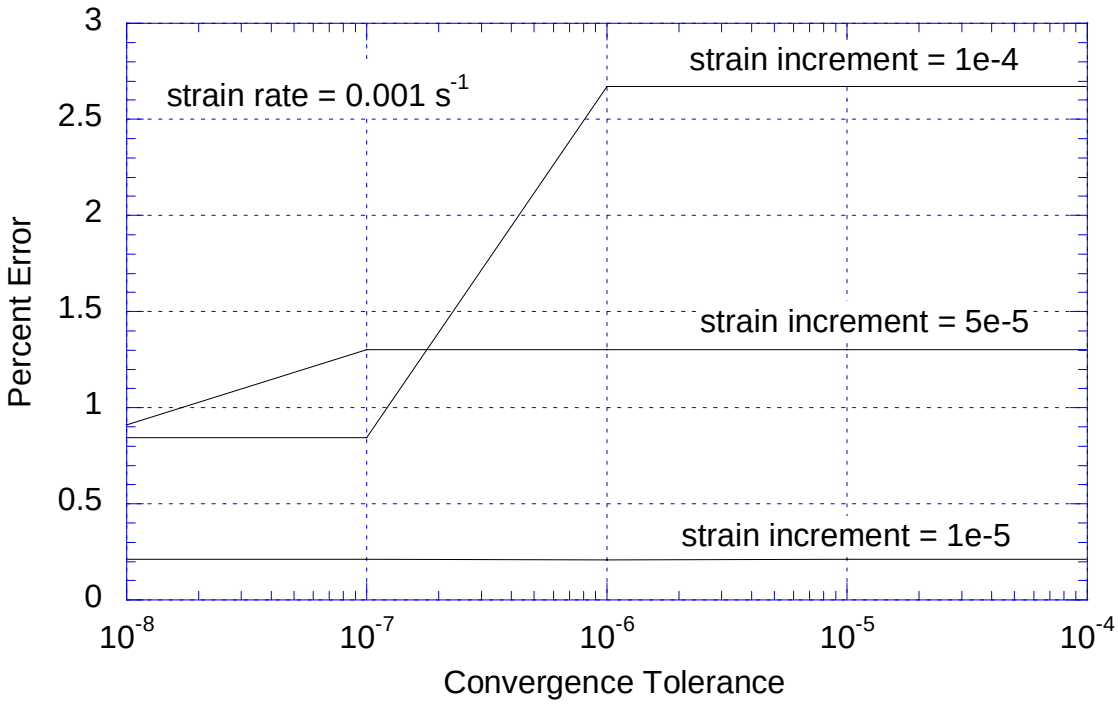

Figure 5.4 Effect of convergence tolerance and the size of the strain increment on the accuracy of the Perzyna method at 5% levels of viscoplastic strain.

5.5.2 Using the Consistency Method

At first sight, the consistency model and Perzyna's model appear to be quite different. Recently, Heeres et al. (2002) compared both approaches by assessing the evolution of the viscoplastic multiplier and the evolution of the internal variable for different loading/unloading conditions. It was shown that for progressive viscoplastic loading, the stress-strain response according to Perzyna's overstress theory and the consistency theory are identical. However, for unloading, due to the assumption that the authors made regarding the viscoplastic strain rate the two theories give different responses. The assumption made by Heeres et al. (2002) was that the viscoplastic strain rate could only monotonically increase, so that upon unloading the viscoplastic strain rate would not decrease to zero. Thus, the yield point was fixed according to $Y(\lambda, \dot{\lambda}^{ultimate})$.

Therefore, the material would transition to a purely elastic state immediately upon the onset of unloading. Furthermore, upon reloading, the material would remain elastic until the fixed yield point was reached. This differs from the Perzyna method as described in the last section. Figure 5.5 shows the results of uniaxial loading and unloading simulations carried out using the consistency method with the Heeres et al. (2002) assumption and the same material parameters used for the Perzyna method. In order to compare the two methods a rate dependent hardening relationship based on uniaxial tension about the materials x-direction equivalent to equation 5.37 was used to define $Y(\lambda,\dot{\lambda})$ (see equation 5.31). Figure 5.6 shows a comparison between the two methods in a blown up view of the region in which they differ.

When the consistency method was first introduced (see Wang et al., 1997), the assumption that the viscoplastic strain rate can only monotonically increase was not stipulated. In fact, it was stated that at the viscoplastic strain rate was to be calculated during each time increment based upon the viscoplastic strain increment. This assumption is more physically reasonable since a non-zero viscoplastic strain rate can not be realized without a non-zero viscoplastic strain increment. When using the method described in Wang et al. (1997) to determine the viscoplastic strain rate without using the assumptions described by Heeres et al. (2002) to fix the viscoplastic strain rate upon unloading, the consistency method and the Perzyna method predict exactly the same results. In fact, using the same material parameters as before, uniaxial tensile simulations were carried out using the consistency method assuming that the viscoplastic strain rate was not fixed upon unloading. The results are presented in Figure 5.7 and are identical to

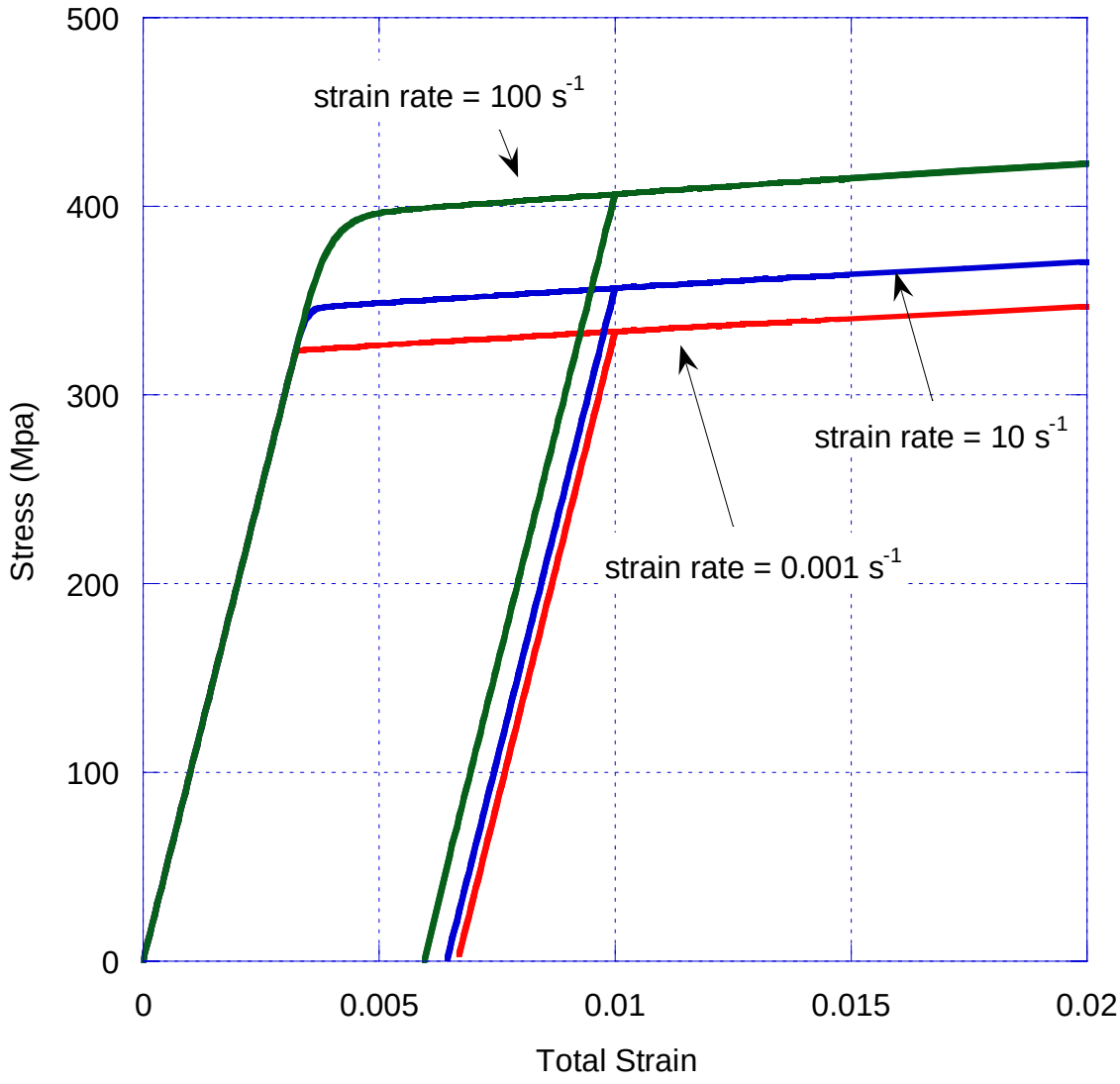

Figure 5.5 Simulation results using the consistency method using the assumptions from Heeres et al. (2002) for various strain rates corresponding to uniaxial tension for loading and unloading conditions.

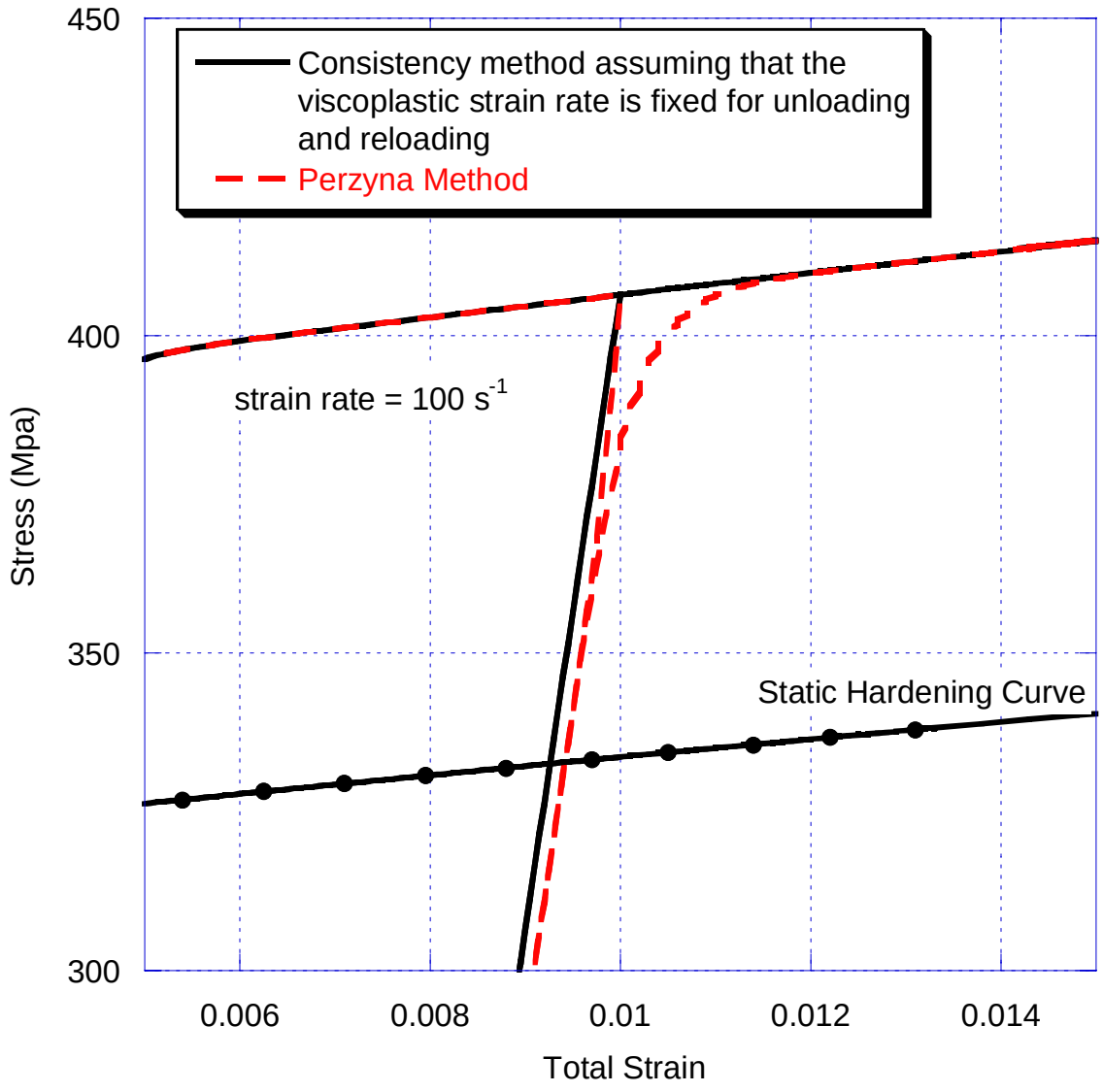

Figure 5.6 Comparison between the Perzyna method and consistency method using the assumptions from Heeres et al. (2002) corresponding to uniaxial tension for loading and unloading conditions.

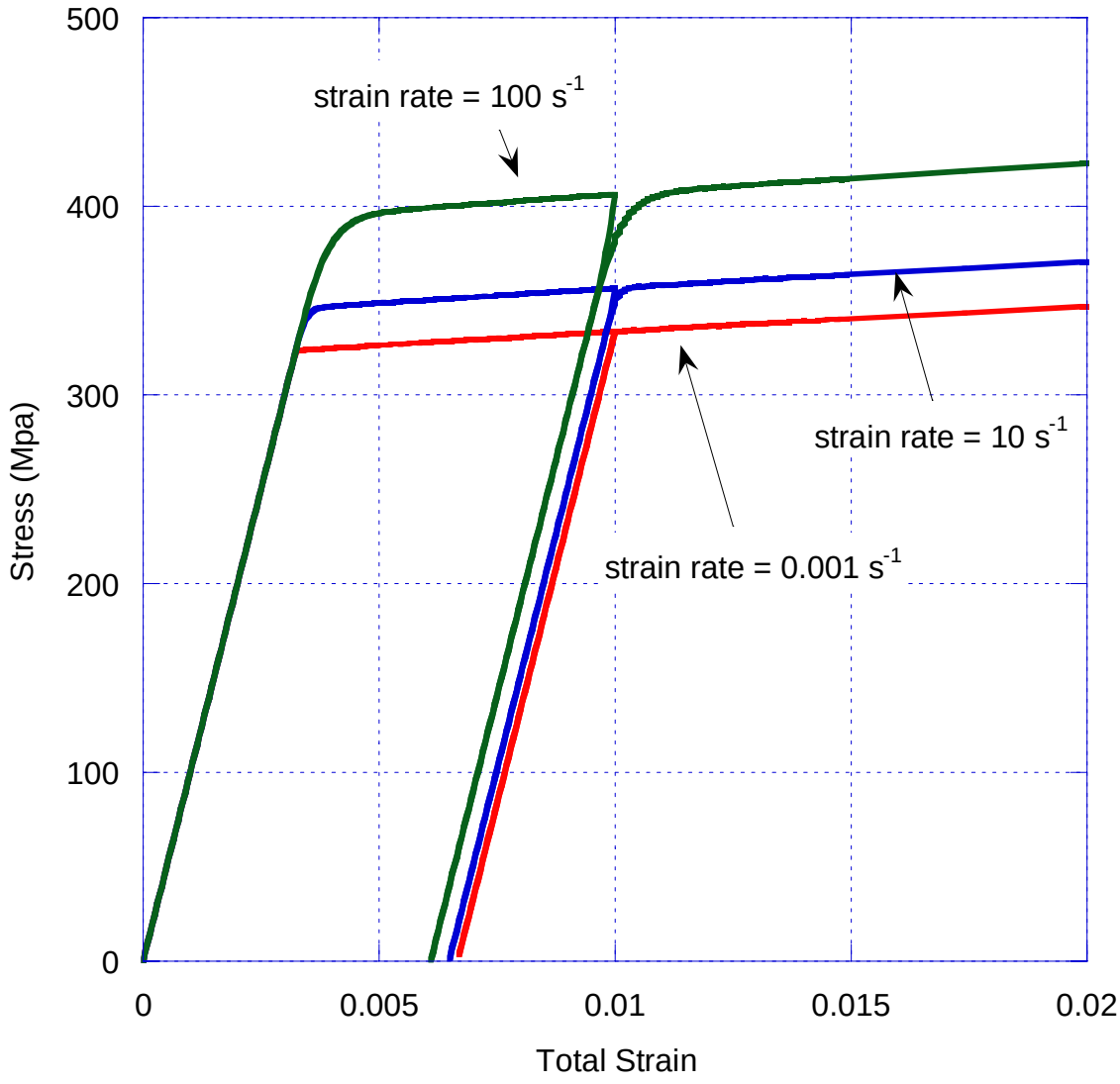

Figure 5.7 Simulation results using the consistency method without using the assumptions from Heeres et al. (2002) for various strain rates corresponding to uniaxial tension for loading and unloading conditions.

the results predicted using the Perzyna method. The uniaxial compression results using the material parameters described by equations (5.35) (5.36) and Table 5.1 with the consistency method were identical to the results shown in Figure 5.2 for the Perzyna method.

The state of stress and strain for a given elastic-viscoplastic increment using the consistency method is accepted as the current state once consistency is restored. Thus, at difference with the Perzyna method, the terms used in the convergence criterion are of stress. Since small differences in stress result in very small differences in strain, the consistency method is not as sensitive to the step size or convergence tolerance as the Perzyna method (see Figure 5.8). Therefore, a strain increment size of $\Delta\varepsilon_{11} = 0.001$ with a convergence tolerance of $1x10^{-4}$ was used.

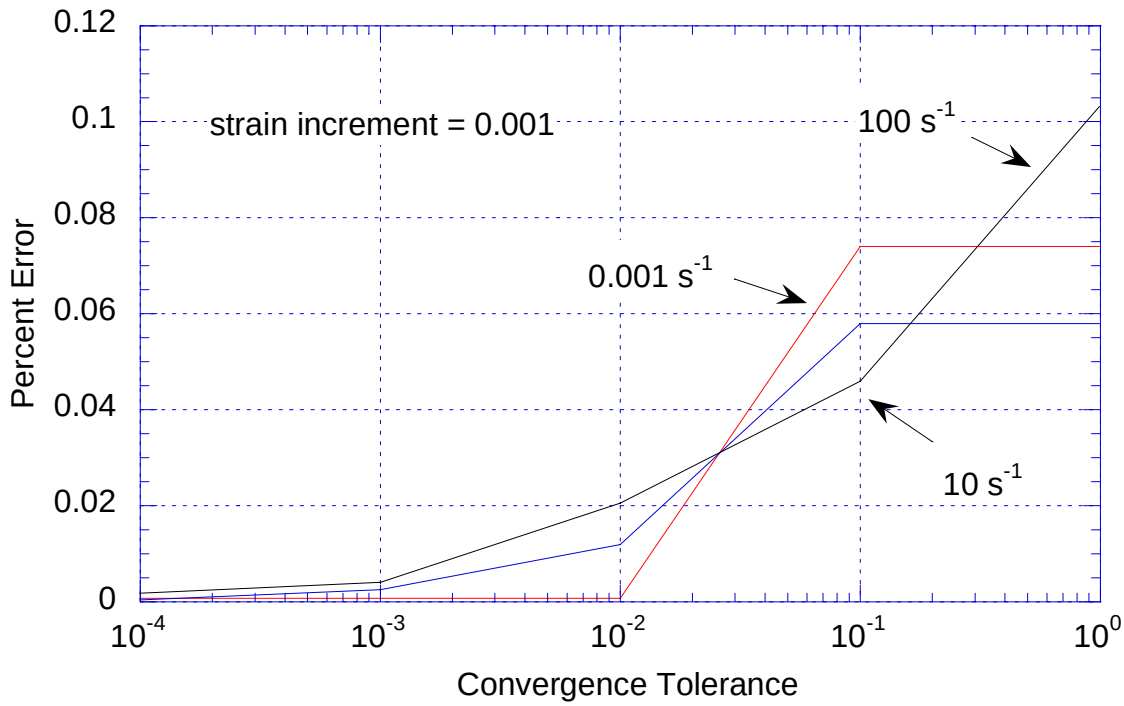

Figure 5.8 Effect of convergence tolerance and the strain rate on the accuracy of the consistency method at 5% levels of viscoplastic strain.

5.6 High-Strain Rate Modeling of the Behavior of Zirconium in Compression

Kaschner et al. (2000) reported results of uniaxial compression tests on a high-purity crystal-bar zirconium. The material was clock-rolled (see section 4.6 for discussion). Mechanical tests were carried out at 76º Kelvin (K) and 298º K (i.e., -197º Celsius (C) and 25º C, respectively), however, we will use only the results for 298º K to validate our approach. Cylindrical compression specimens were machined from the zirconium plate such that the cylindrical axis was originally in the plane of the plate, and tests were carried out at strain rates of 0.001 s^{-1}, 0.1 s^{-1} and 3500 s^{-1}. The tests at the strain rate of 3500 s^{-1} were performed using a split Hopkinson pressure bar. The results of these tests have shown the importance of twinning on the mechanical response of zirconium deformed at high rates of strain. In fact, metallurgical evidence showed an increase in the amount of twinning in the zirconium at the strain rate increased.

The Taylor cylinder impact test (see Figure 5.9) was developed during World War II by G. I. Taylor (Taylor, 1948) to screen materials for use in ballistic applications. The test involves firing a small cylindrical rod at a high velocity against a massive and rigid target producing strain-rates on the order of $10^4 - 10^5\, s^{-1}$. The impact plastically deforms and shortens the rod by causing material at the impact surface to flow radially outward relative to the rod axis. The Taylor impact test involves gradients of stress, strain, and strain rate to produce the final strain distribution. Therefore, a model used to simulate such an event must be able to capture the material's behavior as a function of accumulated viscoplastic strain and strain-rate. Simulations involving the high speed impact of metals typically assumes isotropy using the von Mises yield criterion with a rate-dependent, isotropic hardening relationship (Maudlin et al., 1999a). However, such

assumptions would be incapable of capturing the initial or plastic deformation induced anisotropy of the material, and thus would only be capable of predicting a circular cross section for the post test specimen. The proposed model, on the other hand, would be able to capture the initial anisotropy of the specimen, as well as the anisotropy evolution due to the plastic deformation during the high strain-rate deformation.

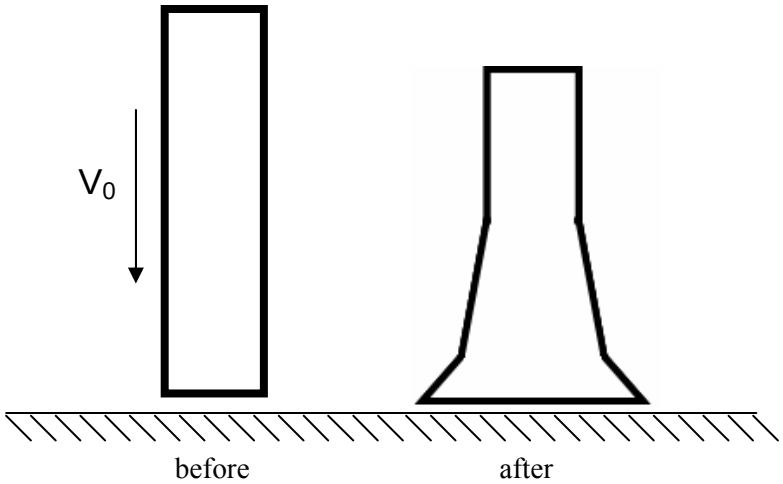

Figure 5.9 Schematic of the Taylor impact test

Taylor impact experiments were conducted using zirconium specimens made from a clock-rolled plate of high purity crystal-bar zirconium (see Maudlin et al., 1999b). The cylindrical specimens (50.8 mm long, 7.62 mm diameter) were machined such that the specimen's cylindrical axis would have originally been in the plane of the plate. The specimen was fired from a gas driven gun and impacted a steel anvil target at 243 m/s. Photographs of the post-test specimens and the strain profile as a function of specimen height were presented.

In this section, we attempt to model the high strain-rate behavior of zirconium by introducing both anisotropy and the anisotropic evolution of the yield surface behavior of zirconium using the proposed model. Due to the capability of both methods to predict the same material response, only the Perzyna method was used for simulation.

Before the aforementioned rate-dependent model can be utilized, a description of a material's yield behavior must be obtained. Due to deformation twinning, hexagonal closed packed metals such as zirconium exhibit a strong reorientation of the crystallographic texture with accumulated plastic deformation (Tome et al., 2001), and thus a pronounced evolution of the shape of its yield surface. This concept was earlier discussed in Chapters 1 and 4, with the representation of the yield surface evolution for a clock-rolled plate of pure zirconium subjected to in-plane compression out to levels of 35% effective plastic strain presented in Chapter 4 for static analysis. During the Taylor impact experiment, plastic strains of greater than 50% are expected. Thus, the yield surface evolution for a clock-rolled plate of zirconium subjected to in-plane compression out to levels of 60% effective plastic strain were determined using the vpsc model by prestraining the material to a given level of plastic deformation. The polycrystal was then numerically probed along different strain paths to determine the yield surface corresponding to the updated texture. Furthermore, the material's yield behavior due to applied shear stresses was determined using the vpsc model. These results are presented in Figure 5.10, with vpsc calculations represented by symbols, the yield surface determined by the proposed orthotropic yield criterion (3.16) represented by solid lines, and intermediate yield surfaces representing the evolution determined using the interpolation method (4.27) represented by dashed lines. It is evident from Figure 5.10 that at high levels of plastic deformation, the material's texture is significantly changed by twinning. It will be necessary to capture this behavior when simulating the high deformation, high strain-rate Taylor impact test discussed later in this section. The

coefficients used by the proposed yield criterion for the surfaces depicted in Figure 5.10 are listed in Table 5.2.

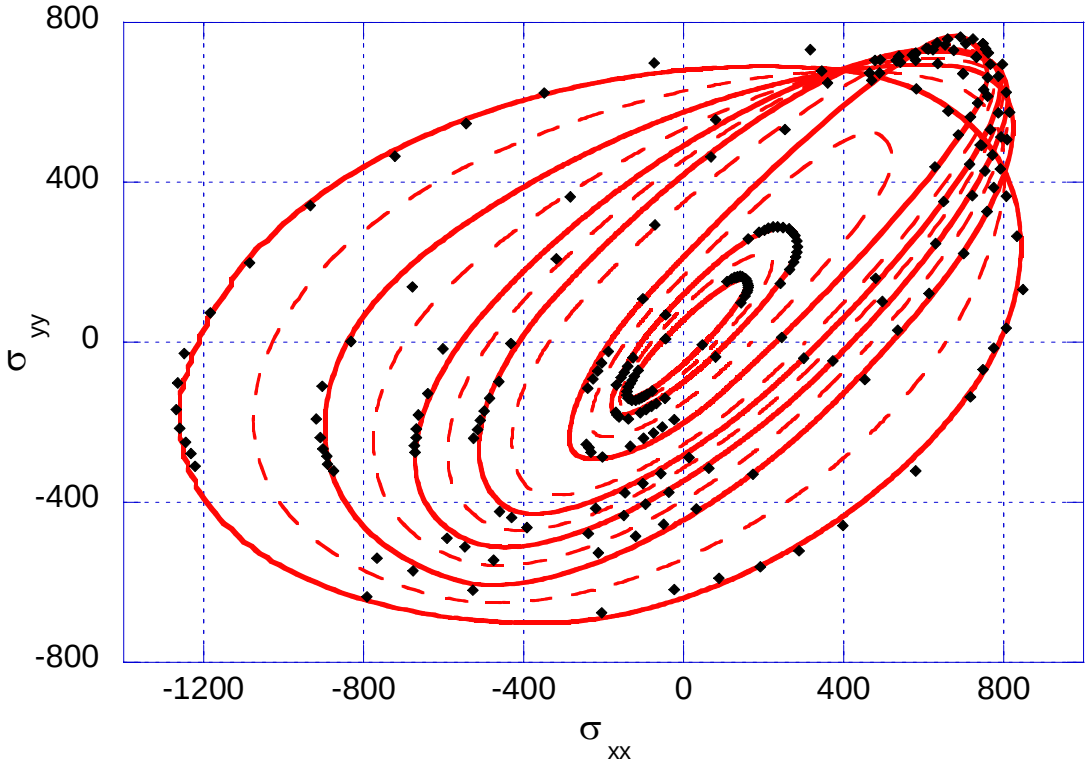

Figure 5.10 Yield surface evolution for a clock-rolled plate of zirconium subjected to in-plane compression about the x-axis for 0.2%, 1%, 5%, 25%, 35%, 45% and 60% levels of effective plastic strain. Symbols represent calculations using the vpsc model. Solid lines represent yield surface representation using the proposed yield criterion. Stresses in Mpa.

Table 5.2 Zirconium coefficients corresponding to the yield surface for in-plane compression

	a	k	L_{12}	L_{13}	L_{22}	L_{23}	L_{33}	L_{44}	L_{55}	L_{66}
0.2%	2	0.0706	2.8831	1.8747	1.2517	1.9649	1.2040	0.9890	1.0750	3.9560
1%	2	0.2242	2.1498	1.4068	1.1789	1.4383	0.8922	0.6041	0.6167	1.6914
5%	2	0.5001	2.9227	1.8231	0.8649	1.7452	0.4181	0.9844	1.1450	2.9802
25%	2	0.2632	2.7041	1.7271	1.8211	2.0558	0.8686	0.9493	0.7906	1.4031
35%	2	0.1738	2.5052	1.6829	2.3196	2.0535	1.0118	0.8888	0.6942	1.0977
45%	2	-0.2692	0.8528	1.4444	1.1429	0.6238	1.0072	0.6379	0.4607	0.6646
60%	2	-0.2200	0.7655	0.8583	0.6371	0.8999	0.6435	0.2985	0.1888	0.2547

In addition to the yield surface evolution due to plastic deformation, the effect of strain rate on the constitutive behavior on the material must also be characterized in order to model the material at high rates of strain. Such information is presented in Kaschner et al. (2000), and is necessary to determine the strain rate coefficients γ and m (5.15) used in the Perzyna method. The coefficients $\gamma = 2500s^{-1}$ and $m = 7.0$ were found to give the best fit for the in-plane compression data (see Figure 5.11). The constitutive behavior for the in-plane compression corresponding to strains beyond the experimental data was estimated based upon vpsc calculations. Since the Taylor impact experiment (Kaschner et al., 1999b) primarily involves in-plane compression, the coefficient B (see equation 5.14) was chosen such that the effective stress reduces to in-plane compression.

The proposed model using the Perzyna method was implemented into an ABAQUS/EXPLICIT user material subroutine using the yield surface evolution according to in-plane compression (see Figure 5.10) to model the Taylor impact test for the zirconium specimen. Due to the lack of experimental data to characterize the zirconium at high temperatures, the effect of temperature increase resulting from mechanical work was neglected. As a comparison to isotropic hardening, a simulation was also carried out using the Perzyna method assuming isotropic hardening based on the 0.2% yield surface of zirconium shown in Figure 5.10. Due to the orthotropic symmetry of the material, only a quarter of the cylinder was modeled. The zirconium cylinder was modeled using 2117 ABAQUS C3D8R linear brick elements with free boundary conditions and an initial velocity of 243 m/s. The step size used to simulate the event was Δt=2e-8 s and was conducted until 90 μs. At 90 μs the specimen had rebound off of

the target, and all plastic deformation had ceased. The anvil target was modeled as an analytical rigid surface. The predicted logarithmic strain profile along the major and minor axes of the post-test specimen is presented in Figure 5.12 and compared to the experimental data. Figure 5.13 display a visual comparison between the simulated and experimental major and minor profiles and footprint of the post-test specimen. Figures 5.14 – 5.15 present the same information except the simulation results were obtained using isotropic hardening based on the 0.2% yield surface.

Figures 5.12 and 5.13 reveal that the results using the proposed rate dependent model are in good agreement with the experimental data. The differences between the experimental data and the simulation results are most likely related to the increase of temperature due to the large viscoplastic deformations, and a possible difference in the shape of the yield surface at high strain-rates due to the higher levels of twinning and the shape of the yield surface for static conditions used for simulation.

Initially, the yield behavior for the zirconium specimen is highly anisotropic with a very strong through thickness direction as compared to the in plane directions. However, as the Taylor specimen deforms by in-plane compression at very high strain rates along the axis of the rod, twinning acts to change the texture producing a more isotropic texture as the deformation progresses. While the proposed method is capable of capturing this phenomena, an isotropic hardening assumption can not. This is evident in figures Figures 5.14 and 5.15, which illustrate that an isotropic hardening assumption is not a good approximation for modeling the high strain-rate, large deformation behavior of zirconium.

A study of the mesh density and the step size on the accuracy of the solution was also conducted using the Perzyna method. The mesh density was increased by approximately 40% with very little effect on the final solution. Similarly, the time step was cut in half with little to no effect on the solution. Therefore it was determined that using 2117 elements with a time step of Δt=2e-8 s was a good choice (see Figure 5.16).

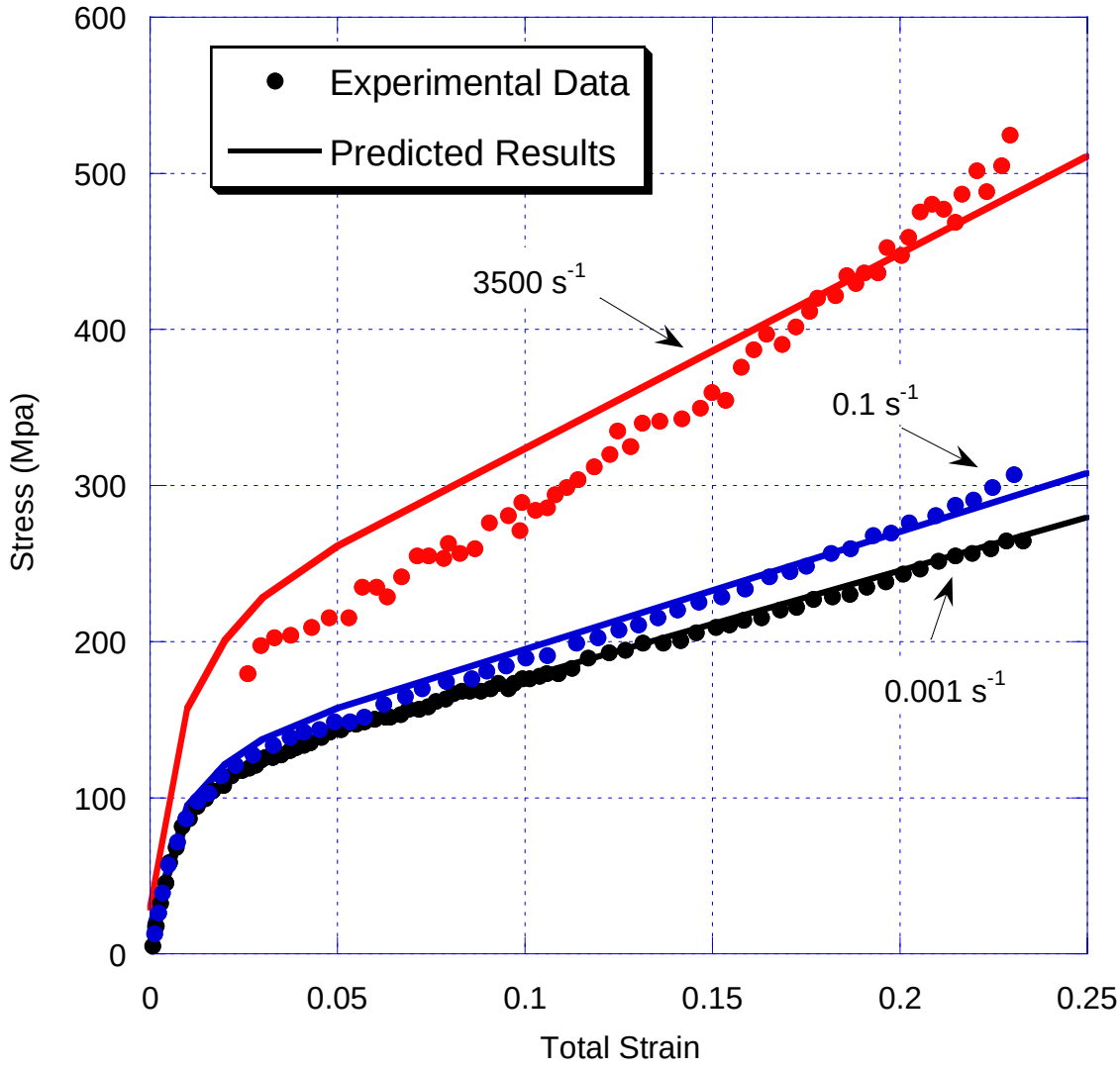

Figure 5.11 In-plane compression simulation results using the both the Perzyna method and the consistency method with the proposed yield criterion and hardening law (solid lines) in comparison with experimental data (symbols).

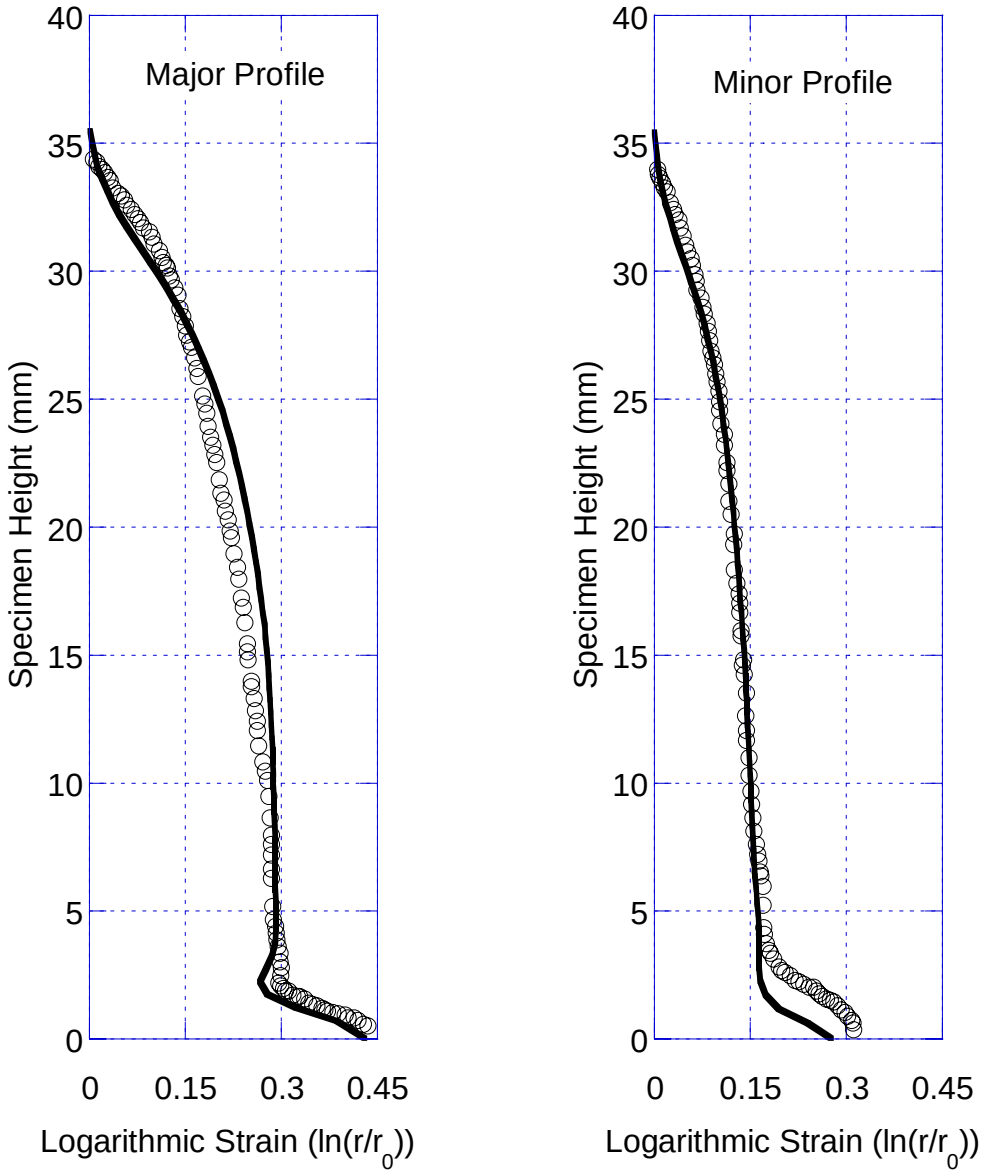

Figure 5.12 Comparison of predicted (Perzyna's method) and experimental (symbols) logarithmic strain profile for the post test zirconium Taylor impact specimen. The simulation results were obtained using 2117 linear brick elements and a step size of Δt=2e-8 s. Data after Maudlin et al. (1999b).

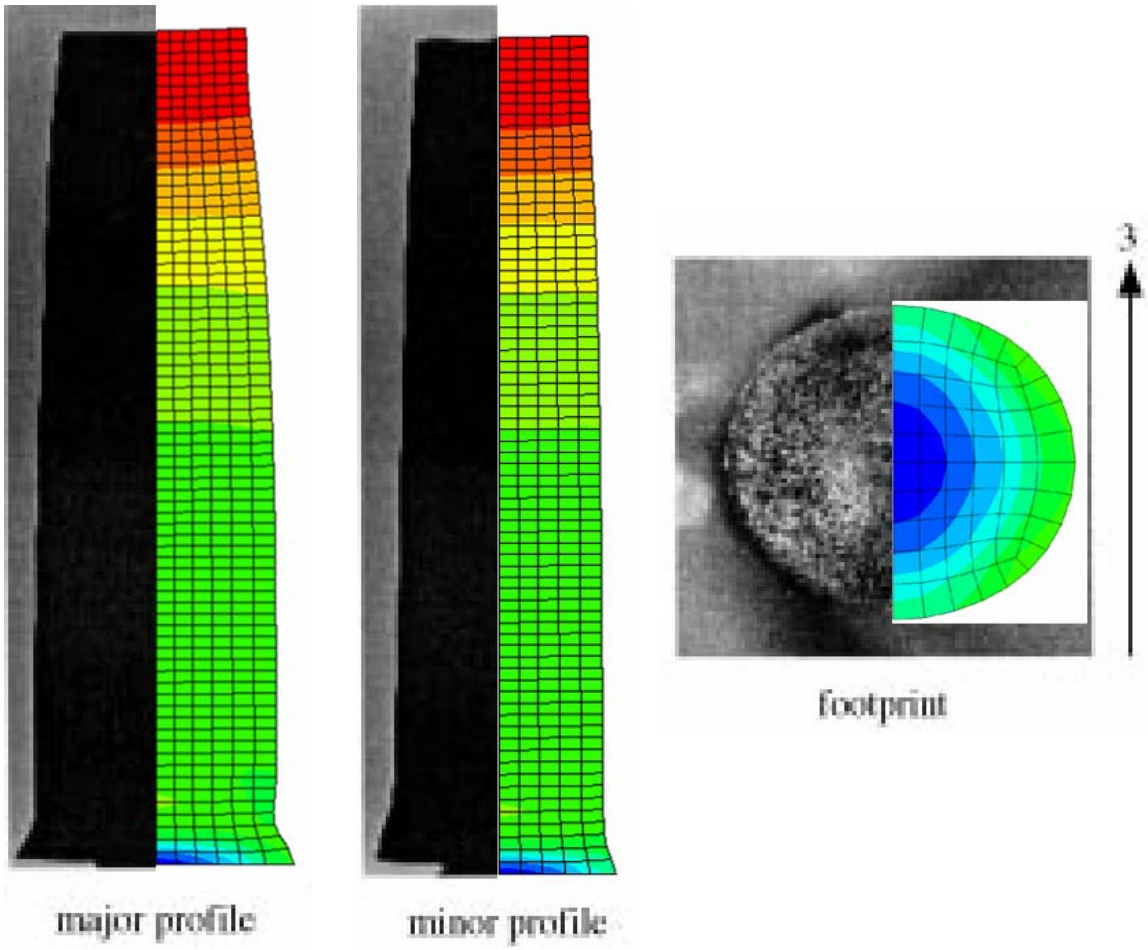

(a) (b) (c)

Figure 5.13 Comparison of the simulated (Perzyna's method) and experimental cross-sections of the post-test zirconium Taylor impact experiment for (a) the major profile, (b) the minor profile, and (c) the footprint. Data after Maudlin et al. (1999b).

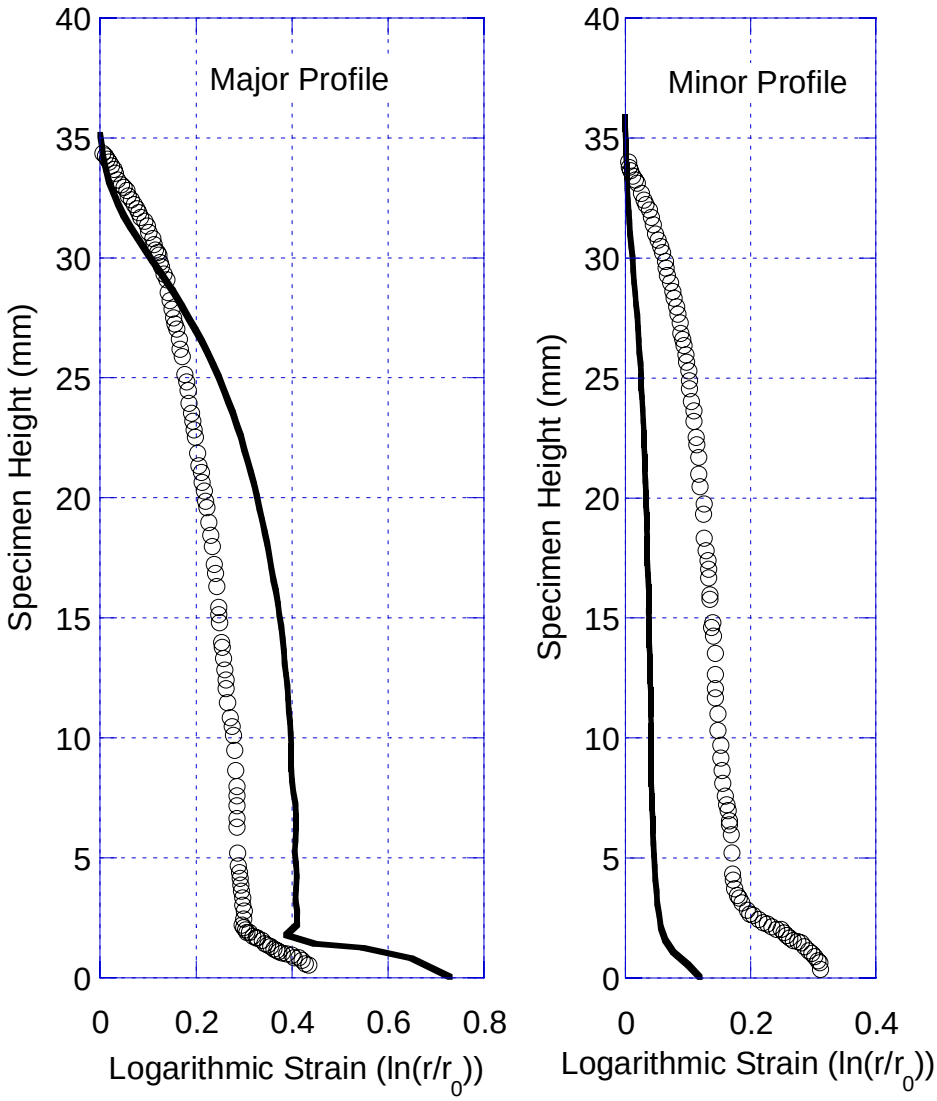

Figure 5.14 Comparison of predicted (assuming isotropic hardening) and experimental (symbols) logarithmic strain profile for the post test zirconium Taylor impact specimen. The simulation results were obtained using 2117 linear brick elements and a step size of Δt=2e-8 s. Data after Maudlin et al. (1999b).

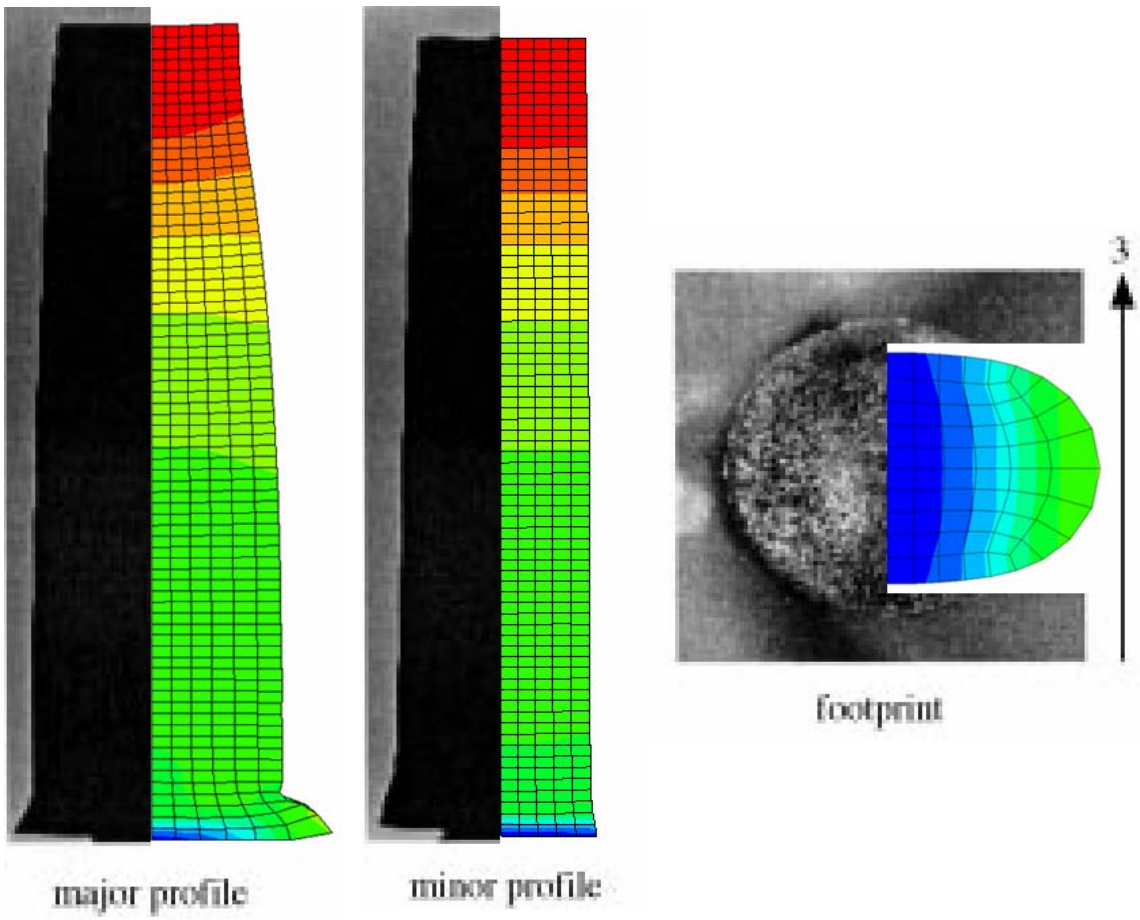

(a) (b) (c)

Figure 5.15 Comparison of the simulated (assuming isotropic hardening) and experimental cross-sections of the post-test zirconium Taylor impact experiment for (a) the major profile, (b) the minor profile, and (c) the footprint. Data after Maudlin et al. (1999b).

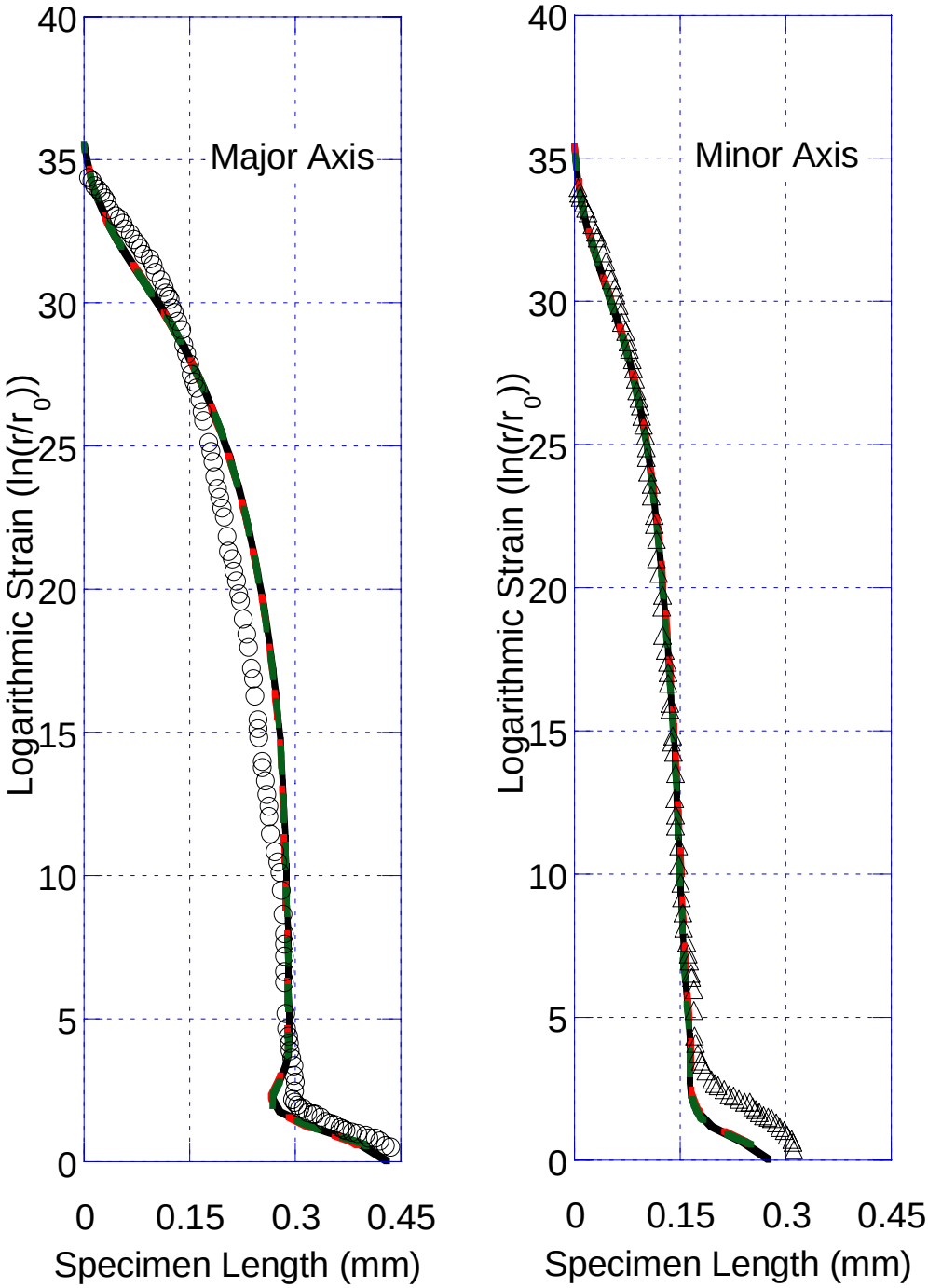

Figure 5.16 Effect of mesh density and time step on the final solution. Black lines represent 2117 elements and $\Delta t = 2e-8s$, red lines represent 2117 elements and $\Delta t = 1e-8s$, and green lines represent 2975 elements and $\Delta t = 2e-8s$. Data after Maudlin et al. (1999b).

5.7 High-Strain Rate Modeling of the Behavior of Tantalum in Compression

Although the proposed model was developed to capture the anisotropic, asymmetric hardening behavior of hcp metals, in this section the versatility of this model is demonstrated by modeling the high strain rate defomation of bcc tantalum.

A material characterization and the results from Taylor impact tests using specimens cut from a rolled plate of tantalum were reported (see Maudlin et al., 1999a). Tantalum is a bcc metal and metallurgical evidence shows negligible texture evolution due to the large viscoplastic deformations of the Taylor impact test. Therefore, isotropic hardening can be assumed while modeling this material. The proposed modeling approach can easily be used to model tantalum by fixing $\Gamma = \tilde{\sigma}$ (see eq 4.31), thus the proposed model reduces to isotropic hardening. Furthermore, since tantalum is a cubic metal, the yield in tension and compression is equal, and the proposed yield criterion can be used to represent the yield behavior of tantalum by setting the strength differential coefficient k to zero.

Based upon the initial texture of the tantalum plate, a Taylor-Bishop-Hill polycrystal model was used to construct a yield surface by probing the material along different loading directions (see Maudlin et al., 1999a). Using the information from the polycrystal analysis, coefficients were determined to best reproduce the yield surface using the proposed orthotropic yield criterion. Figure 5.17 shows the polycrystal calculations from Maudlin et al. (1999a) as symbols and the corresponding yield surface using the proposed orthotropic criterion as a solid line on the biaxial plane. The coefficients used by the proposed criterion to construct this surface are listed in Table 5.3. Due to a lack of information regarding the yield behavior due to shear stress, yield in

shear can be assumed to be isotropic. For instance, according to the von Mises isotropic yield criterion, yield due to pure shear is 0.577 times that due to uniaxial tension.

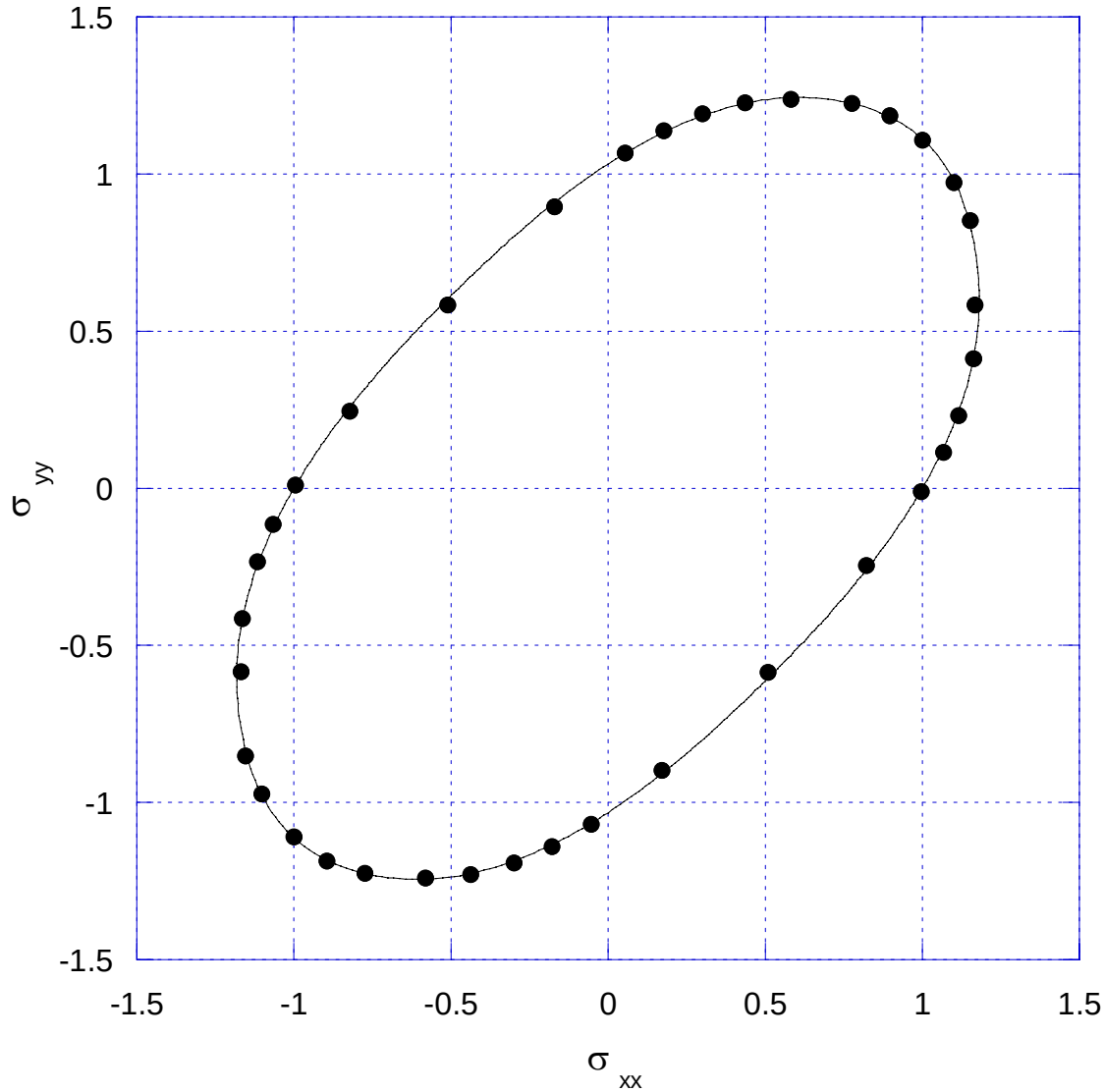

Figure 5.17 Yield surface corresponding to a rolled sheet of tantalum. Polycrystal calculations (symbols). Yield surface using the proposed yield criterion (solid line). Data after Maudlin et al. (1999a).

Table 5.3 Tantalum coefficients for the proposed orthotropic criterion

a	k	L_{11}	L_{12}	L_{13}	L_{22}	L_{23}	L_{33}
2	0	1.0000	-0.1911	-0.0687	1.0411	0.0067	1.1366

In the same manner as for zirconium, the uniaxial stress strain curve for tantalum for static conditions was represented using the interpolation method. Based on experimental data published from Maudlin et al. (1999a), the rate coefficients of equation (5.15) were chosen to be $\gamma = 1500 s^{-1}$ and $m = 5$. The predicted results for uniaxial compression simulations using the Perzyna method are compared to experimental data in Figure 5.18. Note the change in the hardening rate as the strain rate increases. In order to better model the very high strain-rate Taylor impact test, the strain hardening rate was chosen to give a better fit to the higher strain-rate data to model the constitutive response of the tantalum specimen.

In addition to the high strain rate data collected for room temperature conditions, Maudlin et al. (1999a) also presents stress strain data collected for various high temperatures. In order to model the effect of temperature on the constitutive response of tantalum, a temperature dependant stress strain curve of the form shown in equation (5.33) was used in the expression of equation (5.15).

$$Y\left(\bar{\varepsilon}_{vp}, T\right) = \left[\xi(\bar{\varepsilon}_p) \cdot Y^j + (1 - \xi(\bar{\varepsilon}_p)) \cdot Y^{j+1}\right]\left[1 - \left(\frac{T - T_{rm}}{T_{melt} - T_{rm}}\right)^h\right] \tag{5.33}$$

In equation (5.33), T_{rm} is the room temperature (typically 25 degrees C), T_{melt} is the materials melting temperature, and h is a material parameter. The temperature portion of equation (5.33) is the temperature contribution from the Johnson-Cook model (Johnson and Cook, 1983). Choosing $h = 0.42$ to give a best average fit to the experimental data and using $T_{melt} = 3250K$ for tantalum along with the strain rate parameters previously mentioned for tantalum, uniaxial compression simulations were carried out using the Perzyna method and are compared to experimental data in Figure 5.19. Due to the

similarity between the results using the Perzyna method and the consistency method, tantalum was modeled only using the Perzyna method.

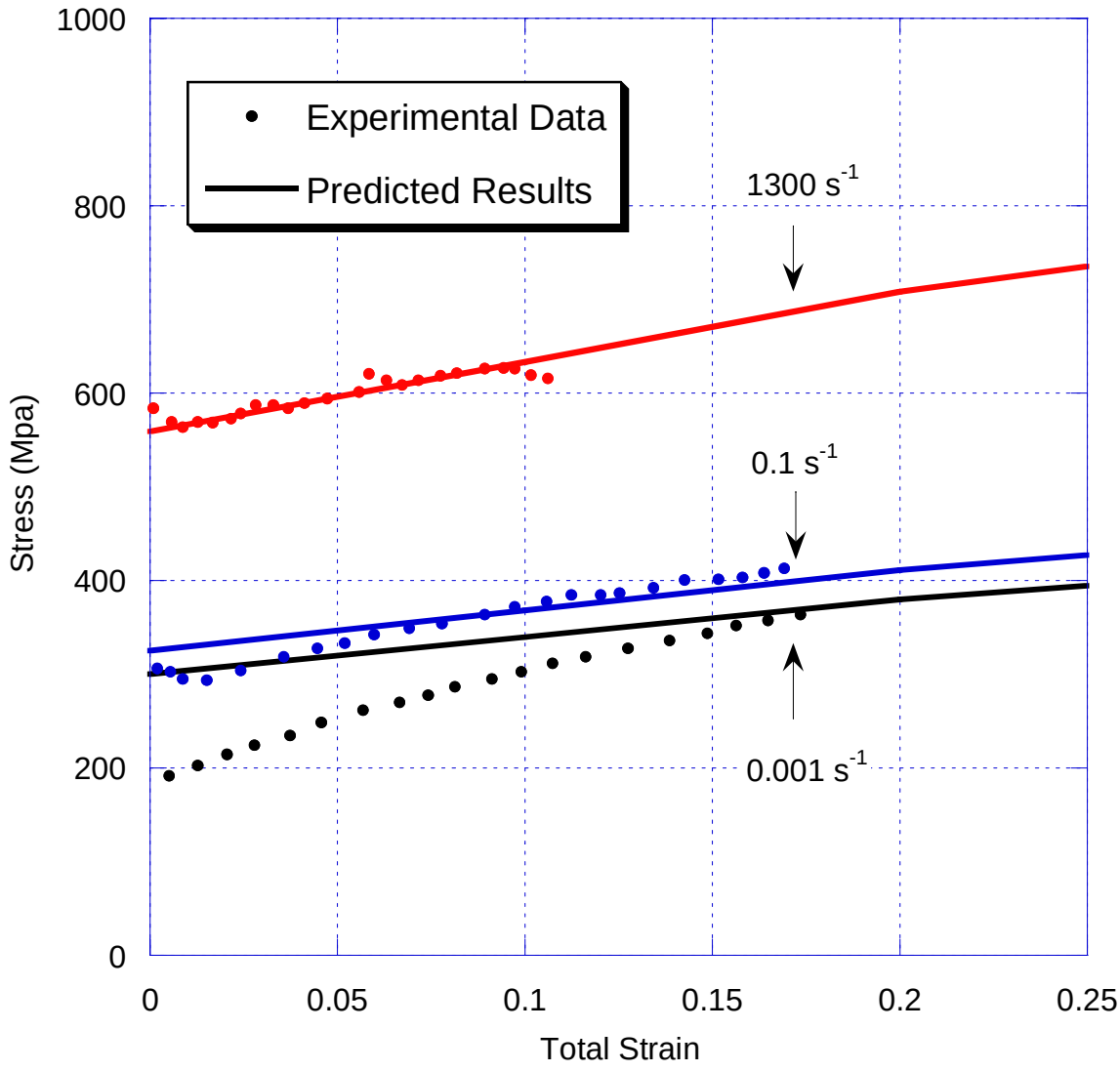

Figure 5.18 Uniaxial simulation results (solid lines) for various strain rates at 25ºC in comparison with experimental data (symbols). Data after Maudlin et al. (1999a).

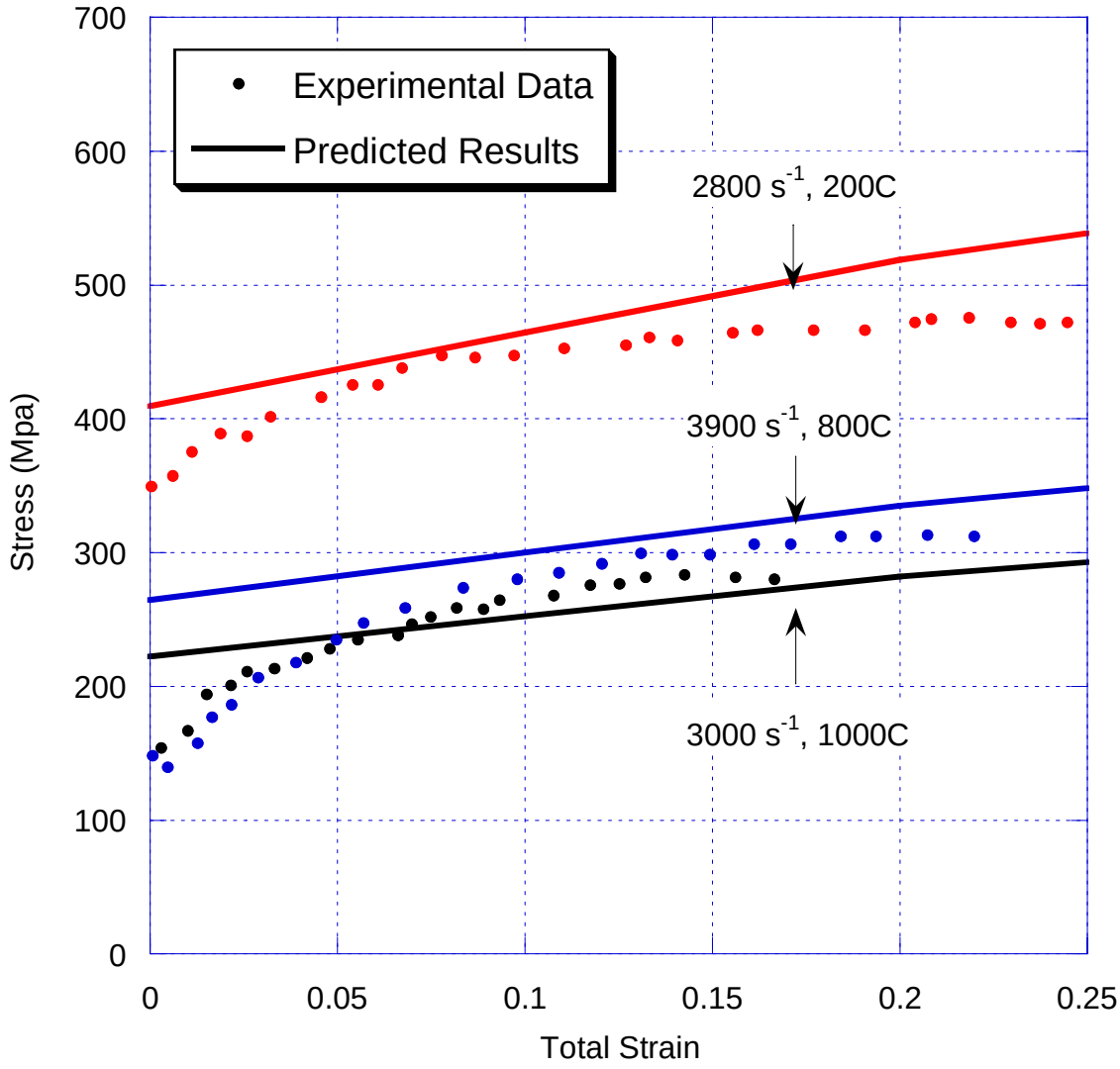

Figure 5.19 Uniaxial simulation results (solid lines) for various strain rates and temperatures in comparison with experimental data (symbols). Data after Maudlin et al. (1999a).

Using the yield surface, temperature, and strain rate parameters for tantalum along with equation (5.10) to calculate the rise in temperature due to mechanical deformation ($\rho = 16640\, kg/m^3$, $c_p = 140\, J/kgK$), the proposed model was implemented into an ABAQUS/EXPLICIT user material subroutine to model the Taylor impact experiment reported in Maudlin et al. (1999a) for tantalum. The experiment consisted of a specimen cut from a tantalum plate such that the cylindrical axis of the specimen was either from the 1 or the 2 direction of the plate (see Figure 5.20). The cylindrical specimens were 7.62 mm in diameter with a length of 38.1 mm.

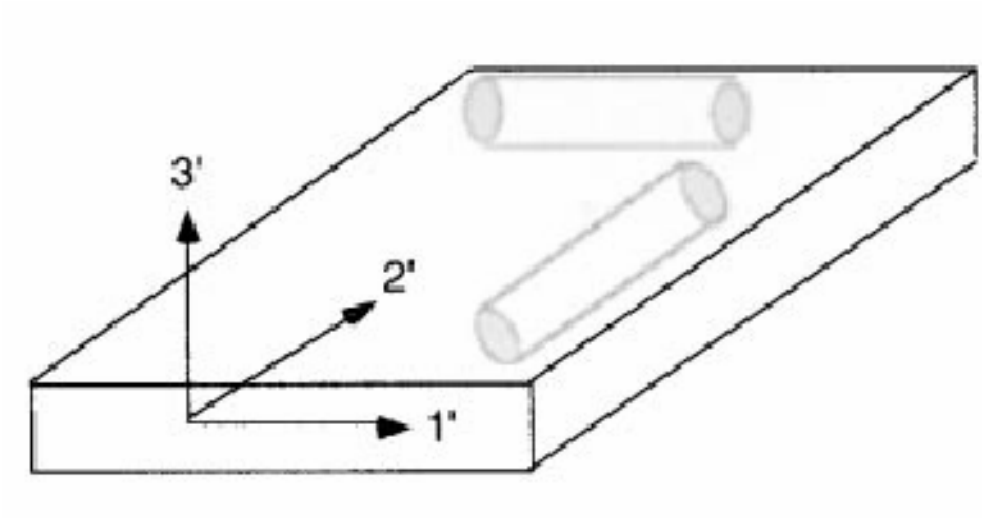

Figure 5.20 Schematic of the orientation of cylindrical specimens cut from a tantalum plate

Due to the nearly isotropic yield behavior in the plane of the plate, simulations were only carried out assuming that the cylindrical axis was along the 1 direction of the plate. A quarter section of the cylindrical specimen was modeled due to the ortotropic symmetry of the material using 8170 ABAQUS C3D8R linear brick elements with free boundary conditions and an initial velocity of 175 m/s. The step size used to simulate the event was Δt=2e-8 s and was conducted until 100 μs. At 100 μs the specimen had

rebound off of the target, and all plastic deformation had ceased. The anvil target was modeled as an analytical rigid surface. The higher number of elements used for the tantalum simulations as compared to the zirconium simulations was due to the larger deformations of the tantalum specimen. The simulated and experimental profiles of the major and minor axis of the specimen's post test elliptical cross section are compared in Figure 5.21 with excellent agreement. The simulated and experimental footprints of the post test specimen are compared in Figure 5.22. The data shown in Figures 5.21 – 5.22 are the results from three separate experiments conducted for different specimens under the same conditions. The simulated and experimental post test specimens are visually compared in Figure 5.23. The calculated post test temperature distribution is shown in Figure 5.24

In Maudlin et al. (1999a), the tantalum Taylor impact test was simulated by introducing anisotropy through using a direct link between the Taylor-Bishop-Hill polycrystal model and the finite element code EPIC, assuming that each integration point was a polycrystal. Their results were also in very good agreement with the experimental data. However, Figures 5.21 – 5.23 clearly demonstrate that introducing anisotropy into the high strain rate simulations using the proposed method can also produce very accurate results, but at a fraction of the computational expense.

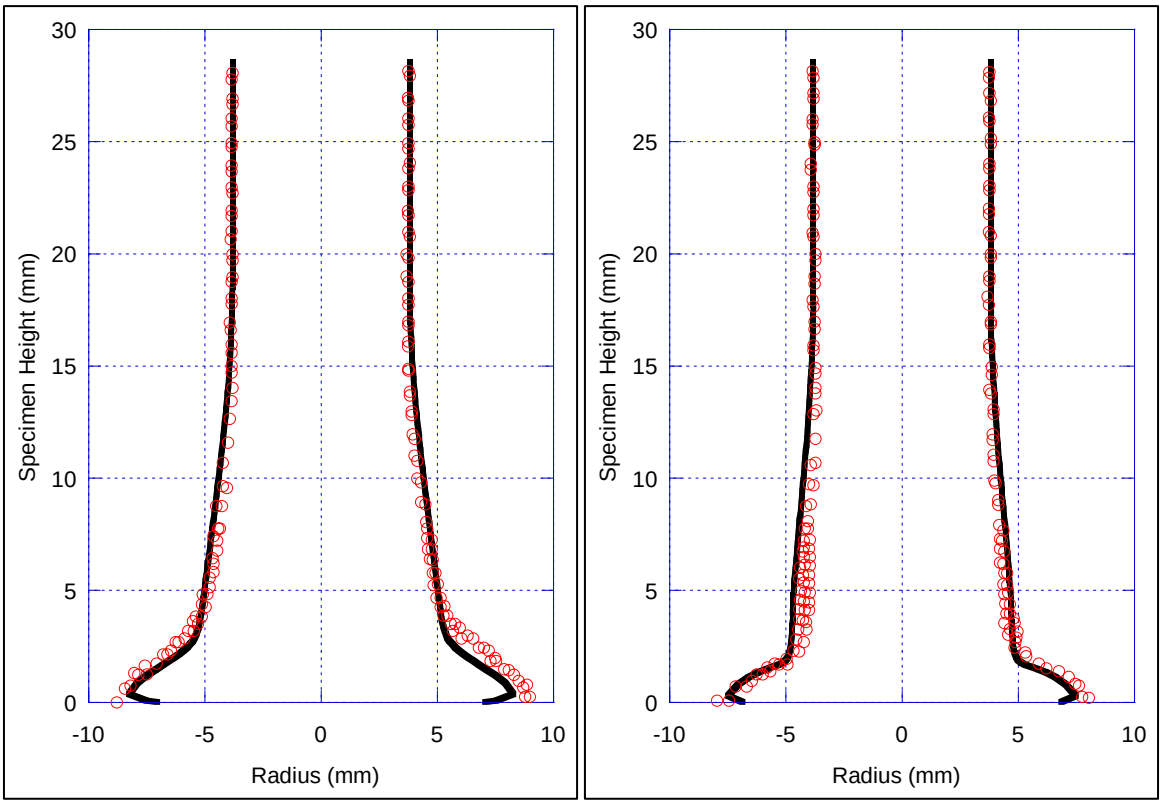

(a) (b)

Figure 5.21 (a) Major and (b) minor profiles for the tantalum Taylor impact specimen. Solid lines represent simulation results, symbols represent experimental data. Data after Maudlin et al. (1999).

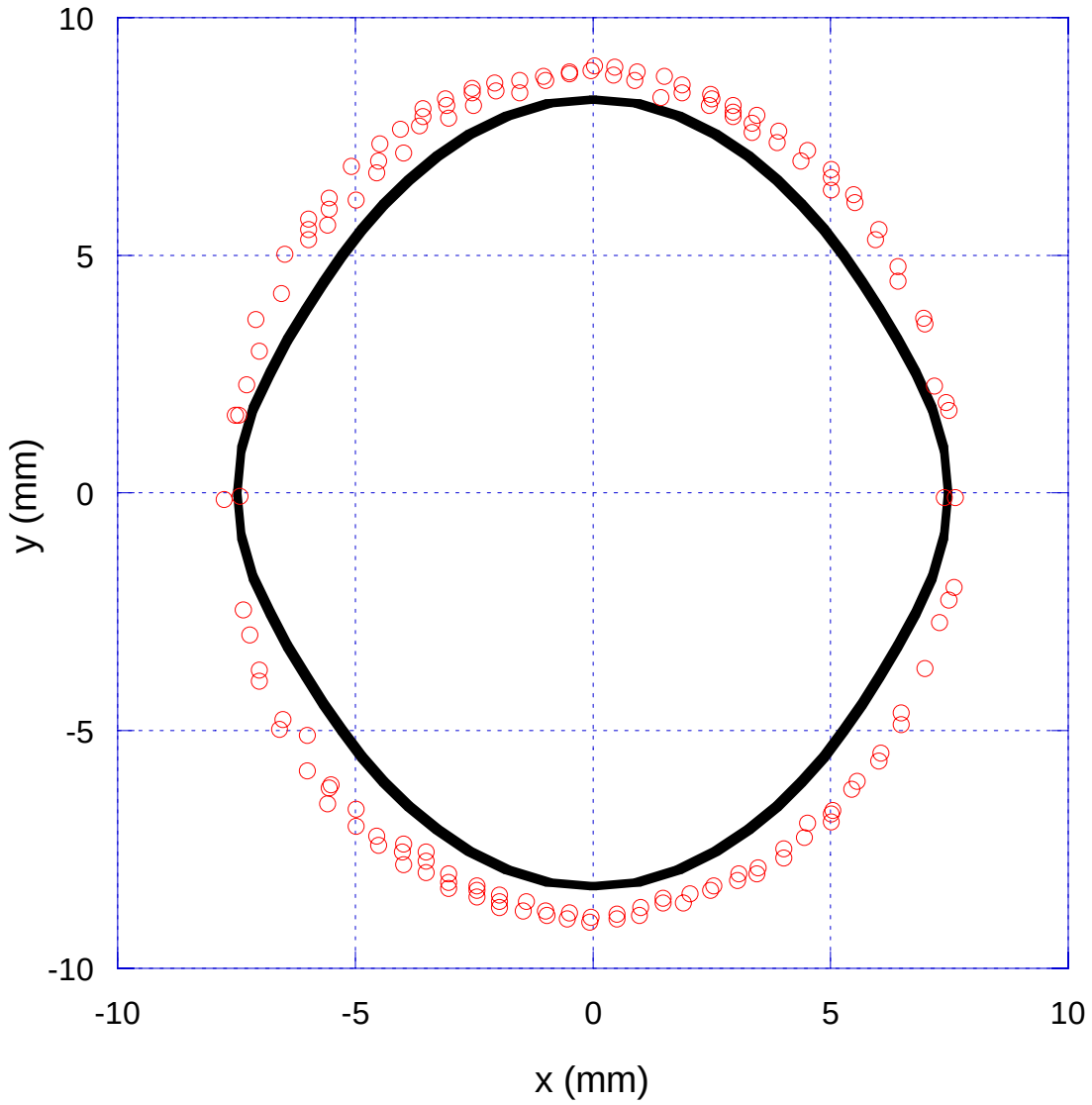

Figure 5.22 Footprint for the tantalum Taylor impact specimen. Solid lines represent simulation results, symbols represent experimental data. Data after Maudlin et al. (1999).

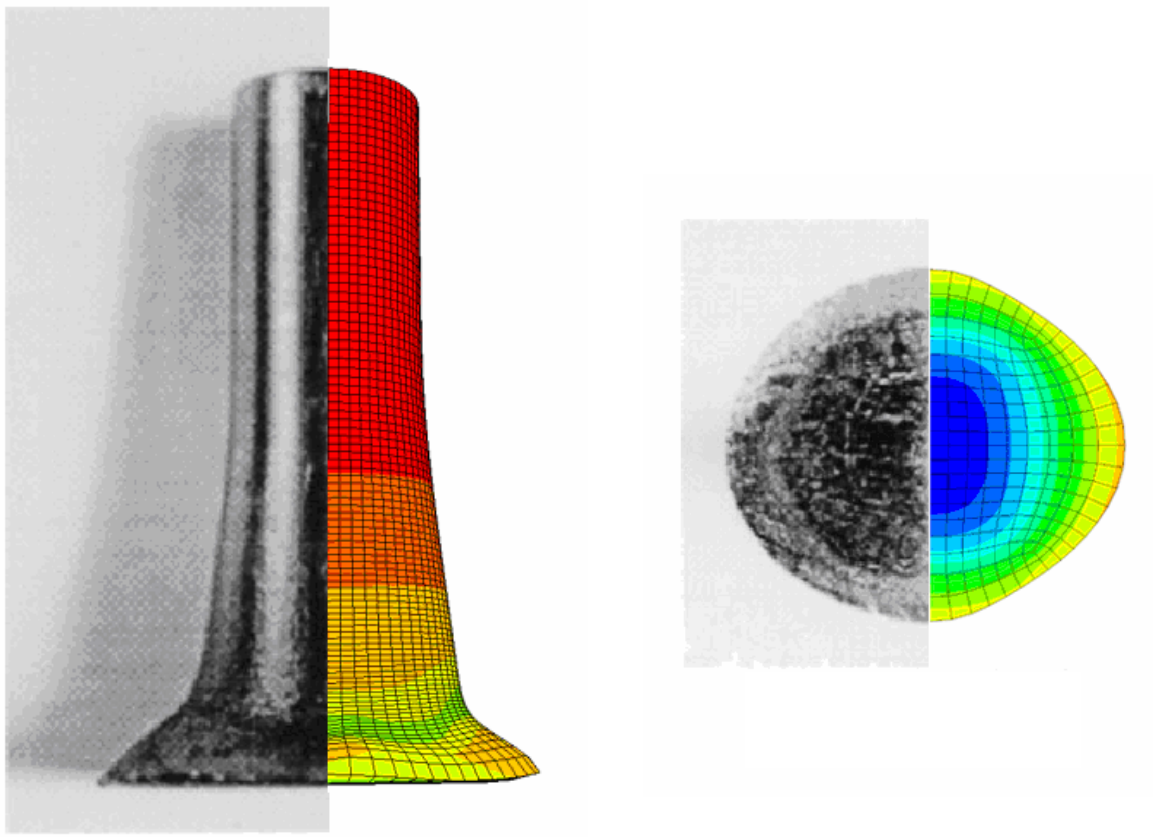

(a) (b)

Figure 5.23 Visual comparison between simulated and experimental tantalum Taylor impact specimens for the (a) major side profile and (b) footprint.

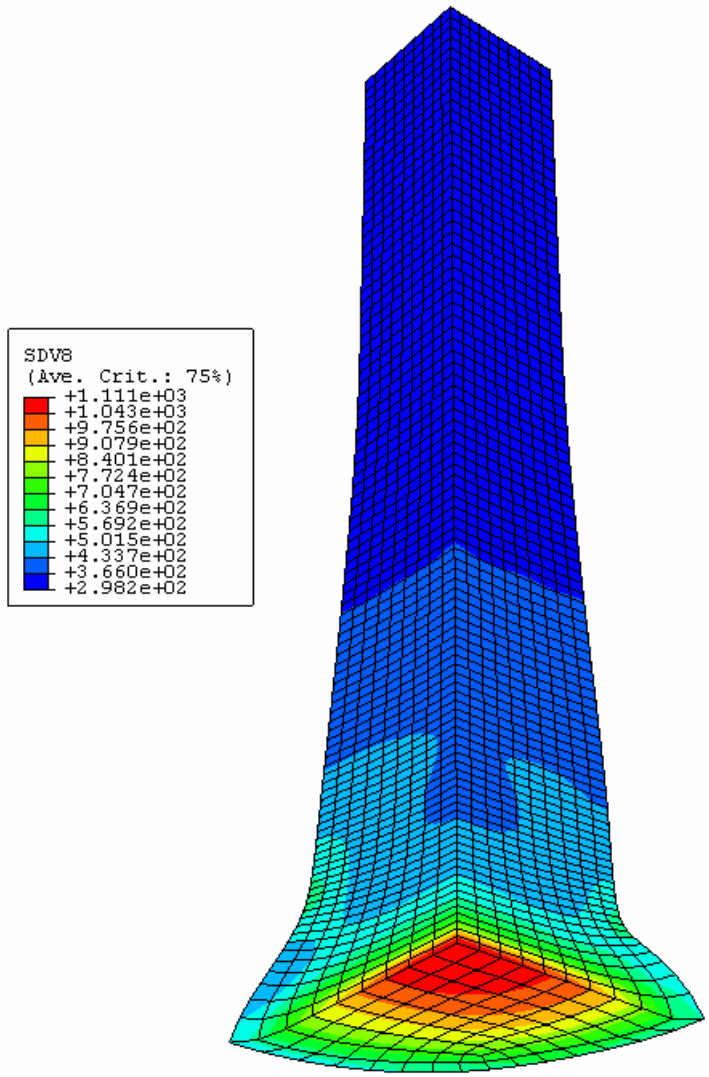

Figure 5.24 Calculated temperature (degrees K) contours for the post test tantalum Taylor impact specimen.

CHAPTER 6
MODIFICATION OF THE PROPOSED YIELD CRITERION – COMPARISON TO 2090-T3 ALUMINUM

Barlat et al. (2005) demonstrated that when large amounts of data are available for yield surface representation, anistotropy coefficients from one linear transformation may not be adequate. In fact, as discussed in section 1.2, Barlat et al. (2005) introduced Yld2004-18p as a modification of Yld91 to include two linear transformations with a total of 18 anisotropy coefficients. The proposed orthotropic yield criterion (3.16), can be extended to include two linear transformations.

$$\begin{aligned}&\left(\left|\Sigma_1\right| - k\Sigma_1\right)^a + \left(\left|\Sigma_2\right| - k\Sigma_2\right)^a + \left(\left|\Sigma_3\right| - k\Sigma_3\right)^a + \\ &\left(\left|\Sigma'_1\right| - k'\Sigma'_1\right)^a + \left(\left|\Sigma'_2\right| - k'\Sigma'_2\right)^a + \left(\left|\Sigma'_3\right| - k'\Sigma'_3\right)^a = F\end{aligned} \tag{6.1}$$

This modified yield criterion includes 18 anisotropy coefficients from the two transformed tensors $\boldsymbol{\Sigma} = \boldsymbol{LS}$ and $\boldsymbol{\Sigma}' = \boldsymbol{L'S}$, along with two strength differential coefficients k and k'. Equation (6.1) reduces to equation (3.16) when $\boldsymbol{\Sigma} = \boldsymbol{\Sigma}'$ and $k = k'$.

An asymmetry between tensile and compressive yield has been experimentally observed in the aluminum alloy 2090-T3 (Yoon et al., 2000). In Yoon et al. (2000), uniaxial tensile and compressive yield strengths and Lankford coefficients for 7 different orientations with respect to the rolling direction of the sheet, along with the yield strength for balanced biaxial tension were presented to describe the initial yield surface. The tensile data and Lankford coefficients were used as input for Yld96 (2.19). Since (2.19) requires that yield in tension is equal to yield in compression, it was not able to accurately represent the compressive data. As a remedy, Yoon et al. (2000) translated the

stress axes until the uniaxial yield stresses for 0º and 90º to the rolling direction of the sheet for both tension and compression could simultaneously be captured. While translating the stress axes allowed the uniaxial predictions for 0º and 90º to the rolling direction of the sheet to capture the respective data, Yld96 (2.19) could not accurately represent the intermediate orientations between 0º and 90º.

It is more appropriate to represent the yield data for a metal that exhibits an asymmetry between tension and compression using a yield criterion that can allow for such phenomena. Since the published data in Yoon et al. (2000) includes 22 data points to describe the initial yield surface, the modified orthotropic yield criterion (6.1) was used. The ability for (6.1) to represent this data is shown in Figure 6.1, and the corresponding yield surface is given in Figure 6.2. The coefficients for the criterion (6.1) calculated from the experimental data and used in Figures 6.2 and 6.3 are presented in Table 6.1.

For cubic metals such as aluminum, it is typical to simulate forming operations such as cup drawing using an isotropic hardening law as describe in section 2.2. Yoon et al. (2000) presents the earing profile for an experimentally formed cup along with the simulated earing profile using Yld96 (1.19) with and without the translation of the stress axes assuming isotropic hardening. The specific dimensions of the tools as specified in Yoon et al. (2000) are given in Table 6.2. The schematic view of the cup drawing process is shown in Figure 6.3.

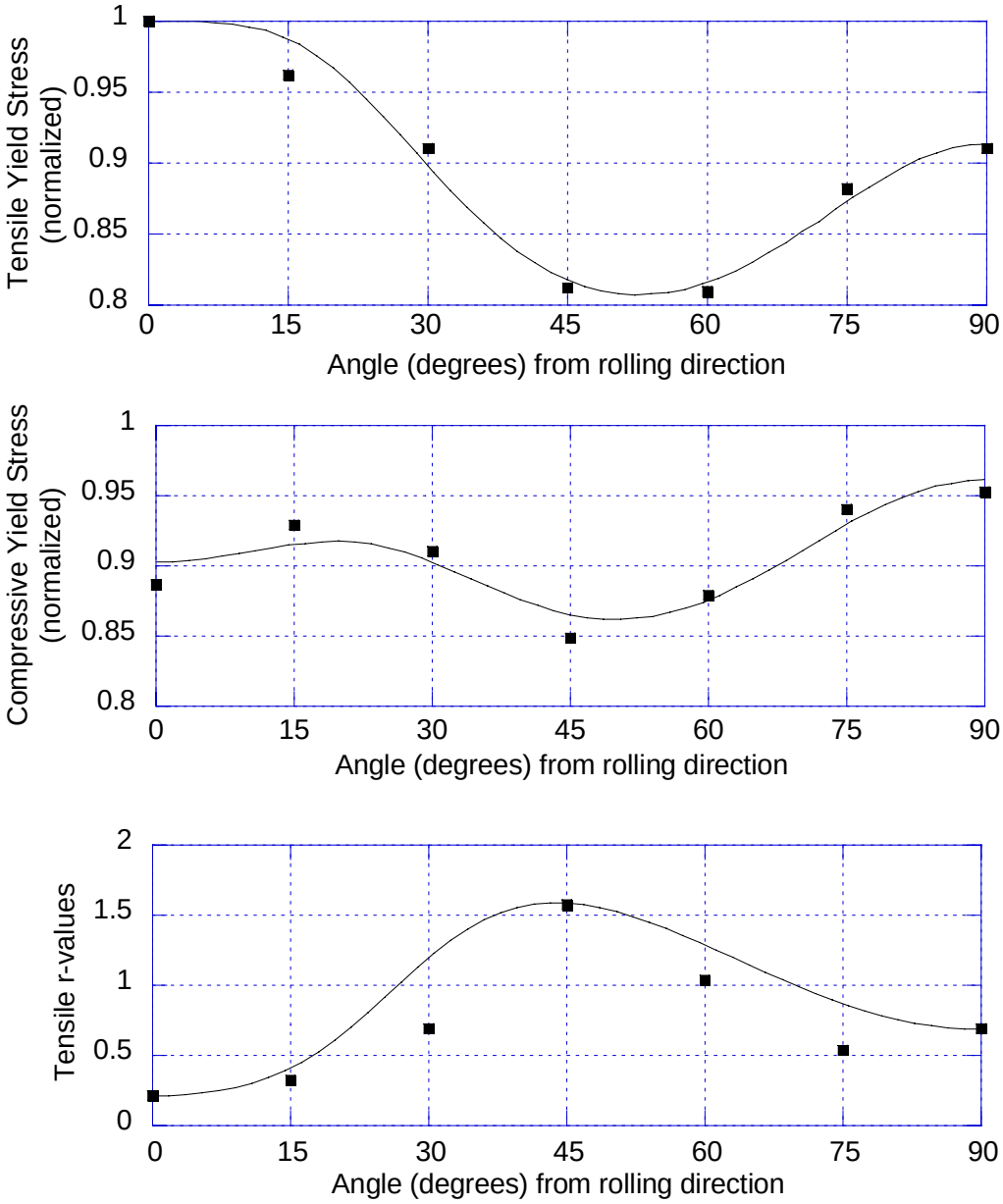

Figure 6.1 Comparison between predicted (solid line) and experimental (symbol) variation of yield stress and r-values with sheet orientation.

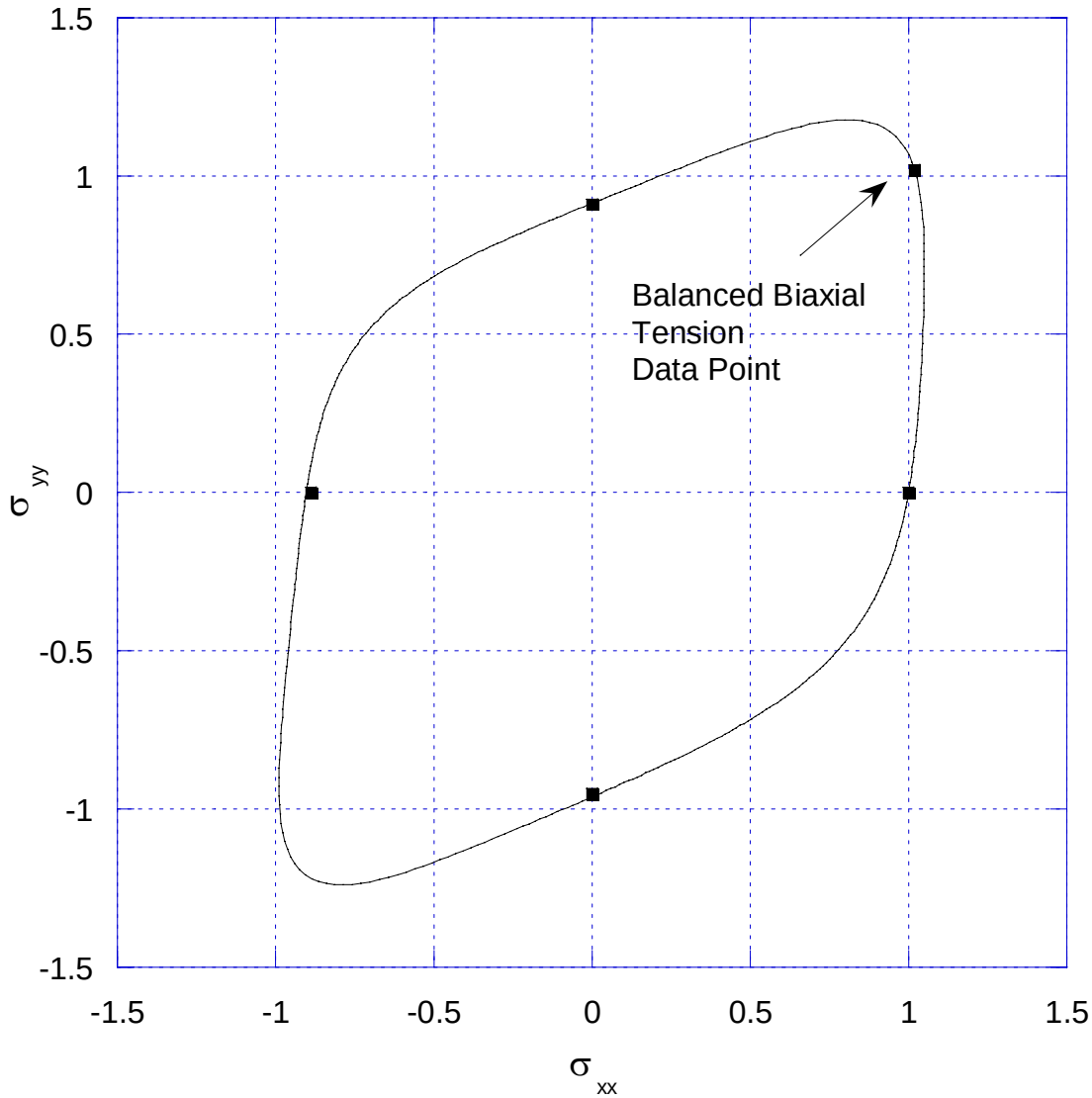

Figure 6.2 Predicted initial yield surface for 2090-T3 aluminum.

Table 6.1 2090-T3 aluminum coefficients

k	L_{11}	L_{12}	L_{13}	L_{22}	L_{23}	L_{33}	L_{44}	L_{55}	L_{66}
0.1553	1.0	0.0323	-0.6781	0.9958	-0.0085	0.7699	-0.7470	-0.7470	-0.7470

k’	L'_{11}	L'_{12}	L'_{13}	L'_{22}	L'_{23}	L'_{33}	L'_{44}	L'_{55}	L'_{66}
-0.0536	1.0	-0.0705	0.0789	1.2900	-0.2759	0.1314	1.7340	1.7340	1.7340

a
5.0

Table 6.2 Tool dimensions used for cup drawing simulations

Punch diameter	D_p = 97.46 mm
Punch profile radius	r_p = 12.70 mm
Die opening diameter	D_d = 101.48 mm
Die profile radius	r_d = 12.70 mm
Blank diameter	D_b = 158.76 mm
Blank thickness	t_0 = 1.6 mm

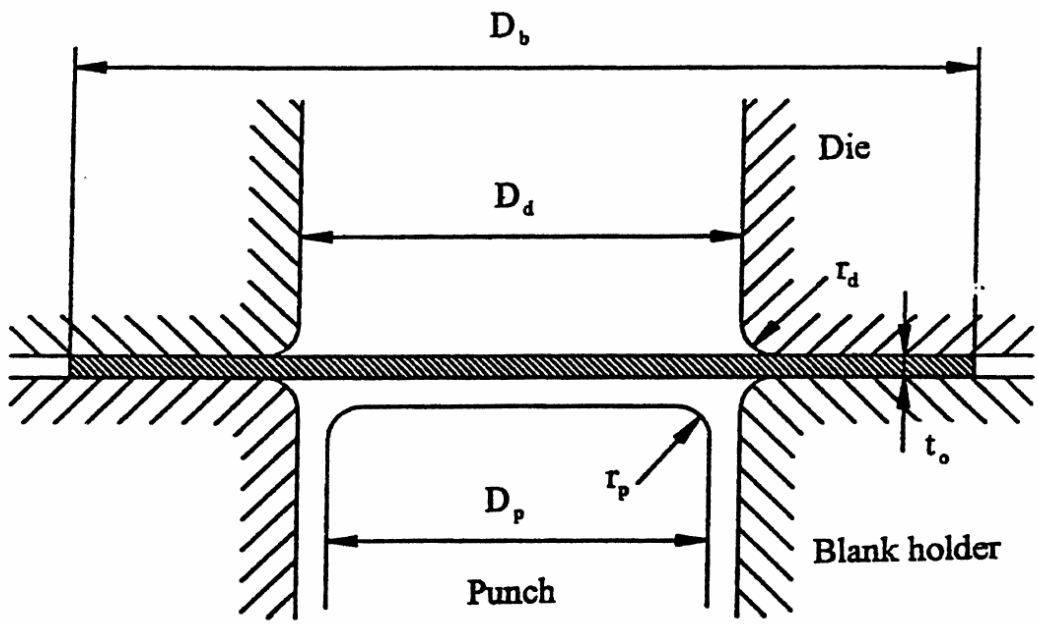

Figure 6.3 Schematic of circular cup drawing.

The proposed modified criterion (6.1) and an isotropic hardening law were implemented into an ABAQUS user material subroutine to simulate the experimental cup from Yoon et al. (2000). Only a quarter section of the cup was analyzed due to the orthotropic material symmetry of the aluminum sheet. The finite element mesh was composed of 1407 nodes and 780 three-dimensional linear brick elements (see Figure 6.4). The blank holding force used in the simulation was 22.2 kN (5.55 kN for a quarter cup section), and the Coulomb coefficient of friction was 0.1. The resulting earing profile using the proposed yield criterion (6.1) along with the experimental data and the results from Yld96 (2.19) are given in Figure 6.5. The proposed extended criterion (6.1)

predicts the height of the bottom of the ears much much more accurately than Yld96 especially for 0º and 180º, while both criteria predict the height of the top of the ear to within the spread of the data, and similar ear widths. The same results using the proposed criterion (6.1) are compared to Yld96 (2.19) with translation of the stress axes in Figure 6.6. The proposed criterion (6.1) and Yld96 (2.19) with translation of the stress axes both predict similar earing heights, however, (6.1) more accurately captures the width of the ear.

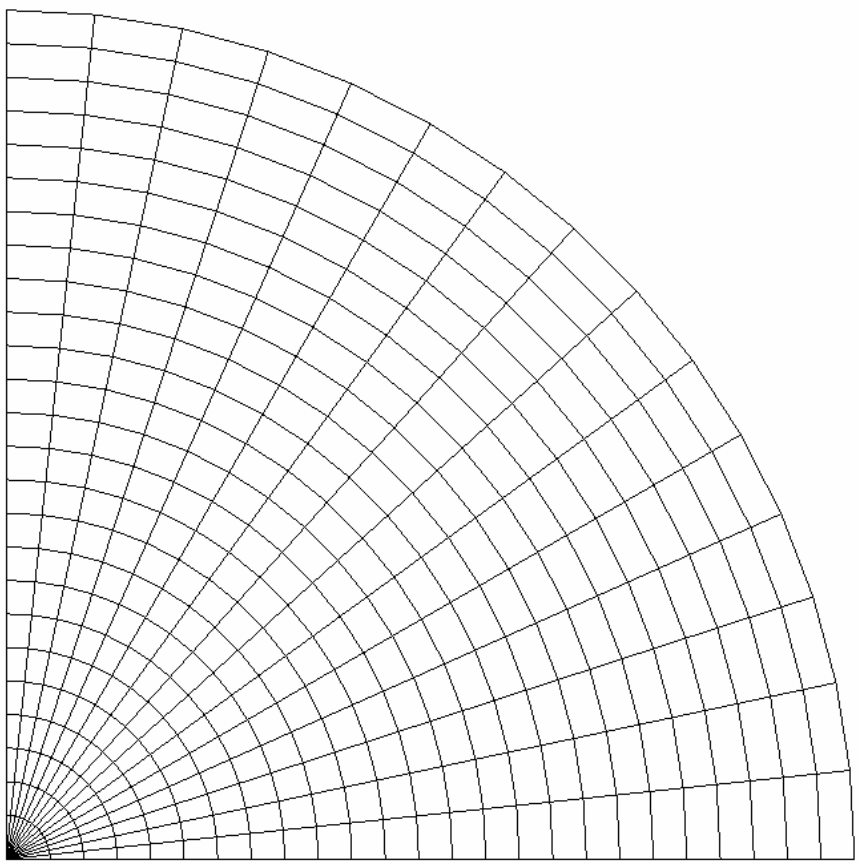

Figure 6.4 Finite element mesh used for cup drawing simulation of 2090-T3 aluminum

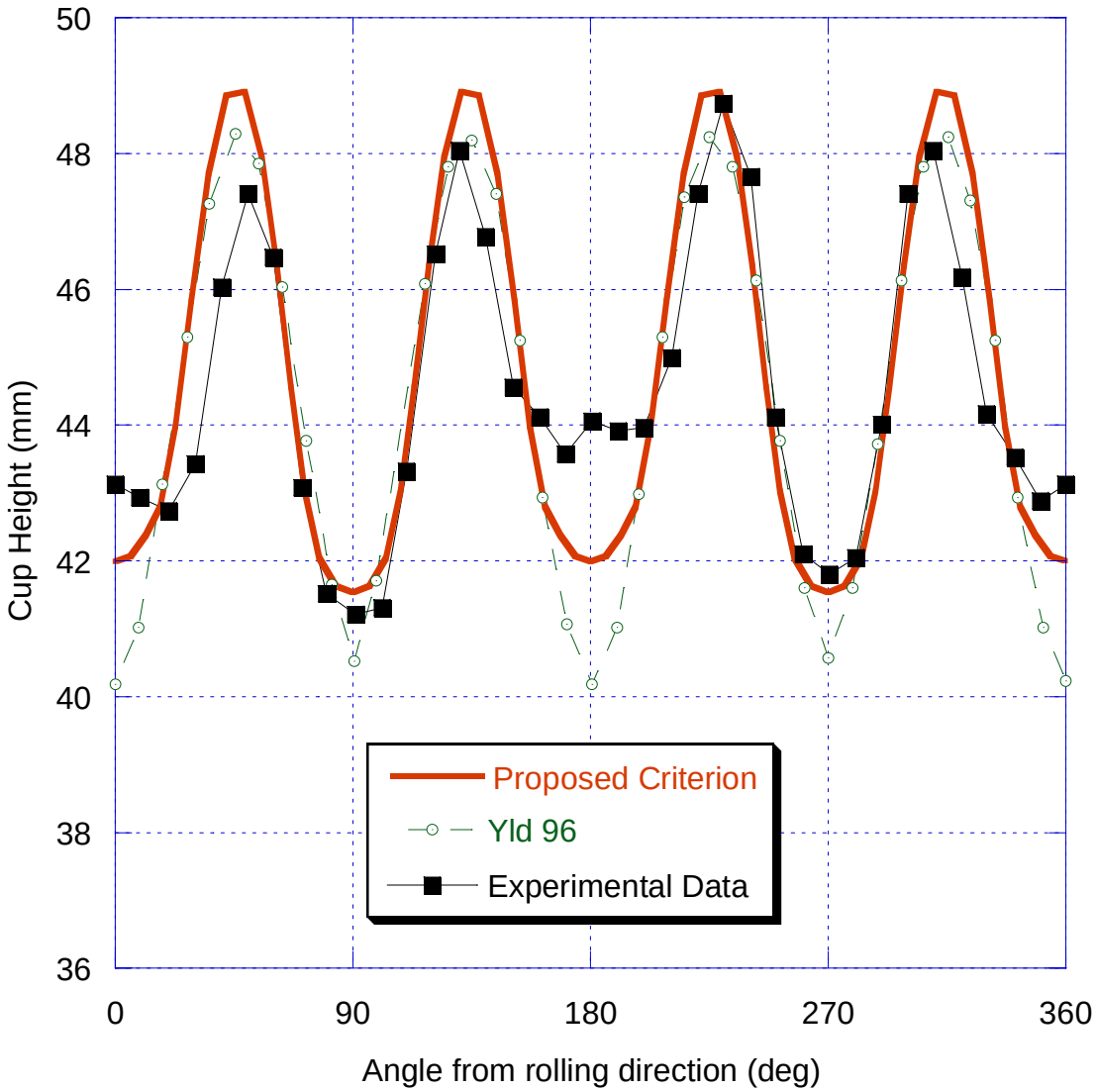

Figure 6.5 Predicted and experimentally determined earing profile for a drawn cup of 2090-T3 aluminum.

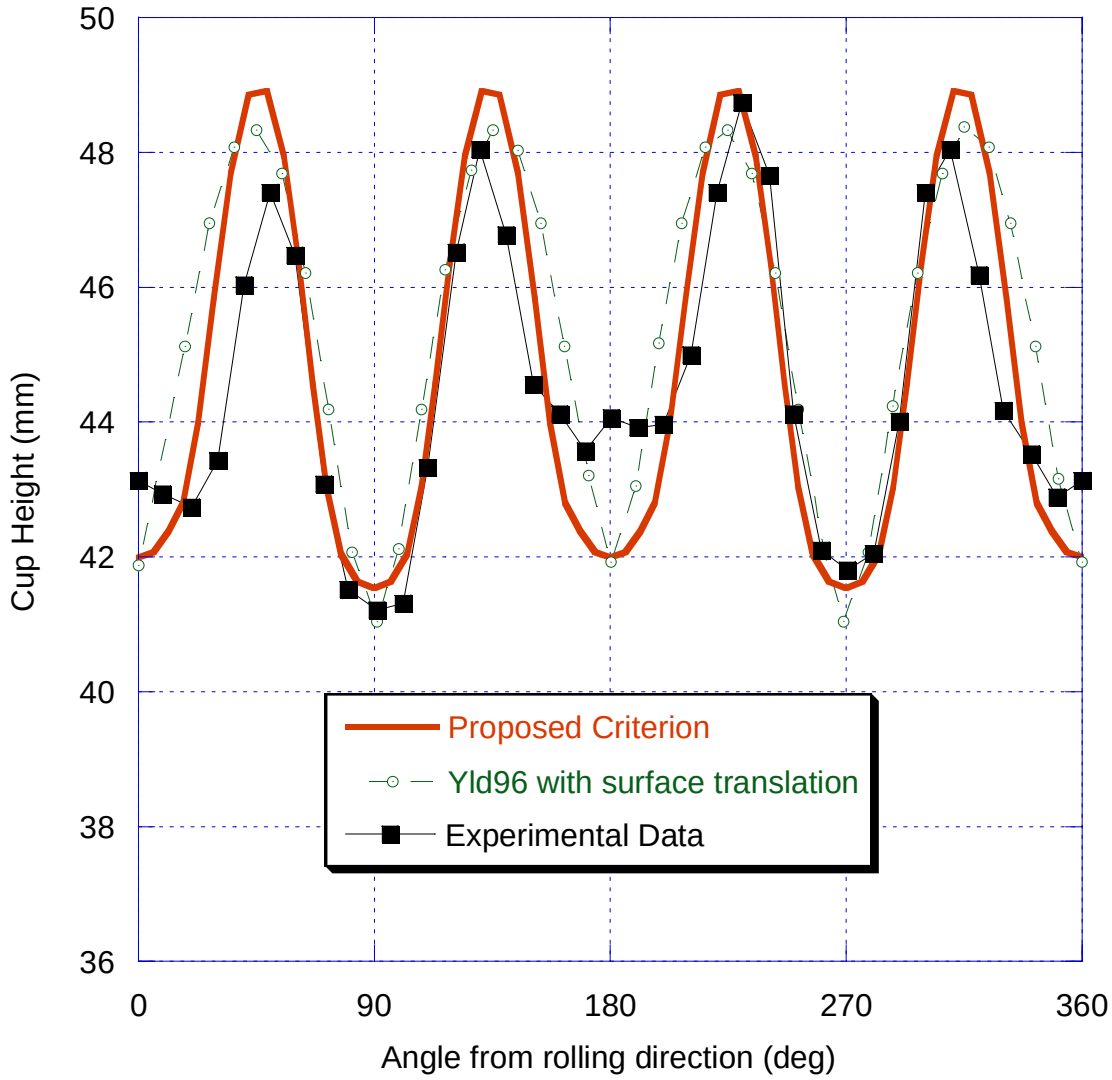

Figure 6.6 Predicted and experimentally determined earing profile for a drawn cup of 2090-T3 aluminum.

CHAPTER 7
SUMMARY AND FUTURE WORK

An isotropic criterion that can describe the asymmetry in yielding between tension and compression of pressure insensitive metals was proposed. This criterion is expressed in terms of the principal values of the stress deviator and involves two parameters: the parameters a which gives the degree of homogeneity of the yield function and the parameter k, which for a fixed value of the parameter a depends only on the ratio between the tensile and compressive yield strengths. The yield function was proven to be convex when the constant k belongs to a given numerical range: [-1, 1], for any value of a. The macroscopic yield locus was demonstrated to be capable of capturing the asymmetric yield locus for randomly oriented bcc, fcc, and hcp polycrystals deforming solely by twinning as computed using the vpsc model. The proposed isotropic criterion reduces to von Mises when $k = 0$ and $a = 2$.

The proposed isotropic criterion was extended such as to describe orthotropy by using a linear transformation on the deviatoric stress tensor. The proposed criterion involves 11 parameters, including 9 anisotropy coefficients along with k and a from the isotropic criterion. The procedure for identification of these parameters from simple tests was outlined. The orthotropic criterion was then used to describe the strong asymmetry and anisotropy observed in textured binary Mg-Th and Mg-Li alloy sheets (data after Kelley and Hosford, 1968) and for 4Al-1/4 O_2 titanium sheet (data after Lee and Backofen, 1966). Very good agreement between theoretical and experimental yield loci corresponding to different levels of total strain was obtained.

A macroscopic anisotropic hardening model that can describe the influence of evolving texture on the plastic response of hexagonal metals was proposed. Initial yielding was described using the proposed yield criterion that accounts for both anisotropy and asymmetry between yielding in tension and compression. Yield stresses calculated using a polycrystal model were used to determine the evolution of the macroscopic yield surface with accumulated deformation. The proposed model was implemented into the implicit finite element code ABAQUS. Simulations of the three dimensional deformation of pure zirconium beams subjected to a four-point bend test were performed. Predicted and measured macroscopic strain fields and beam sections are in very good agreement. Similar simulations were conducted for AZ31B magnesium which again demonstrated the effectiveness of the proposed model over using isotropic hardening, however no experimental data for AZ31B was available for comparison. The simulation results for zirconium and magnesium suggest that a computationally efficient macro-scale modeling, when used in conjunction with polycrystalline modeling, can accurately describe the strength differential effect and the anisotropic hardening observed in hcp metals.

The proposed model was extended to include the effects of strain-rate and temperature using two common approaches: the overstress method of Perzyna, and a rate-dependant consistency method. Both methods were shown to produce identical or nearly identical results depending on the assumptions made regarding unloading for the consistency model. The rate dependent model was implemented into an ABAQUS/EXPLICIT user material subroutine to simulate high strain-rate events.

Simulations of the Taylor impact test for zirconium and tantalum were performed and the results were shown to be in good agreement with experimental data.

For situations when a vast amount of experimental data is available for the determination of a material's yield surface, the proposed orthotropic yield criterion was modified through the addition of a second linear transformation, thus doubling the amount of available anisotropy coefficients. Using this modified criterion, the yield surface was represented for an aluminum alloy for which strength differentials between tensile and compressive yield have been experimentally observed. Using this criterion, circular cup drawing simulations were carried out, with the results shown to be in good agreement with experimental data.

In order to better capture the true behavior of the material, an appropriate anisotropic damage and anisotropic failure model need to be developed and incorporated into the proposed modeling approach. Furthermore, a more generalized approach to simultaneously capture the evolution of both yield stresses and r-values for any given strain path out to high levels of plastic deformation is needed.

LIST OF REFERENCES

ABAQUS Version 6.4 Reference Manuals, 2003. Pawtucket, RI.

Agnew, S. R., Yoo, M. H., Tomé, C.N., 2001. Simulation of texture simulation to understanding mechanical behavior of Mg and solid solutions alloys containing Li or Y, Acta mater.49, 4277-4289.

Agnew, S. R., Ashutosh, J., 2005. Anisotropic and asymmetric yield behaviour of magnesium alloy sheet assessed using a combined experimental and theorietical approach, Proceedings of 2005 NSF DMII Grantees Conf., Scottdale, AZ.

Banabic, D., Bunge, H-J, Pohlandt, K., Tekkaya, A.E., 2000. Formability of metallic materials: plastic anisotropy, formability testing, forming limits, Springer, Berlin, pp. 119-172.

Banabic, D., Cazacu, O., Barlat, F., Comsa, D.S., Wagner, S., Siegert, K., 2002. Description of anisotropic behaviour of AA3103-O aluminium alloy using two recent yield criteria. Journal de Physique IV 105**,** 297-304.

Barlat, F., Lege, D.J., Brem, J.C., 1991. A six-component yield function for anisotropic materials. Int. J. Plasticity 7, 693-712.

Barlat, F., Becker, R.C., Hayashida, Y., Maeda, Y., Yanagawa, M., Chung, K., Brem, J.C., Lege, D.J., Matsui, K., Murtha, S.J., Hattori, S., 1997. Yielding description of solution strengthened aluminum alloys. Int. J. Plasticity 13, 185-401.

Barlat, F., Brem, J.C., Yoon, J.W., Chung, K., Dick, R.E., Lege, D.J., Pourboghrat, F., Choi, S.-H., Chu, E., 2003. Plane stress yield function for aluminum alloy sheet-Part I: Theory. Int. J. Plasticity 19, 1297-1319.

Barlat, F., Aretz, H., Yoon, J.W., Karabin, M.E., Brem, J.C., Dick, R.E., 2005. Linear transformation-based anisotropic yield functions. Int. J. Plasticity 21, 1009-1039

Bishop, J. W. F, Hill, R. 1951. A theoretical deviation of the plastic properties of a polycrystalline face-centered metal. Phil. Mag. Ser. 7 42, 1298-1307.

Blewitt T. H., Coltman R. R., Redman J. K. 1957. Low-temperature deformation of copper single crystals. Journal of Applied Physics 28**,** 651.

Boehler, J. P., 1978. Lois de comportement anisotrope des milieux continues. J. Mec 17, 153-190

Bron, F., Besson, J. 2004. A yield function for anisotropic materials Application to aluminum alloys. Int. J. Plasticity 20, 937-963

Cazacu, O., Barlat, F., 2001. Generalization of Drucker's yield criterion to orthotropy. Mathematics and Mechanics of Solids 6, 613-630.

Cazacu O. and Barlat, F. 2003. Application of representation theory to describe yielding of anisotropic aluminum alloys. Int. J. of Engng. Sci. 41, 1367-1385.

Cazacu O. and Barlat, F. 2004. A criterion for description of anisotropy and yield differential effects in pressure-insensitive metals. Int. J. Plasticity. 20, 2027-2045.

Chin, G. Y., Mammel, W. L., Dolan, M.T., 1969. Taylor analysis for $\{111\}\langle 112\rangle$ twinning and $\{111\}\langle 110\rangle$ slip under conditions of axisymmetric flow. Trans. TMS-AIME 245, 383-388.

Crisfield M.A., 1991. Non-linear finite element analysis of solids and structures. Wiley, West Sussex, England.

Dafalias, Y.F., 1984. The plastic spin concept and a simple illustration of its role in finite plastic transformations. Mechanics of Materials 3, 223–233.

Drucker, D.C., 1949. Relation of experiments to mathematical theories of plasticity. J. Appl. Mech. 16, 349-357.

Drucker, D.C., 1950. Stress-strain relations in the plastic range, a survey of theory and experiment. Report to the Office of Naval Research *NR*-041-032.

Fundenberger, J.J. ,Phillipe, M.J., Wagner, F., Esling, C., 1997. Modelling and predictions of mechanical properties for materials with hexagonal symmetry (zinc, titanium, and zirconium alloys). Acta Mater. 45, 4041-4055.

Heeres, O. M., Suiker, A. S. J., de Borst, R. 2002. A comparison between the Perzyna viscoplastic model and the Consistency viscoplastic model. European J. of Mech. 21, 1-12.

Hershey, A. V. 1954. The plasticity of an isotropic aggregate of anisotropic face centered cubic crystals. J. Appl. Mech. Trans. ASME, 21, 241-249.

Hill, R., 1948. A theory of the yielding and plastic flow of anisotropic metals. Proc. Roy. Soc. London A193, 281–297.

Hill, R., 1950. The Mathematical Theory of Plasticity. Oxford University Press, London.

Hill, R., 1990. Constitutive modelling of orthotropic plasticity in sheet metals. J. Mech. Phys. Solids 38, 405–417.

Hill, R., 1993. A user-friendly theory of orthotropic plasticity in sheet metals. Int. J. Mech. Sci. 35, 19–25.

Hosford, W.F., 1966. Texture strengthening, Metals. Eng. Quarterly, 6, 13-19.

Hosford, W. F., 1972. A generalized isotropic yield criterion, J. Appl. Mech. 39, 607-609.

Hosford, W. F. and Allen, T. J., 1973. Twining and directional slip as a cause for strength differential effect. Met. Trans. 4, 1424-1425.

Hosford, W. F., 1993. The Mechanics of Crystals and Textured Polycrystals. Oxford University Press, New York.

Hosford, W. F., 1996. On the crystallographic asis of yield criteria. Textures and Microstructures, 26-27, 479-493

Huang, J. Y., Wu, Y. K., Ye, H. Q., 1996. Deformation structures in ball milled copper. Acta Metallurgica, 44, 1211-1221.

Johnson, G. R., Cook, W. H., 1983. A constitutive model and data for metals subjected to large strains, high strain rates, and high temperatures. Proceedings of Seventh International Symposium on Ballistics.

Karafillis, A.P., Boyce, M.C., 1993. A general anisotropic yield criterion using bounds and a transformation weighting tensor. J. Mech. Phys. Solids 41, 1859-1886.

Kaschner, G. C. and Gray, G. T., 2000. The Influence of Crystallographic Texture and Interstitial Impurities on the Mechanical Behavior of Zirconium. *Metall. Trans. A.*, 31 A, 1997-2003

Kaschner, G. C., Bingert, J. F., Liu, C., Lovato, M. L., Maudlin, P. J., Sout, M. G., Tome, C. N., 2001. Mechanical response of zirconium – II experimental and finite element analysis of bent beams. Acta Mater 49, 3097-3108.

Kelley, E.W., Hosford, W.F., 1968. Deformation characteristics of textured magnesium. Trans. TMS-AIME 242, 654-661.

Klimanek, P., Pötzsch, A ,2002. Microstructure evolution under compressive plastic deformation of maganesium at different temperatures and strain rates. Mat. Sci. & Eng. A 324, 145-150.

Kocks, U. F., Tome, C. N., Wenk, H. R., 2000. Texture and Anisotropy. Cambridge University Press, Cambridge UK.

Kuwabara, T., Katami, C., Kikuchi, M., Shindo, T. and Ohwue, T., 2001 Cup drawing of pure titanium sheet -finite element analysis and experimental validation. In: Proceedings of the 7th Int. Conf. Numerical Methods in Industrial Forming Processes, Toyohashi, Japan, 18-20 June, pp.781.

Lee, D., Backofen, W. A., 1966. An experimental determination of the yield locus for titanium and titanium-alloy sheet. TMS-AIME 236, 1077-1084

Li, S., Hoferlin, E., Van Bael, A., Van Houtte, P. and Teodosiu, C., 2003. Finite element modeling of plastic anisotropy induced by texture and strain-path change. Int. J. Plasticity, **19**, 647.

Liu, S. I., 1982. On representation of anisotropic invariants. Int. J. Eng. Science 20, 1099-1109

Logan, R. W., Hosford, W. F., 1980. Upper-bound anisotropic yield locus calculations assuming $\langle 111 \rangle$ pencil glide. Int J. Mech Sci. 22, 419-430

Malvern, L. E. 1969. Introduction to the mechanics of a continuous medium. Prentice-Hall. Inc, Upper Saddle River, NJ.

Maudlin, P. J., Bingert, J. F., House, J. W., Chen, S. R., 1999a. On the modeling of the Taylor cylinder impact test for orthotropic textured materials: experiments and simulations. Int J. Plas. 15, 139-166

Maudlin, P. J., Gray, T. G., Cady, C. M., Kaschner, C. G., 1999b. High rate material modeling and validation using the Taylor cylinder impact test. Phil Trans R. Soc. 357, 1707-1729

Molinari, A., Canova, G. R., Ahzi, S., 1987. A self consistent approach of the large deformation polycrystal viscoplasticity. Acta Mater. 35, 2983-2994

Molinari, A., 1997. Self-consistent modeling of plastic and viscoplastic polycrystalline materials. In: Large plastic deformation of crystalline aggregates, Springer, New York, pp. 173-246

Perzyna, P, 1966. Fundamental problems in viscoplasticity, in: Recent Advances in Applied Mechanics, vol. 9, Academic Press, New York, pp. 243–377

Rockafellar, R.T., 1972. Convex Analysis. Princeton University Press, Princeton, NY.

Simo, J. C., Hughes, T. J. R., 1998. Computational Inelasticity. Springer-Verlag, New York.

Simo, J. C., Taylor, R. L., 1985. Consistent tangent operators for rate independent elasto-plasticity. Comput Methods Appl Mech Engrg. 48, 101-118.

Sobotka, Z., 1969. Theorie des plastischen Fliessens von anisotropen Körpern. Zeit. Angew. Math. Mech. 49, 25–32.

Spitzig, W.A, Sober, R.J., Richmond, O., 1976. The effect of hydrostatic pressure on the deformation behavior of Maraging and HY-80 steels and its implication for plasticity theory. Metall. Trans. 7A, 1703-1710.

Spitzig, R.J., Richmond, O., 1984. The effect of pressure on the flow stress of metals. Acta Metall. 32, 457-463.

Staroselsky, A., Anand, L., 2003 A constitutive model for hcp materials deforming by slip and twinning: application to magnesium alloy AZ31B. Int. J. Plasticity 19, 1843-1864.

Styczynski, A., Hartig, C., Bohlen, J., Letzig, D., 2004. Cold rolling textures in AZ31 wrought magnesium alloy. Scripta Mat 50, 943-947.

Takuda,H., Yoshii, T., Hatta, N., 1999. Finite-element analysis of the formability of a magnesium-based alloy AZ31 sheet. J. Materials Processing Techn., 89-90, 135-140.

Taylor, G.I., 1938. Plastic strains in metals. J. Inst. Metals. 62, 307–324.

Taylor, G.I., Quinney, H., 1931. The plastic distortion of metals. Phil. Trans. Roy Soc. A230, 323-362.

Teodosiu, C., Hu, Z., 1995. Evolution of the intragranular microstructure at moderate and large strains: modelling and computational signi.cance. In: Shen, S.F., Dawson, P.R. (Eds.), Simulation of Materials Processing: Theory, Methods and Applications. Balkema, Rotterdam, pp. 173–182.

Tomé, C., Kocks, U. F., 1985. The yield surface of h.c.p crystals. Acta Metall. 33, 603-621.

Tome, C. N., Lebensohn, R. A., Kocks, U. F., 1991. A model for texture development dominated by deformation twinning: Application to zirconium alloys. Acta Mater. 39, 2667-2680

Tome, C. N., Maudlin, P. J., Lebensohn, R. A. and Kaschner, G. C., 2001. Mechanical Response of zirconium-I. Derivation of a polycrystal constitutive law and finite element analysis. Acta Mater. 49, 3085-3096.

Tome, C. N., Lebensohn, R. A., 2004a. Manual for Visco-Plastic Self-Consistent Code version 6.

Tome, C. N., Lebensohn, R. A., 2004b. Self Consistent Homogenization Methods for Texture and Anisotropy. In: Continuum Scale Simulation of Engineering Materials. Wiley-VCH, Weinheim, pp. 473-497

Van Houtte, P., 1978. Simulation of the rolling and shear texture of brass by the Taylor theory adapted for mechanical twinning. Acta Metall. 26, 591-604.

Von Mises, R., 1928. Mechanik der festen Korper im plastisch-deformablen zustand. Nachrichten Konogl, Gesellsch, Wissenschaften Gottinger, Math. 582-592.

Wang, W. M., Sluys, L. J., De Borst, R., 1997. Viscoplasticity for instabilities due to strain softening and strain-rate softening. Int. J. Num. Meth. Engrg. 40, 3839-3864.

Yoon, J. W., Yang, D. Y., Chung, K., Barlat, F., 1999. A general elasto-plastic finite element formulation based on incremental deformation theory for planar anisotropy and its application to sheet metal forming. Int. J. Plasticity 15, 35-67

Yoon, J. W., Barlat, F. Chung, K., Pourboghrat, F., Yang, D. Y., 2000. Earing predictions based on asymmetric nonquadratic yield function. Int. J. Plasticity 16, 1075-1104.

Yoon, J. W., Barlat, F., Dick, R. E., Chung, K., Kang, T. J., 2004. Plane stress yield function for aluminum alloy sheets – part II: FE formulation and its implementation. Int. J. Plasticity 20, 495-522.

BIOGRAPHICAL SKETCH

Brian W. Plunkett was born in Hartsville, SC, on July 3, 1974. He graduated with a Bachelor of Science in Mechanical Engineering from the University of Alabama in December, 1996. Upon graduation, he was commissioned as an officer in the United States Air Force, and served from February 1, 1997, until January 31, 2001, as a mechanical engineer at Robins AFB, GA. Brian was then hired by the Air Force as a civilian weapons test engineer for the Munitions Test Division at Eglin AFB, FL. While working at Eglin AFB, he completed a Master of Engineering degree from the University of Florida in August of 2003. Following an Air Force fellowship as a full-time graduate student working on a PhD at the University of Florida, Brian transferred to the Air Force Research Laboratory at Eglin AFB, FL, in August of 2005.